FINITE ELEMENT AND EXPERIMENTAL STUDIES ON DEFORMATION BEHAVIOR OF NANOGLASS AND METALLIC GLASS STRUCTURES

Ph.D. Thesis

By

HIRMUKHE SIDRAM SAYABANNA

DEPARTMENT OF MECHANICAL ENGINEERING

INDIAN INSTITUTE OF TECHNOLOGY INDORE

NOVEMBER 2021

FINITE ELEMENT AND EXPERIMENTAL STUDIES ON DEFORMATION BEHAVIOR OF NANOGLASS AND METALLIC GLASS STRUCTURES

A THESIS

Submitted in partial fulfillment of the
requirements for the award of the degree
of
DOCTOR OF PHILOSOPHY

by

HIRMUKHE SIDRAM SAYABANNA

DEPARTMENT OF MECHANICAL ENGINEERING
INDIAN INSTITUTE OF TECHNOLOGY INDORE

NOVEMBER 2021

INDIAN INSTITUTE OF TECHNOLOGY INDORE

CANDIDATE'S DECLARATION

I hereby certify that the work which is being presented in the thesis entitled "**Finite Element and Experimental Studies on Deformation Behavior of Nanoglass and Metallic Glass Structures** in the partial fulfillment of the requirements for the award of the degree of **DOCTOR OF PHILOSOPHY** and submitted in the **Department of Mechanical Engineering, Indian Institute of Technology Indore**, is an authentic record of my own work carried out during the time period from December 2017 to November 2021 under the supervision **of Dr. Indrasen Singh, Assistant Professor, IIT, Indore**.

The matter presented in this thesis has not been submitted by me for the award of any other degree of this or any other institute.

(30/03/2022)

Signature of the student with date
(HIRMUKHE SIDRAM SAYABANNA)

This is to certify that the above statement made by the candidate is correct to the best of my knowledge.

30/03/2022

Signature of Thesis Supervisor #1 with date

(DR. INDRASEN SINGH)

HIRMUKHE SIDRAM SAYABANNA has successfully given his Ph.D. Oral Examination held on **March 30, 2022**.

30/03/2022

Signature of Thesis Supervisor #1 with date

(DR. INDRASEN SINGH)

Dedicated

To

My beloved Family

ACKNOWLEDGEMENTS

I would like to express my sincere gratitude to my research supervisor Dr. Indrasen Singh for agreeing to guide me. I am extremely lucky to have a supervisor who cared so much about my work, and who responded to my questions and queries so patiently and promptly. During interaction with him, I have gained profound understanding, knowledge and awareness of scientific and technical aspect of the research. I am very much thankful to him for teaching me how to analyze the results and how to write scientific article. Without his kind encouragement and constant support, it would not have been possible to accomplish this great task. It is a great honour to work under his supervision.

I would like to thank our research collaborator Prof. Horst Hahn and Dr. Harsha Nandam, Karlsruhe Institute of Technology (KIT), Germany for providing nanoglass and metallic glass samples. Also, I would like to thank Prof. U. Ramamurty, Nanyan Technological University (NTU), Singapore, and Dr. Abhishek Chaturvedi, Indian Institute of Science (IISc), Bangalore for access to nanoindentation test facility. I would like to thank Prof. R. Narasimhan, Indian Institute of Science (IISc), Bangalore for providing UMAT code.

I would like to express my sincere gratitude to my PG Student Progress Committee members Dr. S. I. Kundalwal, Department of Mechanical Engineering and Dr. K. E. Prasad, Department of Metallurgy Engineering and Material Science, Indian Institute of Technology (IIT), Indore for their valuable comments and suggestions to improve the quality of this thesis. I would like to thank present and past Head of Department (HOD) and Discipline Post-Graduate Committee (DPGC) Convener for offering all departmental facilities for my research work. I like acknowledge CAD lab manager Mr. Kailash Patel for his support to use CAD lab resources for my research work.

I would like to acknowledge present and past Directors of IIT Indore, Prof. Neelesh Kumar Jain and Prof. Pradeep Mathur for providing a conductive environment for research and opportunity to explore my research capabilities at IIT Indore. I am also thankful to The Dean of Academic Affairs, The Dean of Research and Development and The Dean of Student Affairs, IIT Indore. I would like to thank to all faculties and staff members of IIT Indore who have knowing and unknowingly helped me in completion of my research work. I am thankful to Ministry of Education, Government of India for financial assistance.

I would like to thank my past and present lab mates- Aditya Raj, Sunil Gurjar, Shan Malviya, Gurram Sai Vilas, Prasenjeet Jain, Samiksha Dhote, Swaroop Zanke, Anurag Sharma, Harsh Sharma, Ramanand Dadhich, Sumit Chorma, Apurva Jadhav, Akhilesh Joshi,

Prathmesh Pawar for providing pleasant company and constant support during my time in Computational Solid Mechanics lab. I thoroughly enjoyed technical discussion with Harsh, Prathmesh, Akhilesh and debates on social issues were really thoughtful.

I want to thank my friends come colleague, Dr. P.R. Kale, Dr. A. D. Diwate, Mr. V. V. Ankolekar, Mr. N. B. Pokale, Mr. Santosh Mahajan, Mr. Ganesh Lamdhade, Mr. Vikas Mali for motivating me to pursue doctoral study and helping me in my tough time. It is impossible to express in word how much I owe to all my friends in IIT Indore. However, I especially wish to thank to Mr. Vaibhav Nemane, Mr.Achyut Kulkarni, Dr. Kishor Shingare, Mr. Vaibhav Kathavate, Mr. Aditya Bhardwaj and Mr. Abhinav Sharma for supporting me in my initial stage of PhD. I would like acknowledge especial thanks to Achyut Kulkarni for serving delicious food for one year during my stay in his flat. I like to thank my neighbours at IIT indore, Dr. Vivek, Mr. Omkar, Mr. Akshay, Mr. Manoj, Mr. Birla, Mr. Mahesh, Mr. Palash and their family for giving me and my family a wonderful living atmosphere in J.C. Bose residential apartment.

Finally, I would like thank to my wife Mrs. Jyoti for her love, motivation, valuable prayers and support during good and bad moments at IIT, Indore. I would like express my especial thanks to my daughter Adhira for time spent with her keeps me away from the work stress. I would like to thank my in-laws and brother in-law (Mahesh) for taking care of my wife and daughter without any hesitation during my PhD course work. I would like thank to my sister Dr. Archana for taking care of me and my family during my bad health conditions and motivating me during my tough time at IIT, Indore. I would like to express my deep gratitude towards my Parents and brothers Mr. Anant and Mr. Gunvant for their blessing, constant encouragement and support.

I would like to thanks to all those who helped me directly or indirectly during various stages of this work.

Sidram Hirmukhe

SYNOPSIS

Metallic glasses (MGs) have shown attractive mechanical properties such as high yield strain (~2%), high strength (~ 2Gpa), excellent corrosion resistance and exeptional forming ability making them a potential candidate for structural as well as functional applications including medical implant, micro/nano-electromechanical devices, sports equipements, aerospace and defence industry (Telford, 2004). However, MGs exhibit localization of plastic strain in narrow bands, called as shear band, and fail in brittle manner under tensile loading due to unhindered propagation of crack inside a predominant band (Schuh et al., 2007). The lack of tensile ductility in MGs impedes their employment as structural material, which has motivated researchers to explore various strategies to improve plastic deformation in MGs such as synthesiging nanoglass (NG) architecture (Ivanisenko et al., 2018), NG-MG composites (Adibi et al., 2016; Sha et al., 2017) and MG cellular structures (Sarac and Schroers, 2013b; Zhang et al., 2016).

NGs are comprised of glassy grains separated by fine interfaces which exhibits low density (Sopu et al., 2009; Ritter et al., 2011) and excess free volume (Fang et al., 2012). Consequently, multiple shear bands nucleate from these interfaces which are distributed over the entire volume of the material leading to enhanced tensile ductility in NGs. Recent indentation experiments show that NGs exhibit a higher hardness, *H*, than the melt spun MGs of identical composition (Franke et al., 2014; Nandam et al., 2017). The high *H* in NG is attributed to the Zr rich dense core surrounded by Cu rich interfaces carrying excess free volume (Nandam et al., 2017). However, it is not clear as to why *H* should increase in the presence of free volume rich interfaces. Experimental and numerical studies of indentation on MGs show that the reasons for high *H* in these materials is intimately connected with the pressure sensitive plastic flow taking place beneath the indenter (Patnaik et al., 2004), and *H* appears to increase with the pressure sensitive index, α which quantified the pressure sensitivity (Narasimhan, 2004). Given the amorphous structure of NGs with glassy grains and interfaces, the plastic flow of NGs could be expected to be pressure sensitive which may be the reason for high *H* observed in these materials although it has not been investigated in detail.

Therefore, finite element simulations are performed using the pressure insensitive (Von-Mises) and pressure sensitive (extended Drucker Prager) plasticity model to analyze the indentation behavior of $SC_{75}Fe_{25}$ NGs and MGs. The α for NG and MG ribbons are determined by fitting the *P* vs. *h* curves reported in literature, and α for glassy interface has

also been determined by modeling the microstructure of NGs. Results show that simulation $P-h$ curve obtained by Von Mises criterion (refer curve pertaining to $K=1$ and $\alpha=0^0$ in Fig. 1(a)) deviates significantly from experimental data suggesting that Von Mises criterion does not describe the yield behavior in NGs. However, the curve obtained using extended Drucker Prager plasticity model exhibits good agreement with experimental data (refer curves corresponding to $K=1$ and $\alpha=15-20^0$ in Fig. 1(a)). This suggests that the yield behavior in $Sc_{75}Fe_{25}$ NG is characterized more accurately by pressure sensitive extended Drucker Prager plasticity model. In fact, α for NG is found to be around three times higher than that of MG identical composition (refer curves corresponding to $\alpha=12^0$ and 4^0 in Fig. 1(b)) making former harder than the latter. The indentation simulations performed by modeling the microstructure of NG (i.e. grains and interfaces) show that α for glassy interface is much higher than the grains in $Sc_{75}Fe_{25}$ NG.

Further, the hardness in MGs observed to decrease with increase in the indentation load which is commonly referred to as the indentation size effect (ISE). It has been proposed that the concentration of the geometrically necessary flow defects (GNFDs) such as free volume (Lam and Chong, 2001) or shear clusters (Yang et al., 2007) increases with decrease in indentation depth, which causes enhancement in flow stress of the material. However, it is not clear why the flow stress should increase with increase in flow defects. Some authors disagree with ISE in MGs and have suggested that it is an experimental artifact (Huang et al., 2010) or caused by friction between work piece and indenter (Pang et al., 2012). As pointed out above that the pressure sensitivity in NGs is higher than MG. In this view, a fundamental question" what is the effect of pressure sensitivity on the ISE in glasses" arises. It must be noted that this issue is not investigated and answer to this question would shed light on the mechanism governing ISE in NGs and MGs. Therefore, nanoindentation experiments are performed at different peak loads on a binary $cu_{60}Zr_{40}$ NG and MG. Further, to clearly understand the subsurface deformation behavior, bonded interface experiments are performed using a Vickers indenter. The complementary finite element simulations of nanoindentation are also performed by employing the finite strain viscoplastic constitutive theory for amorphous metals (Anand and Su, 2005).

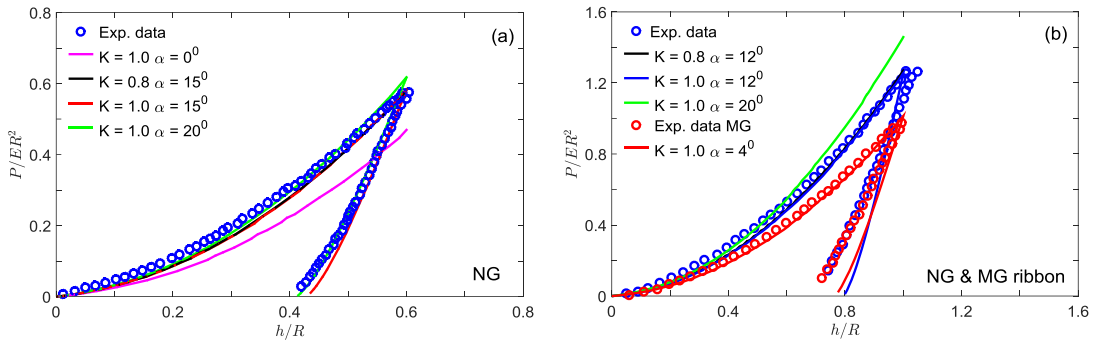

Figure 1 (a) Normalized indentation load, P/ER^2 versus normalized depth, h/R curves for NG corresponding to different values of α and K, along with the experimental data of Liu et al. (2018). (b) Corresponding curves for NG and MG ribbon along with the experimental data of Franke et al. (2014).

The bonded interface experiments reveal smooth and almost semi-circular shaped shear bands in MG, while the formation of wavy shear bands is observed in NG. Further, the primary shear band densities in the MG are higher than that in NG, while the plastic zone size below the indenter is larger in the latter than the former. Furthermore, nanoindentation experiments show that NGs and MGs exhibit ISE (refer Fig. 2), while ISE is more pronounced in the latter than former. The finite element simulations show that less pronounced ISE in NG than MG is caused by the slower free volume generation leading to slower softening during indentation in the former than the latter. Also, the value of friction coefficient, μ for NG is higher than MG due to higher μ for interfaces in the former. Further, the higher μ retards the free volume generation and hence softening resulting in less pronounced ISE in NG.

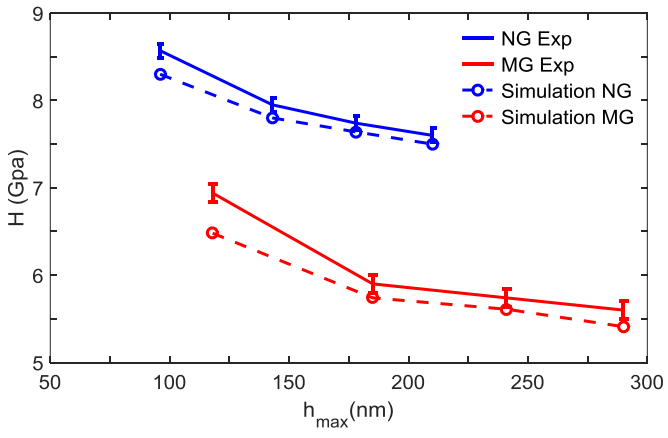

Figure 2 Dependence of indentation hardness, H calculated at the end of the holding stage, on the maximum indentation depth, h_{max} for NG and MG along with corresponding H values obtained from the finite element simulations.

A considerable effort has been made to understand the deformation behavior of NGs under tensile, compressive and indentation loading. However, a few studies have been undertaken to under the fracture response of NGs. The crack tip plasticity and fracture toughness in MGs are found to be significantly influenced by mode-mixity (Tandaiya et al., 2009). However, such investigation has not been performed for NGs which is essential because complex loading in actual applications may lead to mixed-mode fracture in NG components. Therefore, 2D plane strain, small scale yielding (SSY), finite element analysis on the stationary crack in NG and MG under mixed mode loading conditions are performed using the constitutive model of Anand and Su (2005). Results show that the crack tip plasticity are markedly affected by mode-mixity for both NG and MG. For given mixed mode loading, the plastic zone size in front of notch tip is larger in NG than MG. Further, the strain-based fracture criterion predicts that NGs may not show significant higher fracture toughness in comparison to MG with identical composition, though they exhibit significant larger tensile ductility.

It must be mentioned that NGs with larger thickness cannot be synthesized due to limitation of present manufacturing techniques. Therefore, the idea of developing laminate composites with alternative layers of NG and MG have been proposed to achieve large tensile ductility without compromising strength significantly (Adibi et al., 2016; Sha et al., 2017). Sha et al. (2017) demonstrated from MD simulations that the deformation behavior of such NG-MG composites transitions from shear localization to superplastic flow when MG layer

thickness is reduced below a threshold level which they correlated to the glassy grain size of the NG layers. However, it is not clear as to why and how the glassy grain size of the NG layer controls the threshold thickness of MG layer. To address this issue, 2D plane strain finite element simulations of tensile loading on NG-MG laminate composites are performed using a thermodynamically consistent finite strain non-local plasticity model (Thamburaja, 2011). Results show that interaction stress associated with flow defects such as shear transformation zones (STZs) plays a pivotal role in the deformation response of laminate composites. Also, shear band width in these materials scales with intrinsic material length associated with the interaction stress. Further, the material length with respect to MG layer thickness governs the transition in deformation behavior. The results provide insights about the underlying deformation mechanism.

Further, cellular MGs have been fabricated which are found to be an alternative choice for structural and functional applications owing to light in weight, good energy as well as noise absorption capacity and enhanced plastic deformation (Sarac and Schroers, 2013b). Sarac and Schroers (2013b) have reported transition in deformation mode from global failure caused by localization in a shear band to the local failure by damage confined to few cells with reduction in relative density of specimen from a large to moderate value. The mode of deformation again changes over to the collective buckling of ligaments through row by row collapse when the relative density is decrease to a sufficiently lower level. Similarly, the atomistic simulations (Zhang et al., 2016) on nanoscale cellular MGs have also reported transition from localized but confined to few cells to almost homogeneous deformation with increasing cell size. They have also shown strain localization in a dominant shear band for cell spacing above a threshold value which was correlated to shear bandwidth in monolithic MG of identical composition. However, it is not clear from these simulations as to why and how the shear band thickness in monolithic MG controls the threshold cell-spacing. To address this issue, 2D plane strain finite element simulations of compressive loading are performed on nanoscale cellular MGs using the plasticity model of Thamburaja (2011). The finite element simulations successfully predict the two transitions in deformation mode as observed in atomistic simulations and experiments. Further, results show that the transition in deformation behavior is governed by the ratio of cell-wall thickness to the intrinsic material length associated with interaction stress. Also, the moderate change in sample size has marginal effect on the deformation response of MG cellular structure.

In closing, the present thesis is focused on understanding the deformation and fracture behavior in NGs and MG structures. The insights gained would provide guidelines in developing NGs, NG-MG composites and cellular MG structures capable of showing larger plastic deformation for practical engineering applications.

The organization of the present thesis is as follows:

In Chapter 1, the brief introduction of MGs and NGs and mechanism of plastic deformation in MGs are discussed. Further, pertinent literature review, issues for investigation and objective and scope of thesis also presented.

In chapter 2, axisymmetric finite element indentation simulations are performed using extended Drucker Prager plasticity model. The α for NGs and MGs is determined.

In chapter 3, Micro and nanoindentation experiments on NG and MG are performed and important results from the experiments are also discussed. The complementary finite element nanoindentation simulations are performed using the amorphous metals constitutive model proposed by Anand and Su (2005) to elucidate the underlying mechanism governing ISE in NGs.

In chapter 4, Mixed mode (I and II) loading of a stationary crack in NGs and MGs is studied through finite element simulations under 2D plane strain, SSY condition using constitutive model of Anand and Su (2005). The effect of the presence of interfaces on crack tip plasticity and fracture toughness is examined.

In chapter 5, tensile loading of NG-MG nanolaminate composites are analyzed through 2D plane strain finite element simulations using a thermodynamically consistent finite strain based non-local plasticity model (Thamburaja, 2011). The physical origin of the threshold level of MG layer thickness for transition in deformation behavior from localized to superplastic flow in NG-MG nanolaminate composite is studied.

In chapter 6, compressive loading of nanoscale cellular MGs are analyzed using the model of Thamburaja (2011) and the effect of cell- spacing and role of interaction stress associated with flow defects such STZs on the deformation behavior of nanoscale cellular MGs is discussed.

In chapter 7, the important conclusions drawn from the chapter 2-5 are summarized and the possible further works are also discussed.

List of publication from present thesis work

1. **Hirmukhe S. S.**, Prasad K. E., Singh I. (2019), Finite element analysis of tensile deformation of nanoglass-metallic glass laminate composites, *Computational Material Science*, 161, 83-92. doi.org/10.1016/j.commatsci.2019.01.031 (Impact factor 3.30).
2. **Hirmukhe S. S**, Prasad K. E., Singh I. (2020), Investigation of pressure sensitive plastic flow in nanoglasses from finite element simulations, *Scripta Materialia*, 180, 45-50. doi.org/10.1016/j.scriptamat.2020.01.022 (Impact factor 5.60).
3. **Hirmukhe S. S.**, Prasad K. E., Singh I. (2021), Finite element analysis of deformation and failure mechanism in nanoscale hexagonal cellular structure of metallic glasses, *Mechanics of Materials*, 161, 103940. doi.org/10.1016/j.mechmat.2021.103946 (Impact factor 3.26).
4. **Hirmukhe S. S.**, Sharma A., Nandam S. H., Hahn H., Prasad K. E., Singh I. (2021), Investigation of softening induced indentation size effect in nanoglass and metallic glass, *Journal of Non-Crystalline Solids*, 577, 121316**.** doi.org/10.1016/j.jnoncrysol.2021.121316 (Impact factor 3.53).
5. **Hirmukhe S. S.**, Joshi A. T., Singh I. (2021), Mixed mode (I & II) fracture behavior in nanoglass and metallic glass, *Journal of Non-Crystalline Solids*, 580, 121390**.** doi.org/10.1016/j.jnoncrysol.2021.121390 (Impact factor 3.53).

List of publication out of present thesis work

1. Sharma A., **Hirmukhe S. S.**, Nandam S. H., Hahn H., Singh I., Prasad K.E., A nanoindentation study on the effect of strain rate sensitivity in Cu-Zr based nanoglass and metallic glass (**Manuscript under preparation**).

List of conferences/oral presentations from present thesis work

1. **Hirmukhe S. S.**, Prasad K. E., Singh I. (2021), Quasi-Brittle to ductile transition in metallic glass-nanoglass laminate composites, WCCM2020, 11-15 Jan 2021, Paris, France.

TABLE OF CONTENTS

ACKNOWLEDGEMENTS i-ii

SYNOPSIS iii-ix

LIST OF FIGURES xv-xxiii

LIST OF TABLES xxiv

NOMENCLATURE xxv-xxix

ACRONYMS xxx-xxxi

Chapter 1: Introduction **1-20**

1.1 Plastic deformation in amorphous metals 2

1.2 Constitutive model in MGs 3

1.3 Review of pertinent literature 4

1.3.1 Instrumented indentation Test 4

1.3.2 Deformation response of MGs 6

1.3.2.1 Indentation Response of MGs 6

1.3.2.2 Fracture response in MGs 8

1.3.3 Ductility enhancement in MGs 9

1.3.3.1 Deformation behavior of Nanoglasses 10

1.3.4 Tensile deformation of nanolaminate composite 13

1.3.5 Deformation response of cellular MG structures 14

1.4 Issues for investigation 15

1.4.1 Pressure sensitive plastic flow in NGs 15

1.4.2 Indentation size effect in NGs and MGs 15

1.4.3 Mixed mode (I and II) fracture response in NGs 16

1.4.4 Tensile deformation of NG- MG nanolaminate composite 16

1.4.5 Deformation and failure mechanism of nanoscale cellular structure of MGs 17

1.5 Objective and scope of the thesis 17

1.6 Organization of thesis 19

Chapter 2: Investigation of pressure sensitive plastic flow in nanoglasses from finite element simulations **21-34**

2.1 Introduction 21

2.2 Constitutive model 22

2.3 Modeling aspects 23

2.4 Result and discussion 25

Chapter 3: Investigation of softening induced indentation size effect in nanoglass and metallic glasses **35-56**

3.1 Introduction 35

3.2 Experimental procedure 36

3.3 Constitutive model 37

3.4 Modeling aspects 38

3.5 Result and discussion 42

3.5.1 Subsurface deformed morphology from microindentation Experiments 42

3.5.2 Nanoindentation experiments 43

3.5.3 Finite element simulations of nanoindentation 45

Chapter 4: Mixed mode (I & II) fracture behavior of nanoglass and metallic glass **57-76**

4.1 Introduction 57

4.2 Constitutive model 57

4.3 Determination of material parameters for NG and MG 58

4.4 Modeling aspects of fracture simulations of crack initiation 62

4.5 Result and discussion 65

4.5.1 Evolution of plastic strain near the notch tip 65

4.5.2 The effect of M^e on the evolution of plastic zone size in NG and MG 69

4.5.3 Deformation of notch surface in NG and MG 71

4.5.4 Effect of mode mixity on the fracture toughness of NG and MG 74

Chapter 5: Finite element analysis of tensile deformation of nanoglass-metallic glass laminate composites **77-100**

5.1 Introduction 77

5.2 Constitutive model 78

5.3 Modeling aspects 79

5.4 Result and discussion 82

5.4.1 Deformation behavior of NG-MG laminate composite with single NG layer 82

5.4.1.1 Nominal stress versus strain curve 82

5.4.1.2 Evolution of plastic strain 84

5.4.1.3 Effect of l_c on the deformation behavior 91

5.4.2 Deformation behavior of multi-layer NG-MG laminate Composite 94

Chapter 6: Finite element analysis of deformation and failure mechanism in nanoscale hexagonal cellular structures of metallic glasses **101-118**

6.1 Introduction 101

6.2 Constitutive model 102

6.3 Modeling aspects 102

6.4 Result and discussion 104

6.4.1 Nominal stress versus nominal strain curve 104

6.4.2 Evolution of plastic strain 108

6.4.3 Influence of l_c on the deformation behavior 112

6.4.4 Influence of specimen size on the deformation behavior 116

Chapter 6: Conclusion **119-124**

7.1 Investigation of pressure sensitive plastic flow in nanoglasses from finite element simulations. 119

7.2 Investigation of softening induced indentation size effect in nanoglass and metallic glass 119

7.3 Mixed mode (I and II) fracture behavior in nanoglass and metallic glass. 120

7.4 Finite element analysis of tensile deformation of nanoglass-metallic glass laminate composites 121

7.5 Finite element analysis of deformation and failure mechanisms in nanoscale hexagonal cellular structures of metallic glasses 122

7.6 Scope for future study 123

APPENDIX A **125-126**

REFERENCES **127-140**

LIST OF FIGURES

Figure No.	Caption of Figures	Page No.
1.1	Schematic showing the microscopic deformation mechanisms proposed for MGs. (a) A shear transformation zone (STZ model) (Argon 1979) and (b) local atomic jump model (Free volume model) (Spaepen, 1977). Figures are taken from Schuh et al. (2007).	2
1.2	(a) Experimental and simulated indentation load vs indentation depth curve. The Top view of indentation impressions observed from (b) experiment and (c) simulations using Mohr-coulomb yield criterion, respectively. Images are taken from Vaidyanathan et al. (2001).	6
1.3	The variation of hardness, H, calculated at the end of holding stage with respect to maximum indentation depth, h_{max}, reported by Steenberge et al. (2007).	8
1.4	The optical micrographs showing shear bands near the notch tip region in Zr-based MG subjected to (a) $M^e = 0$ (pure mode II loading) and (b) $M^e = 0.45$. Images are taken from the work of Tandaiya et al. (2009).	9
1.5	(a) The transmission electron microscope (TEM) image of the Ni-based NGs. The dark and light contrast areas correspond to the glassy grains and glassy interfaces, respectively. The inset shows the corresponding selected area diffraction (SAED) pattern. (b) The high-resolution transmission electron microscope (HRTEM) image of Ni-based NGs (the insets display SAED patterns of both glassy grain and glassy interface regions). Images are taken from Li et al. (2018).	11
1.6	(a) The tensile stress-strain curves of the Sc-based NG and MG. (b) The tensile specimen of NG after test. (c) The tensile specimen of MG after test. Images are taken from Wang et al. (2015).	11

1.7	Representative indentation load, P vs depth, h curves of MG ribbon, as-prepared NG and annealed NG. Pop-ins were not observed in NG samples while it was noticed in MG ribbons (indicated by arrows). The image is taken from Nandam et al. (2017).	13
2.1	(a) 2D Axisymmetric finite element model of cylindrical specimen along with 'Berkovich equivalent' conical rigid indenter with half cone angle of 70.3^0 employed in indentation simulations. (b) Finite element model of cylindrical sample considering microstructure of NG in a region A, while homogenized NG in region B. (c) Enlarged view of region A and a grain whose size is characterized by length d_1 and d_2.	24
2.2	(a) Normalized indentation load, P/ER^2 versus normalized depth, h/R curves for NG1 corresponding to different values of α and K, along with the experimental data of Liu et al. (2018). (b) Corresponding curves for NG2 and MG ribbon along with the experimental data of Franke et al. (2014). (c) Corresponding curves for NG3 and MG ribbon along with the experimental data of Wang et al. (2015).	26
2.3	The variation of normalized hardness, H/σ_y^c with normalized indentation strain, $Ea/\sigma_y^c R$ predicted by finite element simulations and expanding cavity model (Narasimhan, 2004).	28
2.4	Contour plots of equivalent plastic strain, $\bar{\epsilon}^p$ corresponding to h/R = 0.6 for (a) NG1 and (b) MG ribbon.	28
2.5	(a) Variation of equivalent plastic strain, $\bar{\epsilon}^p$ along the depth of specimen of NG1 and MG ribbon (b) and (c) corresponding plots for specimen NG2 and MG ribbon and specimen NG3 and MG ribbon, respectively.	29
2.6	(a) Normalized indentation load, P/ER^2 versus normalized depth, h/R curves generated from simulation L, M and N on NG1, along with the experimental data of Liu et al. (2018). (b) Distribution of equivalent plastic strain, $\bar{\epsilon}^p$ below the indenter for NG1 at h/R = 0.125. (c) Evolution of $\bar{\epsilon}^p$ inside a grain, P	32

and interface, Q marked in (b).

2.7 Evolution of equivalent plastic strain, $\bar{\epsilon}^p$ below the indenter at (a) $z/R = 0.5$ and (b) $z/R = 1.0$. 33

3.1 (a) 2D Axisymmetric finite element model of cylindrical specimen along with 'Berkovich equivalent' conical rigid indenter with half cone angle of 70.3^0 employed in indentation simulations of MG and Homogenised NG (HNG). (b) Corresponding finite element model employed for Microstructure NG (MNG) considering microstructure of NG in a 'Region A', while homogenized NG in 'Region B'. (c) Enlarged view of 'Region A' and a grain whose size is characterized by d_1 and d_2. 39

3.2 Scanning electron microscope (SEM) images of the subsurface deformed region at an indentation load of 0.5N for (a) NG and (b) MG. 42

3.3 (a) The indentation load-displacement $(P-h)$ curves corresponding to different peak loads for nanoglasses, NG, obtained from nanoindentation experiments and simulations HNG and MNG. (b) The corresponding curves for metallic glass, MG. 44

3.4 Dependence of indentation hardness, H calculated at the end of the holding stage, on the maximum indentation depth, h_{max} for NG and MG along with corresponding H values obtained from the finite element simulations. 44

3.5 AFM images of indent corresponding to the peak load of 8mN for (a) NG and (b) MG. 45

3.6 Contour plots of maximum principal logarithmic plastic strain $log\lambda_1^p$ for NG (obtained from simulations HNG) at (a) $h = 95\ nm$, (b) $h = 143nm$ and (c) $h = 210\ nm$. The corresponding plots for MG are shown in (d)-(f). 47

3.7 Variation of volume fraction of plastically deformed material, V_f^p with indentation depth, h for NG (obtained from 47

Simulation HNG) and MG.

3.8 Contour plot of maximum principal logarithmic plastic strain, $log\lambda_1^p$ obtained from simulations MNG at $h = 143\ nm$. The inset figure shows an enlarged view of region D. 49

3.9 (a) Variation of shear strain rate underneath the indenter in NG and MG during indentation. (b) Variation of $K\eta$ with h_{max} for NG and MG. (c) The evolution of dynamic hardness, H_d during loading stage of indentation for NG and MG. 51

3.10 The variation of (a) Equivalent plastic strain, $\bar{\epsilon}^p$ and (b) Normalized free volume, $\frac{\eta}{\eta_{cv}}$ with respect to indentation depth, h at point 'C' taken at $z = 0.5R$ (refer Fig. 3.6) for NG (HNG) and MG. (c) The variation of $\frac{\eta}{\eta_{cv}}$ with h inside a grain, F and interface, G marked in Fig. 3.8 obtained from simulations MNG. 54

4.1 (a) Finite element mesh of cylindrical sample along with 'Berkovich equivalent' conical rigid indenter with half cone angle of 70.3^0 used for MG and Homogenised NG (HNG) indentation simulations. (b) Corresponding finite element model employed for simulations MNG where microstructure of NG is modelled in a 'Region A', while homogenized NG is considered in 'Region B'. (c) Zoomed view of 'Region A' and grain along with its detailed dimensions. 59

4.2 Normalized indentation load, P/ER^2 versus normalized indentation depth, h/R curve generated for MG, homogenized NG, and microstructured NG along with the experimental data of NG and MG (Franke et al., 2014). 62

4.3 Finite element mesh employed for mixed mode simulation of MG showing (a) the full domain that is modelled and (b) zoomed view of the region around the notch tip. 63

4.4	Finite element mesh employed for mixed mode (I and II) fracture simulation on NG showing (a) the full domain consisting of 'Region D' where microstructure of NG (i.e., discrete glassy grain and interfaces) is modelled, and 'Region C' where homogenised NG is considered. (b) The magnified view of the 'Region C'. (c) Zoomed in view of the region around the notch tip.	64
4.5	Contour plots of maximum principal logarithmic plastic strain, $log\lambda_1^p$ for NG, corresponding to $M^e = 0$ at (a) normalized effective stress intensity factor, $\|K\|/c_{og}\sqrt{b_0} = 2.3$, (b) $\|K\|/c_{og}\sqrt{b_0} = 11.6$ and (c) $\|K\|/c_{og}\sqrt{b_0} = 15.7$. The corresponding plots for MG are shown in (d) - (f).	66
4.6	Contour plots of $log\lambda_1^p$ for NG corresponding to $M^e = 0.25$ at (a) $\|K\|/c_{og}\sqrt{b_0} = 3.0$, (b) $\|K\|/c_{og}\sqrt{b_0} = 11.6$ and (c) $\|K\|/c_{og}\sqrt{b_0} = 15.7$. The corresponding plots for MG are shown in (d) - (f).	66
4.7	Contour plots of $log\lambda_1^p$ for NG corresponding to $M^e = 0.75$ at (a) $\|K\|/c_{og}\sqrt{b_0} = 4.8$, (b) $\|K\|/c_{og}\sqrt{b_0} = 11.6$ and (c) $\|K\|/c_{og}\sqrt{b_0} = 15.7$. The corresponding plots for MG are shown in (d) - (f).	68
4.8	Contour plots of $log\lambda_1^p$ for NG for $M^e = 1$ at (a) $\|K\|/c_{og}\sqrt{b_0} = 6.7$, (b) $\|K\|/c_{og}\sqrt{b_0} = 11.6$ and (c) $\|K\|/c_{og}\sqrt{b_0} = 15.7$. The corresponding plots for MG are shown in (d) – (f).	68
4.9	Variation of volume fraction of material undergoing in plastic yielding, V_f^y with normalized effective stress intensity factor, $\|K\|/c_{0g}\sqrt{b}$ corresponding to different mixed mode loading conditions in (a) NG and (b) MG.	70
4.10	The deformed notch profile for NG and MG corresponding to $M_e = 0.25$ at $\|K\|/c_{og}\sqrt{b_0} = 15.7$.	71
4.11	(a) Schematic representation of notch opening	73

displacement, δ_I and notch shear displacement, δ_{II}. The variation of δ_I with normalized energy release rate, $J/c_{og}b_0$ pertaining to different mode mixities for (b) NG and (c) MG. The corresponding plots for δ_{II} are displayed in (d) and (e).

4.12 The variation of predicted normalized fracture toughness, $\frac{J_c}{J_0}$ with mode mixity, M^e for NG and MG obtained using critical strain based fracture criterion. 75

5.1 (a) Finite element model of NG-MG laminate composite having single NG layer, employed in plane strain tension simulations. (b) Enlarged view of a NG grain. Dimensions d_1 and d_2 are width of grain in X_1 and X_2 directions, respectively. 80

5.2 Nominal stress versus nominal strain curves of monolithic MG and NG-MG laminate composites corresponding to different NG layer thickness, t_{NG} for $l_c = 124\ nm$. 83

5.3 Variation of normalized peak stress, $\hat{\Sigma}/c_o$ (refer left ordinate) with volume fraction, $V_{f,MG}$ of MG layer in the composites for $l_c = 124\ nm$. Here, values denoted by 'o' symbol are obtained from finite element simulations, whereas solid line curve is a best fitting of these values. Also displayed in the figure is the variation of volume fraction of material undergoing plastic yielding, $V_{f,MG}^{y}$ at the peak stress stage (right ordinate) against $V_{f,MG}$. 84

5.4 Contour plots of maximum principle logarithmic plastic strain $log\lambda_1^p$ for composite samples with $l_c = 124\ nm$ at (a) E_2 = 0.02, (b) E_2 = 0.025 and (c) E_2 = 0.04 for NG layer thickness t_{NG} = 4.8 *nm*. The corresponding plots for t_{NG} = 24 and 38.4 nm are shown in (d)-(f) and (g)-(i), respectively. 86

5.5 Variations of maximum principle logarithmic plastic strain $log\lambda_1^p$ with normalized distance, s/l_c across the shear band for (a) t_{NG} = 4.8 *nm*, (b) t_{NG} = 24 *nm* and (c) t_{NG} = 38.4 *nm* at different levels of E_2 corresponding to l_c = 124 *nm*. 88

5.6	Variations of maximum principle logarithmic plastic strain $log\lambda_1^p$ with normalized distance, s/l_c across the shear band for (a) t_{NG} = 4.8 *nm*, (b) t_{NG} = 24 *nm* and (c) t_{NG} = 38.4 *nm* at different levels of E_2 corresponding to l_c = 217 *nm*.	89
5.7	Variations of maximum principle logarithmic plastic strain $log\lambda_1^p$ with normalized distance, s/l_c across the shear band for (a) t_{NG} = 4.8 *nm*, (b) t_{NG} = 24 *nm* and (c) t_{NG} = 38.4 *nm* at different levels of E_2 corresponding to l_c = 310 *nm*.	90
5.8	Normalized macroscopic nominal stress versus strain curves pertaining to various values of l_c for t_{NG} = 24 *nm*.	91
5.9	Contour plots of normalized interaction stress, τ_{int}/c_0 at E_2 =0.015 for sample with t_{MG} = 24 *nm* corresponding to a (a) l_c = 124 *nm* and (b) l_c = 310 *nm*.	92
5.10	Variation of normalized peak stress, $\widehat{\Sigma}/c_o$ with volume fraction, $V_{f,MG}$ of MG layer in the composites for different values of l_c. Here, values denoted by 'o', '□' and '*' symbols pertain to l_c = 124, 217 and 310 *nm*, respectively, and corresponding best fit curves are shown by line plots.	93
5.11	Contour plots of $log\ \lambda_1^p$ for sample S1 pertaining to l_c = 310 *nm* at (a) E_2 = 0.02, (b) E_2 = 0.04 and (c) E_2 = 0.065. The corresponding plots for sample S2 are displayed in (d)-(f).	95
5.12	Nominal stress versus nominal strain curves for different composite samples with multiple NG layers for l_c = 310 *nm*.	96
5.13	Contour plots of $log\ \lambda_1^p$ for NG-MG nanolaminate composite sample (a) S1 and (b) S2 at E_2 = 0.05 for l_c = 124 *nm*.	97
5.14	Contour plots of $log\ \lambda_1^p$ for NG-MG nanolaminate composite sample S3 at E_2 = 0.085 for l_c = 124 *nm*.	97
5.15	Nominal stress versus nominal strain curves for NG-MG nanolaminate composites sample S3 corresponding to l_c = 124 *nm*.	98
5.16	Contour plots of normalized interaction stress, τ_{int}/c_o at E_2 = 0.015 for sample S2 corresponding to (a) l_c = 124 *nm* and (b)	99

l_c = 310 nm.

6.1 Finite element model of hexagonal cellular structure employed in plane strain compression simulations. Here, $d, t,$ and l denotes cell width, cell-wall thickness, and inclined edge of cell, respectively. Also, θ is cell's alignment with respect to loading axis. 103

6.2 Normalized nominal stress versus nominal strain curves for monolithic MG and cellular MG specimens corresponding to $l_c = 31\ nm$. The stages of global and local failures are marked by '×' and '*' symbol, respectively. 105

6.3 (a) The variation of normalized peak stress, $\hat{\Sigma}/c_0$ (refer left ordinate) with respect to relative density, ρ^*/ρ of cellular MG for $l_c = 31\ nm$. Also, displayed in this figures is the volume fraction of material yielded, V_f^y near peak stress stage (right ordinate) versus ρ^*/ρ curve. (b) The variation of the slope of stress-strain curves, E_s recorded for all the samples versus their relative density, ρ^*/ρ. Here symbol 'o' corresponds to values obtained from finite element simulations, while solid line curve represents best fitting of these values. 107

6.4 Contour plots of maximum principal logarithmic plastic strain, $log\lambda_1^p$ for sample H_4 with $l_c = 31\ nm$ at (a) $E_2 = 0.015$, (b) $E_2 = 0.02$, and (c) $E_2 = 0.03$. 108

6.5 Contour plots of maximum principal logarithmic plastic strain, $log\lambda_1^p$ for sample H_2 with $l_c = 31\ nm$ at (a) $E_2 = 0.025$, (b) $E_2 = 0.035$, and (c) $E_2 = 0.045$. 109

6.6 Contour plots of maximum principal logarithmic plastic strain, $log\lambda_1^p$ for sample H_1 with $l_c = 31\ nm$ at (a) $E_2 = 0.04$, (b) $E_2 = 0.05$, and (c) $E_2 = 0.08$. 109

6.7 Variation of $log\lambda_1^p$ with normalized distance, s/l_c across the shear band for (a) H_2, (b) H_3, (c) H_4 at different level of global strain, E_2 corresponding to $l_c = 31\ nm$. 111

6.8	Normalized nominal stress versus nominal strain curves pertaining to various values of l_c for sample H_2. The stages of global and local failures are marked by $'\times'$ and $'*'$ symbol, respectively.	113
6.9	Contour plots of $log\lambda_1^p$ for sample H_2 at nominal strain, E_2 of 0.045 for (a) $l_c = 186\ nm$ and (b) $l_c = 5\ nm$.	114
6.10	Contour plots of normalized interaction stress, τ_{int}/c_0 at $E_2 = 0.02$ for sample H_2 with (a) $l_c = 186\ nm$, (b) $l_c = 31\ nm$, and (c) corresponding plots at $E_2 = 0.03$ for sample H_1 with $l_c = 31\ nm$.	115
6.11	Normalized macroscopic stress versus global strain curves for sample H_2 with $l_c = 186\ nm$ corresponding to specimen A and specimen B.	117
6.12	Contour plots of $log\lambda_1^p$ for specimen A having arrangements of cells similar to H_2 with $l_c = 186\ nm$ at (a) $E_2 = 0.02$ and (b) $E_2 = 0.045$. Corresponding plots for specimen B are shown in (c) and (d).	117
A1	Schematic showing (a) spherical tip of the 'Berkovich equivalent' conical indenter in contact with the specimen. (b) Conical surface of the 'Berkovich equivalent' conical indenter also in contact with the specimen.	126

LIST OF TABLES

Table No.	Caption of Tables	Page No.
3.1	The values of material parameters used for finite element simulations of nanoindentation.	41
4.1	The values of material parameters used for finite element simulations of nanoindentation.	60
5.1	Number of NG layers, thickness of NG and MG layer in different nanolaminate composite samples.	94
6.1	Cell features used to study deformation behavior of hexagonal cellular MG structure.	104

NOMENCLATURE

T_g	Glass transition temperature
P	Indentation load
P_{max}	Maximum indentation load
h	Indentation depth
h_{max}	Maximum indentation depth
H	Hardness
H_d	Dynamic hardness
E	Young's modulus
S	Contact stiffness
A_c	Projected area of contact
h_c	Contact depth
ν	Poisson's ratio
μ	Internal friction coefficient
α	Pressure sensitive index
α_g	Pressure sensitive index for glassy grain
α_i	Pressure sensitive index for glassy interface
C	Constraint factor
σ_y^c	Compressive yield strength

ϵ_y^c	Compressive yield strain
M^e	Mode mixity parameter
σ_m	Hydrostatic stress
J_2	Second invariant of deviatoric stress tensor
J_3	Third invariant of deviatoric stress tensor
R	Spherical tip radius
L_s	Length of specimen
H_s	Height of specimen
a	Contact radius
$\bar{\epsilon}^p$	Equivalent plastic strain
r_p	Plastic zone size
r_p^{NG}	Plastic zone size in NG
r_p^{MG}	Plastic zone size in MG
V_f^g	Volume fraction of glassy grain
$\tau^{(\alpha)}$	Resolved shear stress acting on α^{th} slip system
$\sigma^{(\alpha)}$	Compressive normal traction on α^{th} slip system
$\dot{\gamma}^{(\alpha)}$	Rate of plastic shearing on α^{th}slip system
$\dot{\gamma}_0$	Reference plastic shearing rate
c	Cohesion

c_0	Initial cohesion
c_{0g}	Initial cohesion of glassy grain
c_{0i}	Initial cohesion of glassy interface
η	Free volume
$log\lambda_1^p$	Maximum principal logarithmic plastic strain
V_f^p	Volume fraction of plastically deformed material
W_e	Elastic energy
W_p	Plastic energy
W_t	Total energy
k_B	Boltzmann constant
T	Test temperature
Ω	Atomic volume
Δf	Volume fraction of material having potential jump sites
ΔG	Activation energy
$\dot{\epsilon}$	Shear strain rate
b_0	Notch tip diameter
R_0	Radius of circular domain
K_{Ic}	Mode I fracture toughness
K_{IIc}	Mode II fracture toughness

K_I	Mode I stress intensity factor
K_{II}	Mode II stress intensity factor
$\|K\|$	Effective stress intensity factor
δ_I	Notch opening displacement
δ_{II}	Notch shearing displacement
J	Energy release rate
ϵ_c	Critical plastic strain
r_c^{ϵ}	Critical radial distance
ξ	Free volume concentration
ξ_0	Initial free volume
ξ_T	Free volume concentration in fully annealed glass at absolute temperature
ζ	Free volume creation coefficient due to plastic shearing
G	Shear modulus
k	Bulk modulus
s_1	Gradient free energy coefficient
s_2	Defect free energy coefficient
s_3	Resistant to free volume generation
$\bar{\tau}$	Mises equivalent stress
τ_{int}	Interaction stress

$\bar{p}$	Hydrostatic pressure
f_0	Frequency of atomic vibration
W_0	Width of specimen
L_0	Length of specimen
t_{NG}	Thickness of NG layer
t_{MG}	Thickness of MG layer
l_c	Intrinsic material length scale
Σ_2	Nominal stress in X_2 direction
E_2	Nominal strain in X_2 direction
$V_{f,MG}$	Volume fraction of MG layer
$\hat{\Sigma}$	Peak stress
V_f^y	Volume fraction of material undergoing plastic yielding near peak stress stage
s	Shear band width
d	Cell width
t	Cell-wall thickness
l	Length of inclined edge of cell
ρ^*	Density of cellular MG sample
ρ	Density of monolithic MG sample

ACRONYMS

AFM	Atomic force microscope
ECM	Expanding cavity model
GNFD	Geometrically necessary flow defect
GND	Geometrically necessary dislocation
HNG	Homogeneous nanoglass
HRTEM	High resolution transmission electron microscope
IGC	Inert gas condensation
IIT	Instrumented indentation test
ISE	Indentation size effect
MD	Molecular dynamics
MG	Metallic glass
MNG	Microstructure nanoglass
NG	Nanoglass
PSB	Primary shear band
PSR	Proportional specimen resistance
RP	Reference point
SAED	Selected area electron diffraction
SEM	Scanning electron microscope

SSB	Secondary shear band
SSY	Small scale yielding
STZ	Shear transformation zone
TEM	Transmission electron diffraction
UMAT	User material
2D	Two dimensional

CHAPTER 1
Introduction

Metallic glasses (MGs) have gained much attention due to many attractive mechanical properties such as high elastic limit, high strength, excellent corrosion resistance, and significant fracture toughness (Schuh et al., 2007) making them a potential candidate for structural as well as functional applications including medical implant, micro/nano electromechanical devices and cellular structures for packing purposes (Telford, 2004; Miracle et al., 2008; Schuh et al., 2007; Liu et al., 2014; Liu et al., 2016). However, MGs exhibit localization of plastic strain in narrow bands, called as shear band, and fail in brittle manner under tensile loading due to unhindered propagation of crack inside a predominant band. The lack of tensile ductility in MGs impedes their employment as structural material (Schuh et al., 2007), which has motivated researchers to explore various strategies to improve plastic deformation in MGs such as synthesizing MG composites (Hofmann et al., 2008; Qiao et al., 2016; Wang et al., 2020), nanoglass (NG) architecture (Ivanisenko et al., 2018), NG-MG laminate composites (Adibi et al., 2016; Sha et al., 2017) and MG cellular structures (Sarac et al., 2012; Sarac and Schroers, 2013b; Chen et al., 2014; Liu et al., 2016; Zhang et al., 2016). MG composites exhibit significant tensile ductility, but their strength is compromised considerably due to lower yield strength of the soft phases making them less viable choice (Schuh et al., 2007; Qiao et al., 2016).

NGs which are synthesized from MGs have been reported to exhibit significantly large ductility under tensile loading (Wang et al., 2015). The laminate NG-MG composites with alternate layers of NGs and MGs have also been reported to show enhanced tensile ductility (Sha et al., 2017). Consequently, there has been considerable scientific curiosity in understanding the deformation and fracture behavior of these materials. A few experiments and atomistic simulations performed in the past have provided some insights on the underlying mechanics/mechanism of deformation and fracture in NGs (Sopu et al., 2009; Ritter et al., 2011; Adibi et al., 2013, 2014; Franke et al., 2014; Sha et al., 2014) and NG-MG composites (Adibi et al., 2016; Sha et al., 2017). Yet, there are several unresolved issues which need to be addressed for the safe deployment of these materials in actual applications. In particular, NGs are reported to be harder than MGs with identical composition (Nandam et al., 2017), and their hardness is noticed to drop with increase in load, though mechanistic reasons for these behaviors are not explained in the literature. In addition, the effect of mode

mixity on the evolution of crack tip plasticity and the fracture toughness in NGs are not investigated till now. Further, the deformation behavior of NG-MG laminate composites transitions from localized to superplastic flow, though mechanistic reasons are not well understood. The cellular MG structures have also been synthesized and they showed enhanced plasticity, but the mechanics of the deformation behavior is not well understood. In the view of above discussion, indentation experiments and complementary finite element simulations are performed on NGs as well as MGs in this thesis. In addition, deformation behavior of NG-MG laminate composites and cellular MGs are analyzed through finite element simulations. The relevant background is briefly presented below.

1.1 Plastic deformation in amorphous metals

The plastic deformation in amorphous metals like MGs is believed to occur through local atomic rearrangement of clusters of around 30-100 atoms under the application of shear stress (Argon 1979) as displayed in schematic shown in Fig 1.1(a). These clusters are known as shear transformation zone (STZs) and are considered to be as flow defects responsible for plastic deformation in MGs. Spaepen (1977) looked plastic deformation in MGs as consequence of creation of excess free volume (i.e., material exhibits dilatation) due to the jump of an atom into smaller interstitial space in their immediate neighborhood under the application of shear stress (refer schematic Fig 1.1(b)). The model proposed by Spaepen (1977) is commonly referred to as "Free volume model". Although there is difference in atomic motion perceived in the above models, the operation of STZs as well as atomic jump leads to generation of local free volume which is associated with local inelastic dilatation making macroscopic plastic flow in MGs pressure sensitive (Narasimhan, 2004; Patnaik et al., 2004).

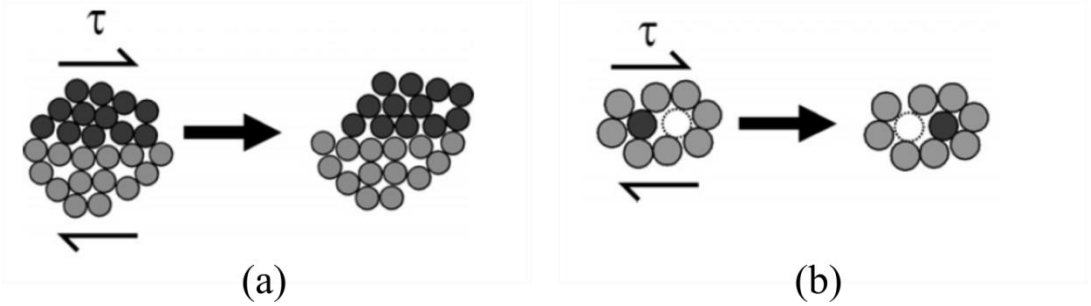

Figure 1.1 Schematic showing the microscopic deformation mechanisms proposed for MGs. (a) A shear transformation zone (STZ model) (Argon 1979) and (b) local atomic jump model (Free volume model) (Spaepen, 1977). Figures are taken from Schuh et al. (2007).

Above glass transition temperature, T_g, MGs exhibit viscous flow in which profuse activation of the STZs occurs and their stress fields relaxes instantaneously resulting in the homogeneous deformation (Schuh et al., 2007). On contrary, at high applied stress and at the temperature well below T_g, the plastic deformation in MGs localizes in the form of narrow bands which are known as shear bands. The shear bands exhibit accumulation of large STZs and excess free volume which results in flow softening during the deformation (Sopu et al., 2009). The large accumulation of free volume also leads to crack nucleation inside a shear band. Thus, almost all MGs fail catastrophically immediately after commencement of plastic yielding under tensile loading due to crack propagation inside a predominant shear band. However, under the constraint loading such as compression and indentation, significant plastic deformation is observed due to nucleation of multiple shear bands (Lu and Ravichandran, 2003; Patnaik et al., 2004; Schuh et al. 2007). Further, the deformation of MGs is found to be sensitive to loading rate at temperature near T_g or in supercooled liquid regime (Liu and Ravichandran, 2003). On the other hand, it is almost rate insensitive at room temperature (Bruck et al., 1996; Subhash et al., 2002; Lu and Ravichandran, 2003).

1.2 Constitutive model in MGs

Several constitutive models (Vaidyanathan et al., 2001; Huang et al., 2002; Patnaik et al., 2004; Anand and Su, 2005; Gao, 2006; Yang et al., 2006; Thamburaja and Ekambaram, 2007; Jiang and Dai, 2009; Thamburaja, 2011) have been proposed to characterize the deformation behavior of MGs. The brief descriptions of these models are reviewed in this section. Vaidyanathan et al. (2001) and Patnaik et al. (2004) employed pressure/normal stress sensitive Mohr-Coulomb and extended Drucker Prager plasticity model to investigate the plastic deformation in MGs, respectively. These models can capture tension-compression anisotropy in the yield strength in MGs, but fails to capture the free volume induced softening, which is most important characteristic of amorphous metals. By extending the free volume theory of Spaepen (1977) to multi-axial stress states, Huang et al. (2002) proposed a model within small strain framework which considered free volume in MGs to evolve due to stress-driven creation, annihilation, and diffusion of free volume. Jiang and Dai (2009) proposed non-local, small strain, coupled thermo-mechanical plasticity model to investigate the shear band instability in MGs subjected to thermal, mechanical, or combined loading conditions. Although models of Huang et al. (2002) and Jiang and Dai (2009) have

incorporated an intrinsic material length scale, these are not consistent with law of thermodynamics and also developed using small strain formulation.

Anand and Su (2005) proposed a thermodynamically consistent finite deformation Mohr-Coulomb type plasticity model for MGs which has been shown to capture the deformation behavior of MGs under bending, compression, tension and indentation. In addition, this model has been reported to successfully predict the shear band patterns near the notch root under mixed mode (I and II) loading (Tandaiya et al., 2009). Anand and Su (2007) extended this constitutive model to study the deformation behavior of MGs at high homologous temperature regime and showed that the revised model successfully captures the major features of strain rate dependent stress-strain curves. However, this model does not have an intrinsic material length scale, hence unable to predict the size-dependent response in MGs as reported by nano-tension experiments (Jang and Greer, 2010).

Thamburaja and Ekambaram (2007) proposed a thermodynamically consistent, finite deformation, non-local plasticity model using free volume theory of Spaepen (1977). In this model, the evolution of free volume is assumed to be governed by four fundamental mechanisms: free volume diffusion, free volume creation by plastic shearing and hydrostatic stress and free volume annihilation by structural relaxation. This model was found to be suitable to predict the deformation behavior of MGs near and above the glass transition temperature. To analyze the deformation behavior of MGs at room temperature, Thamburaja (2011) modified the constitutive theory of Thamburaja and Ekambaram (2007) which has been successfully shown to capture the size-dependent deformation behavior in MGs (Thamburaja, 2011; Singh and Narasimhan, 2016; Dutta et al., 2018), MG composites (Shete et al., 2016, 2017; Dutta et al., 2020), Nanaglasses (Singh et al., 2014).

1.3 Review of pertinent literature

1.3.1 Instrumented indentation Test

Instrumented Indentation Test (IIT) is widely used to estimate the mechanical properties such as hardness and young's modulus of material (Oliver and Pharr, 2004). In this test, the indentation load, P and indentation depth, h are continuously recorded and plotted as P vs h curve during the experiments. Oliver and Pharr (2004) proposed a methodology to calculate hardness, H and young's modulus, E of material from $P-h$ curve which is commonly known as Oliver - Pharr method. To this end, contact stiffness, S, projected area of contact,

A_c and reduced modulus, E_r need to be determined. The equations required to calculate these parameters are taken from the work of Oliver and Pharr and are briefly discussed below. The contact stiffness, S is determined by taking the slope of unloading portion of $P - h$ curve and it is defined as:

$$S = \frac{dP}{dh} \tag{1.1}$$

Further, A_c is given by:

$$A_c = 3\sqrt{3}h_c^2 \tan^2\theta \approx 24.5h_c^2, \tag{1.2}$$

where, θ is the half tip angle, for Berkovich indenter $\theta = 65.3^0$. The depth h_c is the contact depth and it can be determined by:

$$h_c = h_{max} - \frac{\boldsymbol{\epsilon} P_{max}}{S}. \tag{1.3}$$

Here, P_{max} and h_{max} are maximum applied load and indentation depth, respectively, while $\boldsymbol{\epsilon}$ is a constant which depends on the indenter geometry, it is taken as 0.75 for Berkovich indenter. Once A_c is estimated, the hardness is determined as:

$$H = \frac{P_{max}}{A_c}. \tag{1.4}$$

The reduced modulus can be determined as:

$$E_r = \frac{\sqrt{\pi}S}{2\boldsymbol{\beta}\sqrt{A_c}}. \tag{1.5}$$

Here, the constant $\boldsymbol{\beta}$ depends upon the indenter geometry and for Berkovich indenter it is generally taken as 1.034. After estimating E_r, Young's modulus of the specimen can be determined as:

$$\frac{1}{E_r} = \frac{1 - \nu_i^2}{E_i} + \frac{1 - \nu_s^2}{E_s}. \tag{1.6}$$

Here, ν is Poisson's ratio. The subscript s and i in above equation denotes the specimen and indenter under investigation, respectively.

The advantages of IIT are: (1) Mechanical properties of small samples like thin films and ribbons can be easily estimated. (2) This technique is non-destructive in nature as it makes a small impression on the surface.

1.3.2 Deformation response of MGs

In this section, the deformation response with primary focus on the indentation and fracture response of MGs is discussed.

1.3.2.1 Indentation Response of MGs

Vaidyanathan et al. (2001) performed micro and nanoindentation experiments as well as complementary finite element simulations using various constitutive models on Zr-based bulk MG. They showed that finite element predictions of indentation response and shear band patterns around the imprint corroborate well with the experimental data when Mohr-Coulomb yield criterion with friction coefficient, $\mu = 0.13$ was employed (refer Figs. 1.2(a)-(c)). Narasimhan (2004) modified the expanding cavity model of Johnson's (1970) by employing the Drucker Prager yield criterion to explain the mechanics of indentation in pressure sensitive solids. This modified theory predicts that the plastic zone size beneath the indenter enhances with increase in pressure sensitivity index, α. Also, the mean contact pressure and constraint factor, $C = H/\sigma_y^c$ (σ_y^c being compressive yield strength) increases with increase in α. Patnaik et al. (2004) determined from spherical indentation and complementary finite element simulations that $\alpha = 20^0$ and $C > 3$ for Zr- based bulk MG. Keryvin (2007) has also reported C is greater than 3 for Pd- and Zr- based bulk MG irrespective of the indenter geometry.

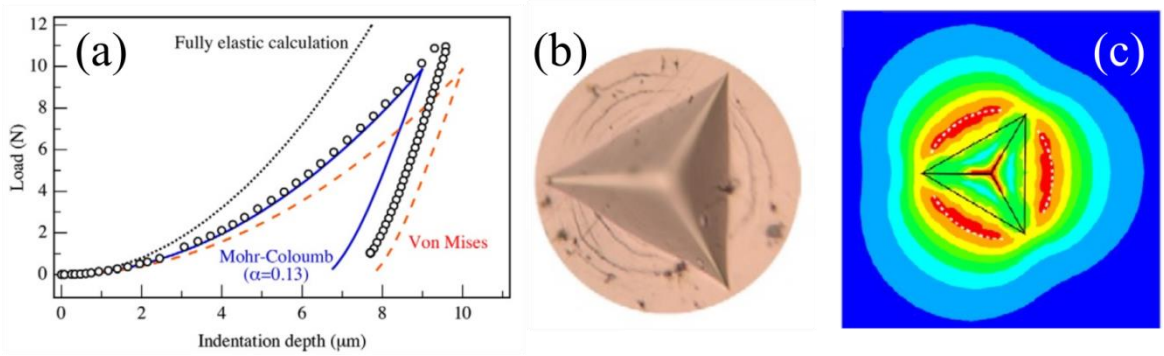

Figure 1.2 (a) Experimental and simulated indentation load vs indentation depth curve. The Top view of indentation impressions observed from (b) experiment and (c) simulations using Mohr-coulomb yield criterion, respectively. Images are taken from Vaidyanathan et al. (2001).

The hardness is frequently observed to decrease with increase in the indentation load during the indentation experiments equipped with geometrically self-similar pyramidal indenters such as Vickers and Berkovich indenters, which is commonly referred to as the indentation size effect (ISE) (Jang et al., 2011). The ISE in crystalline materials is considered to be caused by various factors such as surface roughness (Gerberich et al., 2002), the friction between the indenter facets and test sample (Li et al., 1993), and strain hardening caused by the increase in the density of the geometrically necessary dislocations (GNDs) during initial stages of indentation (Nix and Gao, 1998). However, it is well accepted fact that the ISE in crystalline materials is mainly governed by the GNDs induced strain hardening. Interestingly, the ISE-like behavior has also been observed in bulk MGs which are free from dislocations and exhibit strain softening (Lam and Chong, 2001; Ramamurty et al., 2005; Manika and Maniks, 2006; Yang et al., 2007; Steenberge et al., 2007; Li et al., 2008, 2009; Fornell et al., 2009; Xu et al., 2014; Xue et al., 2016; Li et al., 2017; Zhou et al., 2019). For example, Wright et al. (2001) observed drop in the indentation hardness of Zr-based bulk MG with an increase in indentation load which they attributed to the reduction in intrinsic material resistance for shear band nucleation with increasing loads.

Steenberge et al. (2007) performed nanoindentation experiments on as-cast and thermally relaxed Zr-based bulk MGs and reported more pronounced ISE in the former than in the latter (refer Fig. 1.3). They expressed the hardness in terms of strain rate and initial free volume by invoking the flow equation of Spaepen (1977) and Argon (1979) and explained that ISE in MGs is caused by increase in free volume during indentation. They further argued that the accumulation of free volume during indentation was less pronounced due to lesser initial free volume in the relaxed glass resulting in less pronounced ISE in them. Jang et al. (2011) hypothesized that ISE in MGs is caused by increase in plastic zone, hence enhanced activities of STZs below the indenter with increase in indentation load. Further, to explain the ISE in Zr-based bulk MGs, Lam and Chong (2001) and Yang et al. (2007) proposed analytical models by adopting the perspective of strain gradient plasticity theory analogous to the Nix-Gao model for crystalline materials. They argued that the concentration of the geometrically necessary flow defects (GNFDs) such as free volume (Lam and Chong, 2001) or shear clusters (Yang et al., 2007) increases with decrease in indentation depth which causes enhancement in flow stress and hence hardness.

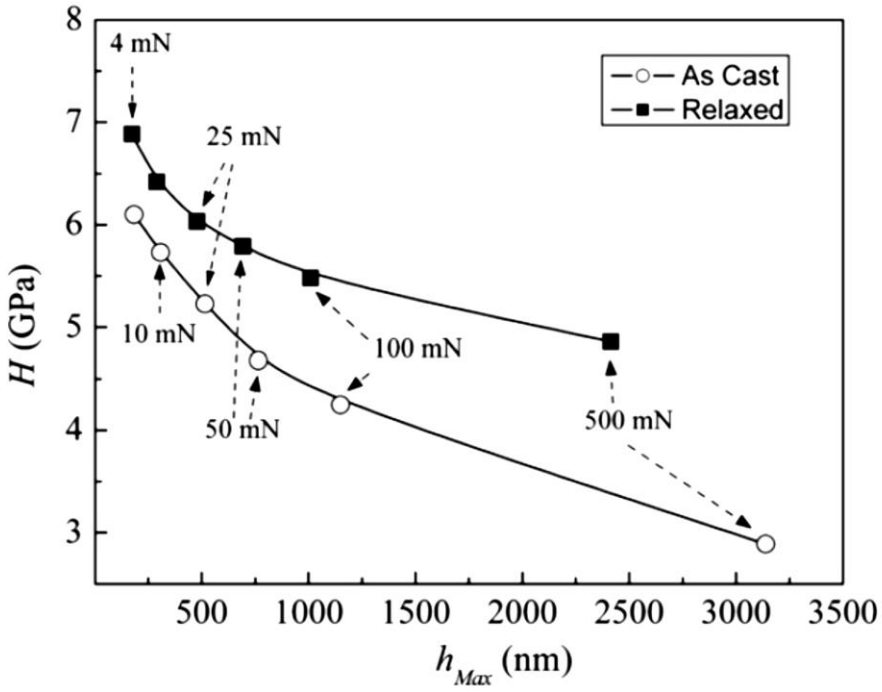

Figure 1.3 The variation of hardness, H, calculated at the end of holding stage with respect to maximum indentation depth, h_{max} , reported by Steenberge et al. (2007).

In contrast to the above studies, Huang et al. (2010) showed that the ISE in bulk MGs can be effectively eliminated by considering the pile-up effect at different indentation loads and hence they deduced that the ISE in bulk MGs is an experimental artefact. Pang et al. (2012) performed nanoindentation experiments on binary $Cu_{50}Zr_{50}$ MG thin film and reported almost negligible ISE. They applied proportional specimen resistance (PSR) model to explain the indentation response and deduced that the friction between indenter facets and test specimen was negligible which resulted in negligible ISE in MG thin film. On the contrary, Rauf et al. (2018) reported significant ISE in MG thin films and melt-spun ribbons of $Cu_{50}Zr_{50}$ and $Cu_{64}Zr_{36}$.

1.3.2.2 Fracture response in MGs

Conner et al. (1997) determined the mode I fracture toughness, K_{IC} of Zr-based MG as $57MPa\sqrt{m}$ from three-point bend fracture experiments. Flores and Dauskardt (2006) reported that mode II fracture toughness, K_{IIC} of these glasses is significantly higher than K_{IC}. Tandaiya et al. (2009) performed mixed mode (I and II) fracture experiments and complementary finite element simulations on Zr-based bulk MG to investigate the deformation behavior under mixed mode loading conditions. They noticed that the upper part

of notched surface sharpens while the lower part blunts under mixed mode loading. They also found that the crack tip fields are markedly influenced by mode mixity. Further, they noticed shear bands emanating from notch tip were straight and extending over long distance ahead of notch in mode II dominant loading (refer Fig. 1.4(a)). On the other hand, they witnessed profuse shear bands with increase in mode I contribution (refer Fig. 1.4(b)). In addition, they revealed fracture toughness increases with increasing the mode-I loading component. Narayan et al. (2015) also reported higher K_{IC} than K_{IIC} in Zr- based MGs. By contrast, Chen et al. (2019) noticed stable plastic flow and large bearing loads due to enhancement in density of shear bands with increase in mode II loading component.

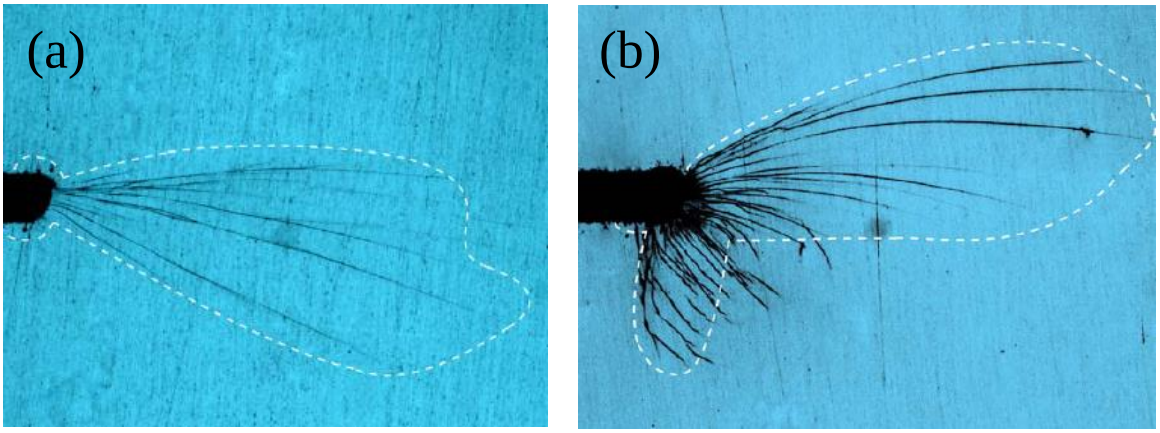

Figure 1.4 The optical micrographs showing shear bands near the notch tip region in Zr-based MG subjected to (a) $M^e = 0$ (pure mode II loading) and (b) $M^e = 0.45$. Images are taken from the work of Tandaiya et al. (2009).

1.3.3 Ductility enhancement in MGs

The lack of tensile ductility in MGs impedes their employment as structural material (Schuh et al., 2007), which has motivated researchers to explore various strategies to enhance the plastic deformation in MGs such as synthesizing MG composites (Hofmann et al., 2008; Qiao et al., 2016; Wang et al., 2020), MG laminate composites (Kim et al., 2011), nanoglass (NG) architecture (Ivanisenko et al., 2018). The MG composites are developed by introducing soft crystalline phases by controlling the crystalization-kinetics, by adding fibers/particles of crystalline materials in a glassy matrix (Qiao et al., 2016) or by suction casting a glassy phase in a foam of crystalline material (Wang et al., 2020). Multiple shear bands nucleate from glass-crystalline phase interfaces which either cut through or get deflected by them causing nucleation of secondary and tertiary shear bands leading to delayed localization and enhanced

tensile ductility in MG composites. However, the strength of such composites is compromised considerably due to lower yield strength of the soft phases. An alternate approach to achieve good tensile ductility in MGs is synthesizing Nanoglasses (NGs) architecture and developing laminate composites with alternate layers of two different materials. The pertinent literature is reviewed in the following sections.

1.3.3.1 Deformation behavior of Nanoglasses

Nanoglasses (NGs) were synthesized for the first time by Jing et al. (1989) using inert gas condensation (IGC) followed by cold compaction at high pressure of around 5 GPa. It was revealed through Mossebauer spectroscopy that NGs are comprised of dense amorphous regions, commonly referred to as glassy grains, separated by fine amorphous glassy interfaces (Jing et al., 1989). The transmission electron microscopy (TEM) has also shown that NGs manufactured by different methods such as multi-phase electron deposition technique (Guo et al., 2017, 2019; Li et al., 2018), magnetron sputtering (Chen et al., 2013) and cold compaction (Fang et al., 2012; Nandam et al., 2017, 2020) consists of nanoscale dense glassy grains separated by glassy interfaces (refer Fig 1.5(a) and (b)). The average size of the grains is reported to be around 5-20 *nm* depending on the compositions and the manufacturing techniques, while the interfaces width is around 1~2 *nm* (Ivanisenko et al., 2018). It is important to note that glassy grains and interfaces are amorphous in nature which has been confirmed through the selected area electron diffraction (SAED) and the high-resolution transmission electron microscope (HRTEM) (refer Fig. 1.5(a) and (b)). It has been shown that interfaces in NGs exhibit excess free volume (Sopu et al., 2009; Ritter et al., 2011) or lower density (Fang et al., 2012) and defective short-range order (Ritter et al., 2011).

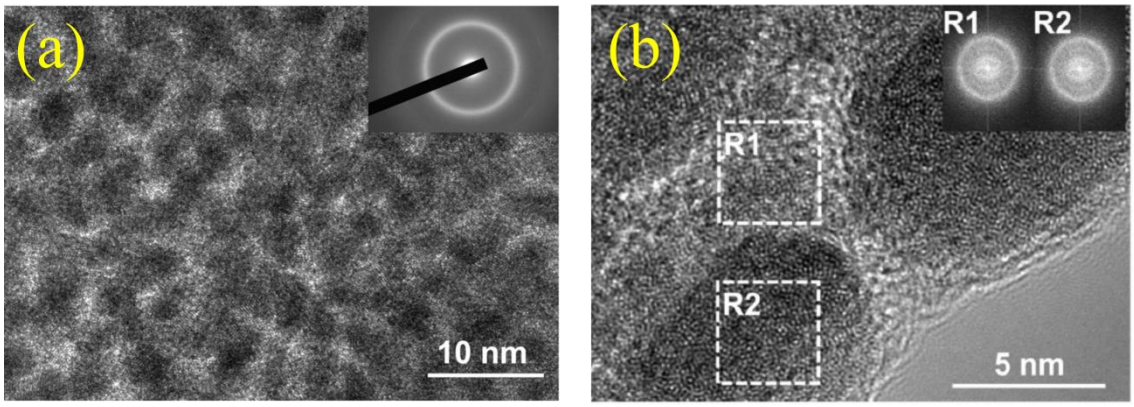

Figure 1.5 (a) The transmission electron microscope (TEM) image of the Ni-based NGs. The dark and light contrast areas correspond to the glassy grains and glassy interfaces, respectively. The inset shows the corresponding selected area diffraction (SAED) pattern. (b) the high-resolution transmission electron microscope (HRTEM) image of Ni-based NGs (the insets display SAED patterns of both glassy grain and glassy interface regions). Images are taken from Li et al. (2018).

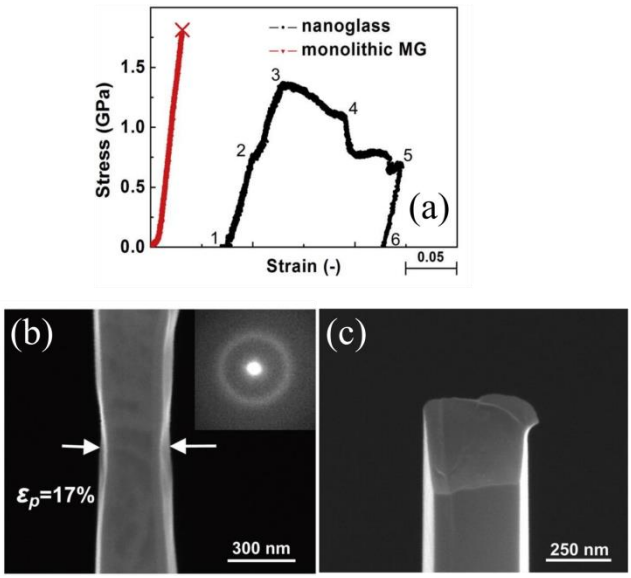

Figure 1.6 (a) The tensile stress-strain curves of the Sc-based NG and MG. (b) The tensile specimen of NG after test. (c) The tensile specimen of MG after test. Images are taken from Wang et al. (2015).

NGs have been reported to exhibit significant large tensile ductility, unlike MGs which fails in a brittle manner under tensile loading (Wang et al., 2015; Liu et al., 2018; Li et al., 2018). For example, Wang et al. (2015) reported around 17% plastic strain and failure

through necking in $Sc_{75}Fe_{25}$ NGs, whereas they noticed almost negligible plastic strain and catastrophic failure through shear band in MGs with identical composition during *in-situ* tension experiments (refer Fig. 1.6). The molecular dynamics (MD) simulations have shown that ductility in NGs enhances with decrease in grain size and eventually they exhibit superplastic flow for grain size below a threshold level (Adibi et al., 2013, 2014; Sha et al., 2015). Singh et al. (2014) explained through continuum simulations by employing the model of Thamburaja (2011) that the spatial distribution of stress arising due to interaction between flow defects such as STZs plays a pivotal role in the deformation behavior of NGs. They showed that the ratio of intrinsic material length associated with this interaction stress and grain size governs the transition from localized to superplastic flow in NGs.

Nandam et al. (2017) performed nanoindentation experiments on $Cu_{50}Zr_{50}$ binary NGs and MG ribbon, and reported smooth indentation load, P vs. depth, h curves with no noticeable displacement bursts (refer Fig. 1.7). They reported a hardness value of 7.4 GPa for NG, while 6.7 GPa for MG ribbon. Franke et al. (2014) have also reported a higher hardness and reduced modulus in $Sc_{75}Fe_{25}$ NG. They argued that high affinity of Sc to oxygen leads to the contamination of NG samples with oxygen leading to an increase in E_r, although the mechanistic reason for higher H of NGs is not discussed in detail. On the other hand, the hardness of Ni-based NG thin films (Guo et al., 2019) and Pd-based NGs (Nandam et al., 2020) are reported to be lower than their MG counterparts. This was rationalized through higher initial free volume in Ni-based NG thin films and the presence of weaker $Pd-Pd$ metallic bonds in the interfaces of Pd-based NGs. Recently, Sharma et al. (2021b) reported higher ISE in as prepared than that in annealed $Cu_{60}NG_{40}$ NGs. They showed by employing the hypothesis of Steenberge et al. (2007) that the different softening characteristic in as-prepared and annealed NGs resulted in different ISE in these materials.

It must be mentioned that though a considerable amount of research has been devoted to understand the deformation behavior of NGs, a few works have been undertaken in investigating their fracture behavior. Sha et al. (2014) analyzed the tensile response of notched samples of Cu-based NGs through atomistic simulations and reported that the notch size with respect to the grain size governs the transition in deformation behavior from localized to superplastic flow.

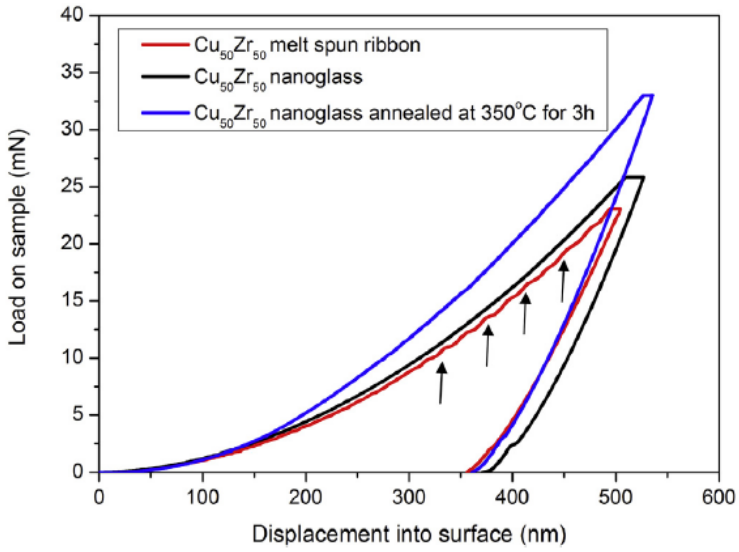

Figure 1.7 Representative indentation load, P vs depth, h curves of MG ribbon, as-prepared NG and annealed NG. Pop-ins were not observed in NG samples while it was noticed in MG ribbons (indicated by arrows). The image is taken from Nandam et al. (2017).

1.3.4 Tensile deformation of nanolaminate composite

As discussed earlier, a good tensile ductility in MGs can be achieved by synthesizing laminate composites with alternative layers of two materials. Kim et al. (2011) investigated tensile behavior of nanolaminate with alternating layers of $16 - 900\ nm$ thick $Cu_{50}Zr_{50}$ MG and $16\ nm$ thick nanocrystalline Cu and reported marginal enhancement in ductility of 4% without compromising strength when the critical MG layer thickness fall below $120\ nm$. Therefore, one of the major research challenge is to find a suitable layer material that can hinder or accommodate the shear bands resulting in improved ductility without compromising strength. Adibi et al. (2016) performed MD simulations of tensile loading on MG-MG as well as NG-MG nanolaminate composites. They noticed that the presence of planer soft interface between MG layers in MG-MG laminate composites delayed strain localization while in the case of NG-MG laminate composites, both planar interface and NG layer contribute to the plastic deformation leading to high plastic strains of 15%. Another important observation made by Adibi et al. (2016) was that NG-MG composites failed through necking as opposed to shear banding in the case of MG-MG composites. Sha et al. (2017) also reported tensile deformation of laminate composites markedly affected by thickness of NG and MG layers. They noticed that laminate composite with thinner NG layer shear bands initiated from NG layer which propagate into MG layer with increase in applied

load. On the other hand, for the laminate composite with thicker NG layer shear bands were always confined in the NG layer. Also, peak stress attained in these composites don't follow rule of mixture. Further, they reported a transition in deformation behavior from shear localization to superplastic flow in composites having multiple NG and MG layers, when MG layer thickness was reduced below a threshold level which they correlated to the glassy grain size of the NG layers.

1.3.5 Deformation response of cellular MG structures

In the last decade, cellular MGs have been fabricated which are found to be an alternative choice for structural and functional applications owing to light in weight, good energy as well as noise absorption capacity and enhanced plastic deformation (Sarac et al., 2012; Sarac and Schroers, 2013b; Chen et al., 2014; Liu et al., 2016). Indeed, Sarac et al. (2012) performed uniaxial in-plane compression experiments on cellular structures of bulk MG and other materials. They noticed that energy absorbing capacity of MG based cellular structure is superior than that of other materials. Sarac and Schroers (2013b) synthesized hexagonal cellular structures from Zr- based bulk MG and investigated the effect of the relative density cellular structures on their deformation behavior under quasi-static compressive loading. They revealed three distinctive deformation modes: collective buckling of ligaments through row by row collapse in specimens with very low relative density to local failure by damage confined in few cells for intermediate values of density. On the other hand, they found global failure with nearly negligible global plasticity due to localization in a shear band in samples with large density. In addition, they noticed nonlinear behavior of peak stress attained in the samples with respect to relative density. Zhang et al. (2016) also reported a transition from localized plastic deformation but confined to few cells to almost homogeneous deformation in nanoscale MG cellular structures from atomistic simulations by increasing cell size. They have also demonstrated that a dominant shear band forms when cell spacing along diagonal direction increases beyond a critical level which they correlated with the shear band thickness in monolithic MG of identical composition.

1.4 Issues for investigation

Based on the literature reviewed in section 1.3, the following issues have been identified for investigation in this thesis.

1.4.1 Pressure sensitive plastic flow in NGs

Recent indentation experiments show that NGs exhibit a higher hardness than MGs of identical compositions (Franke et al., 2014; Nandam et al., 2017). Nandam et al. (2017) attributed the high hardness of NGs to the presence of Zr rich dense core surrounded by Cu rich interfaces carrying excess free volume. However, it is not clear as to why hardness should increase in the presence of free volume rich interfaces. Further, as discussed in section 1.3.2.1, higher hardness, H in MGs is intimately connected with the pressure sensitive plastic flow taking place beneath the indenter and H appears to increase with the pressure sensitive index α. Given the amorphous structure of NGs with glassy grains and glassy interfaces, the plastic flow of NGs could be expected to be pressure sensitive which may be reason for high hardness observed in these materials although it has not been investigated in detail. It is important to mention that no finite element simulations have been performed till now to study the pressure sensitive behavior of NGs. In this connection, following questions arise: what is value of α for NG compared to their MG counterpart? Does the glassy grains and glassy interfaces have the same α? If not, what are the differences between them?

1.4.2 Indentation size effect in NGs and MGs

As mentioned in section 1.3.2.1, there in consensus in the literature on the ISE in the MG ribbons which suggest that understanding of the mechanics of ISE in these materials is far from complete. Further, the indentation experiments on as prepared and annealed NGs by Sharma et al. (2021b) suggest that the internal microstructure of NGs has marked effect on the deformation behavior and hence ISE in them. Given the completely different microstructures of NGs and MGs, the ISE in the former is expected to be significantly different than the latter with identical composition, though it has not been investigated till now. Further, as pointed earlier that the pressure sensitivity of NGs might be significantly different than that of MGs. However, the effect of pressure sensitivity on the ISE in glasses is not investigated and thus, the mechanism governing ISE in NGs and MGs is not well understood.

1.4.3 Mixed mode (I and II) fracture response in NGs

Sha et al. (2014) were performed atomistic simulations on notched samples of NGs under pure mode-I loading conditions. However, in practical application, structural components are generally subjected to complex stress fields/multi-axial states of stress, which may prone to mixed mode fracture. For example, even in unidirectional loading condition, the crack initiated from the flaws would be oriented at an arbitrary angle to the loading direction. These factors emphasize the requirement of a detailed study of fracture mechanism under mixed mode loading conditions on a given material. In addition, the contrasting trends on the crack tip plasticity in bulk MGs under mixed mode loading conditions presented in section 1.3.2.2 motivates to study the fracture response of NGs as these are synthesized from MGs only. The finite element simulations of mixed mode (I and II) fracture would help gaining the primary understanding on the development of the crack tip plasticity in NGs. This information may provide guidelines in performing fracture experiments on NGs in near future. However, such continuum study of mixed mode (I and II) fracture on NGs have not been undertaken till now.

1.4.4 Tensile deformation of NG- MG nanolaminate composite

MD simulations have shown that NG-MG laminate composites can exhibit significantly large tensile ductility (Adibi et al., 2016; Sha et al., 2017). In addition, Sha et al. (2017) reported peak stress attained in NG-MG laminate composites not following the rule of mixture, whereas they did not explain the mechanistic reasons for this trend. Further, they also reported a transition in deformation behavior from shear localization to superplastic flow in laminate composite having multiple NG and MG layers, when MG layer thickness is reduced below a threshold level which they correlated to the glassy grain size of the NG layer. However, it is not clear from these simulations as to why and how the glassy grain size of NG layer controls the threshold thickness of MG layer. The finite element simulations using a non-local plasticity model would help understanding the deformation of NG-MG laminate composites from a mechanics viewpoint. However, no such finite element simulations on these composites have been undertaken till now.

1.4.5 Deformation and failure mechanism of nanoscale cellular structure of MGs

Cellular MGs have been found to be a potential candidate for structural and functional applications due to their attractive properties such as high strength to weight ratio, excellent energy absorption and enhanced plastic deformation. As mentioned in section 1.3.5, the peak stress attained in cellular structure of MGs varies nonlinearly with respect to their relative density (Sarac et al., 2012; Sarac and Schroers, 2013b), whereas the mechanistic reason for this behavior is not well understood. Zhang et al. (2016) reported a transition from localized plastic deformation but confined to few cells to almost homogeneous deformation in nanoscale MG cellular structures from MD simulations by increasing cell size. They have also demonstrated that a dominant shear band forms when cell spacing along diagonal direction increases beyond a critical level which they correlated with the shear band thickness in monolithic MG of identical composition. However, it is not clear from these simulations as to why and how the shear band thickness in monolithic MG controls the threshold cell spacing. In the context of MG cellular structures, although some understanding on the deformation behavior has been gained through experiments and atomistic simulations, the mechanistic reasons for above noted transitions are not well understood. The continuum simulations on MG cellular structures using non-local plasticity theory may help explaining the mechanistic reasons for the transition in their deformation behavior. However, such simulations have not been performed.

1.5 Objective and scope of the thesis

Based on issues identified in the previous section, the objectives of the current work are framed as follows:

- To perform axisymmetric finite element indentation simulations using the pressure insensitive (Von-Mises) and pressure sensitive (extended Drucker Prager) plasticity model with associated flow rule to analyze the indentation behavior of $Sc_{75}Fe_{25}$ NGs and MGs.
    - To determine the pressure sensitive index, α for NG and MG by fitting simulated $P-h$ curves with the corresponding experimental data.
    - To determine α for glassy interfaces by modeling the microstructure (i.e., discrete grains and interfaces) of NGs.

- To perform micro- as well as nano-indentation experiments and complementary finite element simulations on binary $Cu_{60}Zr_{40}$ NG and MG to investigate ISE in both alloys.
    - To clearly understand the subsurface deformation behavior from bonded interface experiments through micro indentation.
    - To elucidate the underlying mechanism governing ISE in NGs through finite element nanoindentation simulations by employing a finite strain viscoplastic constitutive theory for amorphous metals.
- To conduct finite element simulations of crack initiation in NGs and MGs under mixed mode (I and II) loading conditions using constitutive model for amorphous metals proposed by Anand and Su (2005).
    - To study the evolution of crack tip plasticity in the NG and MG under mixed mode (I and II) loading conditions.
    - To estimate the plastic zone size and fracture toughness in NGs and MGs for various mode mixity.
- To conduct 2D plane strain finite element simulations of tensile loading on NG-MG nanolaminate composites using a thermodynamically consistent finite strain based non-local plasticity model proposed by Thamburaja (2011).
    - To find the mechanistic reasons for peak stress attained in NG-MG laminate composite not following the rule of mixture.
    - To examine the role played by interaction stress between the flow defects (STZs) on the deformation response of the nanolaminate composite.
    - To investigate the physical origin of the threshold level of MG layer thickness corresponding to transition in deformation behavior from localized to superplastic flow in NG-MG nanolaminate composite.
- To conduct 2D plane strain finite element simulations of compressive loading on nanoscale cellular MGs using thermodynamically consistent finite strain non-local plasticity model of Thamburaja (2011).
    - To investigate the effect of cell-wall thickness and the role played by interaction stress associated with flow defects such as STZs on the deformation behavior of nanoscale cellular MGs.
    - To investigate the effect of change in specimen size on the deformation mechanism of nanoscale cellular MGs.

All the simulations and experiments reported in this thesis are performed under the assumptions of quasi static, monotonic loading at room temperature under isothermal conditions.

1.6 Organization of thesis

The remaining parts of the thesis are organized as follows:

In chapter 2, axisymmetric finite element indentation simulations are performed using extended Drucker Prager plasticity model. The values of α for NGs and MGs are determined. Also, the mechanistic reasons for higher hardness in NGs than MGs are explained.

In chapter 3, micro and nanoindentation experiments on NG and MG are performed and important results from the experiments are also discussed. In addition, the complementary finite element nanoindentation simulations are performed using the amorphous metals constitutive model proposed by Anand and Su (2005) to elucidate the underlying mechanism governing ISE in NGs.

In chapter 4, mixed mode (I and II) loading of a stationary crack in NGs and MGs is studied through finite element simulations under 2D plane strain, SSY conditions using the same constitutive model as in Chapter 3. The effect of mode mixity on the evolution of crack tip plasticity in NGs is investigated and it is compared with that of MGs. The variation of fracture toughness with mode mixity in NGs and MGs is also estimated using a critical strain-based failure criterion.

In chapter 5, tensile loading of NG-MG nanolaminate composites are analyzed through 2D plane strain finite element simulations using a thermodynamically consistent finite strain based non-local plasticity model. The physical origin of the threshold level of MG layer thickness corresponding to transition in deformation behavior from localized to superplastic flow in NG-MG nanolaminate composite is studied.

In chapter 6, compressive loading of nanoscale cellular MGs are analyzed using the same constitutive model as in chapter 5 and the effect of cell wall thickness and the role played by interaction stress associated with flow defects such as STZs on the deformation behavior of nanoscale cellular MGs is discussed.

In chapter 7, the important conclusions drawn from chapters 2-5 are summarized and the possible further works are also discussed.

The governing equations in expanding cavity model for sphero-conical indenter are discussed in Appendix A. In addition to this, estimation of young's modulus for glassy interfaces using iso-strain and iso-stress conditions are discussed.

CHAPTER 2

Investigation of pressure sensitive plastic flow in nanoglasses from finite element simulations

2.1 Introduction

Nanoglasses (NGs), are found to exhibit good amount of tensile ductility compared to their parent materials, metallic glasses (MGs). The increase in ductility is intimately connected to the underlying "microstructure" of these materials which typically comprises of glassy grains separated by amorphous boundaries often referred to glassy interfaces (Jing et al., 1989; Sopu et al., 2009; Chen et al., 2011; Ritter et al., 2011; Fang et al., 2012; Chen et al., 2013; Gleiter 2013; Franke et al., 2014; Guo et al., 2017; Liu et al., 2018; Li et al., 2018; Adjaoud and Albe, 2019). It has been argued that the glassy interfaces facilitate nucleation of multiple shear bands, thereby avoiding the shear localization and improvement in tensile ductility (Adibi et al., 2013; Singh et al., 2014; Wang et al., 2015).

Recent indentation experiments on $Cu_{50}Zr_{50}$ binary system show that NGs exhibit a higher hardness than MG ribbons of identical composition (Nandam et al., 2017), which has been attributed to the Zr rich dense core surrounded by Cu rich interfaces carrying excess free volume. However, it is not clear as to why hardness should increase in the presence of free volume rich interfaces. Franke et al. (2014) have also reported a higher hardness in NGs than MGs, but they did not discuss the mechanistic reason for this behavior. A large number of experiments and numerical studies conducted on MGs shows that the reasons for high hardness in these materials is intimately connected with the pressure sensitive plastic flow taking place beneath the indenter (Vaidyanathan et al., 2001; Patnaik et al., 2004; Schuh and Nieh, 2004; Ramamurty et al., 2005; Keryvin 2007; Prasad et al., 2007; Keryvin, 2008; Keryvin et al., 2008; Fornell et al., 2009; Prasad et al., 2009, Rodriguez et al., 2012; Aliaga et al., 2013; Chen et al., 2013b; Bhattacharyya et al., 2015) and hardness appears to increase with the pressure sensitive index α which quantified the pressure sensitivity (Narasimhan, 2004). Given the amorphous structure of NGs with glassy grains and glassy interfaces, the plastic flow of NGs could be expected to be pressure sensitive which may be the reason for high hardness observed in these materials although it has not been investigated in detail.

Therefore, in this chapter, finite element simulations of indentation are performed using the pressure insensitive (Von-Mises) and pressure sensitive (extended Drucker Prager) plasticity

model to analyze the indentation behavior of $SC_{75}Fe_{25}$ NGs and MG ribbons. The organization of this chapter is as follows. The constitutive model is briefly described in section 2.2, and modeling details are explained in section 2.3. Finally, the important results obtained from this study are discussed in section 2.4.

2.2 Constitutive model

The advantage of using extended Drucker Prager constitutive model is that it can be reduced to original Drucker Prager model as well as to Von-Mises model by choosing appropriate material parameters (Abaqus 2017). Further, from a numerical implementation perspective, the extended Drucker Prager yield criterion is easier because it consider second and third invariant of deviatoric stress. Also, it obeys an associative flow rule with continuous varying normal. Furthermore, this model can be used to check the influence of shape parameter, K on yield surface.

The yielding in the material is assumed to be governed by extended Drucker Prager yield criterion is given as (Abaqus 2017)

$$f(\sigma_{ij}, \sigma_y^c) = \frac{\bar{\tau}}{2}\left[1 + \frac{1}{K} - \left(1 - \frac{1}{K}\right)\left(\frac{r}{\bar{\tau}}\right)^3\right] + \sigma_m tan\alpha - \left(1 - \frac{1}{3}tan\alpha\right)\sigma_y^c = 0. \tag{2.1}$$

Where,

$$\bar{\tau} = \sqrt{3J_2} \tag{2.2}$$

$$r^3 = \frac{27}{2}J_3 \tag{2.3}$$

$$\sigma_m = \frac{1}{3}(\sigma_1 + \sigma_2 + \sigma_3). \tag{2.4}$$

In above equations, $(\sigma_1, \sigma_2, \sigma_3)$ are principal stresses of the stress tensor σ_{ij}. $\bar{\tau}, \sigma_m$ and σ_y^c are Mises equivalent stress, hydrostatic stress and compressive yield strength of material, respectively. Further, J_2 and J_3 are second and third invariant of deviatoric stresses of stress tensor. The parameter α and K are pressure sensitive index and shape parameter of yield surface. Note, Eq. (2.1) represents as conical surface in principal stress space whose apex lies on hydrostatic tension axis. The shape of yield surface on deviatoric plane (π plane) is non-circular and its shape is controlled by K. To maintain convexity of yield surface K should be greater than 0.778. Further, Eq. (2.1) reduces to original Drucker Prager yield function with $K = 1.0$, which represents circular yield surface. While, Eq. (2.1) reduces to the pressure

insensitive Von- Mises yield function for $K = 1.0$ and $\alpha = 0^0$. In this study most of the simulations are performed with $K = 1.0$, whereas few simulations are undertaken with $K = 0.8$ to assess the effect of shape of yield surface on indentation response.

2.3 Modeling aspects

The axisymmetric finite element simulations of Berkovich indentation on cylindrical specimens are performed using 'Berkovich equivalent' conical indenter with spherical tip (R = 200 *nm*) and semi-apex angle of 70.3^0 which has identical projected area to depth function to that of standard Berkovich indenter (Lichinchi et al., 1998). Fig. 2.1(a) displays finite element discretization of sample using four-node quadrilateral axis symmetric elements in $r - z$ plane along with the indenter geometry. The size of the specimen is chosen as 40 $(L_s/R) \times 30$ (H_s/R) to ensure that plastic zone is well contained below indenter so that boundary effects on indentation response could be minimized (Patnaik et al., 2004). Further, all nodes on the bottom and left side edges are constrained to move in z and r direction, respectively, while a constant displacement rate is applied to the rigid indenter through a reference point RP attached to it (refer Fig. 2.1(a)).

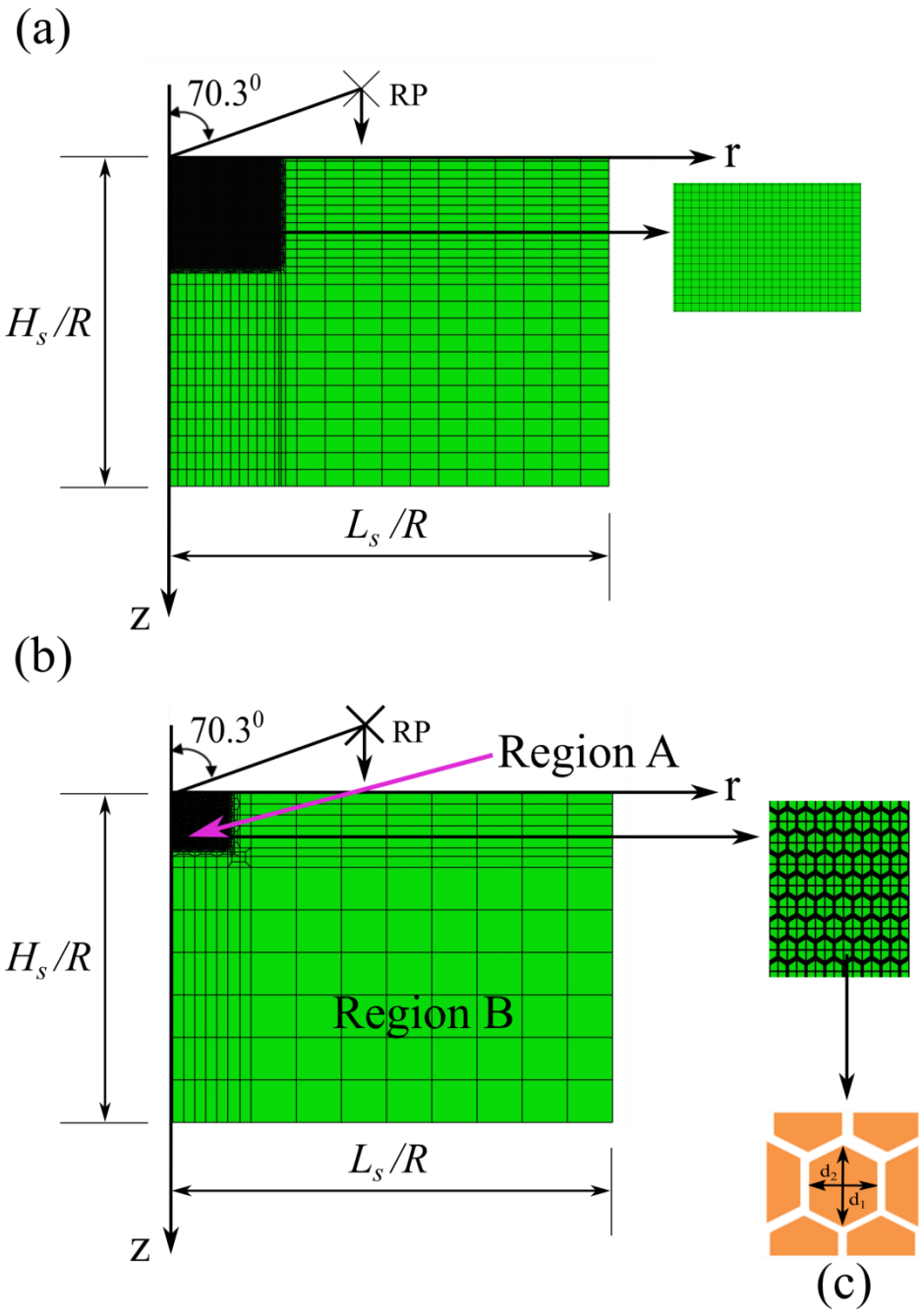

Figure 2.1 (a) 2D Axisymmetric finite element model of cylindrical specimen along with 'Berkovich equivalent' conical rigid indenter with half cone angle of 70.3^0 employed in indentation simulations. (b) Finite element model of cylindrical sample considering microstructure of NG in a region A, while homogenized NG in region B. (c) Enlarged view of region A and a grain whose size is characterized by length d_1 and d_2.

A highly refined mesh is employed to capture larger strain gradient below the indenter. Furthermore, contact between indenter and specimen is assumed to be frictionless. In this chapter, on NG two types of indentation simulations are performed, in first type of

simulation microstructure of NG is not modeled and homogeneous NG is considered (refer Fig. 2.1(a)), While in second type of simulation microstructure of NG (i.e., discrete glassy grains and glassy interfaces) is modeled (refer Fig. 2.1(b)). The modeling details for the latter will be discussed in section 2.4.

The constitutive behavior of NG and MG is assumed to be governed by the plasticity model described in section 2.2 and the aim of present study is to determine α for $Sc_{75}Fe_{25}$ NGs synthesized by Liu et al. (2018), Franke et al. (2014) and Wang et al. (2015) by fitting simulated indentation load, P vs. depth, h curves to the experimental data reported by respective authors. Although composition of NGs of all three authors is identical, indentation response has been found to be marginally different due to marginal difference in their yield properties. Therefore, to avoid confusion, NGs of Liu et al. (2018), Franke et al. (2014) and Wang et al. (2015) are referred to as NG1, NG2 and NG3, respectively. Further, to compare the pressure sensitivities of NG and MG, α of $Sc_{75}Fe_{25}$ MG ribbon is also determined by fitting experimental data of Franke et al. (2014) and Wang et al. (2015). NGs and MGs are assumed to exhibit elastic perfectly plastic response. The compressive yield strain, $\epsilon_y^c = \frac{\sigma_y^c}{E}$ (E is Young's modulus) of NG1, NG2 and NG3 are taken as 0.02, 0.014 and 0.013, respectively (Liu et al., 2018; Franke et al., 2014; Wang et al., 2015), while for MG ribbon, it is approximated to 0.02 (Franke et al., 2014; Wang et al., 2015). Further, Poisson's ratio is taken as 0.36 for both NGs and MG (Schuh et al., 2007).

2.4 Result and discussion

Fig. 2.2(a) Displays the normalized indentation load, $\frac{P}{ER^2}$, versus normalized depth, $\frac{h}{R}$ curve obtained from finite element simulation on NG1 for different values of α and K is plotted against the experimental curve reported by Liu et al. (2018). It can be seen that *for K = 1 and $\alpha = 0^o$, the curve deviates significantly from experimental data suggesting that Von-mises criterion does not describe the yield behavior in NGs.* While the curves corresponding to $K = 1$ and $\alpha = 15 - 20^o$ shows good agreement with experimental data except for the marginal differences in values of load for smaller h/R. This *suggests that the yield phenomena in $Sc_{75}Fe_{25}$ NG is characterized more accurately by pressure sensitive extended Drucker Prager plasticity model*.

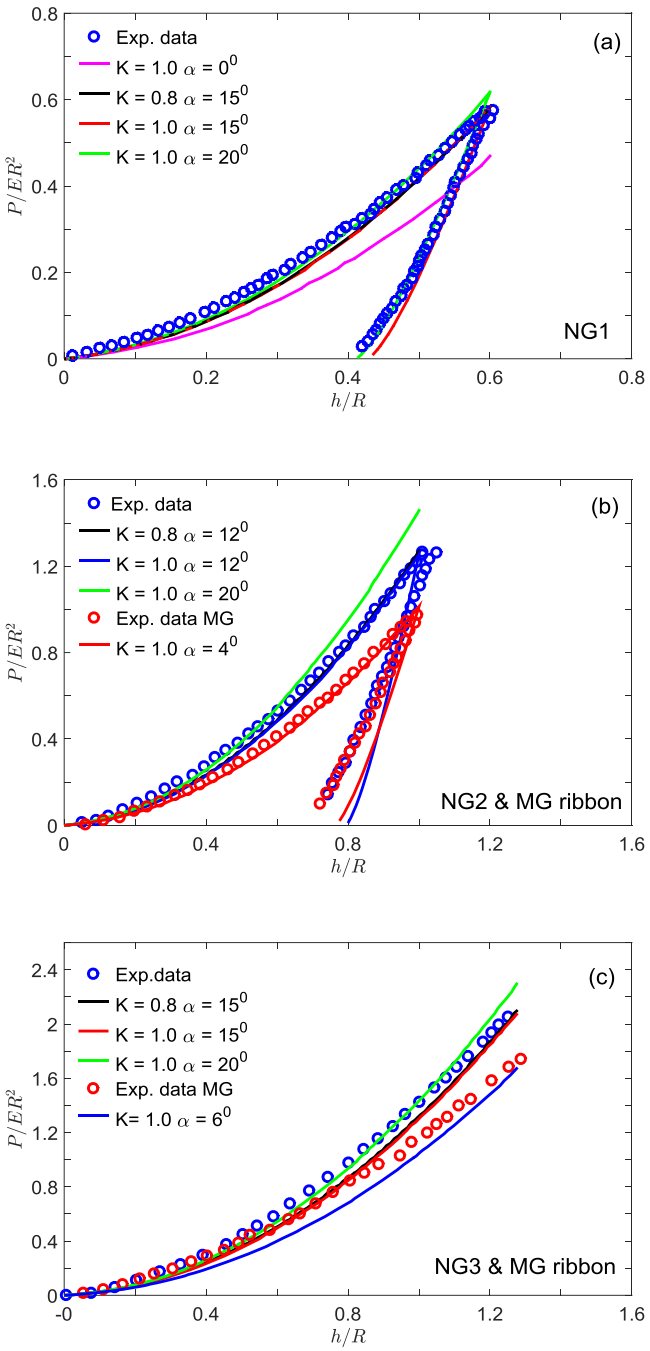

Figure 2.2 (a) Normalized indentation load, P/ER^2 versus normalized depth, h/R curves for NG1 corresponding to different values of α and K, along with the experimental data of Liu et al. (2018). (b) Corresponding curves for NG2 and MG ribbon along with the experimental data of Franke et al. (2014). (c) Corresponding curves for NG3 and MG ribbon along with the experimental data of Wang et al. (2015).

Fig. 2.2(b) compares indentation load, P vs. depth, h response of NG2 and MG ribbon with experimental results of Franke et al. (2014). Note that curves corresponding to $\alpha \sim 12^o$

and 4^o for NG2 and MG, respectively, corroborate better with experimental data suggesting that α *for* $SC_{75}Fe_{25}$ *NGs is much higher than* $SC_{75}Fe_{25}$ *MG ribbon*. Further, α for NG3 and MG synthesized by Wang et al. (2015) is determined to be around 15^o and 6^o, respectively (refer Fig 2.2(c)). Thus, *it can be concluded that value of* α *is* ~$12 - 20^o$ *for* $Sc_{75}Fe_{25}$ *NG, while it is*~ $4 - 6^o$ *for MG ribbon. In other words, indentation response of* $Sc_{75}Fe_{25}$ *NGs is more pressure sensitive than MG with identical composition.* Comparison of curves for $K = 1$ and 0.8 in Fig. 2.2(a) and (b) suggest little influence of *shape of yield surface on indentation response of NGs* consistent with the literature observations (Patnaik et al., 2004).

In Fig. 2.3 variation of normalized hardness, H/σ_y^c (also referred to as constraint factor, *C*) with normalized indentation strain, $Ea/\sigma_y^c R$ for NG1 (with $\alpha = 20^o$) and MG ribbon (with $\alpha = 4^o$) predicted by finite element simulations and expanding cavity model (ECM) proposed by Narasimhan (2004) are displayed. The governing equations in expanding cavity model for sphero-conical indenter are numerically integrated by considering geometry of indenter to be spherical at low contact loads, while conical shape at higher indentation loads (refer Appendix A.1). The value of *C* for NG1 reported by Liu et al. (2018) is also marked by 'o' symbol in Fig. 2.3. Note that predictions of finite element simulations and expanding cavity model are in good agreement for NG1, and they differ by less than 10% for MG ribbon. The values of *C* for NG1 and MG increases with $Ea/\sigma_y^c R$ during early stages of loading, and at around $Ea/\sigma_y^c R = 20$, *C* for NG1 reaches very close to that of experimentally measured value. Although, such comparison could not be made for MG ribbon due to lack of experimental data, the value of *C* for MG ribbon at $Ea/\sigma_y^c R = 20$ in Fig. 2.3 is comparable to that for Zr-based bulk MG reported by wright et al. (2001) from Berkovich indentation and falls within the range of C for MGs suggested by Schuh et al. (2007). It is important to note that values of *C* of NG1 are higher than MG ribbon which can be explained by noting higher α in the former. Expanding cavity model predicts that *C* in pressure sensitive solids increases with increase in α (Narasimhan, 2004; Patnaik et al., 2004; Bardia and Narasimhan, 2006; Subramanya et al., 2009) and/or decrease in ϵ_y^c (Gao et al., 2006). Since ϵ_y^c of NG1 and MG ribbon is almost identical, hence higher *C* in NG1 is solely attributed to higher α. Thus, it can be concluded that $Sc_{75}Fe_{25}$ *NGs exhibit higher C than* $Sc_{75}Fe_{25}$ *MG ribbon because of their higher* α.

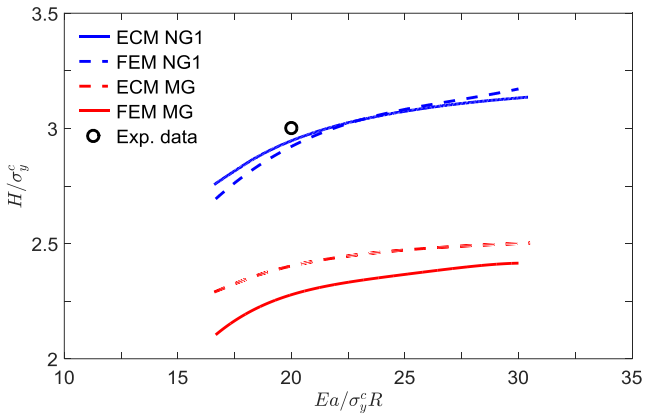

Figure 2.3 The variation of normalized hardness, H/σ_y^c with normalized indentation strain, $Ea/\sigma_y^c R$ predicted by finite element simulations and expanding cavity model (Narasimhan, 2004).

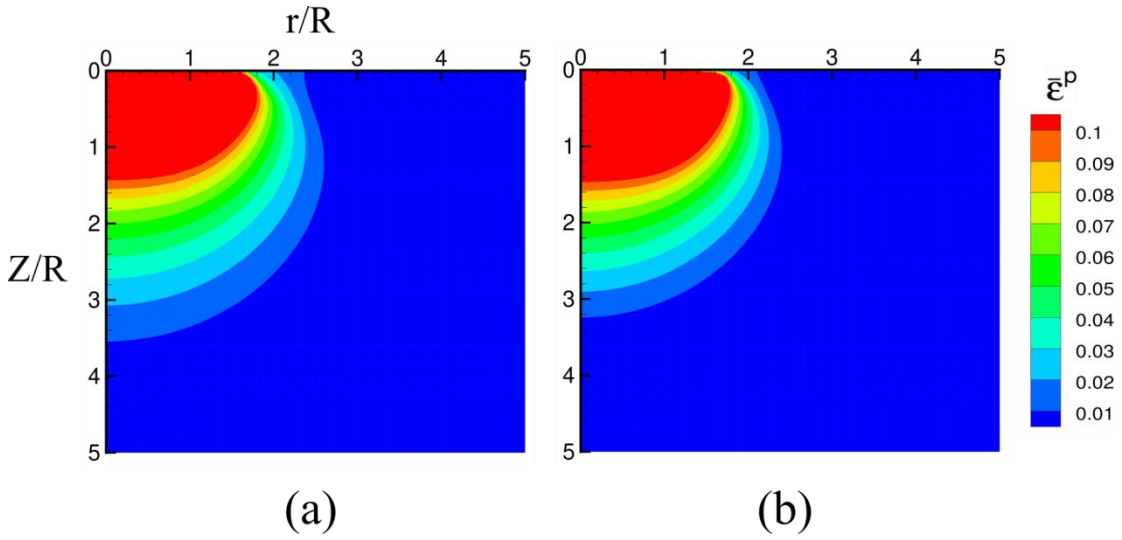

Figure 2.4 Contour plots of equivalent plastic strain, $\bar{\epsilon}^p$ corresponding to h/R = 0.6 for (a) NG1 and (b) MG ribbon.

To understand the effect of α on plastic strain distribution below indenter, contour plots of equivalent plastic strain, $\bar{\epsilon}^p$ at h/R of 0.6 are shown in the undeformed configuration for NG1 and MG ribbon (with $\alpha = 4^o$) in Figs. 2.4(a) and (b), respectively. As expected, $\bar{\epsilon}^p$ is maximum just below indenter, but decreases with increase in z (Prasad et al., 2011). Comparison of Figs. 2.4(a) and (b) indicates that plastic zone size in NG1 is marginally larger than MG. To confirm this, variation of $\bar{\epsilon}^p$ with z along the line $r = 0$ is plotted in Fig 2.5(a). Note that $\bar{\epsilon}^p$ at $z = 0$ is higher in MG than NG1, while it drops more rapidly with increasing z in the former than latter. Assuming that material at a point has

yielded if $\bar{\epsilon}^p > 0.005$, it can be noticed that plastic zone size, r_p^{NG1} in NG1 is larger than plastic zone size, r_p^{MG} in MG (inset diagram, Fig. 2.5(a)). These observations are found to be true for NG2 and NG3 also (refer Fig. 2.5(b) and (c)). Thus, the present study reveals that *plastic zone size in NGs is larger than MG having identical composition which is because of higher* α in NGs.

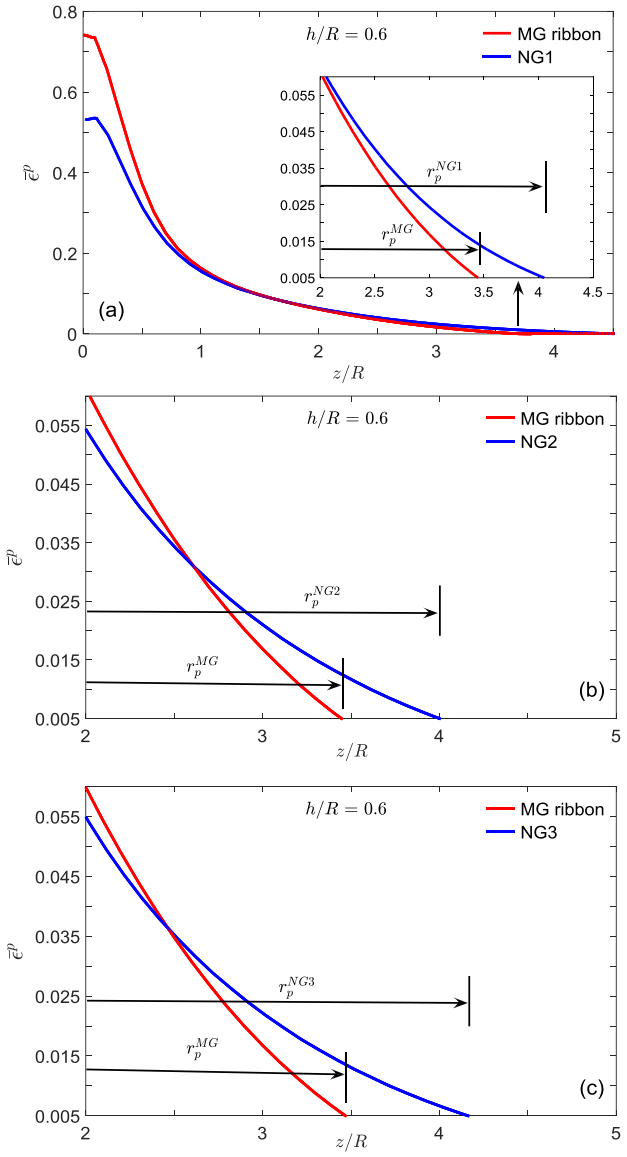

Figure 2.5 (a) Variation of equivalent plastic strain, $\bar{\epsilon}^p$ along the depth of specimen of NG1 and MG ribbon (b) and (c) corresponding plots for specimen NG2 and MG ribbon and specimen NG3 and MG ribbon, respectively.

As noted above, higher C and larger r_p in NGs are due to their high α, which might be because of presence of free volume rich glassy interfaces. Therefore, a fundamental question

"what is value of α for interfaces in NGs?" arises. To address this, finite element simulations of indentation on NG1 are repeated by modeling the microstructure of NG (i.e. glassy grains and glassy interfaces), as displayed finite element model in Fig. 2.1(b). Since α is expected to influence deformation only after commencement of plastic yielding, microstructure is modeled only in the region (region 'A' in Fig. 2.1(b)) just underneath indenter, while a homogenized NG is considered outside this region i.e., region 'B' (Fig. 2.1(b)). Note that region A is significantly larger than r_p^{NG1} noted in Fig. 2.5(a). Following (Singh et al., 2014), shape of the glassy grains is assumed to be hexagonal, and their size is characterized by dimensions $d_1$and d_2 along r and z directions, respectively (Fig. 2.1(c)). Here, d_1 and d_2 are chosen as 9 and 11 *nm*, respectively, to achieve average grain size of 10 *nm*, as observed in experiments (Liu et al., 2018), while interface width is taken as 1 *nm* (Liu et al., 2018) which results in a volume fraction of glassy grains, V_f^g = 0.73. The material in regions A and B are assumed to follow extended Drucker Prager plasticity model, as discussed in section 2.2. The ϵ_y^c and α_{NG1} for homogenized NG in region B are taken to be 0.02 (as used previously) and 15^o (determined in Fig. 2.2(a)), respectively. Further, assuming almost identical chemical composition and free volume distribution in glassy grains and parent MG, which were used to produce NGs, the yield properties of the former can be considered similar to that of the latter. Therefore, ϵ_y^c and pressure sensitive index, α_g for glassy grains are taken as 0.02 (Franke et al., 2014; Wang et al., 2015), and 4^o (determined in Fig. 2.2(b)), respectively. However, σ_y^c of glassy interface is taken 15% lower than that of glassy grains (Ritter et al., 2011; Singh et al., 2014; Wang et al., 2015; Li et al., 2018). Assuming that modulus follows rule of mixture, E for glassy interfaces is determined by employing iso-strain and iso-stress conditions (refer Appendix A.2), and simulations performed using E predicted by former and latter approaches are named as Simulation M and N, respectively. In addition, another set of simulations are performed by taking E for glassy grains as well as glassy interfaces identical to that of homogenized NG in region B. These simulations are named as Simulations L. The value of pressure sensitive index, α_i for glassy interfaces is determined by fitting simulated indentation load-depth curves to the experimental data for NG1 (Liu et al., 2018).

Fig. 2.6(a) shows comparison of experimental indentation load, *P* vs. depth, *h* curves (Liu et al., 2018) with the simulated ones obtained from Simulations L, M, and N by employing different α_i values. Note, all three simulations predict almost identical indentation response for a given α_i. Also, finite element results for a $\alpha_i \sim 30^o$ are in good agreement with

experimental data indicating the fact *that α for glassy interfaces is much higher than the glassy grains in $Sc_{75}Fe_{25}$ NGs*. This may be attributed to the presence of excess free volume in these regions which could be the *raison d'etre* for increased plasticity of NGs. Further, since $V_f^g = 0.73$ in the model, present study suggests that α in NG does not follow rule of mixture. Moreover, contour plot of equivalent plastic strain, $\bar{\epsilon}^p$ displayed in Fig. 2.6(b) which are generated from simulation M shows a higher strain inside glassy grains than glassy interfaces despite their lower strength. To clarify this, evolution of equivalent plastic strain, $\bar{\epsilon}^p$ inside a glassy grain, 'P' and glassy interfaces, 'Q' taken at a distance of z/R of 0.5 (refer Fig. 2.6(b)) is shown in Fig. 2.6(c). It can be noted from this figure that evolution of $\bar{\epsilon}^p$ inside glassy interface begins first and propagates into the glassy grain with increasing h/R. However, the growth of $\bar{\epsilon}^p$ is faster inside the glassy grain than glassy interface (refer Fig. 2.6(b)) which can be attributed the lower α_g and marginally lower ϵ_y^c in glassy grains. To get more insight of effect of these parameter (pressure sensitive index, α and yield strain, ϵ_y^c) on the evolution of equivalent plastic strain, $\bar{\epsilon}^p$ below the indenter, finite element simulations are performed on homogenized NG (i.e., without modeling microstructure, refer Fig. 2.1(a)) employing extended Drucker Prager yield criterion and using different values of ϵ_y^c and α. Fig. 2.7(a) shows development of $\bar{\epsilon}^p$ at a point below indenter located at a distance of $z/R = 0.5$. It can be seen that strain evolution retards when α or ϵ_y^c is increased, while it accelerates on decrease in ϵ_y^c. Similar trend can be observed for $z/R = 1.0$ too (refer Fig. 2.7(b)). Thus, the retarded strain evolution inside glassy interface (refer Fig. 2.6(c)) also suggest that glassy interface offers higher resistance for development of $\bar{\epsilon}^p$ in a NG, which is in line with atomistic simulations showing glassy interfaces as barriers for shear localization in NGs (Sopu et al., 2011).

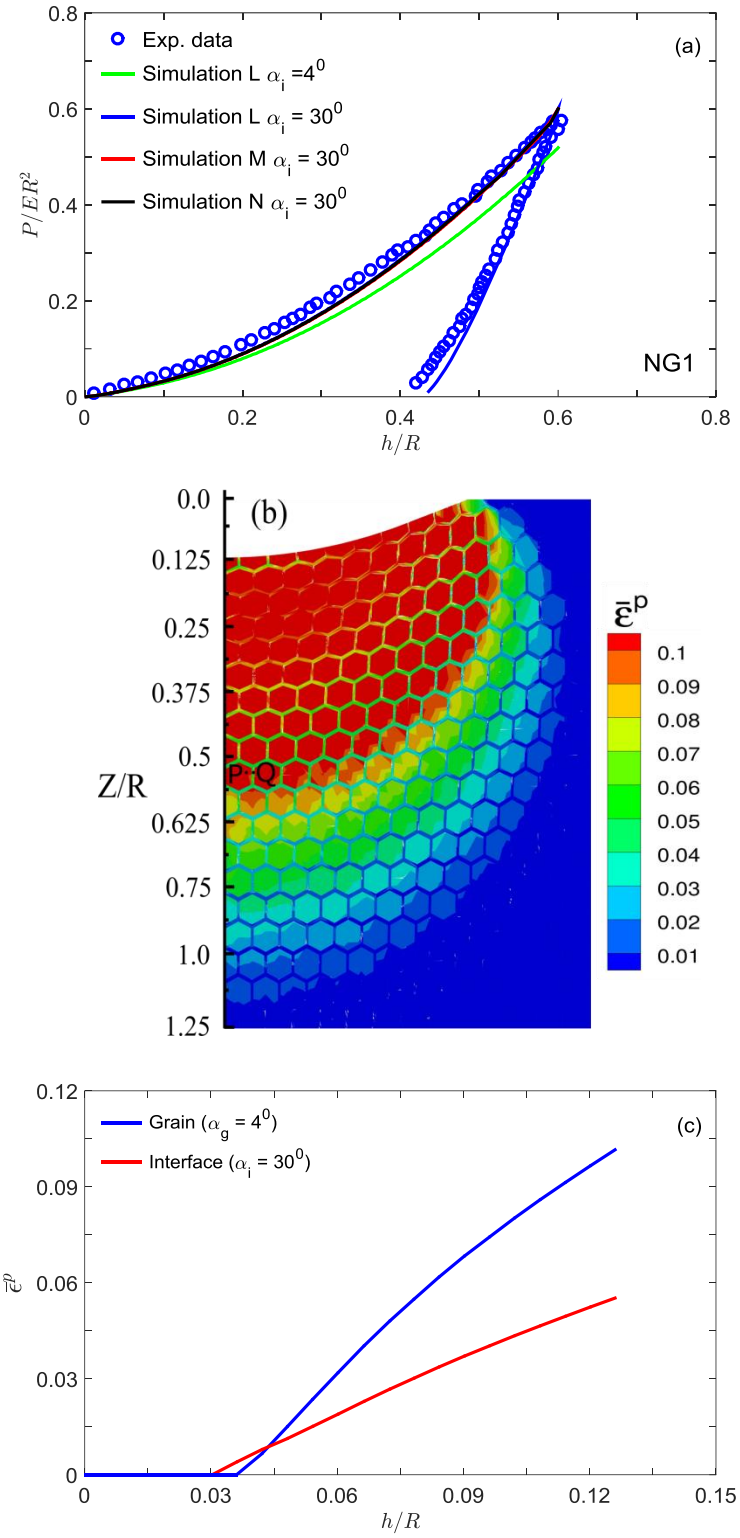

Figure 2.6 (a) Normalized indentation load, P/ER^2 versus normalized depth, h/R curves generated from simulation L, M and N on NG1, along with the experimental data of Liu et al. (2018). (b) Distribution of equivalent plastic strain, $\bar{\epsilon}^p$ below the indenter for NG1 at h/R = 0.125. (c) Evolution of $\bar{\epsilon}^p$ inside a grain, P and interface, Q marked in (b).

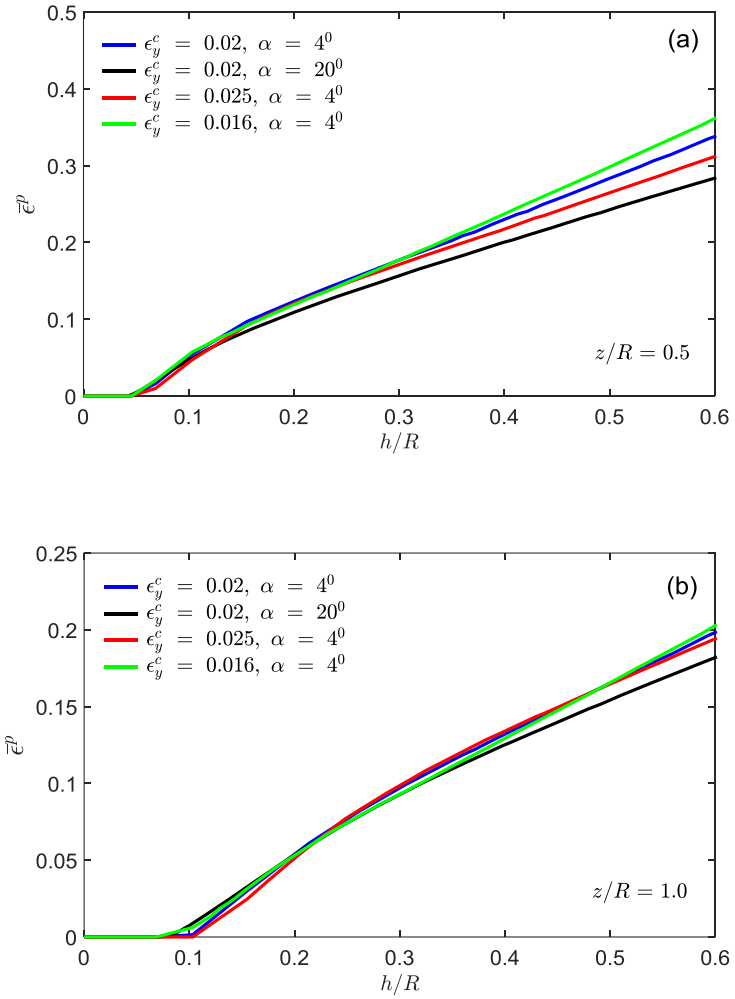

Figure 2.7 Evolution of equivalent plastic strain, $\bar{\epsilon}^p$ below the indenter at (a) $z/R = 0.5$ and (b) $z/R = 1.0$.

In summary, finite element simulations of indentation on $Sc_{75}Fe_{25}$ NGs and MG ribbons are performed using extended Drucker-Prager and Von-Mises plasticity model and the value of pressure sensitive index, α for these alloys is determined by fitting recent experimental data. The value of α for interfaces in NGs is also determined. Note that the hardness in MGs is observed to decrease with increase in the indentation load which is commonly referred to as the indentation size effect (ISE). The effect of the sensitivity of plastic flow to the pressure or normal stress on the ISE in glasses is not investigated. Thus, the mechanism governing ISE in NGs and MGs is not well understood. Therefore, in next chapter, nanoindentation experiments and complementary finite element simulations are performed to study the ISE in these alloys.

CHAPTER 3

Investigation of softening induced indentation size effect in nanoglass and metallic glasses

3.1 Introduction

The hardness is frequently observed to decrease with increase in the load during the indentation experiment, which is commonly referred to as the indentation size effect (ISE) (Jang et al., 2011). As mentioned in chapter 1, ISE has also been reported in MGs, and many authors have attributed it to the free volume induced softening during the indentation (Lam and Chong, 2001; Ramamurty et al., 2005; Manika and Maniks, 2006; Yang et al., 2007, Steenberge et al., 2007; Li et al., 2008, 2009; Fornell et al., 2009; Xu et al., 2014; Xue et al., 2016; Li et al., 2017; Zhou et al., 2019), while, Huang et al. (2011) argued that ISE in MGs is an experimental artifact. Thus, the understanding of the mechanics of ISE in MGs is far from complete. Recently, Sharma et al. (2021b) performed nanoindentation experiments on as prepared and annealed $Cu_{60}Zr_{40}$ NGs and reported different ISE. They argued that the difference in ISE is caused by change in the internal microstructure in the annealed NGs. Given the completely different microstructure of NGs and MGs, the ISE in the NGs is expected to be significantly different than that of MGs, although it has not been investigated till now. Further, it has been shown in Chapter 2 that the plastic deformation in NGs is more pressure sensitive than MGs due to high pressure sensitivity of interfaces in the former. However, the effect of pressure sensitivity on the ISE in glasses is not investigated and thus, the mechanism governing ISE in NGs and MGs is not well understood.

Therefore, nanoindentation experiments are performed at different peak loads on $cu_{60}Zr_{40}$ NGs and MGs to investigate ISE in both the alloys. Further, bonded interface experiments through micro indentation are also performed to clearly understand the subsurface deformation behavior. In addition, complementary nanoindentation finite element simulations are performed to elucidate the underlying mechanism governing ISE in NGs. The organization of this chapter is as follows. In section 3.2, the experimental procedure is presented briefly. The constitutive model employed in finite element simulations is briefly discussed in section 3.3, while the modeling aspects and material parameters are discussed in section 3.4. Finally, important results and discussion are presented in section 3.5.

3.2 Experimental procedure

The $Cu_{60}Zr_{40}$ NG and MG samples are obtained from Prof. Horst Hahn group, Karlsruhe Institute of Technology (KIT), Germany. The detailed process of synthesis of both materials is explained in the work of Nandam et al. (2017).

The quasi-static nanoindentation experiments are carried out using a Berkovich diamond indenter with a tip radius of $300\ nm$. The area function of the indenter is calibrated using a standard quartz sample. All the experiments are performed under load-controlled mode within the load range of 2 to $8\ mN$. The load function consists of loading, holding, and unloading segments with time intervals of 5, 2, and 5s, respectively. The surfaces of samples are carefully polished to a mirror finish using diamond paste. At least 16 indents are taken for each load to get reliable and statistically presentable data. The spacing between the successive indentations is set to be almost ten times of the maximum indentation depth to avoid the interaction of plastic boundaries. The hardness, H and elastic modulus, E are evaluated using equation discussed in section 1.3.1.

$$H = \frac{P_{max}}{A_c}, \tag{3.1}$$

$$E_s = (1 - \nu_s^2)\left[\frac{2\sqrt{A}}{\sqrt{\pi}S} - \frac{1 - \nu_i^2}{E_i}\right]^{-1}, \tag{3.2}$$

where, P_{maxi} and A_c are the maximum indentation load and projected area of contact, respectively. Further, in Eq. (3.2) the parameter S and ν are contact stiffness and Poisson's ratio. The subscript s and i denotes specimen and indenter under investigation, respectively. The shear bands formation around the periphery of the indentation impression are examined using an atomic force microscope (AFM).

Further, the bonded microindentation experiments are performed on both the alloys using Vickers indenters to characterize the shear band morphology underneath the indentation. For this purpose, two equal size specimens are taken, and one side of each specimen are polished up to a surface finish of 0.2 μm . The polished side of the specimens are bonded together using a strong adhesive ("super glue") and allowed to soak for 5-7 hrs. The bonded specimen is cold mounted such that the bonded inference is on the top of mould and is carefully polished to mirror finish. Vickers indentations are performed on the interface with maximum applied load of 0.5 N such that the impression of indent coincides with the

interface. After experiments, the bonded interface is opened by dissolving the adhesive in acetone and the subsurface deformed morphology is examined through scanning electron microscope (SEM).

3.3 Constitutive model

In this work, a finite deformation Mohr-Coulomb type plasticity model proposed by Anand and Su (2005) for MGs is employed because it has been shown to capture the deformation behavior of MGs under bending (Anand and Su, 2005), compression (Anand and Su, 2005), tension (Anand and Su, 2005), and indentation (Su and Anand, 2006). This model assumes that the plastic deformation in amorphous metals occurs by plastic shearing accompanied by dilatation relative to six potential slip systems defined relative to the principal directions of Kirchhoff stress. According to this model, the plastic shear strain in α^{th} slip system evolves as:

$$\dot{\gamma}^{(\alpha)} = \dot{\gamma}_0 \left\{ \frac{\tau^{(\alpha)}}{c + \mu\sigma^{(\alpha)}} \right\}^{\frac{1}{m}}, \tag{3.3}$$

where m, $\dot{\gamma}_0$, and μ are strain rate sensitivity parameter, reference plastic shearing rate, and internal friction coefficient. Further, $\tau^{(\alpha)}$ and $\sigma^{(\alpha)}$ represent the resolved shear stress and compressive normal traction acting on α^{th} slip system. The detailed expression for $\tau^{(\alpha)}$ and $\sigma^{(\alpha)}$ can be found in the work of Anand and Su (2005). Furthermore, in Eq. (3.3), c is the cohesion, which is assumed to evolve as following to capture the free volume induced softening in MGs:

$$c = c_{cv} + \left(\frac{b}{e-1}\right)\left\{ e^{\left(1-\left(\frac{\eta}{\eta_{cv}}\right)\right)} - 1 \right\}, \tag{3.4}$$

where, b and c_{cv} are the material constant, while η and η_{cv} are current and saturation level of free volume. The free volume evolution law is given by:

$$\dot{\eta} = \beta \sum_{\alpha=1}^{6} \dot{\gamma}^{(\alpha)} . \tag{3.5}$$

Here, β is the dilatation function which is assumed to evolve with η as:

$$\beta = \frac{g_0}{e-1}\left\{ e^{\left(1-\left(\frac{\eta}{\eta_{cv}}\right)\right)} - 1 \right\}, \tag{3.6}$$

where, g_0 is the initial value of dilatancy parameter. The above model has been implemented in the commercially available finite element program Abaqus 2017 by writing user defined material subroutine UMAT (Tandaiya et al., 2007, 2008, 2011). The integration of the constitutive equations is carried out using the implicit backward Euler method.

3.4 Modeling aspects

The axisymmetric finite element simulations on cylindrical specimens are performed using 'Berkovich equivalent' conical rigid indenter having a semi-apex angle of 70.3^0 and spherical tip with radius, R of $300\ nm$. Fig. 3.1(a) shows finite element discretization of specimen using quadrilateral axis symmetric elements in $r-z$ plane along with the rigid indenter. A highly refined mesh is employed below the indenter to capture the distribution of shear bands better, while relatively coarser mesh is used in the region away from the indenter. The size of the specimen is chosen as $25R(L_s) \times 20R(H_s)$ to ensure that the plastic zone is well contained beneath the indenter and the boundary effects on indentation response are minimized (Patnaik et al., 2004; Chapter 2). Further, all the nodes on the left side and bottom edges are restrained from moving along r and z directions, respectively, while a constant displacement rate is applied to the rigid indenter through a reference point RP attached to it (Fig. 3.1(a)). In this work, two types of indentation simulations are performed on NG which are referred to as simulation HNG and MNG. In simulations HNG, microstructure of NG is not modeled, instead the homogenized NG is considered, while discrete glassy grains and interfaces are modeled in simulation MNG (refer Fig. 3.1(b)). The finite element model displayed in Fig. 3.1(a) is employed for indentation simulations on MGs and Simulations HNG, while the model shown in Fig. 3.1(b) is used to perform simulation MNG. The constitutive behavior of NGs as well as MGs is assumed to be governed by the plasticity theory described in Section 3.3.

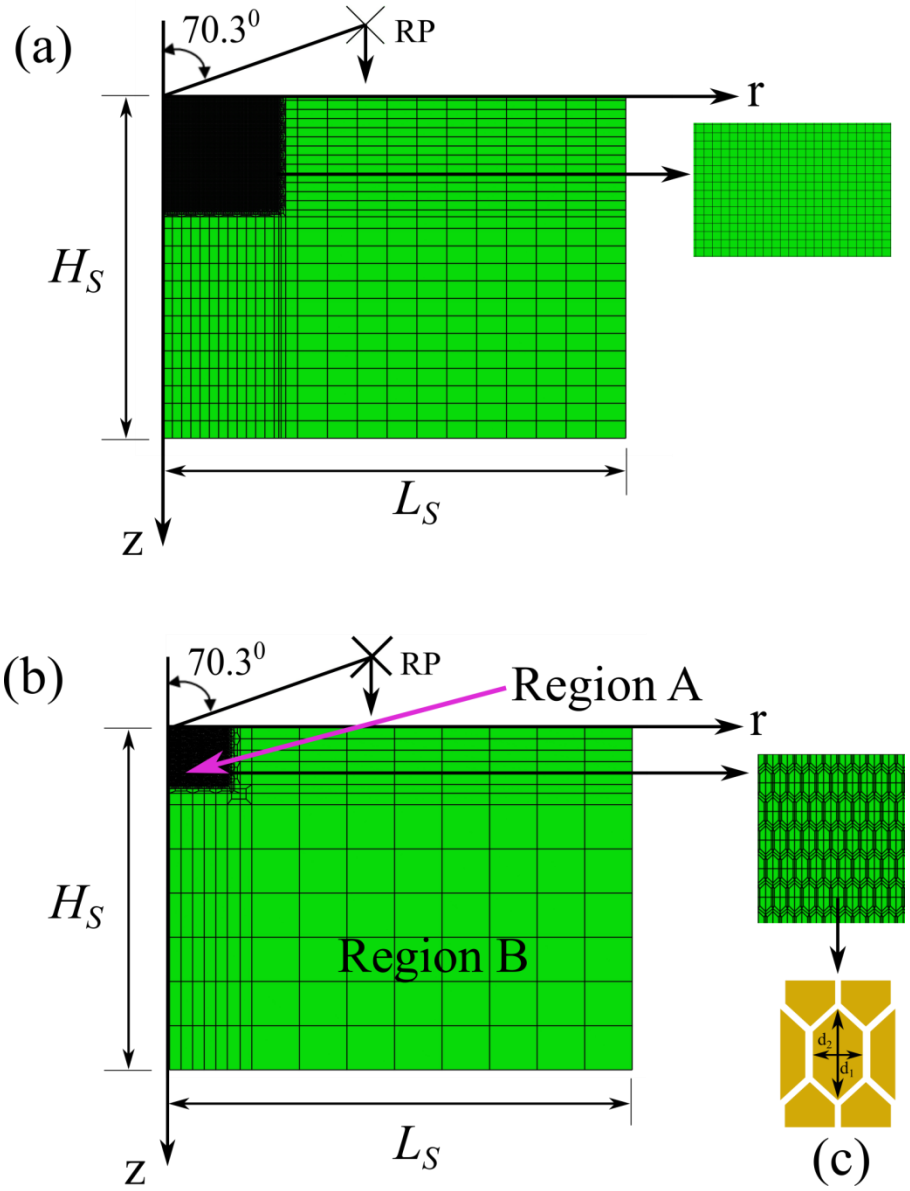

Figure 3.1 (a) 2D Axisymmetric finite element model of cylindrical specimen along with 'Berkovich equivalent' conical rigid indenter with half cone angle of 70.3^0 employed in indentation simulations of MG and Homogenised NG (HNG). (b) Corresponding finite element model employed for Microstructure NG (MNG) considering microstructure of NG in a 'Region A', while homogenized NG in 'Region B'. (c) Enlarged view of 'Region A' and a grain whose size is characterized by d_1 and d_2.

The values of Young's modulus obtained from nanoindentation experiments on NGs and MGs are used in the corresponding simulations. The values of parameters ν, m, $\dot{\gamma}_0$, g_o, c_{cv} and η_{cv} are considered to be identical for MG and NGs (simulations HNG as well as MNG), and these are taken from the work of Anand and Su (2005) and Tandaiya et al.

(2007). The rationale behind choosing identical values for these parameters is as follows. Like MGs, indentation response of NGs is reported to be also almost strain rate insensitive at room temperature (Nandam et al., 2017), therefore, a lower value of m is considered for both the alloys. Further, Singh et al. (2014) argued that the cohesion and free volume distribution should attain approximately the same saturation value at every point inside a shear band that cuts through glassy grains and glassy interfaces in NG. In addition, the free volume and cohesion distribution inside glassy grains in a NG can be assumed to be almost identical to that of MGs used to synthesize them. Therefore, c_{cv} and η_{cv} for MG and NG (glassy grains and glassy interfaces) are also assumed to be identical. The parameter $\dot{\gamma}_0$ is a reference strain rate, which is taken to be identical for all the simulations reported in the present study. Further, the initial cohesion c_0 for MG is taken from the work of Lee et al. (2007), whereas it is assumed to be 15% lower by choosing lower b for NG (in simulations HNG) than that for MG because of lower yield strength and lower steady state flow stress in the former than the latter with identical composition (Wang et al., 2015; Li et al., 2018). The values of μ for MGs and NGs (in simulations HNG) are optimized by performing a large number of simulations to get good agreement between the simulated and experimental indentation load versus displacement and hardness versus indentation depth curves. In order to seed defect sites and trigger the shear bands in both NGs (in simulations HNG) and MGs, the initial cohesion is perturbed by 3% (Tandaiya et al., 2007) about its mean value and randomly assigned to elements.

In simulation MNG, the microstructure of NG is modeled only in the 'Region A' just beneath the indenter to limit the problem size, while homogenized NG is considered outside this region, i.e., 'Region B' (refer Fig. 3.1(b)). The size of 'Region A' is ensured to be sufficiently larger than the plastic zone size below the indenter. Following MD simulations (Sopu et al., 2009; Adibi et al., 2013) and finite element simulations on NGs and NG-MG composites (Singh et al., 2014; Chapter 2, 5), the shape of grains is assumed to be hexagonal whose size is characterized by dimensions d_1 and d_2 along r and z directions, respectively (refer Fig. 3.1(c)). These values are taken to be 4 and $10\,nm$, respectively, to achieve an average grain size of $7\,nm$ which is similar to the size observed in the experiments by Nandam et al. (2017), while interface width is taken as $1\,nm$. The materials in 'Region A' and 'Region B' are assumed to follow the constitutive model discussed in section 3.3. The values of material parameters considered for 'Region B' are the same as used for simulation HNG (i.e., homogenised NG). Following experimental studies on NGs (Fang et al., 2012;

Nandam et al., 2017), the free volume distribution and chemical composition in grains and the parent MGs used to synthesize NGs are assumed to be identical. Therefore, in simulations MNG, the values of material parameters for grains are taken to be identical to that for MG. Since the glassy interfaces in NGs are characterized by excess free volume (Fang et al., 2012; Nandam et al., 2017) or lower density (Fang et al., 2012; Chen et al., 2013), the initial cohesion is taken to be 15% lower than glassy grains. Further, in order to nucleate shear bands from glassy interfaces, as observed in experiments (Wang et al., 2015) and MD simulations (Adibi et al., 2013), the initial cohesion is perturbed by 3% about its mean value and randomly assigned to the elements in the interfaces. The value of μ for interface is determined by fitting the simulated indentation load-displacement curve with the experimental data. The values of all the material parameters used in the simulations on MGs, simulations HNG and MNG are listed in Table 3.1.

Table 3.1 The values of material parameters used for finite element simulations of nanoindentation.

Material Parameter	MG	Homogenized NG (HNG)	Microstructured NG (MNG)	
			Grain	Interface
Young's modulus, E (Gpa)	70	120	120	120
Poisson's ratio, ν	0.36	0.36	0.36	0.36
Internal friction coefficient, μ	0.1	0.26	0.1	0.5
Reference plastic shear strain rate, $\dot{\gamma}_o$	0.001	0.001	0.001	0.001
Strain rate sensitive parameter, m	0.02	0.02	0.02	0.02
Constant in cohesion function, b (GPa)	0.3	0.15	0.3	0.15
Rate of dilatation parameter, g_0	0.04	0.04	0.04	0.04
Plastic volume at saturation, η_{cv}	0.005	0.005	0.005	0.005
Cohesion at saturation, c_{cv} (GPa)	0.660	0.660	0.660	0.660
Initial cohesion, c_0(GPa)	0.960	0.810	0.960	0.810

3.5 Result and discussion

3.5.1 Subsurface deformed morphology from microindentation experiments

Figs. 3.2(a) and (b) display the SEM images of subsurface deformation morphology underneath the Vickers indenter at a peak load of 0.5N for MG and NG, respectively. It can be noticed from these figures that shear bands in MG are smooth and almost semi-circular in shape (Fig. 3.2(a)), while a clear waviness in the shear bands in NG is visible (Fig. 3.2(b)) which is a consequence of interaction of multiple shear bands promoted by discrete microstructure (glassy grains and glassy interfaces) in the latter as pointed out by Sharma et al. (2021a). Also, the primary shear band densities (number of discrete shear bands) in the MG is higher than that in NG. Further, following Sharma et al. (2021a) the normalized deformed zone, $\frac{\lambda}{D}$ is calculated for NG and MG, where, λ is the distance of farthest shear band from the tip of indentation impression and D is the distance of the same band from specimen surface (refer Figs. 3.2(a) and (b)). The ratio $\frac{\lambda}{\mathrm{d}}$ is a measure of plastic zone size which can be correlated with the sensitivity of plastic flow to the hydrostatic pressure in an amorphous metal (Bhowmick et al., 2006; Prasad et al., 2007). Interestingly, it is found that normalized deformed zone beneath the indenter is around 0.8 for NG, and it is 0.7 for MG. Thus, it can be concluded that *the plastic zone size below the indenter is larger in NG than that in MG*, implying that $Cu_{60}Zr_{40}$ *NG is more pressure sensitive than MG of identical composition* and it would further be confirmed by finite element simulations of nanoindentation in subsequent section. The trends in the shear band patterns and $\frac{\lambda}{\mathrm{D}}$ noticed for $Cu_{60}Zr_{40}$ NG and MG in the present study are in corroboration with the recent subsurface indentation experiment performed on Pd- based NG and MG by Sharma et al. (2021a).

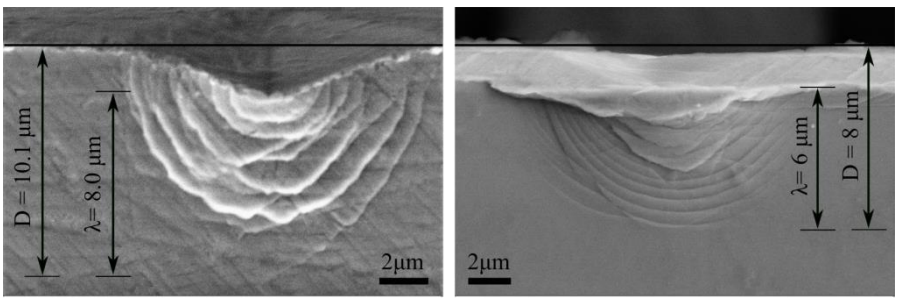

Figure 3.2 Scanning electron microscope (SEM) images of the subsurface deformed region at an indentation load of 0.5N for (a) NG and (b) MG.

3.5.2 Nanoindentation experiments

In Figs. 3.3(a) and (b), the indentation load-displacement ($P-h$) curves obtained from nanoindentation experiments performed at different peak loads are shown by solid lines for NG and MG, respectively. It can be seen from these figures that the depth of indentation increases with increasing in the load for both NGs and MGs, but it is lower in the former than the latter for any given load. In addition, the residual indentation depth after unloading is also lower in the NGs than MGs, suggesting former exhibits a lower elastic recovery than the latter. Most importantly, no pop-in events are noticed in Fig. 3.3(a) for any peak load which signifies almost homogeneous plastic deformation through the nucleation of simultaneous multiple shear bands in NGs. A similar behavior has also been observed in the nanoindentation and compression experiments on Sc-based NGs performed by Wang et al. (2015). On the contrary, many pop-in events are observed in load-displacement curves of MGs which are identified by arrows in Fig. 3.3(b). Note, both the magnitude of the displacement burst in a pop-in and the number of pop-in increase with the indentation depth. Each pop-in event corresponds to the nucleation and propagation of shear bands underneath the indenter, hence this kind of behavior is termed as localized deformation (Wang et al., 2015). A similar finding is reported from indentation studies on bulk MGs (Schuh et al., 2004; Li et al., 2008).

In Fig. 3.4, the variation of nanoindentation hardness, H, determined using Oliver and Pharr method (2004), is plotted against maximum penetration depth, h_{max} as shown by solid line curves for NGs and MGs. Note, the indentation hardness decreases with an increase in the indentation depth signifying significant ISE in both the materials. For instance, H for MGs decreases from 6.94 to 5.60 GPa when h_{max} is increased from 118 to 290 *nm* resulting in around 19% drop in hardness. A similar trend in H with increase in P or h_{max} has also been reported for Zr-, Pd- based bulk MGs (Steenberge et al., 2007; Li et al., 2008) as well as for Cu-Zr based MGs (Rauf et al., 2018) during nanoindentation. On the other hand, in the case of NGs, H declines only by 11% with increasing h_{max}, therefore, *it can be concluded that ISE in NGs is less pronounced as compare to MGs*. Recently, Sharma et al. (2021b) has also reported significant ISE in as prepared as well as annealed NGs.

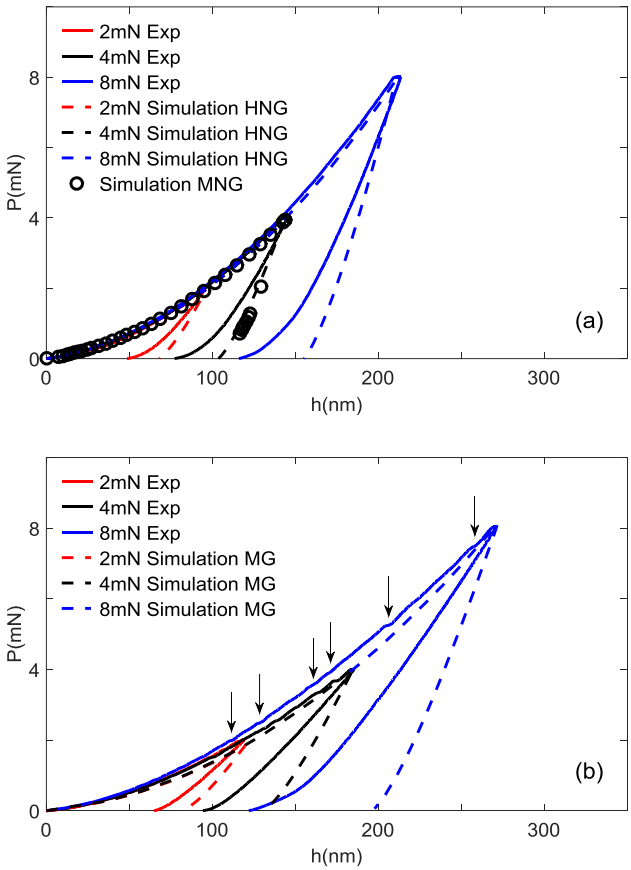

Figure 3.3 (a) The indentation load-displacement $(P-h)$ curves corresponding to different peak loads for nanoglasses, NG, obtained from nanoindentation experiments and simulations HNG and MNG. (b) The corresponding curves for metallic glass, MG.

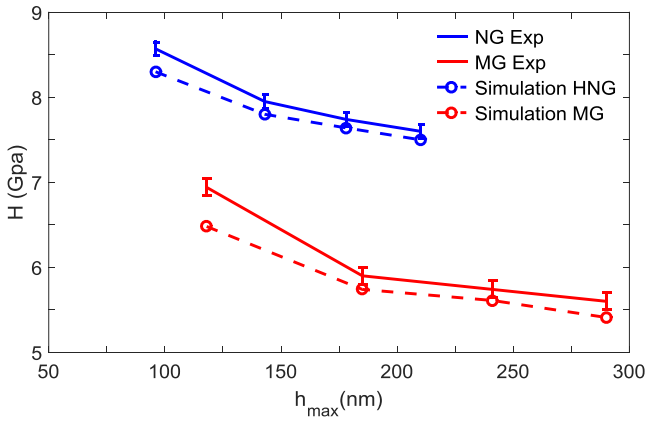

Figure 3.4 Dependence of indentation hardness, H calculated at the end of the holding stage, on the maximum indentation depth, h_{max} for NG and MG along with corresponding H values obtained from the finite element simulations.

To understand the plastic deformation around the indent, AFM images of imprint corresponding to the peak load of $8\,mN$ are displayed in Fig. 3.5(a) and (b) for NGs and MGs, respectively. In Fig. 3.5(a), no shear bands are noticed in the vicinity of indent confirming plastic deformation is completely accommodated underneath the indentation of NGs. On the other hand, one major shear band (marked by arrow) and few minor shear bands at the periphery of the impression are noticed in Fig. 3.5(b) signifying that the plastic flow cannot be completely accommodated in the subsurface deformation zone. The average hardness calculated at the peak load of $8\,mN$ for NGs and MGs are 7.59 ± 0.1 GPa and 5.6 ± 0.12 GPa, respectively, and the young's modulus is determined as 120 ± 4 GPa and 70 ± 10 GPa for the former and latter, respectively. Almost similar values for hardness and modulus for as prepared $Cu_{60}Zr_{40}$ NGs have also been reported by Sharma et al. (2021b). It is noteworthy to mention that higher hardness and Young's modulus in Sc-based NGs than MGs has also been reported by Franke et al. (2014). Furthermore, recently Nandam et al. (2017) performed nanoindentation experiments on $Cu_{50}Zr_{50}$ NGs, and MGs and reported higher hardness and reduced young's modulus in the former than the latter which they attributed to the presence of heterogeneous structure in NGs.

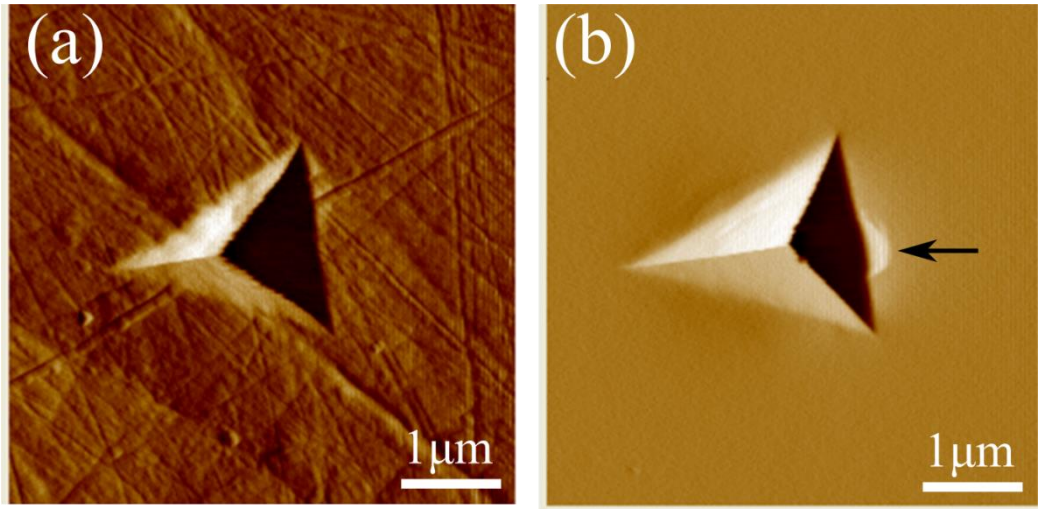

Figure 3.5 AFM images of indent corresponding to the peak load of 8mN for (a) NG and (b) MG.

3.5.3 Finite element simulations of nanoindentation

The value of μ for NG and MG is optimized to achieve an agreement between the simulated and experimental data to be better than 90%. The simulated $P-h$ curves for homogenized NG (HNG) and MG corresponding to optimum μ are displayed by dashed line in Fig. 3.3(a)

and 3.3(b), respectively. A good agreement between experiments and simulations HNG is found for $\mu = 0.26$ (Fig. 3.3(a)). However, the corresponding curves of MGs collaborate better with experimental data for lower μ of 0.1 with a marginal difference in the load values at the initial indentation depth (refer Fig. 3.3(b)). Note that μ for NGs is much higher than that for MGs of identical composition, suggesting indentation response of the former being more sensitive to normal stress than the latter. It is in corroboration with the recent study (Chapter 2), where Sc-based NGs is found to be more pressure sensitive than MGs with identical composition. Further, it must be mentioned that a significant deviation of simulated-unloading curves from the experimental data is observed which may be due to the increasing nonlinearity in material response during unloading (Oliver and Pharr, 2004). The values of hardness from finite element simulations are plotted against h_{max} by dashed line in Fig. 3.4, which shows a good agreement between simulation and experiments for both the alloys, except for lower indentation depth. The reason for this discrepancy will be discussed later.

In order to understand the evolution of plastic flow underneath the indenter in both the alloys, contour plots of maximum principal logarithmic plastic strain, $log\lambda_1^p$ corresponding to three successive stages of indentation depth, h obtained from simulations on MG and simulations HNG are presented in Fig. 3.6 in the undeformed configuration. Figs. 3.6(a)-(c) show the plastic flow distribution in NGs (HNGs) at $h = 95, 143$ and $210\ nm$, respectively, while Figs 3.6(d)-(f) shows the corresponding plots for MGs at the same penetration depths. It can be noticed by comparing Figs. 3.6(a) with (d) that discrete bands with higher plastic strain are developed in MGs, while the shear bands are more diffused, and the plastic strain is relatively uniformly distributed in case of NGs. With increasing indentation depth, the number of shear bands, their length and plastic strain inside them increases in both the materials, but strain distribution remains relatively more homogeneous in NGs (refer Fig. 3.6(b) and (c)) than in MGs (refer Fig. 3.6(e) and (f)). In addition, the magnitude of the plastic strain inside the bands in MGs (refer Fig. 3.6(d-f)) is much higher than the NGs (refer Fig. 3.6(a-c)). Further, assuming that the plastic deformation at a point would occur if $log\lambda_1^p$ at that point has exceeded beyond 0.001, the volume fraction of plastically deforming material, V_f^p is determined and plotted against h in Fig. 3.7 for both NG and MG. It can be seen from this figure that V_f^p in NGs is larger than in MGs for identical indentation depth, and it increases more rapidly in the former than the latter. In other words, *the plastic zone size is larger, and it spreads more rapidly in NGs than in MGs which is a consequence of higher*

pressure sensitivity in the former (Chapter 2). Note that the trends pertaining to shear band patterns and plastic zone size for MG and NG displayed in Fig. 3.6 and 3.7 are in line with the experimental observations in Fig. 3.2.

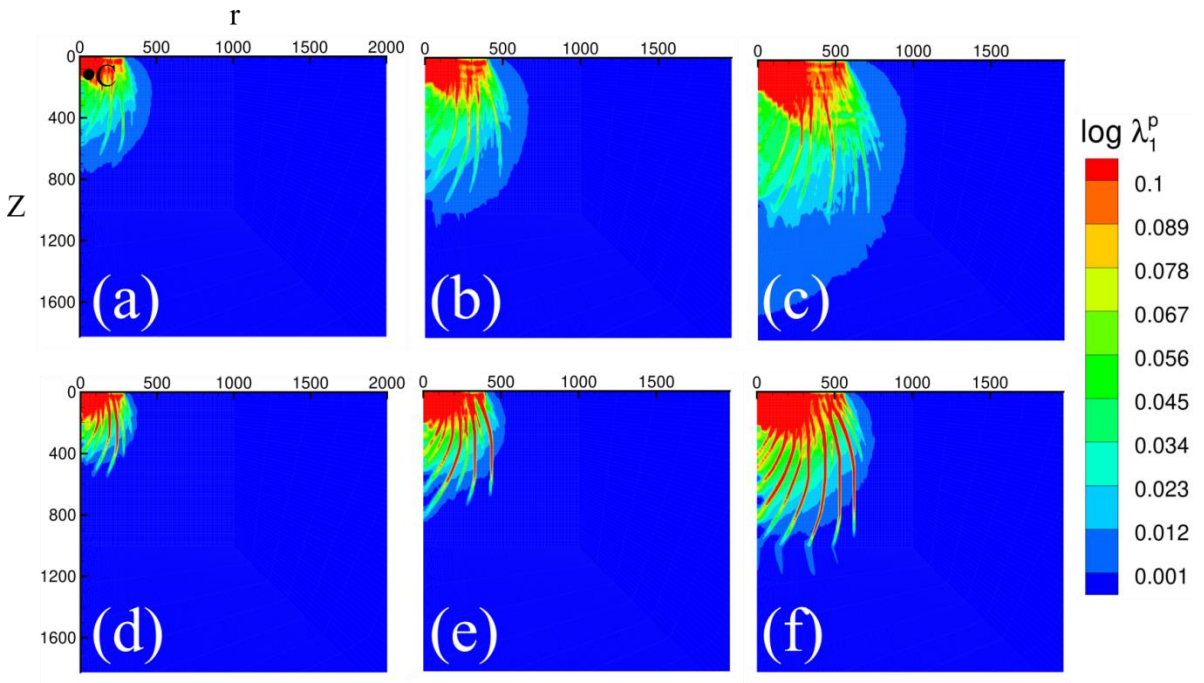

Figure 3.6 Contour plots of maximum principal logarithmic plastic strain $log\lambda_1^p$ for NG (obtained from simulations HNG) at (a) $h = 95\ nm$ (b) $h = 143\ nm$ and (c) $h = 210\ nm$. The corresponding plots for MG are shown in (d)-(f).

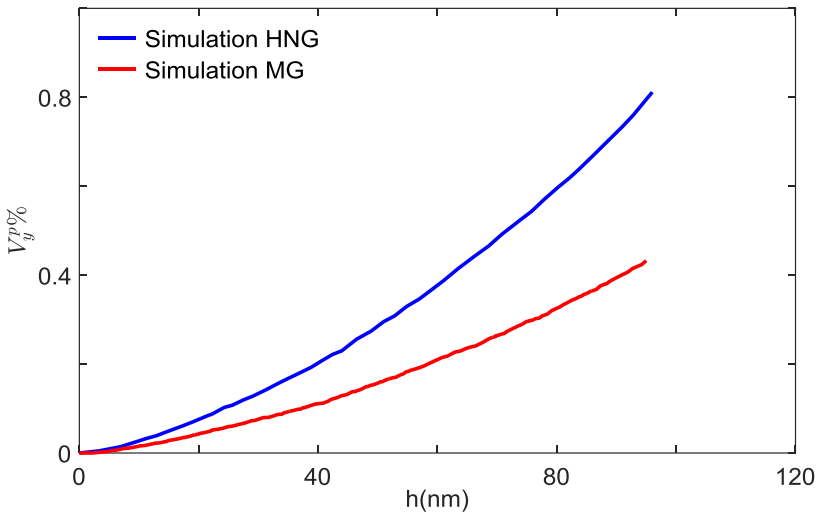

Figure 3.7 Variation of volume fraction of plastically deformed material, V_f^p with indentation depth, h for NG (obtained from Simulation HNG) and MG.

Further, recent finite element simulations of nanoindentation on Sc-based NG and MG performed using extended Drucker-Prager plasticity model have shown that the former exhibits higher pressure sensitivity due to the presence of interfaces. It must be mentioned that though extended Drucker-Prager model are pressure sensitive, they cannot capture free volume induced softening, a most important characteristic of amorphous metals. Therefore, Simulation MNG are conducted by modeling the microstructures of NG to determine μ for interface. The value of μ for interface is determined to be 0.5 by fitting the simulated $P-h$ curve with experimental data (refer Simulated $P-h$ curve of MNG in Fig. 3.3(a)). To get more insights on the role of interfaces on the formation of shear bands underneath the indenter, the contour plot of $log\lambda_1^P$ at $h = 143\ nm$ obtained from simulation MNG is shown in Fig. 3.8. The profuse shear banding giving the impression of almost uniform distribution of plastic strain just below the indenter is observed, whereas, away from the indenter, multiple discrete shear bands seem to have developed. A close observation of zoomed in view of a shear band shows that the glassy grains with large plastic strain have aligned in the form of a band but strain levels inside interfaces are less than 5%. Thus, the glassy interfaces prevent the strain localization in a band, consequently the bands in Fig. 3.8 are not well connected. Fig. 3.8 also displays the formation of secondary shear bands (SSB) bifurcating from primary shear bands (PSB) (refer bands PSB and SSB in Fig. 3.8). The formation of secondary shear bands beneath the indenter has also been reported in recent indentation experiments on Pd-based binary NG (Sharma et al., 2021a).

The present experiments show the presence of ISE in MG and NGs, as evident from Fig. 3.4. Huang et al. (2010) showed that ISE in MGs is an artefact of Oliver-Pharr method and it can be eliminated after correcting the pile-up at different indentation loads. Rodriguez et al. (2012) showed from experiments and complementary finite element simulations on different amorphous materials that the effect of pile-up in hardness values estimated using Oliver-Pharr scheme will be significant if the ratio elastic energy W_e to total energy, W_t obtained from $P-h$ curve is less than 0.5. In order to verify the applicability of Oliver-Pharr method in the present study, the ratio $\frac{W_e}{W_t}$ is determined at different peak loads and found to be around 0.52 and 0.54 for NGs and MGs, respectively. Therefore, it can be concluded that the ISE of hardness obtained from present experiments is not an experimental artefact but true response of the material.

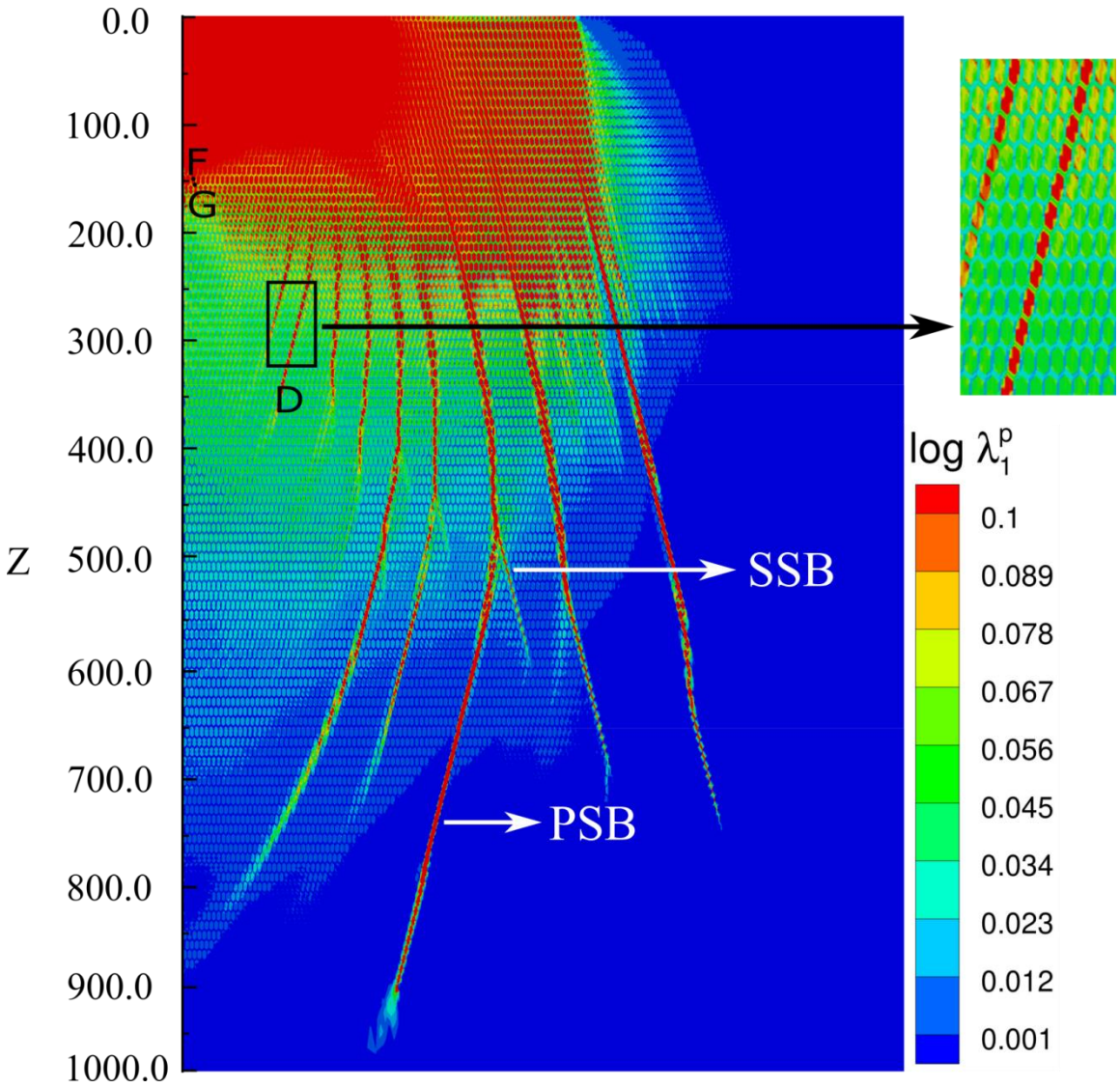

Figure 3.8 Contour plot of maximum principal logarithmic plastic strain, $log\lambda_1^p$ obtained from simulations MNG at $h = 143\ nm$. The inset figure shows an enlarged view of region D.

To explain the ISE in MGs, Lam and Chong (2001) and Yang et al. (2007) developed an analytical model, by adopting the perspective of strain gradient plasticity, analogous to the Nix-Gao model for crystalline materials. According to these models, the strain gradient induced plasticity in amorphous metals should be accommodated by the "geometrically necessary non-crystalline flow defects" such as excess free volume (Yang et al., 2007) or shear clusters (Lam and Chong, 2001). These models propose that the ISE in MGs are due to the increase in geometrically necessary flow defects (GNFDs) at shallow indentation depths akin to the geometrically necessary dislocations (GNDs) in the Nix-Gao model. It must be noted that the enhancement in GNDs causes strain hardening resulting in higher hardness in crystalline materials, whereas an increase in free volume or shear clusters (i.e. GNFDs)

should induce strain softening rather than hardening in MGs (Bei et al., 2006; Yoo et al., 2009). Thus, it is still not clear as to why the presence of GNFDs leads to an increase in hardness of MGs at low penetration depths. Therefore, GNFDs based mechanism cannot satisfactorily explain the ISE in NGs and MGs. Jang et al. (2011) correlated the hardness of MGs at an applied load with the volume of the material undergoing plastic deformation, and hence, with the activities of STZs and shear bands beneath the indenter. They argued that the volume of the material where plastic deformation has occurred is smaller at lower loads resulting in lesser activities of STZs and fewer shear bands below the indenter, but it enhances with increasing load causing more softening and lesser hardness at higher loads.

Steenberge et al. (2007) also looked ISE in MGs as a consequence of rapid softening induced by rapid accumulation of free volume during indentation. For this purpose, they correlated the hardness in an amorphous metal with the shear strain rate, $\dot{\epsilon}$, and the concentration of free volume, η using flow equation of Spaepen (1977) and Argon (1979) as:

$$H = \frac{6\sqrt{3}k_B T}{\Omega}\ \mathrm{Sinh}^{-1}\left(\frac{\dot{\epsilon}}{2f_0\Delta f\eta}\exp\left(\frac{\Delta G}{k_B T}\right)\right). \tag{3.7}$$

Here, k_B, T, Ω, f_0, Δf, ΔG are Boltzmann constants, test temperature, atomic volume, frequency of atomic vibration, volume fraction of material having potential jump sites, and activation energy, respectively. For load-controlled indentation experiments, the strain rate $\dot{\epsilon} = 1/h(dh/dt)$ underneath the indenter drops rapidly with increase in h and eventually saturating at larger h. The saturation level of $\dot{\epsilon}$ was almost identical for all maximum applied load (Steenberge et al., 2007) and hence it was concluded that the drop in H in MG is mainly due to the enhancement in η during indentation (Bhowmick et al., 2006; Steenberge et al., 2007). The variation of $\dot{\epsilon}$ in NGs and MGs for present indentation experiments is plotted against h in Fig. 3.9(a), which also shows almost identical drop in $\dot{\epsilon}$ for both the alloys, irrespective of applied load. Also, the values of $\dot{\epsilon}$ at h_{max} for any load is almost similar. Thus, Eq. (3.7) suggests that difference in ISE in NG and MG should be due to the difference in rate of free volume evolution in both the alloys. To estimate the free volume generation and subsequent softening during indentation, Eq. (3.7) can be further simplified as (Li et al., 2009):

$$K\eta = \left(\frac{f_0\Delta f\left(\frac{\Omega}{k_B T}\right)\exp\left(-\frac{\Delta G}{k_B T}\right)}{3\sqrt{3}\dot{\epsilon}}\right)\eta = \frac{1}{H} \tag{3.8}$$

The $K\eta$ versus h_{max} plots displayed in Fig. 3.9(b) suggest that free volume increases in both MG and NGs during indentation causing both the alloys to exhibit ISE. Most importantly, enhancement in free volume is faster in MG than NG resulting in rapid softening thereby leading to faster drop in flow stress in the former than the latter. This, in turn, results in faster drop in the hardness of MG than NG.

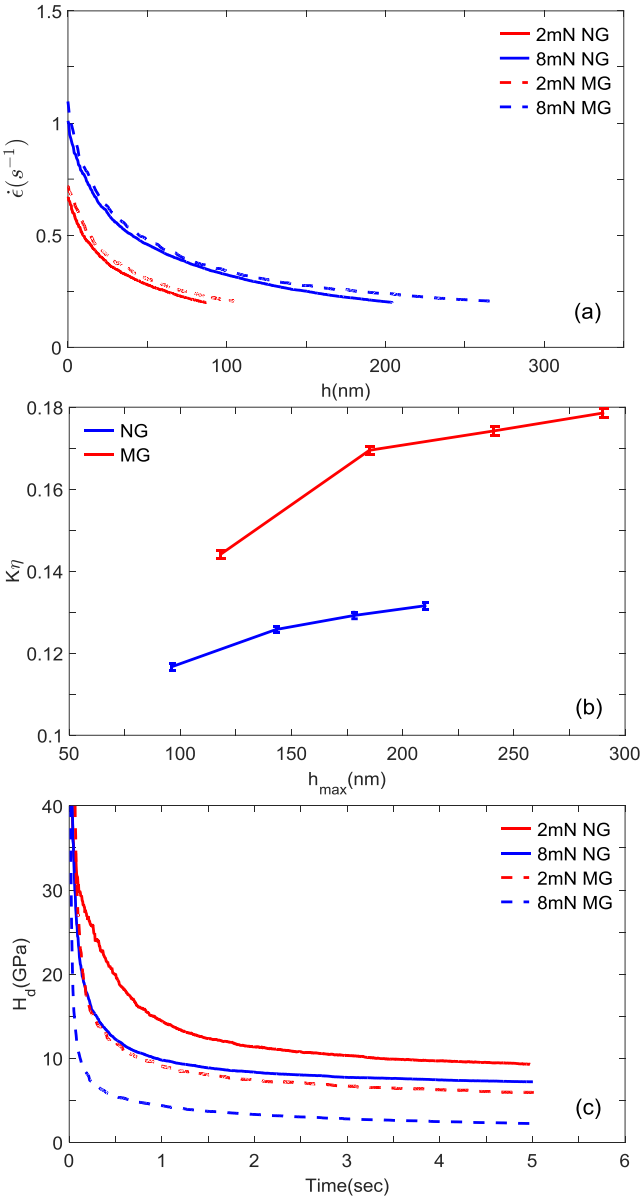

Figure 3.9 (a) Variation of shear strain rate underneath the indenter in NG and MG during indentation. (b)Variation of $K\eta$ with h_{max} for NG and MG. (c) The evolution of dynamic hardness, H_d during loading stage of indentation for NG and MG.

The difference in free volume generated in NGs and MGs during the indentation experiments can be further confirmed by monitoring the dynamic hardness, H_d, defined as the

ratio of instantaneous force to the instantaneous projected contact area (Concustell et al., 2005; Steenberge et al., 2007). By taking the instantaneous projected area as $24.65h^2$ for Berkovich indenter (Oliver and Pharr, 2004) and employing the Oliver-Pharr method (Oliver and Pharr, 2004; Concustell et al., 2005) the evolution of H_d is computed from the loading part of $P-h$ curves corresponding to different peak loads for NG and MG and displayed in Fig. 3.9(c). It can be noticed from this figure that irrespective of peak load, H_d drops with time and levels off at sufficiently longer time for both alloys. It is important to note that H_d drops more rapidly and saturates to a lower value in MG than that in NG, which signifies larger amount of free volume being generated during plastic deformation in the former than the latter (Steenberge et al., 2007). The larger free volume will cause more softening and hence higher drop in hardness leading to more pronounced ISE in MG (Steenberge et al., 2007). Thus, Fig. 3.9 and Eq. (3.7) suggest that the faster softening in MG than NG is a primary reason for higher ISE in the former. It must be mentioned that flow equation used in the analysis of Steenberge et al. (2007) does not account for the effect of hydrostatic pressure or normal stress which is an important characteristic of the plastic deformation in the amorphous metals (Patnaik et al., 2004; Chapter 2).

In order to understand the effect of μ on the softening underneath the indenter, the evolution of equivalent plastic strain, $\bar{\epsilon}^p$ and free volume η at a point 'C', taken at a depth of $0.5R$, (refer Fig. 3.6) is recorded from simulations on MG and HNG and plotted against h in Figs. 3.10(a) and (b), respectively. Due to lower initial cohesion, yielding begins at early stages of indentation causing plastic strain to evolve earlier in NG, but the rate of enhancement in plastic strain is higher in MG than NG in Fig. 3.10(a). This, in turn, results in faster free volume generation in MG than NG, as evident from Fig. 3.10(b) (also refer Eq. (3.5)). Consequently, MG exhibits relatively rapid drop in cohesion (i.e., softening) in comparison to NG during initial stages of indentation as can be understood from Eq. (3.4). The slower softening in NG observed in the present simulations is caused by two factors. First, initial cohesion in NG is lower while saturation cohesion is identical to that of MG, consequently, drop in cohesion in NG is slower (see Eq. (3.4)). Secondly, the higher μ for NG should reduce the shear strain rates which would result in slower evolution of free volume and slower drop in cohesion (refer Eqs. 3.3-3.5). In order to contrast the influence of these two factors on the evolution of free volume, one simulation on NG (simulation HNG) is performed by setting μ identical to that used in simulations for MG. The evolution of plastic strain and free volume at point same C obtained from this simulation are displayed by dashed

line in Fig. 3.10(a) and (b), respectively. Note from these figures that the rate of evolution of plastic strain and free volume increases when μ is reduced from 0.26 to 0.1, though it remains slightly lower than the MG. Therefore, *it can be concluded that the softening in NG during indentation is significantly influenced by their sensitivity to the normal stress (i.e., μ). In other words, slower softening caused by the higher μ is an important factor to be considered to explain the lesser ISE in NG than their MG counterpart*.

In order to understand the role played by interfaces on overall softening on NGs, the evolution of free volume inside a grain and interface marked by Points F and G, respectively, taken at a depth of around $0.5R$ (see Fig. 3.8), is extracted from simulations MNG and compared in Fig. 3.10(c). This figure shows that the rate of free volume generation inside interfaces is slower than that in grains. This is due to the fact that μ for interface is much higher than that for grains which results in slower strain rate and hence slower growth in η in the former than the latter (refer Eq. (3.5)). Consequently, cohesion drops slowly (refer Eq. 3.4) leading to slow softening inside interfaces. This, in turn results in, slower softening in an aggregate NG (considering both grain and interface) and lesser ISE.

It must be mentioned that a significant gradient in η below the indenter has been noticed in the present finite element simulations for lower h which vanishes when h is increased. The presence of free volume gradient would give rise to the interaction stress between flow defects such as STZs (Thamburaja, 2011). The interaction stress developed around the curved surfaces such as notches in nanometer-sized MG specimens imparts considerable strain hardening (Singh and Narasimhan, 2016). Since there would be a considerable curvature in the indent impression, therefore, strain hardening promoted by interaction stress during shallow indentation is expected to influence ISE in MGs and NGs. It must be mentioned that the plasticity model employed in the present finite element simulations is local and the stress arising due to free volume gradient is not incorporated in it. This is one of the reasons for significant discrepancy between experimentally measured hardness and the corresponding finite element predictions in Fig. 3.4 for lower h_{max}.

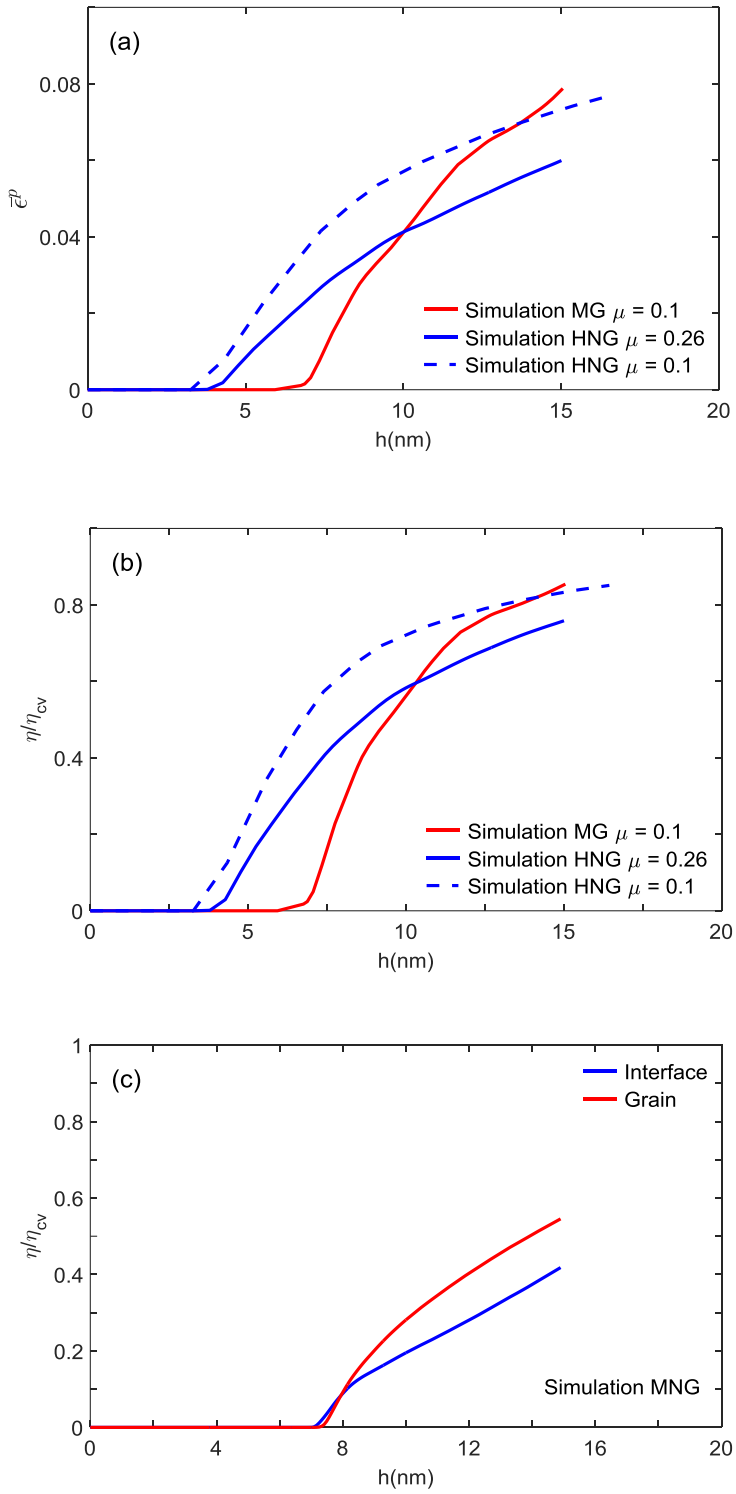

Figure 3.10 The variation of (a) Equivalent plastic strain, $\bar{\epsilon}^p$ and (b) Normalized free volume, $\frac{\eta}{\eta_{cv}}$ with respect to indentation depth, h at point 'C' taken at $z = 0.5R$ (refer Fig. 3.6) for NG (HNG) and MG. (c) The variation of $\frac{\eta}{\eta_{cv}}$ with h inside a grain, F and interface, G marked in Fig. 3.8 obtained from simulations MNG.

In summary, microindentation as well as nanoindentation experiments are performed on both $Cu_{60}Zr_{40}$ NGs and MGs. In addition, complementary finite element simulations of indentations are performed by employing the finite strain viscoplastic constitutive theory for amorphous metals. It must be mentioned that a considerable amount of research has been devoted to understanding the deformation response of NGs, but a few works have been undertaken to investigate their fracture behavior. Therefore, finite element simulations using constitutive model discussed in this chapter are performed in the next chapter to study the mixed mode (I and II) fracture behavior in NGs and MGs.

CHAPTER 4

Mixed mode (I & II) fracture behavior of nanoglass and metallic glass

4.1 Introduction

A considerable amount of effort has been made to understand the deformation behavior of NGs under tensile, compressive and indentation loading, whereas a few studies have been undertaken to understand the fracture response of NGs. These studies focused to understand the deformation behavior of notched NG samples under pure mode-I loading conditions (Sha et al., 2014). However, in practical application, structural components are generally subjected to complex stress fields/multi-axial state of stress, which may prone to mixed mode fracture. These factors suggest a need of a detailed study of fracture behavior of a given material under mixed mode loading conditions. Therefore, two-dimensional, plane strain, finite element analysis on the stationary crack in nanoglass (NG) and metallic glass (MG) subjected to mixed mode (I and II) loading conditions are performed under small scale yielding (SSY) conditions by employing the constitutive model for MGs. The organization of this chapter is as follows. The constitutive model and the determination of material parameters for NG and MG are briefly described in sections 4.2 and 4.3, respectively. The modeling aspects of fracture simulations of crack initiation are discussed in section 4.4. Finally important results obtained from this study are discussed in section 4.4.

4.2 Constitutive model

A finite deformation, Mohr-Coloumb type plasticity model for MGs proposed by Anand and Su (2005) is employed in this study, as it can precisely represent the deformation behavior of MGs under compression (Anand and Su, 2005), tension (Anand and Su, 2005), indentation (Su and Anand, 2006), and bending (Anand and Su 2005). This model assumes that the plastic flow in amorphous metals occurs by plastic shearing accompanied by dilatation relatively to six potential slip systems defined with respect to the principal directions of Kirchhoff stress. The detailed derivation of this plasticity model can be found in Anand and Su (2005). The rate of plastic shearing, evolution of cohesion and evolution of free volume are given by Eq. (3.3), (3.4) and (3.5), respectively. The above model has been implemented in the commercially available finite element program Abaqus 2017 by writing user defined material subroutine UMAT (Tandaiya et al., 2007, 2008, 2011). The integration of the constitutive equations is carried out using the implicit backward Euler method.

4.3 Determination of material parameters for NG and MG

In this section, the material parameters appearing in the constitutive model are determined for Sc-based NG and MG which will be used in fracture simulations in the following sections. The values of Young's modulus, E and initial cohesion, c_o for NG and MG are taken from the Franke et al. (2015) and Wang et al. (2015). The values of material parameters $\dot{\gamma}_0$, g_o, c_{cv}, ν, m and η_{cv} are taken from the work of Anand and Su (2005), and following Chapter 3, these are assumed to be identical for NGs and MGs. Further, the material constant b is chosen lower for NG than that for MG owing to lower steady state flow stress in the former than the latter (Wang et al., 2015). The values of μ for NG and MG are obtained by fitting the simulated indentation load, P versus depth, h curves with the corresponding experimental data reported by Franke et al. (2014). For this purpose, axisymmetric finite element simulations of indentation are performed on cylindrical specimens using 'Berkovich equivalent' conical rigid indenter having a semi-apex angle of 70.3^0 and spherical tip ($R = 200\,nm$). Fig. 4.1(a) shows the geometry of rigid indenter and finite element discretization of the specimen using four-noded axisymmetric elements in $r - z$ plane. The size of specimen $\left(40(L_s/R) \times 30(H_s/R)\right)$ is chosen to be sufficiently large to avoid interaction of plastic boundaries with free surfaces of the specimen to ensure boundary effects on indentation response being minimal (Chapter 2, 3). A constant displacement rate in z direction is imposed on the indenter through a reference point RP (refer Fig. 4.1(a)). Further, nodes on the bottom and the left side edges are constrained to move along z and r direction, respectively. Note that the model displayed in Fig. 4.1(a) is employed in determining the values of μ for MG as well as aggregate NG. In the simulations of NG, the discreet glassy grains and glassy interfaces are not modeled, and these simulations are referred to as HNG. The values of μ for NG obtained from simulations HNG represents the friction coefficient of aggregate NG (also referred to as homogenized NG in the following text). The material parameters for MG and aggregate NG are listed in Table 4.1.

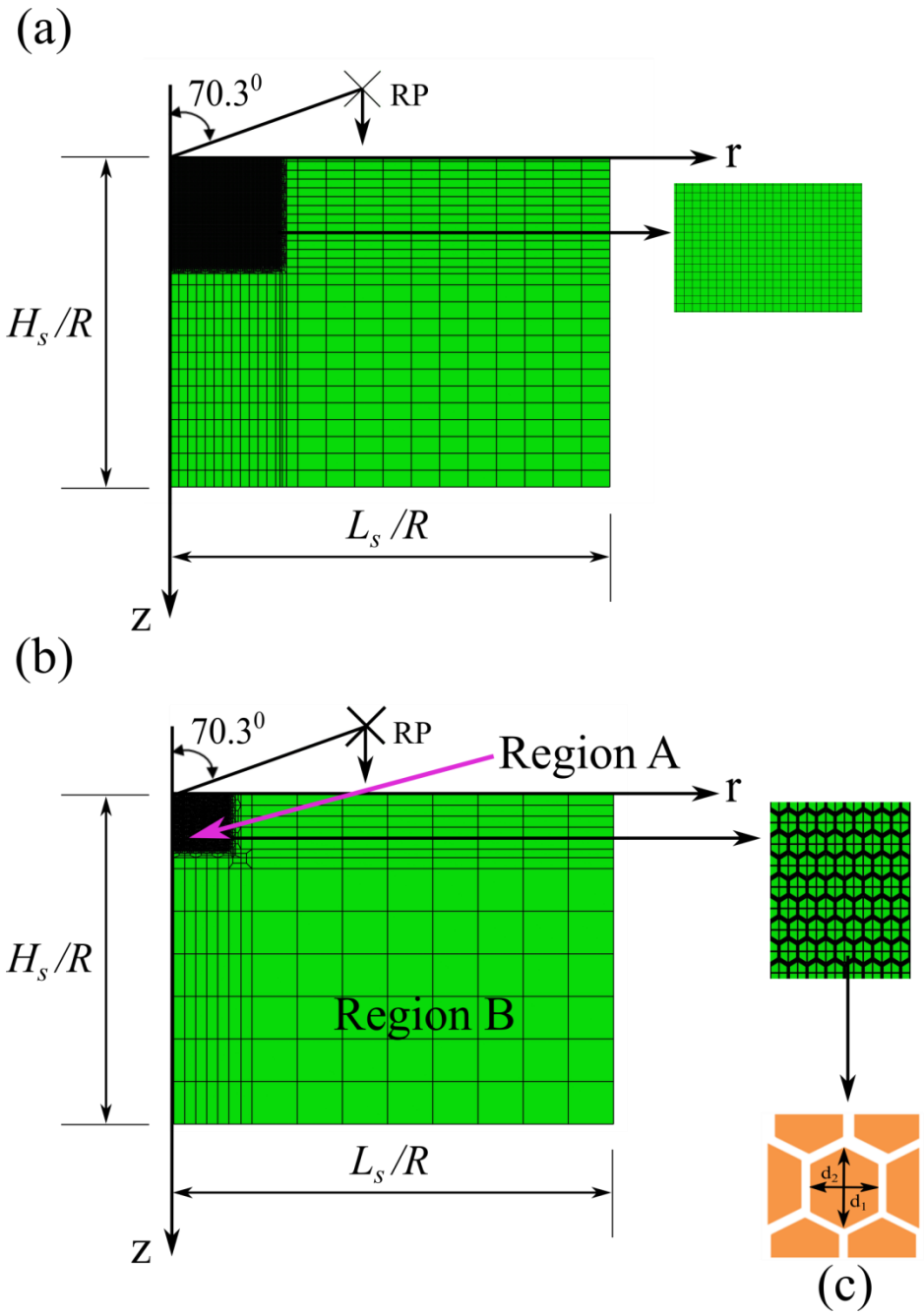

Figure 4.1 (a) Finite element mesh of cylindrical sample along with 'Berkovich equivalent' conical rigid indenter with half cone angle of 70.3^0 used for MG and Homogenised NG (HNG) indentation simulations. (b) Corresponding finite element model employed for simulations MNG where microstructure of NG is modeled in a 'Region A', while homogenized NG is considered in 'Region B'. (c) Zoomed view of 'Region A' and grain along with its detailed dimensions.

Table 4.1 The values of material parameters used for finite element simulations of nanoindentation.

Material Parameter	Simulation MG	Homogenized NG (HNG)	Microstructured NG (MNG)	
			Grain	Interface
E/c_{0g}	96.75	126.80	126.80	126.80
ν	0.36	0.36	0.36	0.36
μ	0.08	0.15	0.08	0.25
$\dot{\gamma}_o$	0.001	0.001	0.001	0.001
m	0.02	0.02	0.02	0.02
b/c_{0g}	0.19	0.04	0.19	0.04
g_0	0.4	0.4	0.4	0.4
η_{cv}	0.005	0.005	0.005	0.005
c_{cv}/c_{0g}	0.81	0.81	0.81	0.81
c_0/c_{0g}	1.0	0.85	1.0	0.85
c_{0g} (Gpa)	---	---	0.765	--

Further, to determine the material parameters for grains and interfaces, another simulation of indentation on NG are performed by modeling discrete glassy grains and glassy interfaces, and these simulations are referred to as MNG. The finite element model displayed in Fig. 4.1(b) is employed in the simulation MNG. The modeling details for simulations MNG are as follows. By following (Chapter 2 and 3), the discrete glassy grains and interfaces are modeled only in the 'Region A' to reduce the computation time, while in 'Region B', homogenized NG is considered (refer Fig. 4.1(b)). While choosing the size of region A, it is ensured that region A is well contained within plastic zone size underneath the indenter. Further, following (Sopu et al., 2011; Adibi et al., 2013; Singh et al., 2014), the hexagonal-

shaped glassy grains with dimensions d_1 and d_2 along r and z directions, respectively, are considered (refer Fig. 4.1(c)). The values of d_1 and d_2 are taken as 9 and 11 nm, respectively, to attain an average grain size of 10 nm, as noticed in Sc-based NGs (Wang et al., 2015; Liu et al., 2018), while the width of the glassy interface is chosen as 1 nm. Following experimental studies on NGs (Fang et al., 2012; Nandam et al., 2017), the chemical composition and free volume distribution in grains and the parent MG used to synthesize NG are assumed to be identical. Therefore, the values of material parameters for glassy grains are chosen to be identical to that of MG (Chapter 3). Following Chapter 3 identical values of the parameters E, ν, m, $\dot{\gamma}_0$, g_o, c_{cv} and η_{cv} are considered for interfaces and grains. However, the initial cohesion for interfaces is taken to be 15% lower than glassy grains by choosing lower b for them, because glassy interfaces exhibit lower density (Fang et al., 2012) and excess free volume (Sopu et al., 2009; Nandam et al., 2017). The value of μ for interfaces is determined by fitting the $P-h$ curves obtained from indentation simulations MNG to the experimental data (Franke et al., 2014). The values of all the materials parameters for interface and grains are listed in table 4.1.

The normalized indentation load, P/ER^2 vs normalized indentation depth, h/R curves obtained using the optimized values of μ (refer Table 4.1) in the simulations on MG, simulations HNG and MNG are compared with experimental data of Franke et al. (2014) in Fig. 4.2. It can be noticed that simulated curves for MG and NG (from simulations HNG as well as MNG) corroborates well with the corresponding experimental data. It must be mentioned that hardness values of NG and MG at peak load computed from finite element simulations is close to that reported from experiments (Franke et at., 2014). The good agreement between the finite element predictions of P/ER^2 vs h/R curves as well as hardness value with the corresponding experimental data validates the modeling strategy and the chosen materials parameters which will be used in the fracture simulations discussed in the following sections.

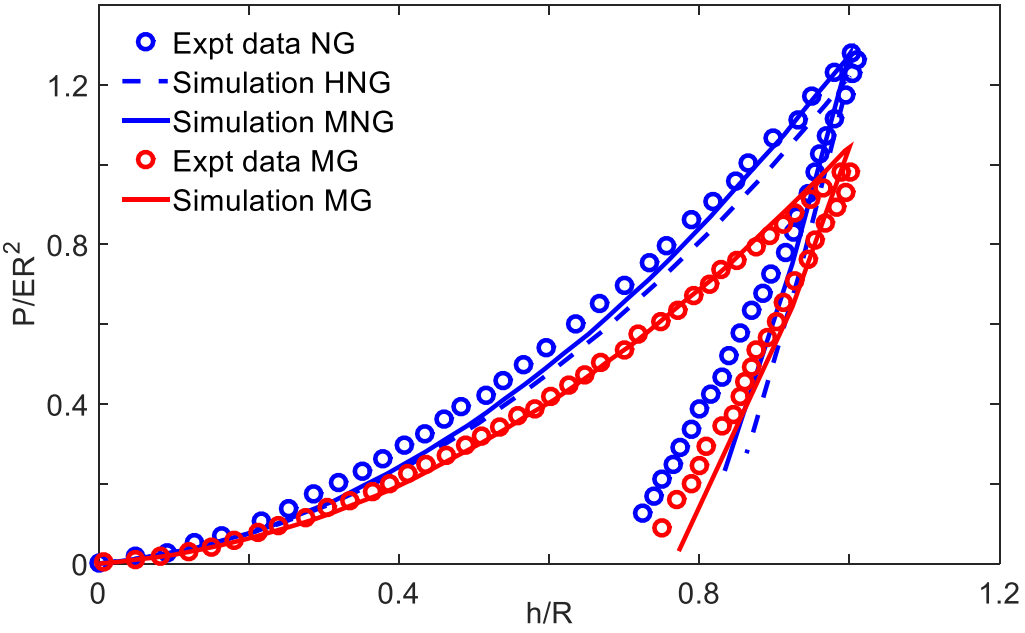

Figure 4.2 Normalized indentation load, P/ER^2 versus normalized indentation depth, h/R curve generated for MG, homogenized NG, and microstructured NG along with the experimental data of NG and MG (Franke et al., 2014).

4.4 Modeling aspects of fracture simulations of crack initiation

In this study, 2D plane strain, boundary layer formulation (i.e., small scale yielding or SSY) is employed. For this purpose, a larger circular domain containing a semi-circular notch along one of its radii (Fig. 4.3) is considered. The outer radius of the circular domain, R_0 is taken as 4000 times of initial notch diameter, b_0 to ensure that the plastic zone is well contained within the domain so that the SSY conditions are maintained throughout the loading history. The centre, O, of the circular domain coincides with the centre of curvature of the notch in the undeformed configuration. The origin of Cartesian coordinate (X_1, X_2) is established at O (refer Fig. 4.3(b)). The entire domain is discretized by four-noded isoparametric quadrilateral elements with lowest element size along the radial direction as $6.2 \times 10^{-6}\ R_0$ (Fig. 4.3(a) and (b)). Thus, a highly refined mesh is employed near the notch root to precisely capture the steep strain gradient and notch blunting. The notch surface is assumed to be traction-free, while the in-plane displacement components based on the first term of the mixed mode (mode I and II) elastic crack tip fields which are given by (Rice, 1968):

$$u_1 = \sqrt{\frac{R_0}{2\pi}}\frac{(1+\nu)}{E}\left[K_I \cos\frac{\theta}{2}\left(k-1+2\sin^2\frac{\theta}{2}\right) + K_{II}\sin\frac{\theta}{2}\left(k+1+2\cos^2\frac{\theta}{2}\right)\right] \quad (4.1)$$

$$u_2 = \sqrt{\frac{R_0}{2\pi}}\frac{(1+\nu)}{E}\left[K_I \sin\frac{\theta}{2}\left(k+1-2\,cos^2\frac{\theta}{2}\right) - K_{II}\cos\frac{\theta}{2}\left(k-1-2\,sin^2\frac{\theta}{2}\right)\right] \quad (4.2)$$

are applied on the outer boundary of the domain. Here, K_I and K_{II} are the mode I and II stress intensity factor, respectively. For plane strain $\kappa = 3-4\nu$, where ν is Poisson's ratio. The loading is applied in steps by gradually increasing the effective stress intensity factor, $|K| = \sqrt{K_I^2 + K_{II}^2}$, while maintaining the remote elastic mode mixity parameter $M^e = \frac{2}{\pi}\tan^{-1}\left(\frac{K_I}{K_{II}}\right)$ constant throughout the loading. The simulations are performed for various values of $M^e = 0-1$. Note that $M^e = 1$ represents pure mode I loading condition, while $M^e = 0$ represents pure mode II loading condition.

For the fracture simulations of crack initiation in MGs, the finite element model displayed in Fig. 4.3(a), which is comprised of 23872 nodes and 23700 elements are employed. To create a defect site and trigger the shear bands in MG, initial cohesion is perturbed by 3% (Tandaiya et al., 2009) about its nominal value of $0.765\ GPa$ and randomly assigned to elements.

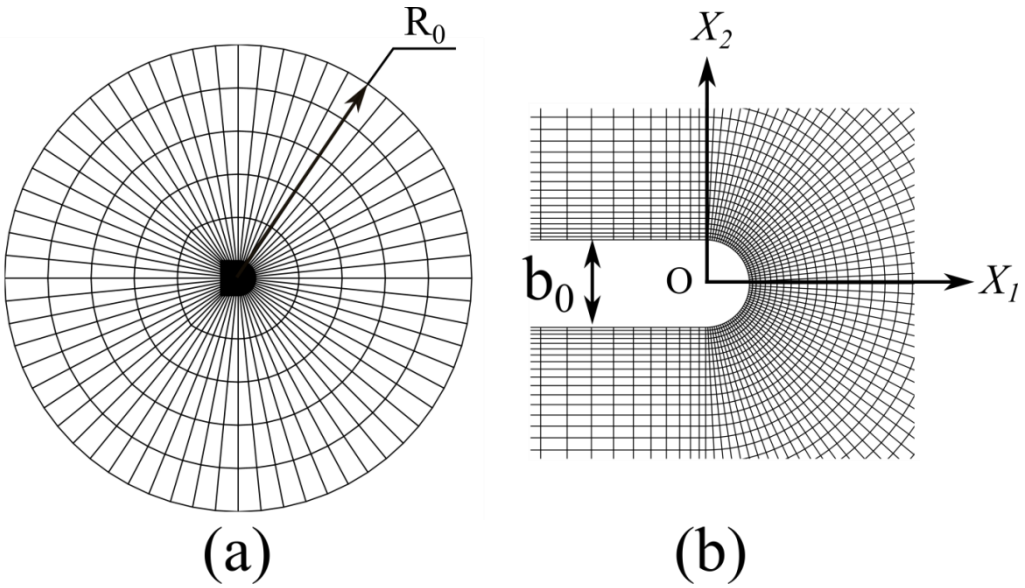

Figure 4.3 Finite element mesh employed for mixed mode simulation of MG showing (a) the full domain that is modeled and (b) zoomed view of the region around the notch tip.

For the analysis of crack-tip plasticity in NGs, the microstructure of NG (i.e., glassy grains and glassy interfaces) is modeled only in a circular region near the notch tip, denoted by Region 'C' in Fig. 4.4(a), to reduce the computation time. The size of this region is chosen to be sufficiently larger than the plastic zone size ahead of the notch tip in NGs. The shape, size of the glassy grains and glassy interface width chosen in section 4.3 are used in Region C. However, in the remaining portion of the circular ring (i.e., Region D in Fig. 4.4(a)), homogenized NG is considered. The plasticity model discussed in section 4.2 is employed to characterize the deformation behavior of glassy grain, interface (in Region C) and homogenized NG in region D. The values of material parameters used for glassy interface and glassy grains in region C and Region D are listed in Table 4.1. Further, in order to nucleate shear bands from glassy interfaces, as observed in experiments (Wang et al., 2015) and molecular dynamic (MD) simulations (Adibi et al., 2013), the initial cohesion of interfaces is perturbed by 3% about its nominal value of $0.650\ Gpa$ and randomly assigned to the elements in the glassy interfaces.

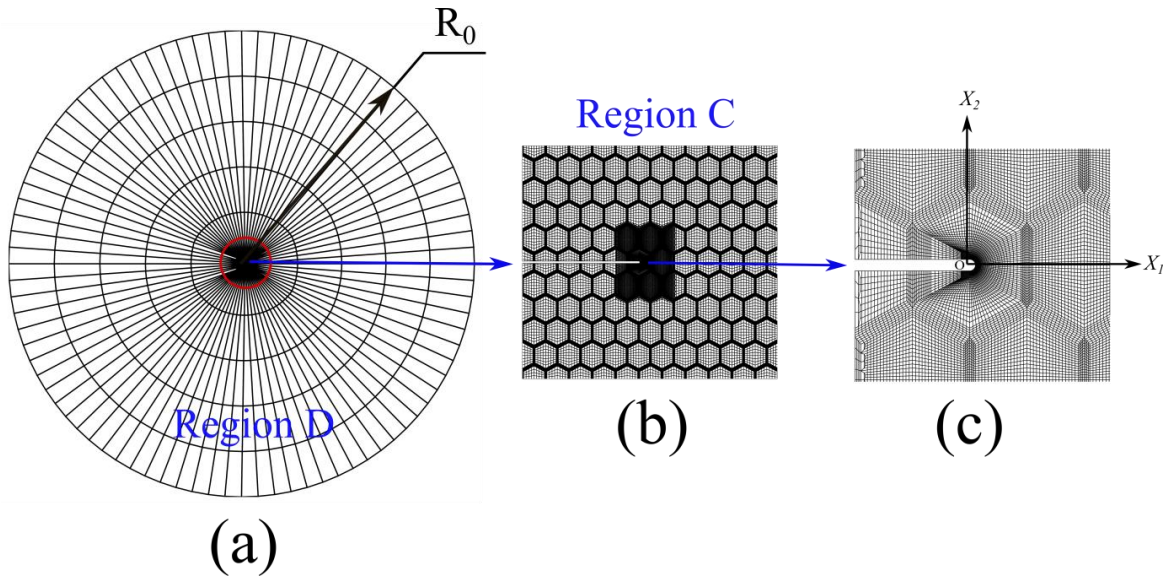

Figure 4.4 Finite element mesh employed for mixed mode (I and II) fracture simulation on NG showing (a) the full domain consisting of 'Region D' where microstructure of NG (i.e., discrete glassy grain and interfaces) is modeled, and 'Region C' where homogenised NG is considered. (b) The magnified view of the 'Region C' (c) zoomed in view of the region around the notch tip.

4.5 Result and discussion

4.5.1 Evolution of plastic strain near the notch tip

Figs. 4.5(a)-(c) show the contour plots of maximum principal logarithmic plastic strain, $log\lambda_1^p$ in NG subjected to pure mode II loading (i.e., $M^e = 0$) at three successive stages of normalized effective stress intensity factor, $|K|/c_{og}\sqrt{b_0} = 2.3, 11.6$ and 15.7, respectively. The corresponding plots for MG are displayed in Figs. 4.5(d)-(f). It can be noticed from Figs. 4.5(a) and (d) that yielding begins at the notch root owing to high stress concentration. With increase in $|K|$, several shear bands emanating from the notch surface, and extending along the radial directions can be observed in NG as well MG (refer Figs. 4.5(b) and (e)). The values of plastic strain inside these bands decreases with increase in distance from notch tip suggesting a large plastic strain gradient inside shear bands. However, in the case of NGs, in addition to radial bands, a family of secondary shear bands which are almost orthogonal to the primary radial bands can also be perceived (Fig. 4.5(b)). Thus, *NG not only exhibits relatively larger number of shear bands but also shows mutually intersecting bands in comparison to MGs, consequently, plastic strain in front of crack tip in NGs appears to be more diffused than that in MGs* (Compare Figs. 4.5(b) with (d)). It can also be noticed that relatively fewer shear bands have developed in the lower part of the notch surface in both the alloys (refer Figs. 4.5(b) and (d)).

The length of the radial shear bands and the plastic strain inside them increases in both the alloys when $|K|$ is further raised (refer Figs. 4.5(c) and (f)). Note that the bands in NG are sharper only near the notch tip, while they become are defused away from the notch tip. On the other hand, the bands in MG remain sharper up to much longer distance. Further, the spread of plasticity along the radial direction is larger in NGs than MG (refer Figs. 4.5(c) and (f)). A careful observation of the deformations of the notch tip in Figs. 4.5(b-c) and 4.5(e-f) indicate the enhancement in the blunting of the lower part along with the sharpening of the upper part of the notch profile with rise in $|K|/c_{og}\sqrt{b_0}$, which is investigated and discussed in section 4.5.3. Furthermore, the longest shear bands in MG and NG are aligned along $\theta \approx -10^0$ (negative in the clockwise direction), measured from the centre of the notch and line ahead of the notch tip in the undeformed configuration (refer dash line in Fig. 4.5(c) and (f)). This observation is in line with the orientation of dominant shear band noticed in mode II fracture experiments performed on Zr- based bulk MGs (Flores and Dauskardt, 2006).

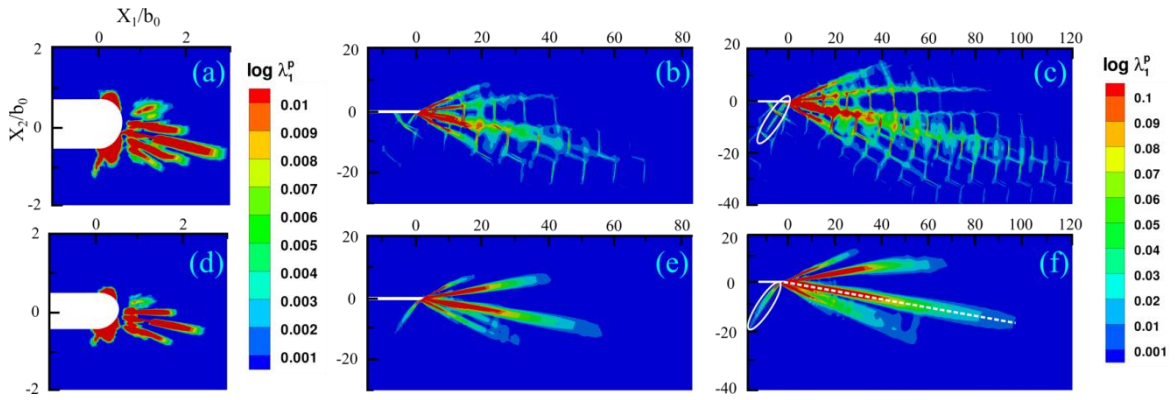

Figure 4.5 Contour plots of maximum principal logarithmic plastic strain, $log\lambda_1^p$ for NG, corresponding to $M^e = 0$ at (a) normalized effective stress intensity factor, $|K|/c_{og}\sqrt{b_0} = 2.3$, (b) $|K|/c_{og}\sqrt{b_0} = 11.6$ and (c) $|K|/c_{og}\sqrt{b_0} = 15.7$. The corresponding plots for MG are shown in (d) - (f).

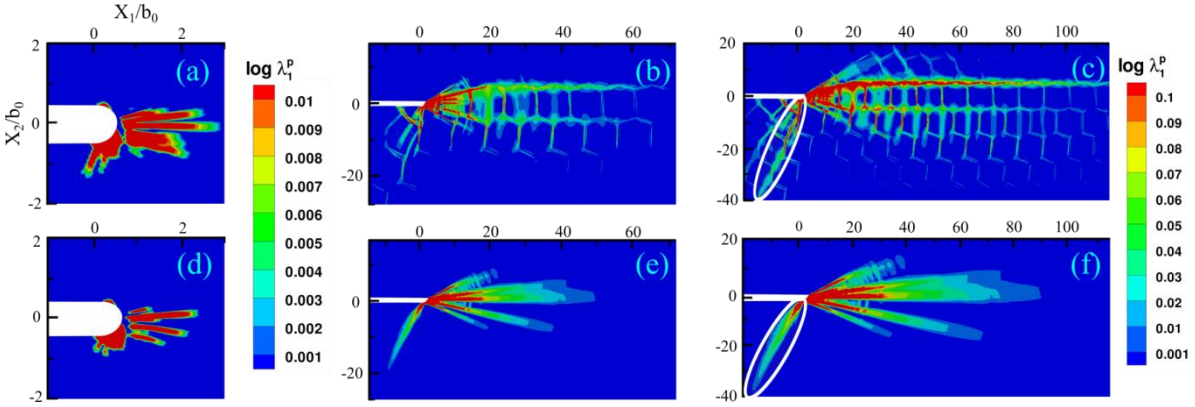

Figure 4.6 Contour plots of $log\lambda_1^p$ for NG corresponding to $M^e = 0.25$ at (a) $|K|/c_{og}\sqrt{b_0} = 3.0$, (b) $|K|/c_{og}\sqrt{b_0} = 11.6$ and (c) $|K|/c_{og}\sqrt{b_0} = 15.7$. The corresponding plots for MG are shown in (d) - (f).

The evolution of plastic strain for $M^e = 0.25$ which represents a mixed mode with mode II dominant loading is displayed in Figs. 4.6(a)-(c) and (d)-(f) for NG and MG respectively. It can be seen from these figures that shear band patterns ahead of the crack tip for $M^e = 0.25$ are almost similar to that for $M^e = 0$ for both the alloys. However, the lobes of plastic strain below the notch surface in both the materials are longer in the case of $M^e = 0.25$ than pure mode II loading (refer plastic lobes enclosed by an ellipse in Fig. 4.6(c) with Fig. 4.5(c) and Fig. 4.6(f) with Fig. 4.5(f)). In addition, the spread of the plastic strain ahead of the crack tip seems have reduced for $M^e = 0.25$ in Fig. 4.6 than for $M^e = 0$ in Fig

4.5, whereas it is more in NG than MG for both the values of M^e. Also, the longest shear band seems aligned along $\theta > 0^o$ for $M^e = 0.25$ in both the alloys in Fig 4.6. Thus, the plastic zone appears to rotate in anticlockwise direction with increase in mode I contribution. The rotation of plastic zone becomes more apparent when M^e is raised to 0.75 which represents a mode I dominant loading (refer Fig. 4.7). In this case, number and the length of shear bands in the lower lobe of the plastic zone increase in both the alloys (compare Figs. 4.7 (a)-(c) with 4.5(a)-(c) and Figs. 4.7 (d)-(f) with 4.5(d)-(f)). However, the spread of plastic strain along the radial direction has further reduced in both the alloys in Figs. 4.7 in comparison to Figs. 4.5. It must be noted from Figs. 4.7and 4.5 that the spread of the plasticity ahead of the crack tip is higher in NG than MG.

Interestingly, for pure mode I loading conditions, the distribution of shear bands is almost symmetric with respect to the line ahead of the notch in both the alloys (refer Figs. 4.8(b-c) and (d-f)). The length of shear band in both the alloys are significantly lower in mode I than that of pure mode II loading (compare Figs. 4.8(b-c) and Figs. 4.5(b-c)). Further, Figs. 4.5-4.8 clearly show that *the spread of the plastic strain ahead of the notch tip reduces with increase in* M^e*, but it is always smaller in MG than NG, irrespective of mode mixity*. It is tempting to conclude from contour plots displayed these figures that the size of the plastic zone in NG as well as MG decreases with increase in M^e, but it is always larger in the former than the latter. It must also be noted that the total area of material undergoing plastic deformation may not directly proportional to the length of the shear band, therefore a systematic of investigation of the effect of M^eon the plastic zone size in NG and MG is required, and it is performed in the next section.

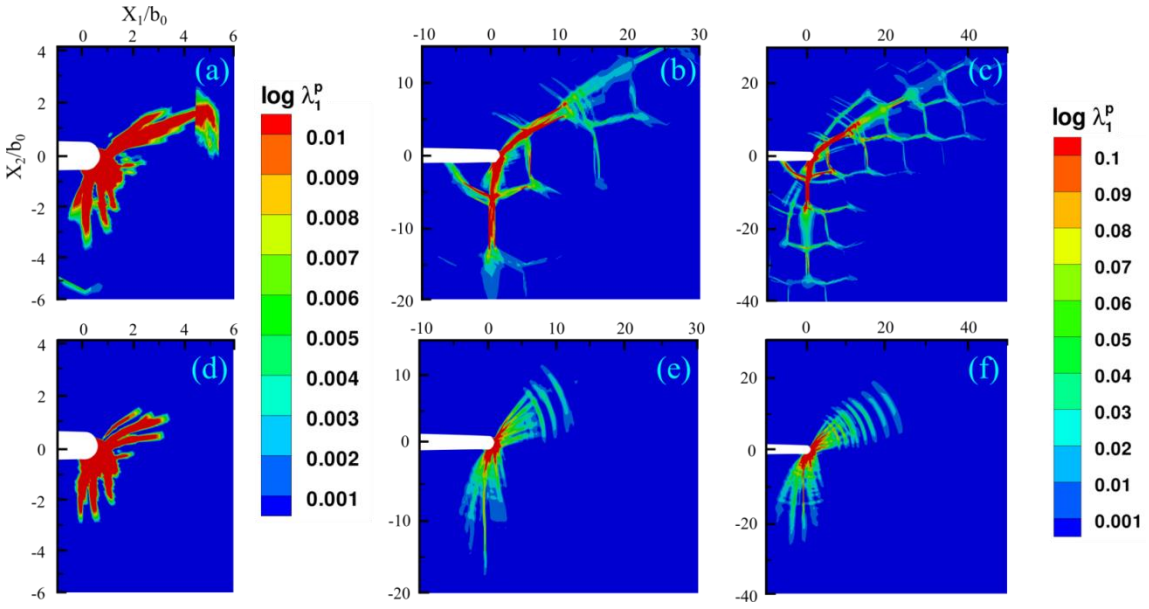

Figure 4.7 Contour plots of $log\lambda_1^p$ for NG corresponding to $M^e = 0.75$ at (a) $|K|/c_{og}\sqrt{b_0} = 4.8$, (b) $|K|/c_{og}\sqrt{b_0} = 11.6$ and (c) $|K|/c_{og}\sqrt{b_0} = 15.7$. The corresponding plots for MG are shown in (d) - (f).

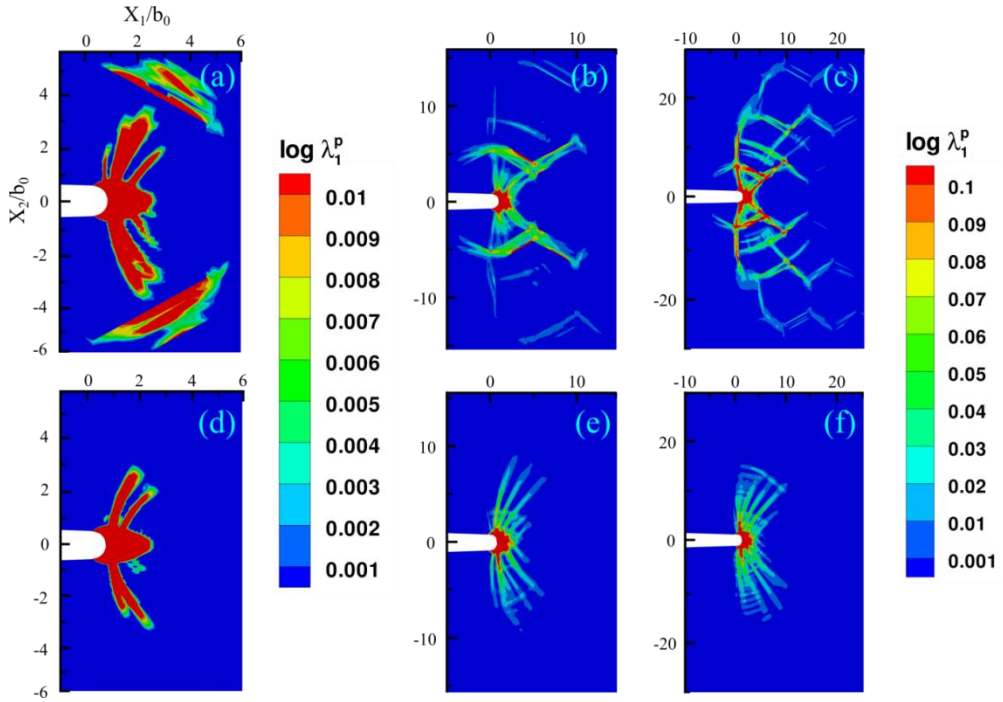

Figure 4.8 Contour plots of $log\lambda_1^p$ for NG for $M^e = 1$ at (a) $|K|/c_{og}\sqrt{b_0} = 6.7$, (b) $|K|/c_{og}\sqrt{b_0} = 11.6$ and (c) $|K|/c_{og}\sqrt{b_0} = 15.7$. The corresponding plots for MG are shown in (d) – (f).

4.5.2 The effect of M^e on the evolution of plastic zone size in NG and MG

In order to understand the growth of plastic zone ahead of the crack tip with the progress of loading, the volume fraction of material undergoing plastic deformation, V_f^y is computed. For this purpose, the plastic yielding at a point is assumed to occur, if maximum principal logarithmic plastic strain, $log\lambda_1^p$ exceeds beyond 0.001 at that point. Using this criterion, V_f^y for both NG and MG are determined and plotted against $|K|/c_{og}\sqrt{b_0}$ for different values of M^e in Fig. 4.9(a) and (b), respectively. It can be seen from Fig. 4.9(a) that irrespective of mode-mixity, V_f^y is almost negligible up to around $|K|/c_{og}\sqrt{b_0} = 5$, but it starts increasing rapidly for further enhancement in $|K|/c_{og}\sqrt{b_0}$ signifying considerable plastic deformation in NG occurs at around $|K|/c_{og}\sqrt{b_0} = 5$. Also, V_f^y enhances faster for lower M^e (compare the slope of the curve for $M^e = 0$ with $M^e = 1$). Fig. 4.9(b) shows that significant plastic deformation in MG takes place at higher $|K|/c_{og}\sqrt{b_0} \approx 7$. Thus, it can be concluded from Figs. 4.9(a) and (b) that *the macroscopic plastic yielding in NG commences earlier than that in MG*. This happens is due to the early onset of yielding in interfaces with lower cohesion in the NG.

Further, similar to the trend seen in NG (in Fig. 4.9(a)), the increase in V_f^y gets retarded with increase in M^e for MG also as evident from Fig. 4.9(b). Similar behavior has also been reported in mixed mode fracture simulations on bulk MGs (Tandaiya et al., 2009). It can also be noticed by comparing Fig. 4.9(a) with (b) that V_f^y in NG is much higher than MG for a fixed value of $|K|/c_{og}\sqrt{b_0}$ and M^e. Thus, it can be concluded that the *plastic zone size in NG is significantly larger than that in MG for identical loading conditions*. This trend could be rationalized by noting higher μ for NG than MG, as plastic zone size increases with enhancement in μ reported by Tandaiya et al. (2009). The development of plastic deformation near the notch tip is accompanied with the deformation of notch as noted in the contour plots displayed in Figs 4.5-4.8. The deformation of notch surfaces of NG and MG are compared in the next section.

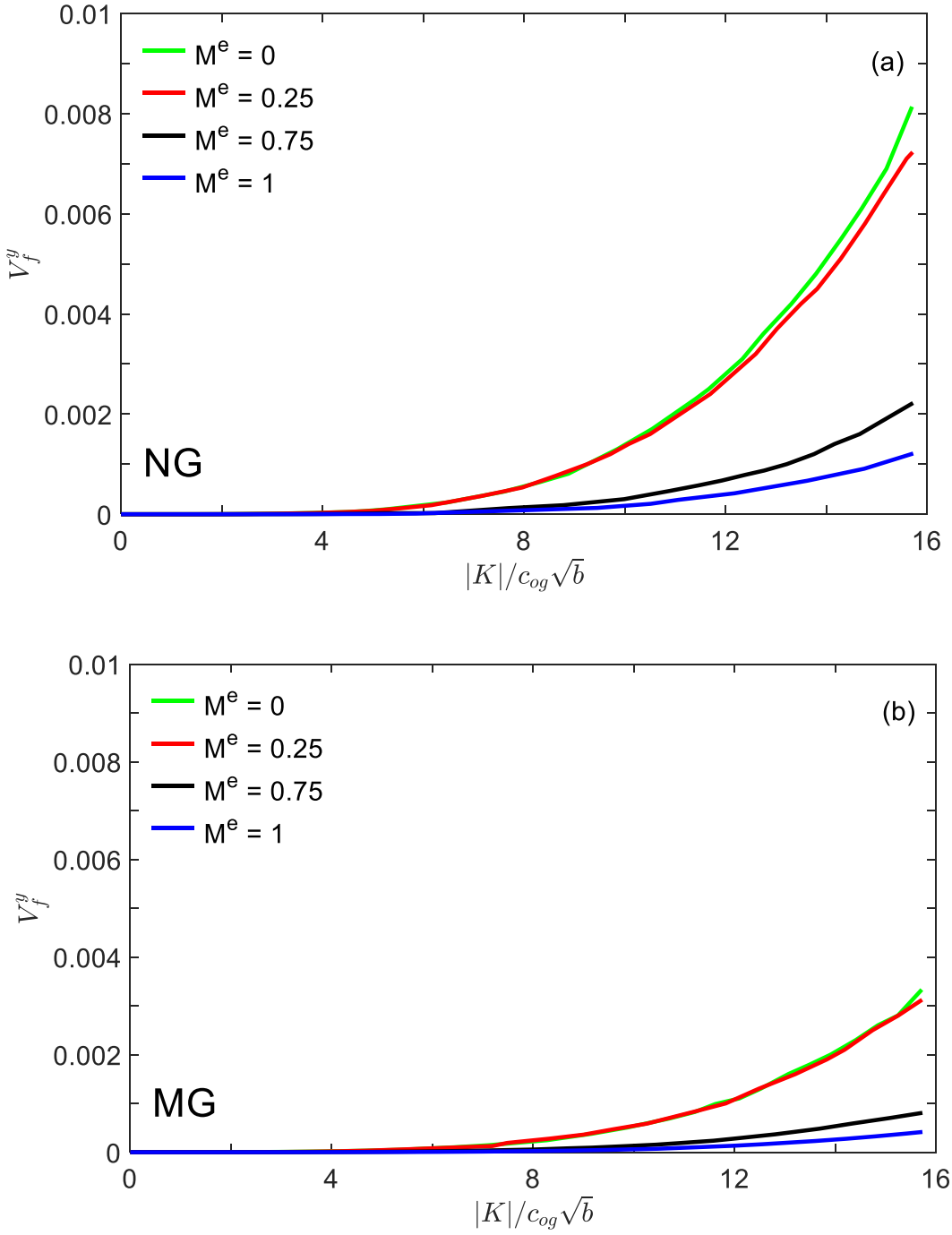

Figure 4.9 Variation of volume fraction of material undergoing in plastic yielding, V_f^y with normalized effective stress intensity factor, $|K|/c_{0g}\sqrt{b}$ corresponding to different mixed mode loading conditions in (a) NG and (b) MG.

4.5.3 Deformation of notch surface in NG and MG

It would be interesting to study the deformation of notch surface under mixed mode loading conditions. Therefore, the deformed notch profiles of NG and MG corresponding to $M^e = 0.25$ at $|K|/c_{og}\sqrt{b_0} = 15.7$ is displayed are Fig. 4.10. It can be perceived that the notch tip of both the alloys NG and MG under mixed mode loading deforms in a shape with a blunted lower part and sharpened upper part which is in agreement with observations from experiments and simulations on amorphous (Tandaiya et al., 2009) and crystalline materials (Aoki et al., 1990; Ghosal and Narasimhan 1994; Roy et al., 1999). Further, it can be noticed that the stretching and bulging forward of the lower part of the notch is more pronounced in the case of NG than MG, while the upper part of the notch profile is sharper in the case of latter. The notch sharpening facilitates the localized deformation and nucleation and propagation of a crack inside shear bands (Tandaiya et al., 2009). Therefore, it can be deduced from Fig. 4.10 that crack may nucleate from the sharpened upper corner of the notch earlier in MG than NG.

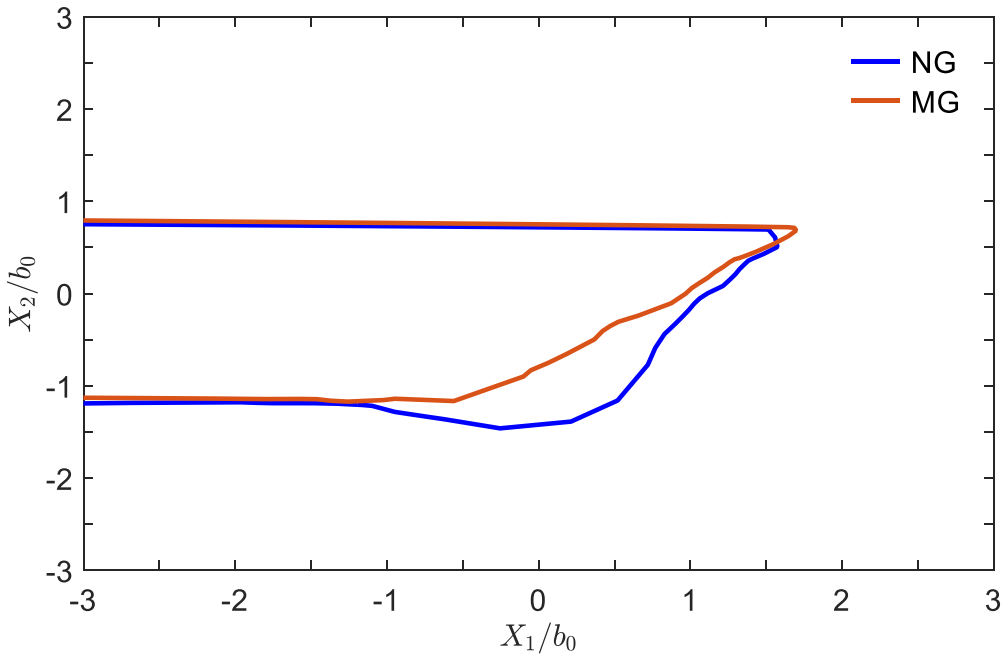

Figure 4.10 The deformed notch profile for NG and MG corresponding to $M_e = 0.25$ at $|K|/c_{og}\sqrt{b_0} = 15.7$.

The notch tip deformation can be further understood by monitoring the evolution of the notch opening displacement, δ_I and notch shear displacement, δ_{II}, (refer schematics of undeformed and deformed notch profiles displayed in Fig. 4.11(a)). Note, in Fig. 4.11(a) point A and B are located above and below the centre of curvature of the notch, respectively, whereas point C is placed at the tip of the undeformed notch profile. These points are marked by A', B', and C' in the deformed notch profile. Thus, δ_I and δ_{II} can be determined by measuring the displacements of above-mentioned points along X_1 and X_2 directions, respectively. The effect of applied mode-mixities on the evolution of δ_I and δ_{II} in NG and MG is shown in Figs. 4.11(b)-(c) and 4.11(d)-(e), respectively. Here, $J = \frac{|K|^2(1-\nu^2)}{E}$ is energy release rate, where E is young's modulus of respective materials. It can be noticed that both δ_I and δ_{II} increases linearly with $J/c_{og}b_0$ for both materials, irrespective of the values of M^e. Also, for any applied $J/c_{og}b_0$, δ_I is highest for $M^e = 0.75$ for both the alloys. Indeed, in the case of NG, δ_I at $J/c_{og}b_0 \approx 1.68$ for $M^e = 0.75$ is around 11.0% higher than that for $M^e = 1.0$ and this difference is even higher around 16.0% in the case of MG. A similar trend has also been noticed in mixed mode fracture simulations on bulk MGs (Tandaiya et al., 2009). These observations are also in line with the asymptotic mixed mode crack tip fields reported for material obeying Von-Mises yield criterion (Symington, 1998). Further, it can be seen that δ_I is almost zero for both NG and MG for pure mode II condition ($M^e = 0$) up to $J/c_{og}b_0 \approx 1.2$ and subsequently, it became negative implying closure of notch profile. However, δ_{II} is larger for pure mode II loading in both the alloys. It can be deduced from Figs 4.11(a) and (b) that, irrespective of mode-mixity, the magnitude of δ_I and δ_{II} in NG is always slightly higher than that in MG which suggests that the former would exhibit slightly higher fracture toughness than the latter. To confirm this, the fracture toughness of both the alloys under mixed mode loading condition is determined from finite element simulations in next section.

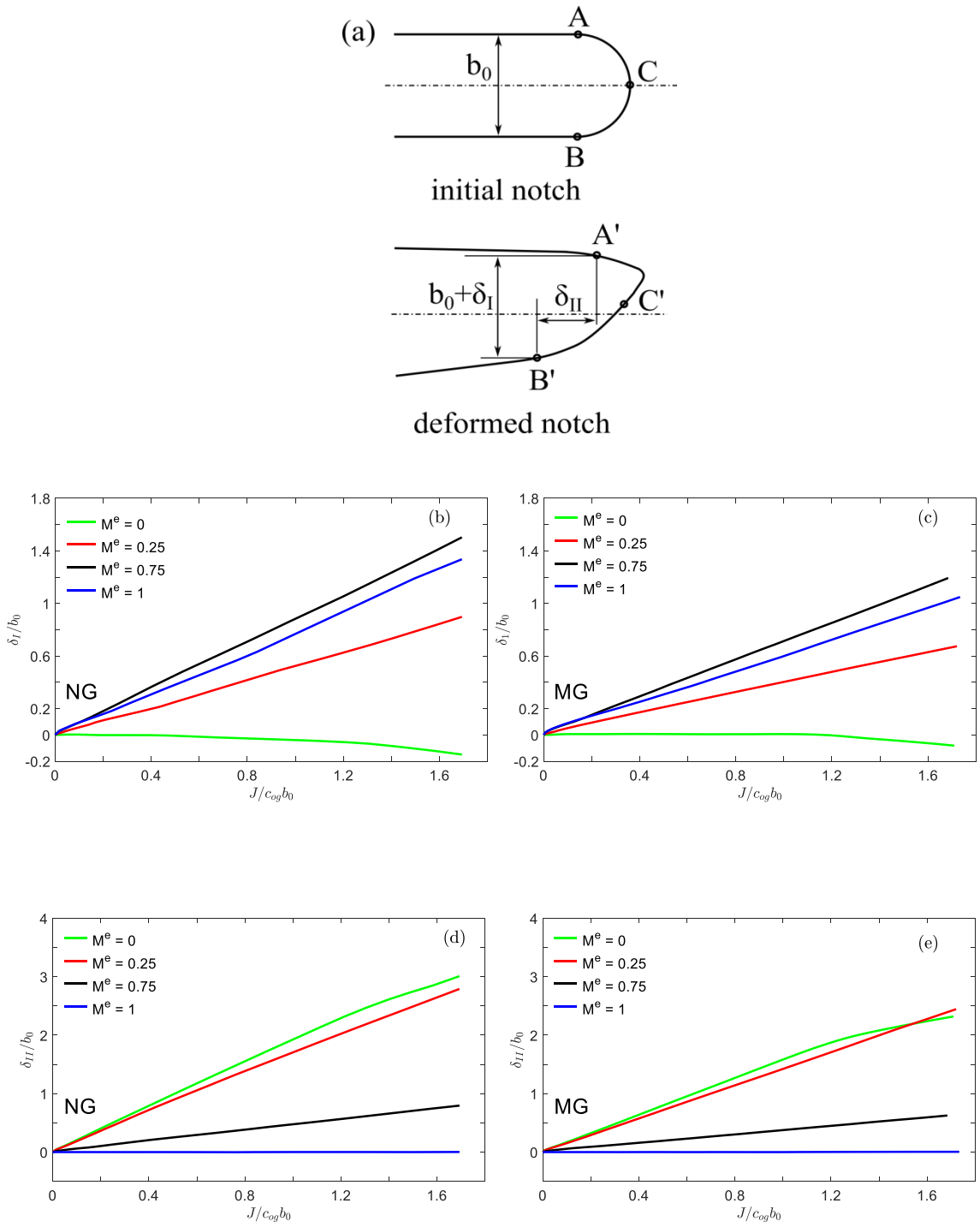

Figure 4.11 (a) Schematic representation of notch opening displacement, δ_I and notch shear displacement, δ_{II}. The variation of δ_I with normalized energy release rate, $J/c_{og}b_0$ pertaining to different mode mixities for (b) NG and (c) MG. The corresponding plots for δ_{II} are displayed in (d) and (e).

4.5.4 Effect of mode mixity on the fracture toughness of NG and MG

Tandaiya et al. (2009) successfully predicted the increase in fracture toughness of Zr-based bulk MGs with changing mode mixity from mode II to mode I dominant loading through finite element simulations by employing a critical strain-based fracture criterion. This criterion is based on the assumption that the crack would propagate in a dominant shear band at some angle θ when the value of $log\lambda_1^p$ in the shear band exceeds a critical value, ϵ_c over a critical radial distance, r_c^ϵ from the notch tip measured in the undeformed configuration. Thus, this fracture criterion is governed by the parameters ϵ_c and r_c^ϵ. Tandaiya et al. (2009) could successfully predict the fracture toughness of Zr-based bulk MG for various mode mixity by considering ϵ_c= 0.1 and $r_c^\epsilon = b_0$. However, the appropriate values of ϵ_c and r_c^ϵ for NGs are not known, therefore various combinations of these parameters are chosen in the following discussion to check the effect of selected parameter $(\epsilon_c, r_c^\epsilon)$ on the predicted fracture toughness. The fracture criterion is imposed by manually inspecting the value of $log\lambda_1^p$ at a point within a circle having a radius r_c^ϵ at different stages of applied $|K|/c_{og}\sqrt{b_0}$. The crack initiation is assumed to begin when $log\lambda_1^p$ over a chosen r_c^ϵ at some angle with respect to the notch line ahead of tip exceeds the chosen ϵ_c.

The variation of normalized fracture toughness, $\frac{J_c}{J_0}$ with mode mixity, M^e for NG predicted by employing various combination of $(\epsilon_c, r_c^\epsilon)$ are displayed in Fig. 4.12. Here, J_0 is estimated fracture toughness of alloy (NG or MG) under discussion using $\epsilon_c = 0.1$ and $r_c^\epsilon = b_0$ for $M^e = 0$. It can be perceived that fracture toughness increase monotonically when M^e is changed from pure mode II ($M^e = 0$) to pure mode I ($M^e = 1$) irrespective of the selected parameter $(\epsilon_c, r_c^\epsilon)$. It can also be noticed that keeping ϵ_c same and selecting the larger r_c^ϵ, the predicted fracture toughness is slightly higher for $M^e < 0.6$, but the difference increases significantly as M^e tends to 1 (compare solid line curves with diamond and square marker). However, keeping r_c^ϵ same and increasing ϵ_c, the predicted fracture toughness elevates for all mode mixities (refer solid line curves with diamond and circle marker).

The predictions of $\frac{J_c}{J_o}$ for MG are also displayed by dashed line curves in Fig. 4.12 to compare the toughness values of NG and MG. Interestingly, it can be noticed that the predicted fracture toughness of NG is almost equal to that of MG for pure mode II loading, irrespective of chosen parameter $(\epsilon_c, r_c^\epsilon)$. However, fracture toughness of NG is slightly higher than that of MG for $M^e > 0.2$ when predictions are made using $\epsilon_c = 0.2$ and $r_c^\epsilon =$

$2.5b_0$. On the other hand, fracture toughness of NG and MG is almost similar for all value of M^e, if ϵ_c and r_c^ϵ are chosen to be 0.1 and b_0, respectively. Thus, Fig. 4.12 suggests that *though NG exhibit significant larger tensile ductility, they may not show significant higher fracture toughness in comparison to MG with identical composition*. Also, at this juncture, it is essential to mention that the trend of predicated fracture toughness, J_c with mode mixity, M^e for both the alloy are qualitatively corroborate with Zr-based bulk MG (Tandaiya et al., 2009). However, an experimental validation is required to confirm these observations.

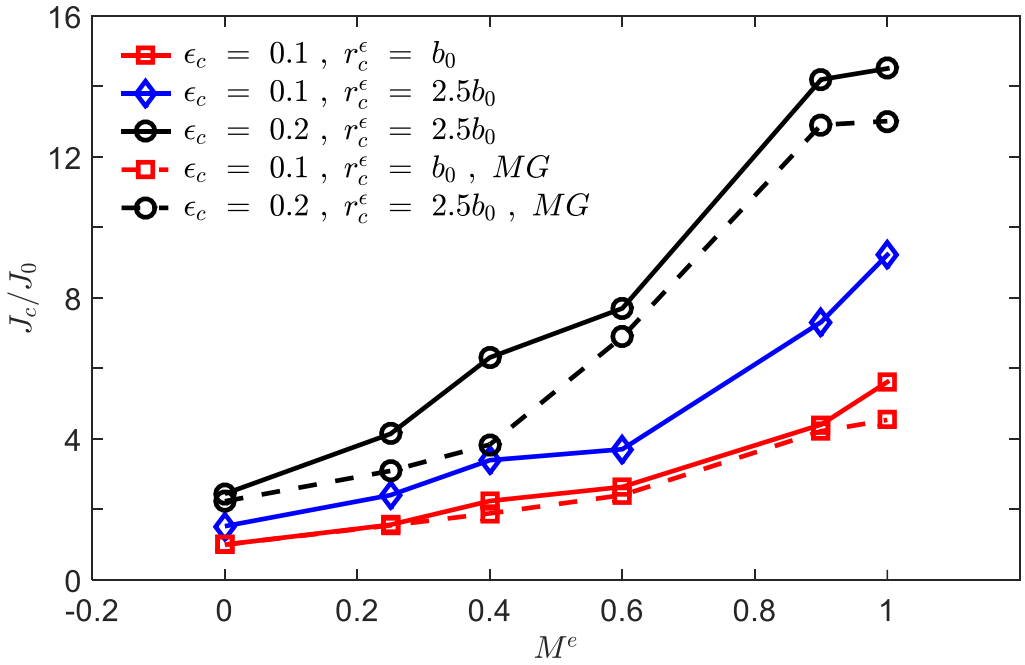

Figure 12 The variation of predicted normalized fracture toughness, $\frac{J_c}{J_0}$ with mode mixity, M^e for NG and MG obtained using critical strain based fracture criterion.

In summary, the stationary crack tip plasticity in NG and MG under the mixed mode (I and II), plane strain, SSY condition has been investigated through finite element simulations using a constitutive model for MGs proposed by Anand and Su (2005). The results collaborate well with the observations made from experiments and continuum simulations of fracture on bulk MGs. It must be mentioned that NGs with larger thickness cannot be synthesized due to limitation of present manufacturing techniques. Therefore, the idea of developing laminate composites with alternative layers of NG and MG have been proposed to achieve large tensile ductility without compromising strength significantly (Adibi et al., 2016; Sha et al., 2017). Sha et al. (2017) demonstrated from MD simulations that the

deformation behavior of such NG-MG composites transitions from shear localization to superplastic flow when MG layer thickness is reduced below a threshold level which they correlated to the glassy grain size of the NG layers. However, it is not clear as to why and how the glassy grain size of the NG layer controls the threshold thickness of MG layer. Hence, the deformation behavior of NG-MG laminate composites is investigated in the next chapter.

CHAPTER 5

Finite element analysis of tensile deformation of nanoglass-metallic glass laminate composites

5.1 Introduction

As discussed in chapter 1, metallic glasses (MGs), exhibit impressive combination of physical and mechanical properties, but they fail catastrophically under tensile loading due to unstable crack propagation inside a predominant shear band which seriously impede their deployment in structural applications (Schuh et al., 2007). This has encouraged researchers to explore various strategies to enhance tensile ductility of MGs such as developing MG composites by introducing soft crystallites phase into the MG matrix (Hofmann et al., 2008; Qiao et al., 2016). These composites exhibit significant tensile ductility, but at the cost of reduction in yield strength.

An alternate approach to achieve good tensile ductility in MGs without compromising strength is developing laminate composites (Adibi et al., 2016; Sha et al., 2017) with alternate layers of Nanoglasses (NG) and MGs. Adibi et al. (2016) reported almost same level of ductility with 20% higher strength in such composites in comparison to NGs. Sha et al. (2017) showed from MD simulations that shear bands nucleate from NG layer which cut through MG layer in composites with thinner NG layer, while these are mainly confined within NG layer for composites having thicker NG layer. Also, peak stress attained in these composites don't follow rule of mixture, whereas mechanistic reasons for this trend is not well understood. Most importantly, Sha et al. (2017) reported a transition in deformation behavior from shear localization to superplastic flow in composites having multiple NG and MG layers, when MG layer thickness is reduced below a threshold level which they correlated to the glassy grain size of the NG layers. However, it is not clear from these simulations as to why and how the glassy grain size of the NG layer controls the threshold thickness of MG layer.

Therefore, in this chapter, 2D plane strain finite element simulations of tensile loading on NG-MG laminate composites are performed using a thermodynamically consistent finite strain based non-local plasticity model for MGs to understand the deformation behavior these composites better. The organization of this chapter is as follows. The constitutive model used in the simulations is briefly described in section 5.2, and the modeling aspects are explained

in in section 5.3. Finally, important results obtained from this study are discussed in section 5.4.

5.2 Constitutive model

A thermodynamically consistent, finite strain, non-local plasticity theory for MGs proposed by Thamburaja (2011) is employed in this study, as it can accurately capture the size-dependent deformation behavior of NGs (Singh et al., 2014), MGs (Thamburaja, 2011) and MG composites (Shete et al., 2016, 2017). Another advantage of using a non-local plasticity theory in finite element simulations is that the predicted deformation behaviors are nearly insensitive to the finite element mesh employed in the analysis (Borg, 2007). This model incorporates four fundamental mechanisms which governs free volume evolution in MGs. These are free volume diffusion, creation by plastic shearing, generation due to hydrostatic stress and annihilation by structural relaxation. Thus, in this model, free volume, ξ evolves as (Thamburaja, 2011):

$$\dot{\xi} = \dot{\xi}_0 \left(\frac{s_1}{s_3}\right)(\nabla^2 \xi) + \zeta \dot{\gamma} - \left(\frac{\xi_0 \bar{p}}{s_3}\right) - \dot{\xi}_0 \left(\frac{s_2}{s_3}\right)(\xi - \xi_T). \tag{5.1}$$

Here, $\dot{\xi}_0 = f_0 \sqrt{\exp\left(-\frac{\phi}{\xi}\right)}$, where $f_0 > 0$ is frequency of atomic vibration and $\phi > 0$ is geometrical factor. The parameter ζ is a free volume creation coefficient due to plastic shearing, and ξ_T is free volume in a fully annealed glass at temperature T. The material constants, s_1, s_2 and s_3 denote gradient free energy (energy per unit length), defect free energy (energy per unit volume) and the resistance to free volume generation, respectively. It must be noted that gradient free energy penalizes the shear band formation (Thamburaja, 2011). Further, in Eq. (5.1), $\bar{p}$ denotes hydrostatic pressure, while $\dot{\gamma}$ represents plastic shear strain rate which is given by (Thamburaja, 2011):

$$\dot{\gamma} = \begin{cases} \dot{\gamma}_o \left(\frac{f}{c}\right)^{\frac{1}{a}} & f = (\bar{\tau} - \tau_{int} - \zeta(s_2(\xi - \xi_T) + \bar{p}) > 0 \\ 0 & f \leq 0 \end{cases} \quad Where\ \tau_{int} = -\zeta s_1 \nabla^2 \xi. \tag{5.2}$$

In this equation, $\dot{\gamma}_o$ and a are the reference shear strain rate and strain rate sensitivity parameter, respectively. Further, f in Eq. (5.2) represents driving force for plastic shearing which includes Von-Mises equivalent stress, $\bar{\tau}$, interaction stress, τ_{int} and back stress, $\zeta(s_2(\xi - \xi_T) + \bar{p})$. Note that τ_{int} signifies the interaction stress between flow defects such as STZs and has energetic origin (Gurtin and Anand, 2010). It can be seen from Eq. (5.2) that

negative τ_{int} enhances f, hence promotes further evolution of plastic strain, while $\tau_{int} > 0$ resist development of strain. Indeed, it has been demonstrated that spatial distribution of τ_{int} plays a decisive role in delaying localized deformation and promoting homogeneous deformation in nano-meter sized unnotched (Thamburaja, 2011) as well as notched MGs (Singh and Narasimhan, 2016; Dutta et al., 2018) and NGs (Singh et al., 2014).

Furthermore, in Eq. (5.2), c denotes current cohesion of the material, which signifies intrinsic material resistance to inelastic deformation. In order to capture free volume induced softening in MGs, c is assumed to evolve as (Thamburaja, 2011):

$$c = c_0 \exp\{K(\xi - \xi_T)\}, \tag{5.3}$$

where, c_0 is initial value of cohesion and $K < 0$ is a fitting constant which controls the drop in cohesion after commencement of yielding. The detail derivation of constitutive model can found in Thamburaja (2011).

A coupled, explicit finite element procedure, with displacement,u and free volume, ξ as nodal variable is employed to solve the governing equation for free volume evolution (Eq. 5.1) and weak form of equation of motion. Former is integrated using forward Euler scheme, while latter is integrated using central difference method. Mass scaling is used to ensure the quasi-static solution and small time step is employed to confirm the stability of the solution. The nodal averaging technique is used to smooth the discrete free volume gradient computed at centroids and generated a C^0 continuous vector field of free volume gradient (similar to the strain smoothing approach of Hinton and Cambell, 1974). By using this continuous free volume at the element integration points is obtained which is used in Eq. (5.2) to compute the interaction stress and update the plastic slip γ. This procedure obviates the need to use a higher order element procedure with free volume and its gradient as nodal variables. From trial analysis of free volume distribution across the shear band, it is noticed that this technique quite robust in computing the Laplacian of the free volume even with modest level of mesh refinement. The details of coupled finite element procedure are can be found in (Singh, 2016).

5.3 Modeling aspects

Fig. 5.1(a) shows finite element discretization of a 2D laminate composite specimen ($48\ (W_o) \times 96\ (L_o)\ nm$) which is comprised of a NG layer sandwiched between

two MG layers. This specimen is subjected to uniaxial stretching with a strain rate of $2 \times 10^{-3} s^{-1}$ under plane strain conditions. In Fig. 5.1(a), thickness of NG and MG layer, denoted by t_{NG} and t_{MG}, are 24 and 35 *nm*, respectively. In order to analyze the effect of thickness of NG layer on the deformation response of composites, various values of t_{NG} ranging from 4.8 to 48 *nm* are considered. In addition, simulations are performed on samples having multiple layers of NGs so as to understand the mechanism that governs transition from localized deformation to super plastic flow in laminate composites as reported by Sha et al. (2017).

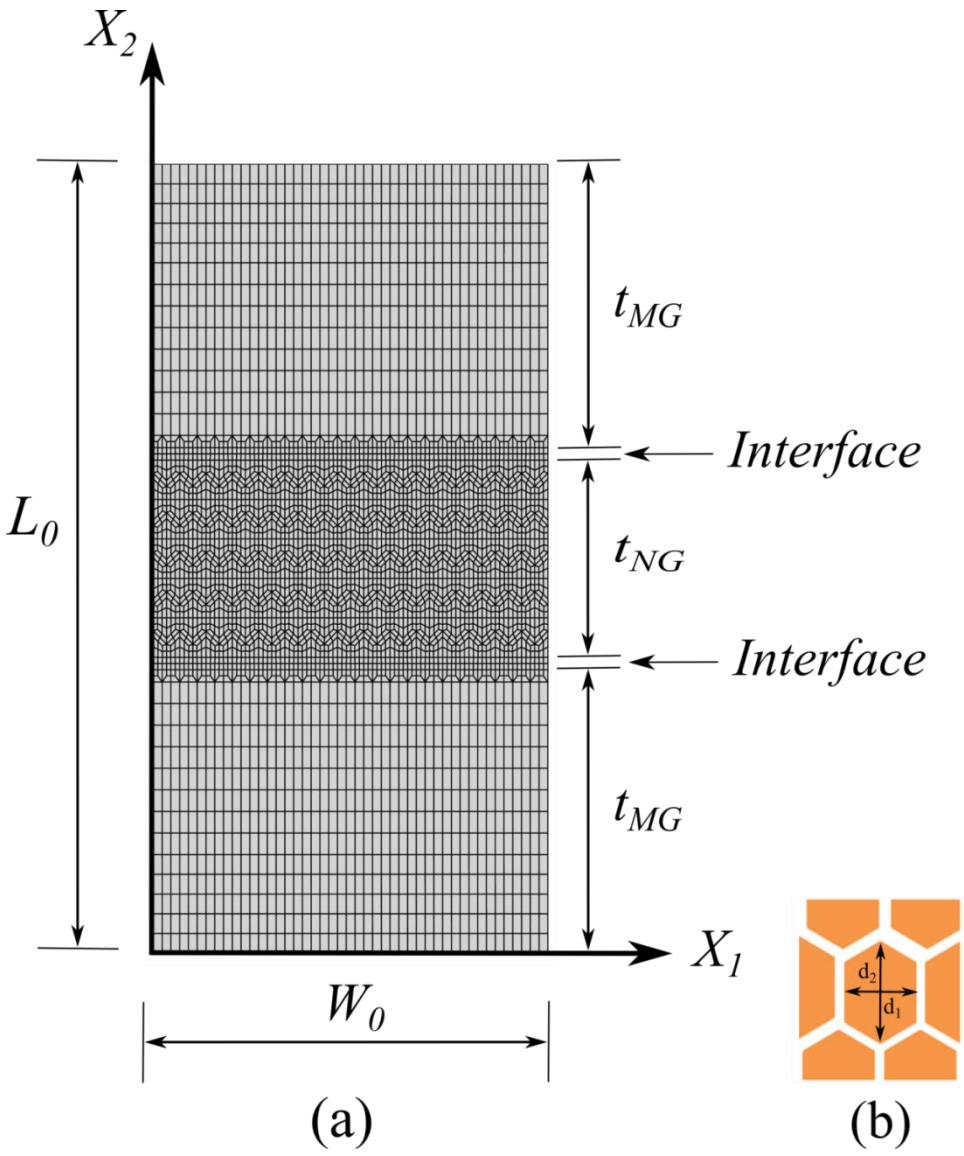

Figure 5.1 (a) Finite element model of NG-MG laminate composite having single NG layer, employed in plane strain tension simulations. (b) Enlarged view of a NG grain. Dimensions d_1 and d_2 are width of grain in X_1 and X_2 directions, respectively.

Following Singh et al. (2014), structure of NG is assumed to be consist of nanosized hexagonal glassy grain separated by fine glassy interfaces. An enlarged view of such a typical grain is shown in Fig. 5.1(b), where dimensions d_1 and d_2 represent grain width along X_1 and X_2 directions, respectively. These values are taken to be 2.2 and 5 *nm* respectively, for all the simulations (Singh et al., 2014). Thus, average grain size in the present work is 3.6 *nm* which falls within the range of grain size of NGs as reported by Jing et al. (1989). Further, motivated from experimental observations (Wang et al., 2015, 2016) the width of interface is taken as 1 *nm*. Moreover, by following Adibi et al. (2016) a fine glassy planner interface (between NG and MG layer) of width of around 1 *nm* has also been introduced between NG and MG layers, as shown in Fig. 5.1(a).

The materials in MG layer, grains in NG layer, and all the interfaces (planner as well as within NG layer) are assumed to follow the constitutive theory described in section 5.2, whereas material properties are taken differently. In the present continuum simulations, the chemical composition of the MG layer and the glassy grains in NG layer is assumed to be identical. Also, following previous studies on NGs (Fang et al., 2012), the free volume distribution inside the glassy grains within NG layer is considered to be similar to that of MG layer. Therefore, the values of material parameters for these regions (MG layer and glassy grains in NG layer) are assumed to be identical, and are taken from the work of Thamburaja (2011). The bulk modulus, κ and shear modulus, G are considered as 166.7 and 35.7 GPa respectively. The parameter ξ_T and f_0 corresponding to T = 295 K are taken as 0.00063 and 214.8 s^{-1}, respectively. The constants $\zeta, s_2, s_3, \phi, a, \dot{\gamma}_0$ and K are assumed to be 0.02, 2800 GJ/m^3, 240 GJ/m^3, 0.15, 0.02, 1.73 x 10^{-3} s^{-1} and - 250, respectively. The initial value of cohesion, c_0 is taken as 1 GPa, and it is perturbed by 1% about this mean value (1Gpa) and assigned randomly to the elements in MG layer, while it is kept uniform for glassy grains in NG layer (Singh et al., 2014). It is important to note from Eq. (5.2) that a material length scale, l_c enters in to the model through constant s_1, and it is taken as $l_c = \sqrt{\frac{s_1}{c_o}}$ following Dutta et al.(2018). Simulations are performed by setting various values of $l_c = 124$ to 310 *nm* to investigate its effect on deformation response the composites.

Further, as discussed in the chapter 1, interfaces in NGs are characterized by low density (Fang et al., 2012) and excess free volume (Sopu et al., 2009; Ritter et al., 2011). Therefore, shear bands nucleate from these interfaces and cut through the grains at later stages of loading (Adibi et al., 2013). In order to capture this behavior in continuum

simulations, Singh et al. (2014) developed strategy to model interfaces. They assign the value of initial cohesion, c_{oi}, constants K and s_1 for interfaces different from grains. The brief description of their modeling approach is as follows: First, they considered initial cohesion c_{oi} of interfaces is 20% lower than the grain interiors to model lower density in them. Next, they assumed slower drop in cohesion after commencement of yielding in interfaces than grain interiors by assuming the fitting constant K as -100. The rationale behind this assumption is that the cohesion should attain approximately same saturation value at every point inside a shear band that cuts through grains and interfaces. Lastly, noting that parameter s_1 penalizes the shear band formation, they assigned a lower value of s_1 for interfaces than grain interior. In addition, they perturbed cohesion by 1% about its mean value of 0.8 GPa and assigned randomly to the elements in interfaces. By this, they could able to nucleate shear bands from interfaces in their continuum simulations. In the present work, the interfaces within NG layer are modeled by employing the methodology adopted by Singh et al. (2014), and the values of c_{oi}, s_1 and K are taken from their work. However, other material parameters for interfaces are assumed to be identical to that for glassy grains. Furthermore, MD simulations on NG-MG laminate composites have shown that plastic deformation starts from both the interfaces (between NG and MG layer, and within NG layer) and thus results in prolonged homogeneous deformation in these materials (Adibi et al., 2016). In order to facilitate nucleation of shear bands from planner interfaces between NG and MG layer as well, the material parameters for these regions are taken to be identical to that for interfaces within NG layer.

5.4 Result and discussion

5.4.1 Deformation behavior of NG-MG laminate composite with single NG layer

5.4.1.1 Nominal stress versus strain curve

In Fig. 5.2, variation of nominal stress Σ_2, normalized by initial cohesion c_0 of MG layer with respect to nominal strain, E_2, are displayed for monolithic MG as well as composites corresponding to different values of NG layer thickness, t_{NG} for $l_c = 124\ nm$. The stress increases linearly with strain during initial stages of deformation for all cases, and the slope of the curves in this regime is identical for monolithic MG and composites, independent of the NG layer thickness. Further, in the case of monolithic MG, stress attains a peak at around E_2 = 0.018 and begins to drop gradually thereafter, owing to occurrence of adequate free

volume induced softening in the sample (Thamburaja, 2011; Singh et al., 2014; Singh and Narasimhan, 2016). Moreover, the peak stress in composites is lower than monolithic MG, and reduces further with increase in t_{NG} which is consistent with the observations of Sha et al. (2017). A steep stress drop signifying rapid strain localization in a shear band (Thamburaja, 2011) can be noticed in monolithic MG at around E_2 = 0.025. A similar stress drop, although with reduced rate can be seen at higher E_2 ~ 0.028 in composite sample with t_{NG} = 4.8 *nm*. Contrastingly such stress drop is not apparent in samples having thicker NG layer. For instance, in the case of t_{NG} = 38.4 *nm*, stress drops abruptly after the peak stress, and a second stress drop (which is noticed in samples with t_{NG} = 4.8 *nm*) is not present.

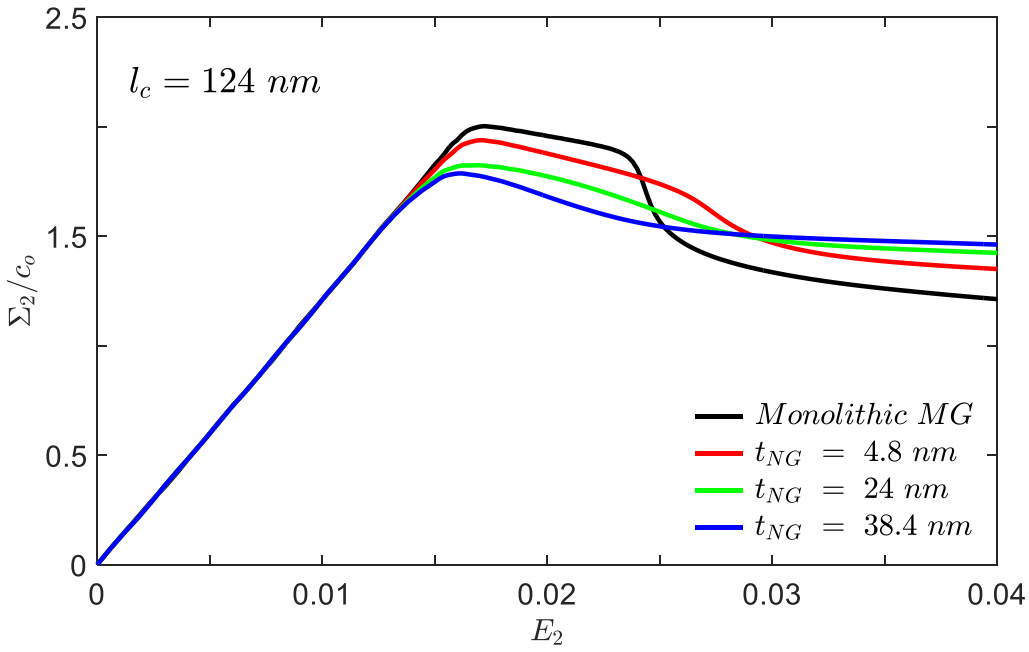

Figure 5.2 Nominal stress versus nominal strain curves of monolithic MG and NG-MG laminate composites corresponding to different NG layer thickness, t_{NG} for l_c = 124 *nm*.

The volume fraction, $V_{f,MG}$ of the MG layer changes with the change in thickness of NG layer, and it would be interesting to analyze its influence on the peak stress exhibited by the composites. Therefore, the variation of normalized peak stress, $\hat{\Sigma}/c_0$, with respect to $V_{f,MG}$ is plotted in Fig. 5.3. Note that $V_{f,MG}$ = 0 corresponds to pure NG sample, while $V_{f,MG} = 1$ pertains to monolithic MG. Fig. 5.3 reveals that peak stress drops abruptly as $V_{f,MG}$ reduces from 1 to 0.7, whereas it changes marginally for further decrease in $V_{f,MG}$. It can be inferred from Fig. 5.3 that, *peak stress in nanolaminate composites reduces rapidly up to 30% volume fraction of NG layer, $V_{f,NG}$, and remains nearly independent of $V_{f,NG}$*

thereafter. Sha et al. (2017) reported qualitatively similar trend from MD simulations on NG-MG nanolaminate composites, which they referred to as inverse Hall-Petch relation. They argued that this relation is likely to be caused by curvature formed at NG surfaces, though the radius of curvature at the peak stress stage was very large in their simulations. In this connection, it must be mentioned that Dutta et al. (2018) investigated the effect of notch root radius on mechanical response of notched MG samples, and they found insignificant change in the peak stress even for enhancement in radius by 400%. Therefore, the observed inverse Hall-Petch relation is not due to the formation of local notches. This trend can be explained with reference to the spatial distribution of plastic strain in the specimen, hence evolution of plastic strain in the samples is analyzed in the next section.

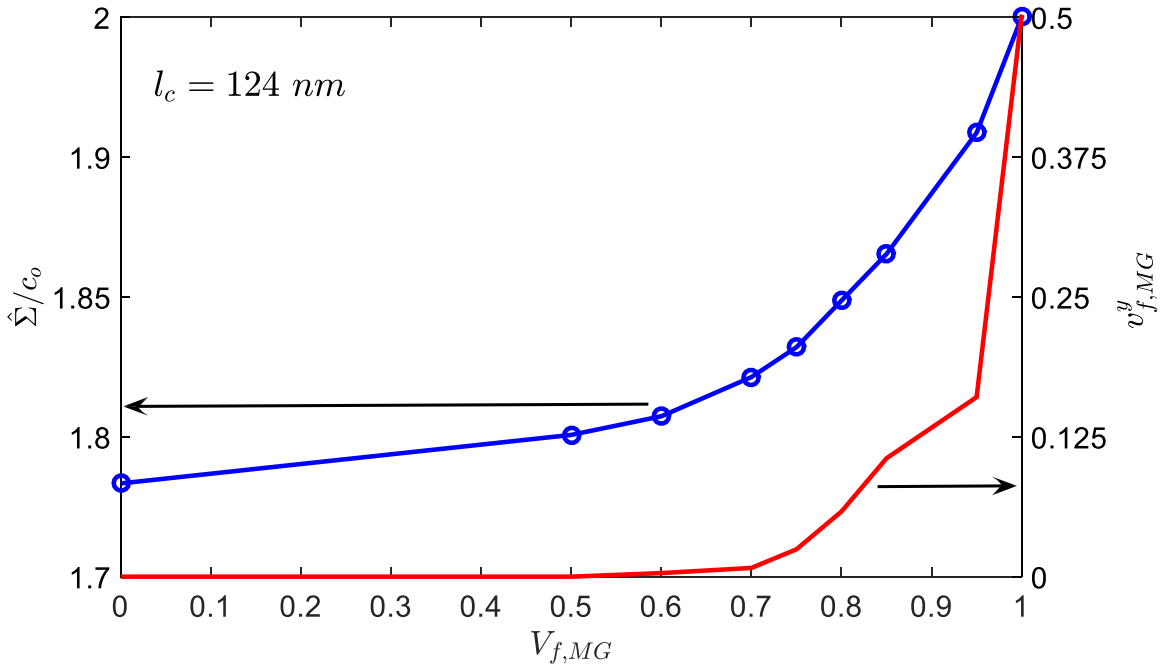

Figure 5.3 Variation of normalized peak stress, $\hat{\Sigma}/c_o$ (refer left ordinate) with volume fraction, $V_{f,MG}$ of MG layer in the composites for $l_c = 124\,nm$. Here, values denoted by 'o' symbol are obtained from finite element simulations, whereas solid line curve is a best fitting of these values. Also displayed in the figure is the variation of volume fraction of material undergoing plastic yielding, $V^y_{f,MG}$ at the peak stress stage (right ordinate) against $V_{f,MG}$.

5.4.1.2 Evolution of plastic strain

Fig. 5.4 displays the contour plots of maximum principle logarithmic plastic strain $\log \lambda_1^p$, corresponding to three levels of macroscopic strain E_2 for the composite samples with $t_{NG} =$

4.8, 24, 38.4 *nm* for a l_c = 124 *nm.* The yielding begins in the weak interfaces resulting in plastic strain to evolve in these regions well before the macroscopic yield has taken place (Singh et al., 2014). Fig. 5.4(a) demonstrates that for t_{NG} = 4.8 *nm*, two lobes of putative shear bands inclined at $\pm 45^{o}$ with respect to loading axis emanate from both the free surfaces of NG layer, and appears to penetrate into the MG layer at a macroscopic strain of around E_2 = 0.02. These symmetric bands meet each other resulting in plastic strain to spread in a diamond-shaped ring (refer Fig. 5.4(a)). Further loading promotes the localization of plastic strain in one of the shear bands (refer Fig. 5.4(b)) leading to a rapid load drop at around E_2 = 0.025 (refer Fig. 5.2). Subsequent loading intensifies the plastic strain in this dominant shear band with a noticeable shear offset across m-m at around E_2 = 0.04 in Fig. 5.4(c).

Contrary to the above observations, for t_{NG} of 24 and 38.4 *nm*, the putative shear bands emanating from the four corners of the NG layer do not propagate in MG layer, instead they expand in NG layer itself (as shown in Fig. 5.4(d) and (g)). It is evident from Fig. 5.4(d) that, the shear bands originating from top and bottom corners of both sides of the free surfaces meet at some point inside the NG layer as indicated by 'A' and 'B'. On further deformation, plastic flow intensify between points 'A' and 'B' and thus spreads from one corner to the diagonally opposite corner of the NG layer (Fig. 5.4(e)). When E_2 is reaches to 0.04, a dominant shear band with noticeable shear offset forms as shown in Fig. 5.4(f). A similar deformation events are noticed even in the case of samples with t_{NG} = 38.4 *nm* as shown in Figs. 5.4(g) to (i).

A comparison of plastic strain distribution (as shown in Fig. 5.4) among the three simulated samples suggests that, in the case of low t_{NG} the shear band nucleates at one side of the NG surface and propagates through the MG layer to the other surface, while in the composites with higher t_{NG} the shear bands are primarily confined to the NG layer. This clearly shows that the net contribution of MG layer to the aggregate plastic deformation decreases as t_{NG} increases. Besides t_{NG}, the volume fraction of MG layer undergoing plastic yielding is also an important parameter as it contributes to the overall mechanical response of NG-MG laminate composites, and hence it needs to be analyzed.

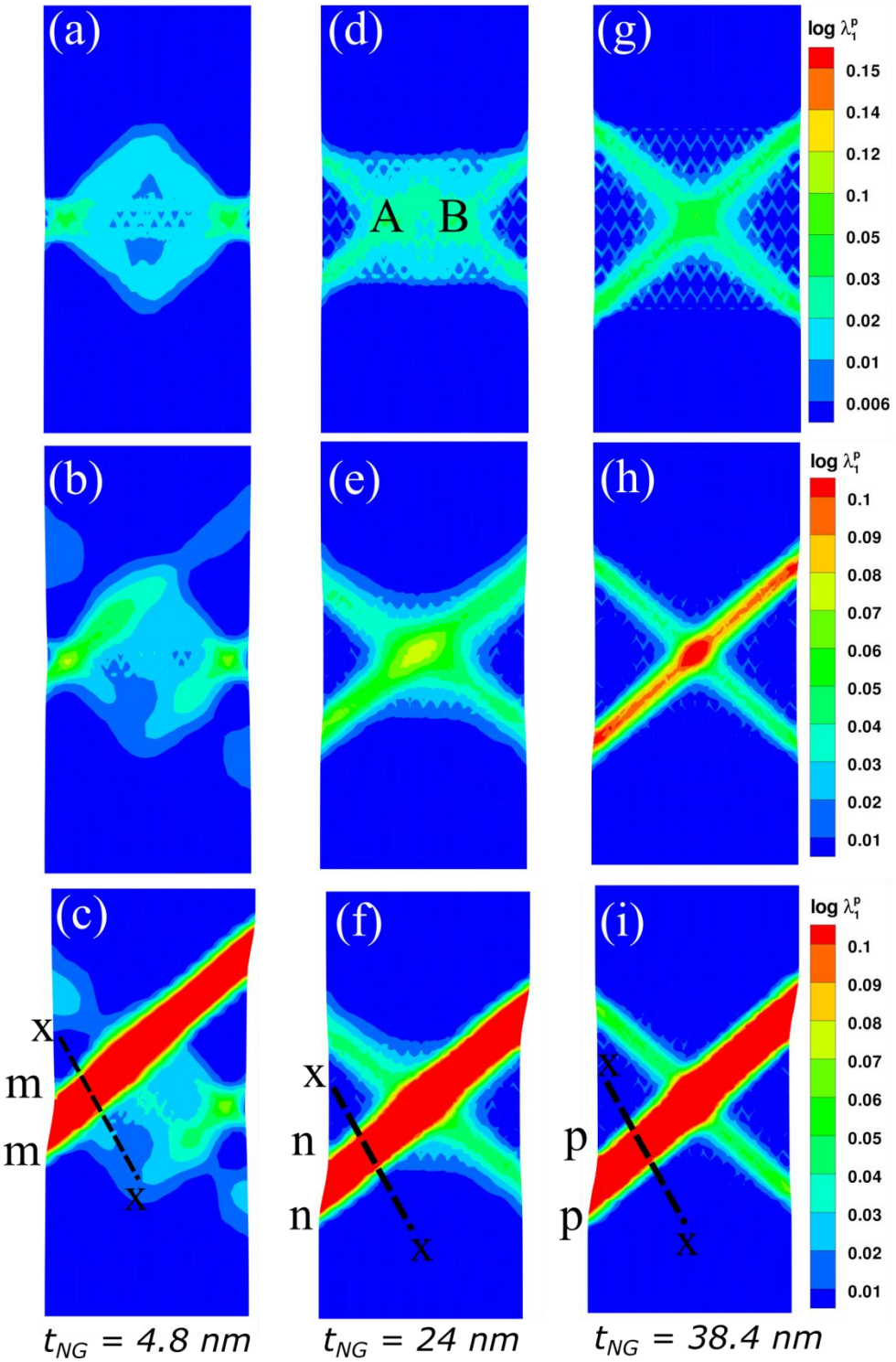

Figure 5.4 Contour plots of maximum principle logarithmic plastic strain $log\lambda_1^p$ for composite samples with $l_c = 124\ nm$ at (a) E_2 = 0.02, (b) E_2 = 0.025 and (c) E_2 = 0.04 for NG layer thickness t_{NG} = 4.8 *nm*. The corresponding plots for t_{NG} = 24 and 38.4 nm are shown in (d)-(f) and (g)-(i), respectively.

For this purpose, plastic yielding at a point assumed to have occurred if $\log \lambda_1^p$ at that point is greater than 0.001 which is much smaller than the initial tensile yield strain of 0.018. It must be mentioned that other choices of this limiting value of $\log \lambda_1^p$ (being smaller compared to the macroscopic yield strain) are tried and found that chosen value does not affect the conclusions made from the following discussion. Using above criterion, the volume fraction of the yielded material in MG layer $V_{f,MG}^y$, near the peak stress is determined and plotted against $V_{f,MG}$ in Fig. 5.3. Note that $V_{f,MG}^y$ drops rapidly as $V_{f,MG}$ is reduced from 1 to 0.7 after which it is nearly independent of $V_{f,MG}$. Thus, the *contribution of MG layer to the aggregate plastic deformation of the laminate composite reduces rapidly when* $V_{f,MG}$ *is decreased from 1 to 0.7.* It is also important to note from Fig. 5.3 that both $\hat{\Sigma}$ and $V_{f,MG}^y$ decreases with $V_{f,MG}$ almost in a similar manner signifying that $\hat{\Sigma}$ is mainly governed by $V_{f,MG}^y$ and poorly by $V_{f,MG}$, therefore peak stress in laminate composite with single NG layer don't follow of mixture.

In order to get further insights into the strain localization in NG-MG laminate composites, line plots of $\log \lambda_1^p$ across the dominant shear band (line X-X of Figs. 5.4(c), (f) and (i)) corresponding to different levels of macroscopic strain are shown against normalized distance, s/l_c for t_{NG} = 4.8, 24 and 38.4 *nm* in Figs. 5.5(a), (b) and (c), respectively. These figures pertain to l_c = 124 *nm*. The maximum value of $\log \lambda_1^p$ inside the band is around 0.05 at E_2 = 0.025 for t_{NG} = 4.8 and 24 *nm* while it is slightly higher for t_{NG} = 38.4 *nm*. An increase in E_2 to 0.04 (for an increase of 60 %), increases $\log \lambda_1^p$ to a value of 0.2 (an increase of about 300 %) indicating a rapid strain localization inside the shear band. Note that irrespective of t_{NG} in the composites, shear band width increases marginally with E_2, and saturates to 0.08-1.2 l_c.

In order to verify the scaling of shear band width with l_c, variation of $\log \lambda_1^p$ across the dominant shear band with respect to s/l_c is plotted for two l_c (~ 217 and 310 *nm*) in Figs. 5.6 and 5.7, respectively, for t_{NG} = 4.8, 24 and 38.4 *nm*. Figs. 5.6 and 5.7, similar to Fig. 5.5, reveal that the *shear band width in NG-MG laminate composites always scales with material length scale as 0.08-1.2*l_c *and is independent of* t_{NG}. Further, the strain levels inside the shear band is higher for lower l_c than higher l_c suggesting that the internal material length l_c control the process of shear localization which will be described in detail in next section.

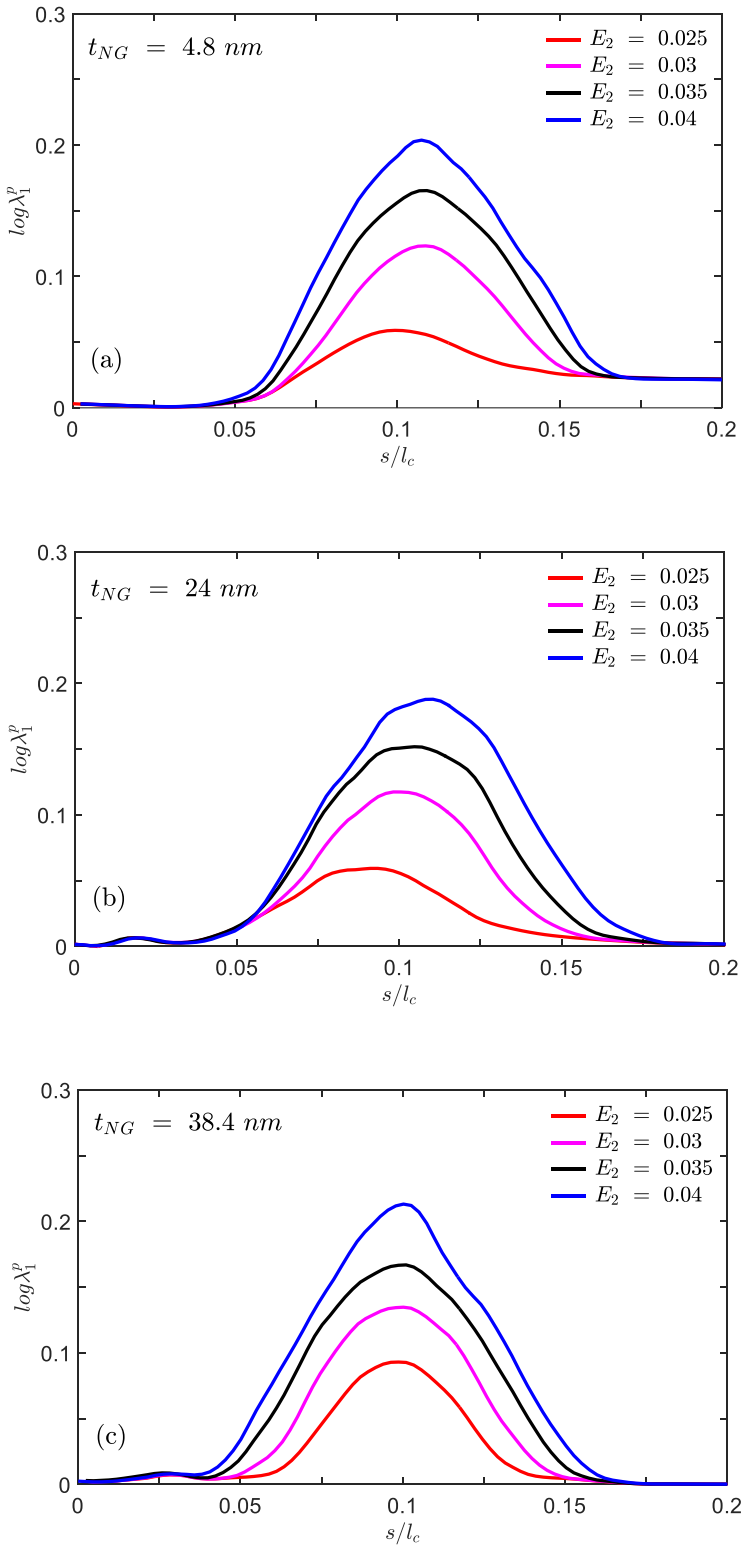

Figure 5.5 Variations of maximum principle logarithmic plastic strain $log\lambda_1^p$ with normalized distance, s/l_c across the shear band for (a) t_{NG} = 4.8 *nm*, (b) t_{NG} = 24 *nm* and (c) t_{NG} = 38.4 *nm* at different levels of E_2 corresponding to l_c = 124 *nm*.

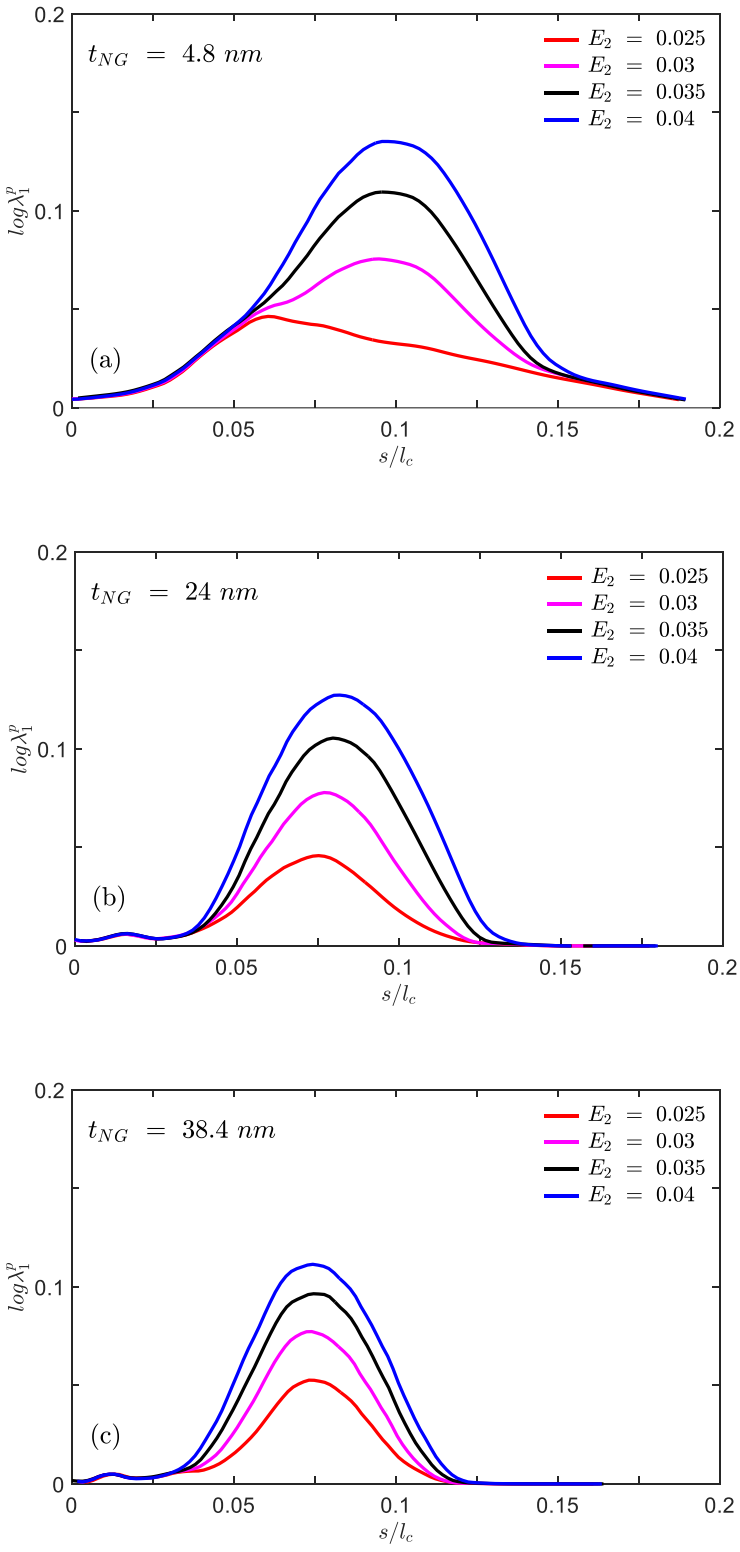

Figure 5.6 Variations of maximum principle logarithmic plastic strain $log\lambda_1^p$ with normalized distance, s/l_c across the shear band for (a) t_{NG} = 4.8 *nm*, (b) t_{NG} = 24 *nm* and (c) t_{NG} = 38.4 *nm* at different levels of E_2 corresponding to l_c = 217 *nm*.

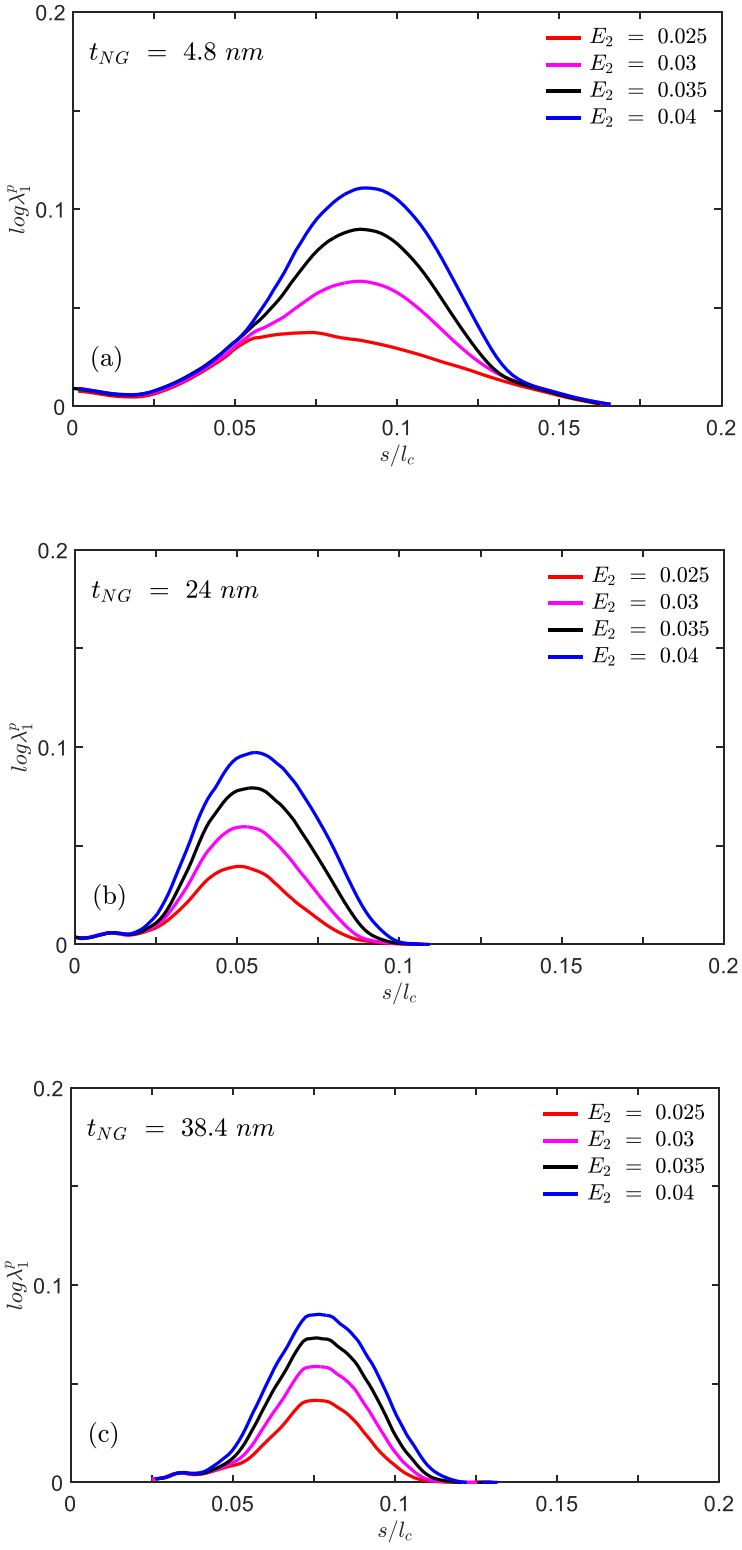

Figure 5.7 Variations of maximum principle logarithmic plastic strain $log\lambda_1^p$ with normalized distance, s/l_c across the shear band for (a) t_{NG} = 4.8 *nm*, (b) t_{NG} = 24 *nm* and (c) t_{NG} = 38.4 *nm* at different levels of E_2 corresponding to l_c = 310 *nm*.

5.4.1.3 Effect of l_c on the deformation behavior

Fig. 5.8 shows nominal stress *vs.* strain curves corresponding to various values of l_c for sample with t_{NG} = 24 *nm*. Note that stress drops rapidly after the peak stress for lower l_c = 124 *nm*, and more gradually for higher l_c suggesting that an increase in l_c retards strain localization. Similar observations have been made for other t_{NG} *confirming that increase in* l_c *retards shear localization in NG-MG nanolaminate composites.*

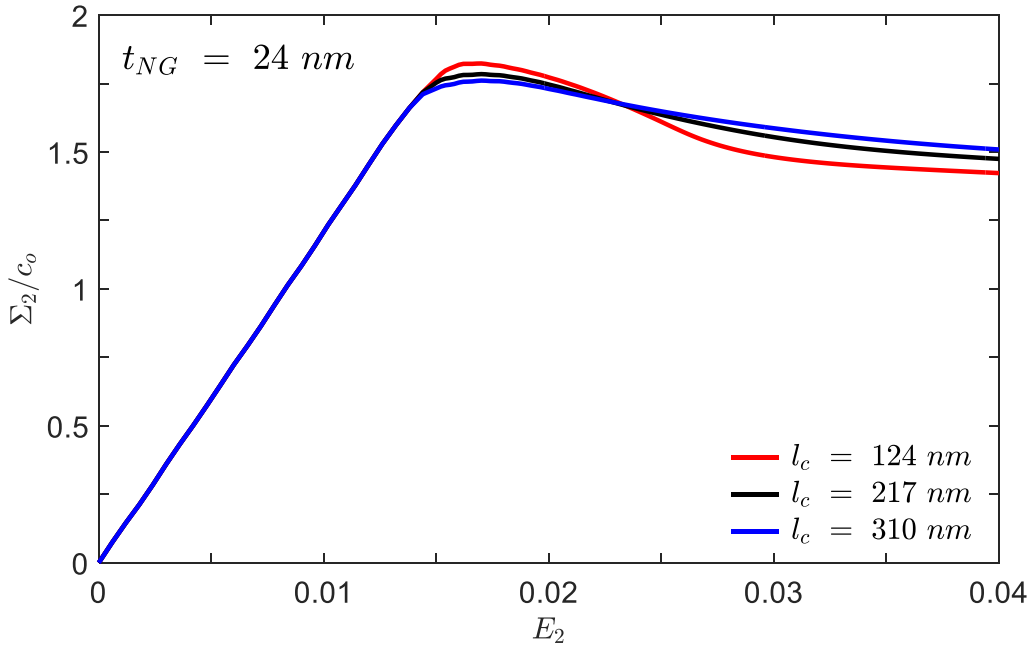

Figure 5.8 Normalized macroscopic nominal stress versus strain curves pertaining to various values of l_c for t_{NG} = 24 *nm*.

What are the mechanistic reasons for the above noted l_c effects? In order to address this question, contour plots of interaction stress, τ_{int}, normalized by c_o at macroscopic strain E_2 of 0.015 for t_{NG} = 24 *nm* and l_c = 124 and 310 *nm* are presented in Fig. 5.9(a) and (b), respectively. The plastic yielding gets initiated at the interface regions due to lower yield strength causing the free volume to evolve (or STZs to accumulate) while the stress state inside the grains and MG layers is still elastic. As a consequence, a large free volume (or STZ concentration) gradient develops giving rise to interaction stress between the flow defects (refer Eq. (5.2)). Note from Fig. 5.9 that τ_{int} is positive inside the interfaces, and negative inside grains. Another observation from Fig. 5.9 is that the positive valued τ_{int} within the interfaces (inside NG layer as well as between NG and MG layer) becomes more positive on increasing l_c, while it becomes more negative in the grains. As mentioned earlier, negative

valued τ_{int} promotes further evolution of plastic strain, while $\tau_{int} > 0$ resist growth of shear strain (refer Eq. (5.19)). Therefore, it can be inferred from Fig. 5.9 that resistance offered by interfaces for localization, and susceptibility of material inside grains for plastic yielding increases with increase in l_c. This delays the shear localization in NG-MG nanolaminate composite with higher l_c.

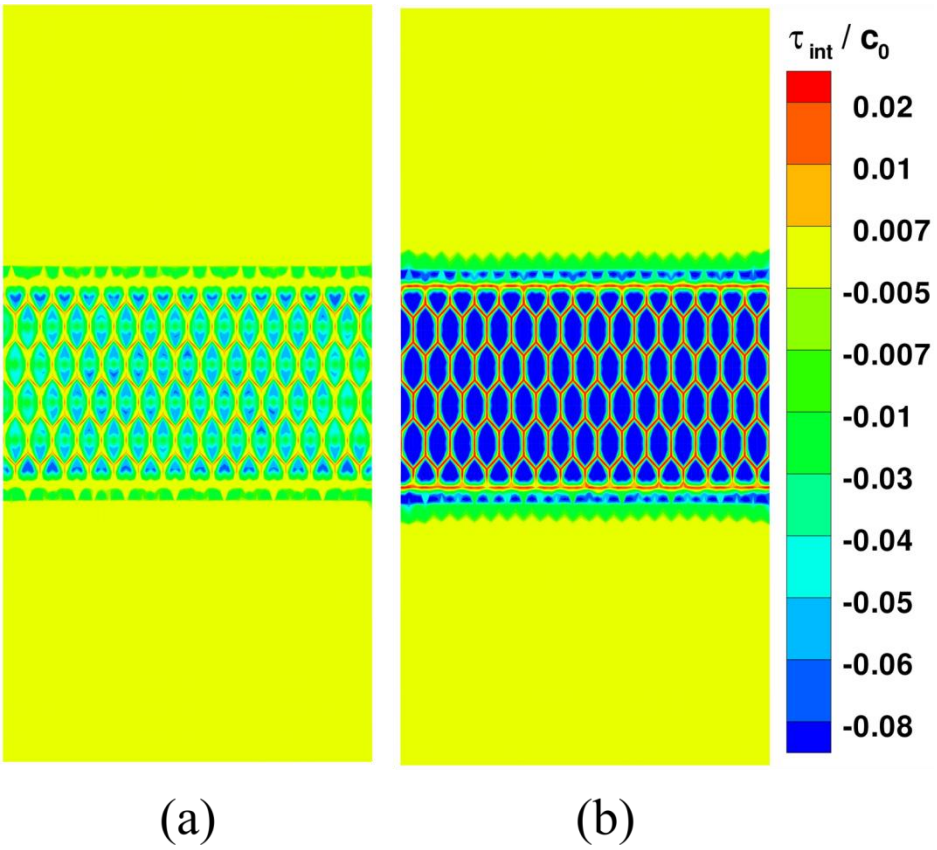

Figure 5.9 Contour plots of normalized interaction stress, τ_{int}/c_0 at E_2 =0.015 for sample with t_{MG} = 24 *nm* corresponding to a (a) l_c = 124 *nm* and (b) l_c = 310 *nm*.

To clearly understand the effect of l_c on the relationship between peak stress attained in the composite samples and the volume fraction of MG layer in them, variation of normalized peak stress, $\hat{\Sigma}/c_o$, with respect to $V_{f,MG}$ is plotted in Fig. 5.10 for different values of l_c. Note that peak stress drops with $V_{f,MG}$ in a similar manner for all values of l_c. At this juncture, it must be mentioned that Zhang et al. (2009) showed from MD simulations of tensile loading on notched CuZr MG specimen that the composition of glass has a profound influence on shear band width. They reported a wider shear band in glass compositions that offer less resistance to change in local atomic arrangements. In another MD study, Zhong et al. (2016) have observed that the critical thickness of the MG samples below which non-localized

plastic deformation takes place strongly depends on the composition of the glass. Recently, Dutta et al. (2018) demonstrated that change in l_c in the model of Thamburaja (2011) resulted similar effect on the deformation behavior of notched MG samples as caused by change in composition of the glass in MD simulations. In fact, they showed a transition in deformation behavior from localization in 'V'-shaped double shear band to necking by increasing l_c to sufficiently large value in their continuum simulations. Most importantly, they were able to reproduce similar transition by altering the composition using MD simulations. Thus, it can be deduced that l_c value in the plasticity model of Thamburaja (2011) corresponds to a MG with specific composition, and the effect of composition on the deformation response of the glass can be captured by changing l_c in the model. In the view of above discussion, it can be concluded from the present continuum analysis that *the peak stress in NG-MG nanolaminate composites do not follow rule of mixture, irrespective of glass composition or intrinsic material length*.

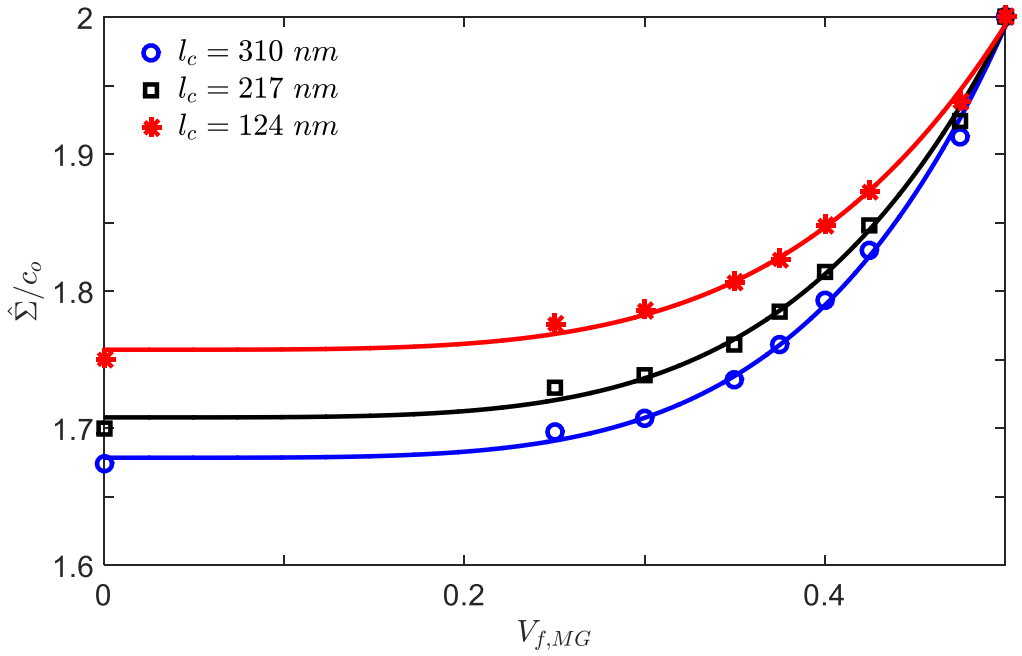

Figure 5.10 Variation of normalized peak stress, $\hat{\Sigma}/c_o$ with volume fraction, $V_{f,MG}$ of MG layer in the composites for different values of l_c. Here, values denoted by 'o', '□' and '*' symbols pertain to l_c = 124, 217 and 310 *nm*, respectively, and corresponding best fit curves are shown by line plots.

5.4.2 Deformation behavior of multi-layer NG-MG laminate composite

In this section, tensile response of three multilayer nanolaminate composites having different number of NG and MG layers, referred to S1, S2 and S3 will be analyzed. The number of NG layers and the thickness of NG and MG layers of these samples are given in Table. 5.1.

Table 5.1 Number of NG layers, thickness of NG and MG layer in different nanolaminate composite samples**.**

Sample	Number of NG layers	Thickness of NG layer, t_{NG} (*nm*)	Thickness of MG layer, t_{MG} (*nm*)
S1	3	24	4.5
S2	10	4.8	3.3
S3	13	4.8	0.98

Figs. 11(a)-(c) display evolution of plastic strain in sample 'S1' corresponding to a l_c of 310 *nm*. Multiple incipient shear bands carrying low plastic strain and cutting through MG layers can be noticed in the earlier stages of deformation as shown in Fig. 5.11(a). The plastic strain in these bands increases with further loading (refer Fig. 5.11(b)) and eventually spread across the entire cross section of the specimen resulting in necking (refer Fig. 5.11(c)) at a macroscopic strain E_2 of 0.065. A similar deformation behavior is noticed in the case of sample S2 as shown in Figs. 5.11(d)-(f). The stress-strain curves displayed in Fig. 5.12 for these specimens demonstrate that the stress decreases gradually beyond the peak stress stage and no abrupt stress drop is observed up to E_2 of 0.075. It must be mentioned that simulations are performed on samples having various combinations of t_{MG} and t_{NG} for l_c = 310 *nm*, and found that samples with t_{MG} lower than 4.5 *nm* showed necking, while the specimen with larger t_{MG} exhibited localized deformation. These observations are in agreement with the MD simulations (Sha et al., 2017) suggesting that the transition in deformation behavior of nanolaminate composites from strain localization to necking is controlled by the t_{MG}.

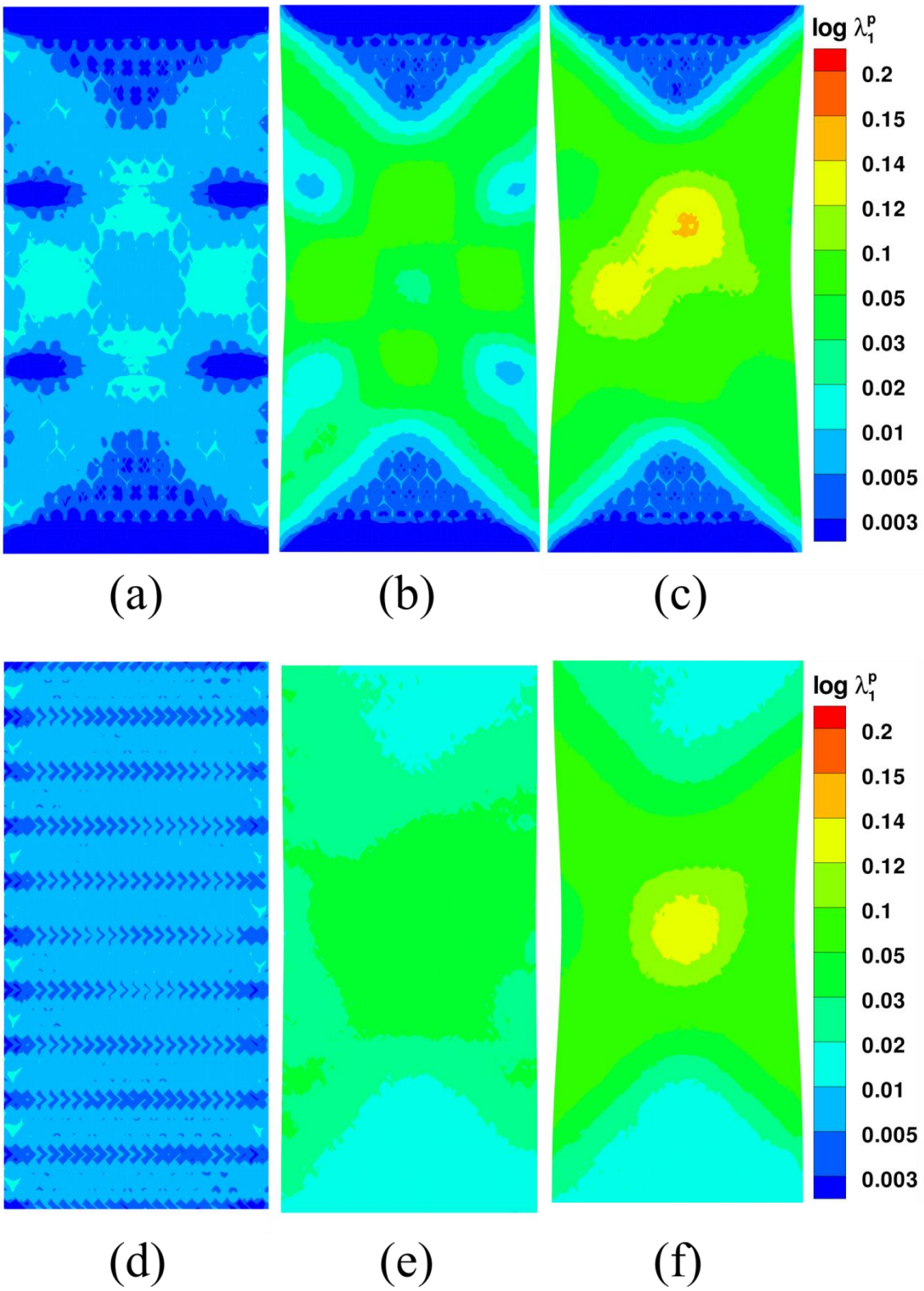

Figure 5.11 Contour plots of $log\ \lambda_1^p$ for sample S1 pertaining to l_c = 310 nm at (a) E_2 = 0.02, (b) E_2 = 0.04 and (c) E_2 = 0.065. The corresponding plots for sample S2 are displayed in (d)-(f).

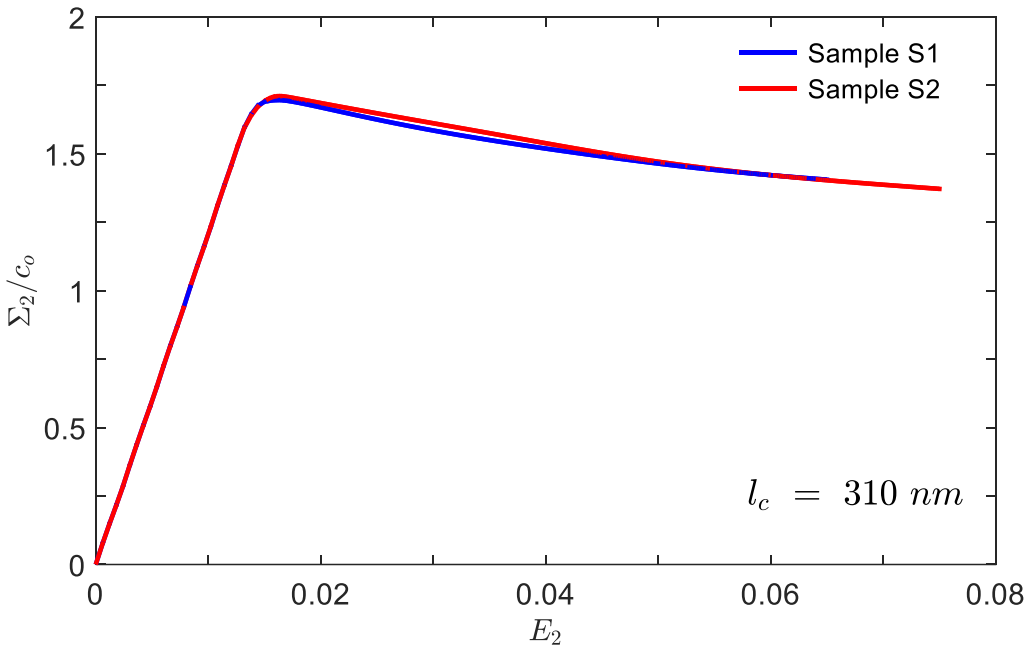

Figure 5.12 Nominal stress versus nominal strain curves for different composite samples with multiple NG layers for l_c = 310 *nm*.

"What governs the threshold level of t_{MG} corresponding to transition?" is an important question that needs to be addressed. To this end, simulations are performed on samples 'S1' and 'S2' by setting lower l_c of 124 *nm*. Figs. 5.13(a) and (b) shows the contour plots of $\log\lambda_1^p$ at E_2 = 0.05 for sample 'S1' and 'S2', respectively. Note that for lower l_c, the strain localization occurs in a dominant shear band with noticeable shear offset (refer Fig. 5.13(a) and (b)) unlike necking for higher l_c (refer Fig. 5.11). These results suggest that *threshold t_{MG} in nanolaminate composites for transition decreases with decrease in intrinsic material length l_c*.

In order to substantiate above statement, simulations are performed on another sample 'S3' while keeping l_c same as in Fig. 5.13. Note that number of NG layers are more, while thickness of MG layer is less in sample 'S3' than sample 'S2' (refer Table. 5.1). The contour plots of $log\lambda_1^p$ at E_2 of 0.085 for sample 'S3' is shown in Fig. 5.14. This figure displays the presence of multiple shear bands even at such a high level of macroscopic strain, though there is tendency for localization in one of the bands. The macroscopic stress-strain curve plotted in Fig. 5.15 for this sample shows no abrupt stress drop beyond peak stress stage till E_2 of 0.085. Thus, it can be concluded that *shear localization in NG-MG nanolaminate composites can be delayed significantly either by increasing material length l_c or reducing the thickness*

of MG layer. In other words, *intrinsic material length l_c with respect to MG layer thickness governs the transition from shear induced failure to necking*.

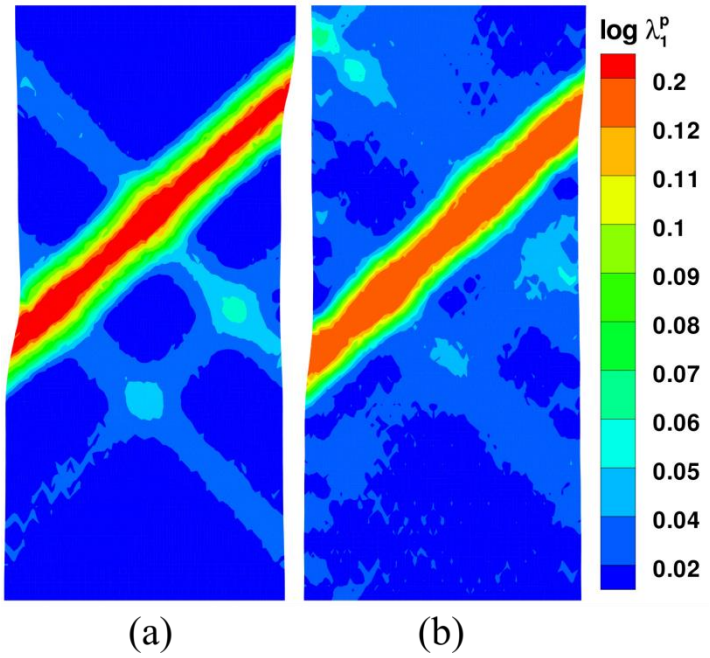

Figure 5.13 Contour plots of $log\ \lambda_1^p$ for NG-MG nanolaminate composite sample (a) S1 and (b) S2 at E_2 = 0.05 for l_c = 124 *nm*.

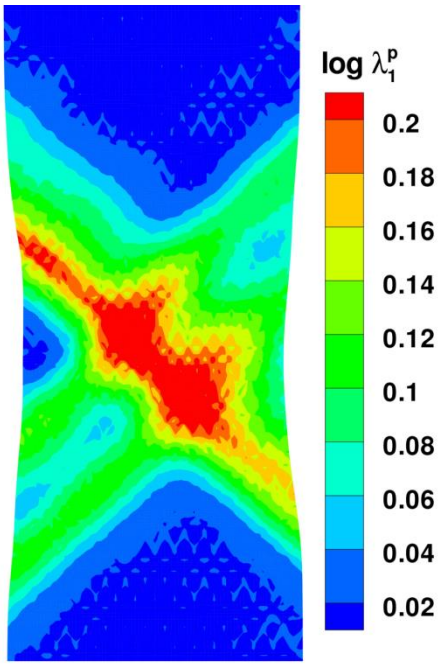

Figure 5.14 Contour plots of $log\ \lambda_1^p$ for NG-MG nanolaminate composite sample S3 at E_2 = 0.085 for l_c = 124 *nm*.

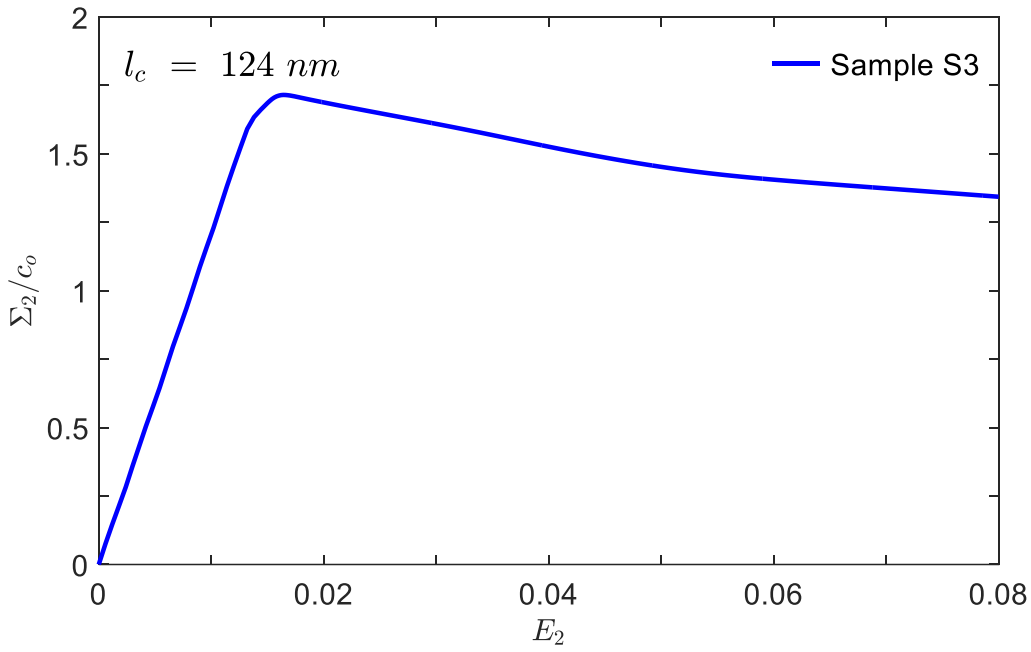

Figure 5.15 Nominal stress versus nominal strain curves for NG-MG nanolaminate composites sample S3 corresponding to l_c = 124 *nm.*

Why does threshold thickness of MG layer increases with l_c? It can be explained by analyzing the effect of l_c on spatial distribution of interaction stress τ_{int}. Therefore, contour plots of τ_{int}/c_o at E_2 = 0.015 for sample 'S2' are shown in Fig 5.16(a) and (b) for l_c = 124 and 310 *nm*, respectively. It can be seen that positive valued τ_{int} prevailing at interfaces (inside NG layer and between NG and MG layers) increases with increase in l_c, whereas τ_{int} becomes more negative inside grains and MG layers. As mentioned earlier, $\tau_{int} > 0$ resist further growth of plastic strain, $\tau_{int} < 0$ promote evolution of plastic strain (refer Eq. 5.19). Thus, the increase in l_c enhances the resistance for localization in a shear bands which cut through the interfaces, while it promotes spread of plastic strain across the specimen through MG layers and glassy grains experiencing strong negative interaction stress. Further, since shear band width scales with l_c (refer Fig. 5.5-5.7), multiple wider shear bands persist for longer time in the sample with higher l_c. Consequently, plastic strain spreads over the entire thickness of the specimen before localization takes place in a dominant band leading to necking of the specimen. On the other hand, thinner shear bands experiencing lesser resistance from interfaces develop in the specimen with lower l_c . As a result, strain localizes in a dominant shear band before plastic strain spreads over entire cross-section.

When thickness of MG layer is reduced by increasing the number of NG layers, localization is retarded significantly. This happens because the probability of triggering enough STZs to align for shear localization is less in sample with thinner MG layer (Thamburaja, 2011; Singh et al., 2014). Also, NG layer acts as a triggering site for shear bands (refer Fig. 5.4), therefore increase in number of NG layers promotes nucleation of multiple shear bands. In addition, a running shear band has to cut through higher number of interfaces which are obstacle for its propagation in a sample with large number of NG layers. As a result, sample 'S3' (having thinner MG layers and higher number of NG layer) is able to show prolonged homogeneous deformation even for lower l_c.

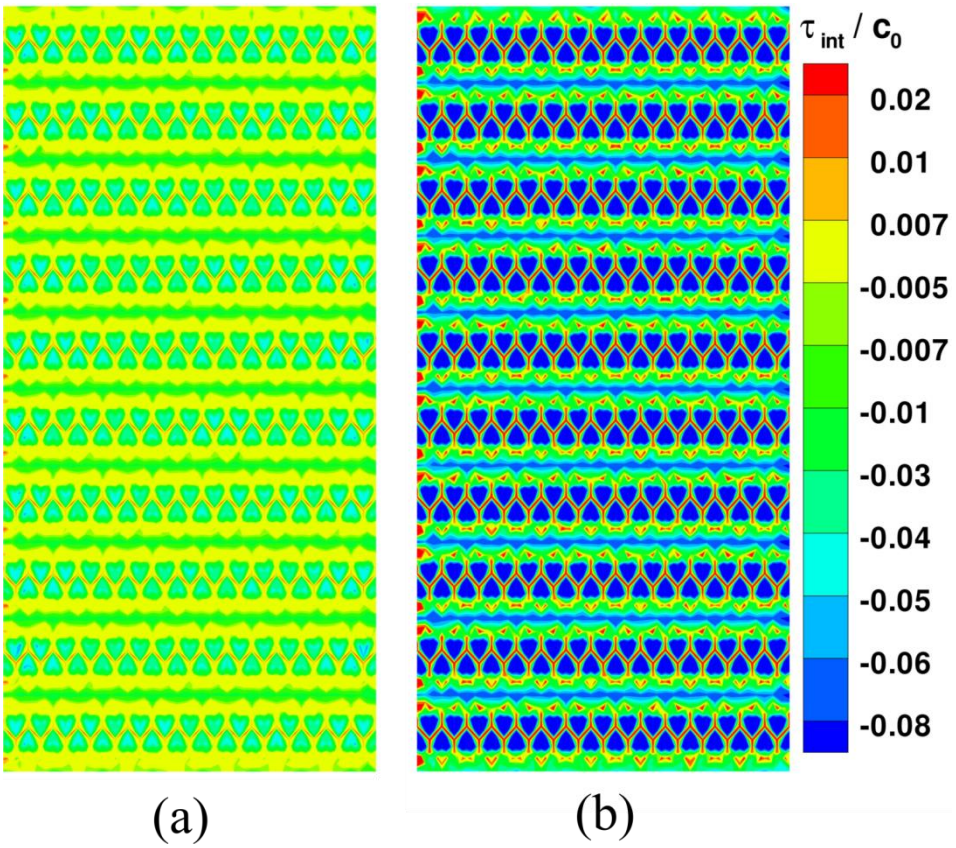

Figure 5.16 Contour plots of normalized interaction stress, τ_{int}/c_o at E_2 = 0.015 for sample S2 corresponding to (a) l_c = 124 *nm* and (b) l_c = 310 *nm*.

An interesting question to pose at this juncture is, "what kind of design insights can be provided from the present continuum analysis to synthesize ductile NG-MG nanolaminate composites? As pointed out earlier, increase in l_c increases threshold MG layer thickness and shear band width in nanolaminate composites. Further, Singh et al. (2014) reported increase in shear band width with enhancement in l_c in monolithic MG which suggest that threshold

MG layer thickness will be higher in a laminate composite synthesized by monolithic MG exhibiting wider shear band. Furthermore, Zhang et al. (2009) reported wider shear band width in $Cu_{20}Zr_{80}$ MG, and thinner shear band in $Cu_{64}Zr_{36}$ glass. Therefore, it can be inferred from present continuum analysis that *threshold MG layer thickness will be lower in the nanolaminate composite synthesized from glass composition which exhibit thinner shear band, while it will be higher for composition showing wider shear band.* In other words, composition of parent glass which is capable of exhibiting wider shear band is more suitable to design nanolaminate composites.

In summary, the deformation behavior of NG-MG laminate composites subjected to plane strain tensile loading has been investigated through finite element simulations using non-local plasticity model. The results are in good qualitative agreement with atomistic simulations (Sha et al., 2017), and also provide insights about the underlying deformation mechanism. The cellular MGs have also been fabricated which are found to be an alternative for structural and functional applications. The failure mechanism of these materials drastically changes with the change in size and wall thickness of cells. However, the mechanistic reasons for such transitions are not well understood. Hence, the deformation behavior of MG cellular structures are investigated in the next chapter.

CHAPTER 6

Finite element analysis of deformation and failure mechanism in nanoscale hexagonal cellular structures of metallic glasses

6.1 Introduction

The cellular metallic glasses (MGs) are found to be an alternative choice for structural and functional applications owing to light in weight, good energy as well as noise absorption capacity and enhanced plastic deformation (Sarac et al., 2012; Sarac and Schroers, 2013b; Chen et al., 2014; Liu et al., 2016). Sarac and Schroers (2013b) reported from compression experiments that the failure in cellular MGs transitions from global failure caused by localization in a shear band to the local failure by damage confined to few cells when the relative density of specimen is reduced from a large to moderate value. Further, the mode of deformation again changes over to the collective buckling of ligaments through row by row collapse when the relative density is decreased to a sufficiently lower level. They also revealed that peak stress attained in the samples varies nonlinearly with respect to relative density, whereas the mechanistic reason for this behavior is not well understood. The atomistic simulations on nanoscale cellular MGs have also reported transition from localized but confined to few cells to almost homogeneous deformation with increasing cell size (Zhang et al., 2016). In addition, these simulations showed strain localization in a dominant shear band for cell spacing along diagonal direction above a threshold value which was correlated to shear bandwidth in monolithic MG of identical composition. However, it is not clear from these simulations as to why and how the shear band thickness in monolithic MG controls the threshold cell-spacing.

In order to better understand the mechanistic reasons for the above noted transitions in the deformation behavior of cellular MG structures, 2D plane strain finite element simulations of compressive loadings are performed on cellular MG structures using non-local plasticity model of Thamburaja (2011). The organization of this chapter are as follows: the constitutive model and the modeling aspects are briefly described in sections 6.2 and 6.3, respectively. The important results obtained from this study are discussed in section 6.4.

6.2 Constitutive model

In the present study, the non-local finite strain plasticity model of MGs proposed by the Thamburaja (2011) is used because it has been successfully shown to capture the deformation behavior in nanometer-sized unnotched MGs (Thamburaja, 2011), notched MGs (Singh and Narasimhan, 2016; Dutta et al., 2018), MG composites (Shete et al., 2016, 2017; Dutta et al., 2020), NGs (Singh et al., 2014) and NG-MG nanolaminates (Chapter 5). The detailed derivation of this plasticity model can be found in Thamburaja (2011). The rate of plastic shearing, the rate free volume generation and evolution of cohesion are given by Eq. (5.1), (5.2) and (5.3), respectively.

A coupled, explicit finite element procedure, with displacement,u and free volume, ξ as nodal variable is employed to solve the governing equation for free volume evolution (Eq. 5.1) and weak form of equation of motion. Former is integrated using forward Euler scheme, while central difference method is used to integrate the latter. Mass scaling and small time step is employed to ensure the quasi-static and stability of the solution. The nodal averaging technique is used to smooth the discrete free volume gradient computed at centroids and generated a C^0 continuous vector field of free volume gradient (similar to the strain smoothing approach of Hinton and Cambell, 1974). By using this continuous free volume at the element integration points is obtained which is used in Eq. (5.2) to compute the interaction stress and update the plastic slip γ.

6.3 Modeling aspects

Fig. 6.1 shows finite element model of a compression specimen $\left(108(W_0) \times 187(L_0)\right) nm$ having six and twelve hexagonal cells along X_1 and X_2 direction, respectively. The cell width (along X_1 direction), cell-wall thickness and the length of inclined edge of a cell are denoted by d, t and l, respectively (refer Fig. 6.1). All the simulations are performed under plane strain conditions at a prescribed strain rate of $2 \times 10^{-3}/sec$. In order to understand the effect of the wall thickness of the cells on the deformation behavior of MG cellular structures, the specimens having different values of $t = 3, 6, 9$ and $12\ nm$ are considered, which are referred to as H_1, H_2, H_3 and H_4. However, the centre-to-centre distance of cells is kept constant in all the specimens. Consequently, angle θ characterizing the cell's alignment with respect to loading axis is 30^o in all the cases. Table 6.1 shows the values of d, t, l and θ for all the specimens. Also shown in this table is relative density, ρ^*/ρ, where ρ^* and ρ represent the

densities of cellular MG sample and the monolithic MG sample, respectively, and are calculated using relation mentioned by Sarac et al. (2012). In most of simulations, dimensions of the specimen are kept constant, while few computations are performed by changing specimen size to investigate its influence on the deformation behavior of cellular structures.

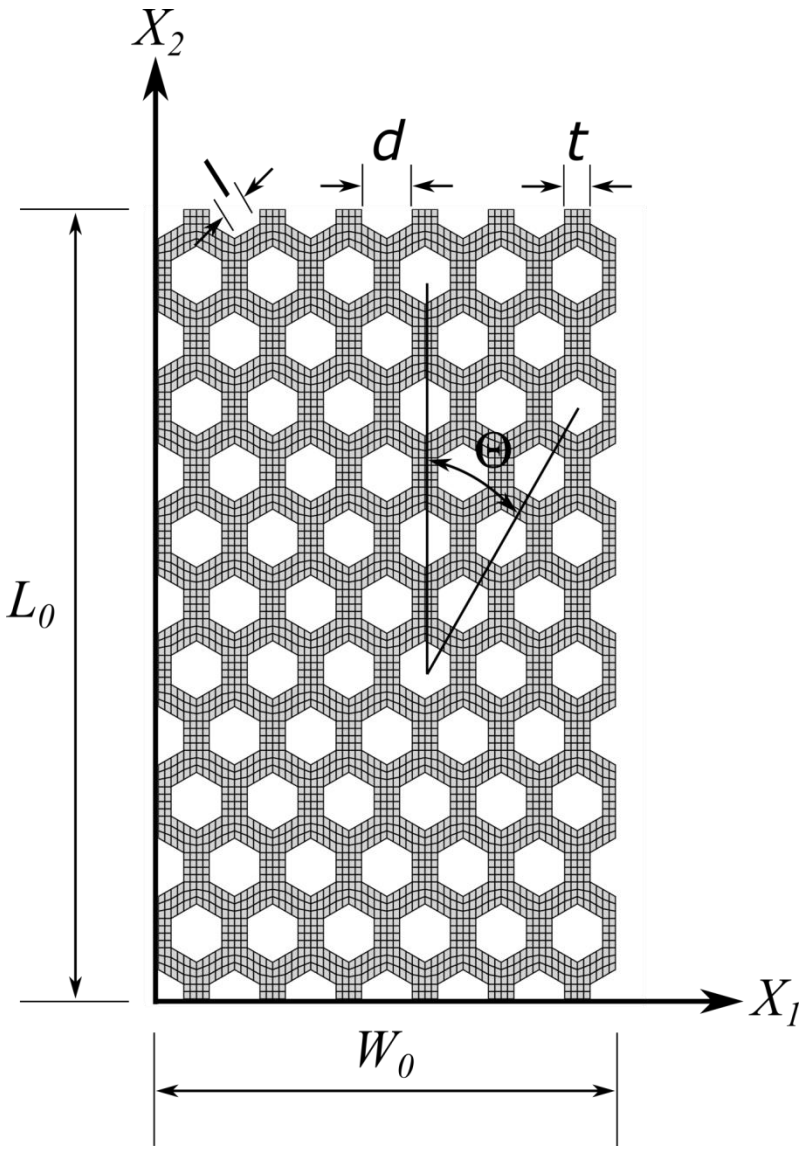

Figure 6.1 Finite element model of hexagonal cellular structure employed in plane strain compression simulations. Here, $d, t,$ and l denotes cell width, cell-wall thickness, and inclined edge of cell, respectively. Also, θ is cell's alignment with respect to loading axis.

Table 6.1 Cell features used to study deformation behavior of hexagonal cellular MG structure.

	H_1	H_2	H_3	H_4
$d\ (nm)$	15	12	9	6
$t\ (nm)$	3	6	9	12
$l\ (nm)$	8.7	6.9	5.2	3.4
ρ/ρ^*	0.31	0.55	0.75	0.89

The material of the specimen is assumed to obey the constitutive model discussed in section 5.2. The material parameters appearing in the model are taken from the work of Thamburaja (2011) which are as follows: The constants $k, G, \zeta, \dot{\gamma}_0, a, \phi, K, s_2, s_3, f_o$ and ξ_T at T = 295 K are considered as 166.7 GPa, 35.7 GPa, 0.02, 1.732 x 10^{-3} s^{-1}, 0.02, 0.076, -250, 2800 GJ/m^3, 240 GJ/m^3, 214.8 s^{-1} and 0.00063, respectively. Further, initial cohesion, c_0 is taken as 1 GPa and it is perturbed by 1% about this value (1Gpa) and randomly assigned to the elements to trigger shear bands in the specimen. It is important to note from Eq. (5.2) that a material length scale, l_c enters into the model through constant s_1, which is taken as $l_c = \sqrt{s_1/c_0}$ following the work of Dutta et al. (2018). Various values of s_1 are considered so that intrinsic material length l_c could be varied from 5 to 186 *nm.* Further, note that Thamburaja and Liu (2014) have shown from finite element simulations using the plasticity model of Thamburaja (2011) that the MG specimens exhibit strain hardening behavior when the boundary condition $\xi = 0$ is imposed. On the other hand, such specimens show strain softening when normal flux of ξ is considered to be zero on specimen surfaces (Thamburaja, 2011). Since both millimeter-sized (Sarac et al., 2012; Sarac and Schroers 2013b) as well as nanometer-sized (Zhang et al., 2016) MG cellular structures exhibit strain softening behavior the normal flux of the ξ is assumed to be zero in all the surfaces to solve the weak form of the equation of the Eq. (5.1).

6.4 Result and discussion

6.4.1 Nominal stress versus nominal strain curve

Fig. 6.2 Shows the variation of the nominal stress, Σ_2, normalized by c_0 with respect to nominal strain E_2 for monolithic MG as well as cellular MG specimens corresponding

to $l_c = 31\ nm$. Note that Σ_2 increases linearly with E_2 in elastic regime for all the cases, whereas the slope of the curve for monolithic MG is larger than that for cellular specimens. Also, for cellular MGs, the slope of the curves reduces with decrease in t (or increase in d) owing to increase in compliance of the specimen (compare slope of the curves for specimen H_4 and H_1). Further, the peak stress in cellular samples are lower than that for monolithic MG, and it drops further with decrease in t. These observations are in corroboration with experimental (Sarac et al., 2012; Sarac and Schroers, 2013b) as well as atomistic simulation results (Zhang et al., 2016). A colossal stress-drop which indicates rapid strain localization in a shear band (Thamburaja, 2011) can be noticed at around $E_2 = 0.025$ for monolithic MG. A similar stress drop at somewhat slower rate can be seen in cellular MG specimens H_4, H_3 and H_2 at around $E_2 = 0.025, 0.028$ and 0.032 respectively. By contrast, such stress drop is not noticed up to E_2 of 0.08 in specimen H_1 which has very thin cell-wall. Thus, it can be concluded that MG cellular structures with thinner cell-wall (or larger cell size) exhibit enhanced plastic deformation.

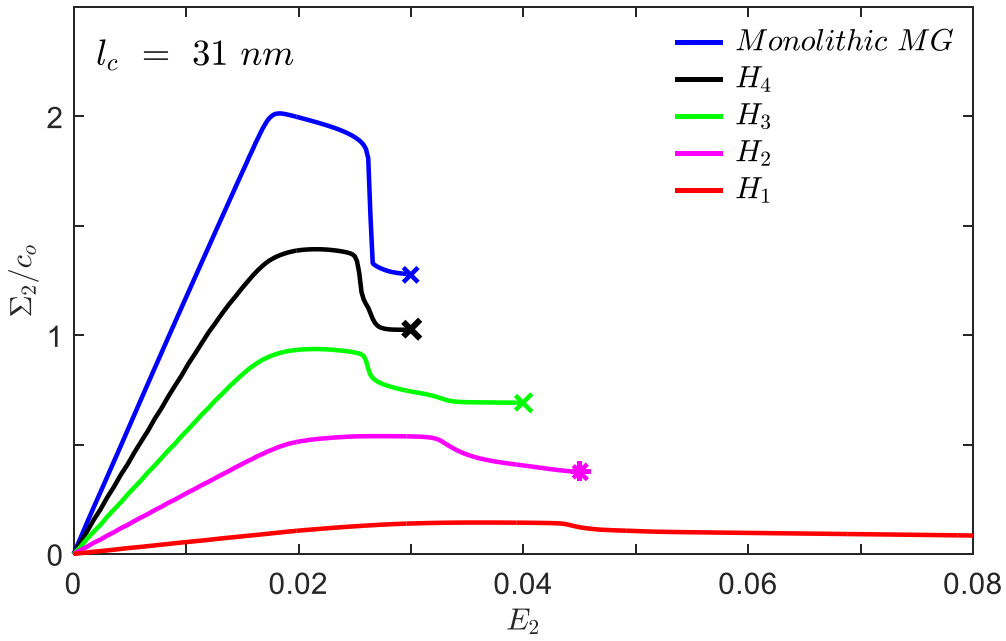

Figure 6.2 Normalized nominal stress versus nominal strain curves for monolithic MG and cellular MG specimens corresponding to $l_c = 31\ nm$. The stages of global and local failures are marked by '×' and '*' symbol, respectively.

In order to get more insights, the value of normalized peak stress, $\widehat{\Sigma}/c_0$ and slope of stress-strain curve, E_s are recorded for all the samples and plotted against relative density

ρ^*/ρ in Figs. 6.3(a) and (b), respectively, for $l_c = 31\,nm$. It can be seen from these figures that both $\hat{\Sigma}/c_o$ and E_s increases nonlinearly with ρ^*/ρ which has been found to be true for other values of l_c. This observation is in line with experimental observations made by Sarac et al. (2012). To understand mechanistic reasons for nonlinear variation in $\hat{\Sigma}/c_o$ with ρ^*/ρ, it would be interesting to analyze the volume fraction of material undergoing plastic deformation near peak stress stage. For this purpose, plastic yielding at a point is assumed to occur if maximum principal logarithmic plastic strain, $log\lambda_1^p$ at that point exceeds beyond 0.001 (significantly lower than the yield strain of monolithic MG in Fig. 6.2). Here, it is important to mention that other choices of limiting value of $log\lambda_1^p$ (smaller compared to the macroscopic compressive-yield strain) are also considered and it is found that chosen value does not alter the conclusions made in the following discussion. The volume fraction of yielded material V_f^y near the peak-stress stage in a cellular structure is determined by employing the above criterion and plotted against ρ^*/ρ in Fig. 6.3(a). Note from this figure both $\hat{\Sigma}/c_0$ and V_f^y increase with relative density in a similar manner which signifies that peak stress is mainly controlled by V_f^y and weakly by relative density. Consequently, peak stress in cell structure of MG enhances nonlinearly with respect to relative density.

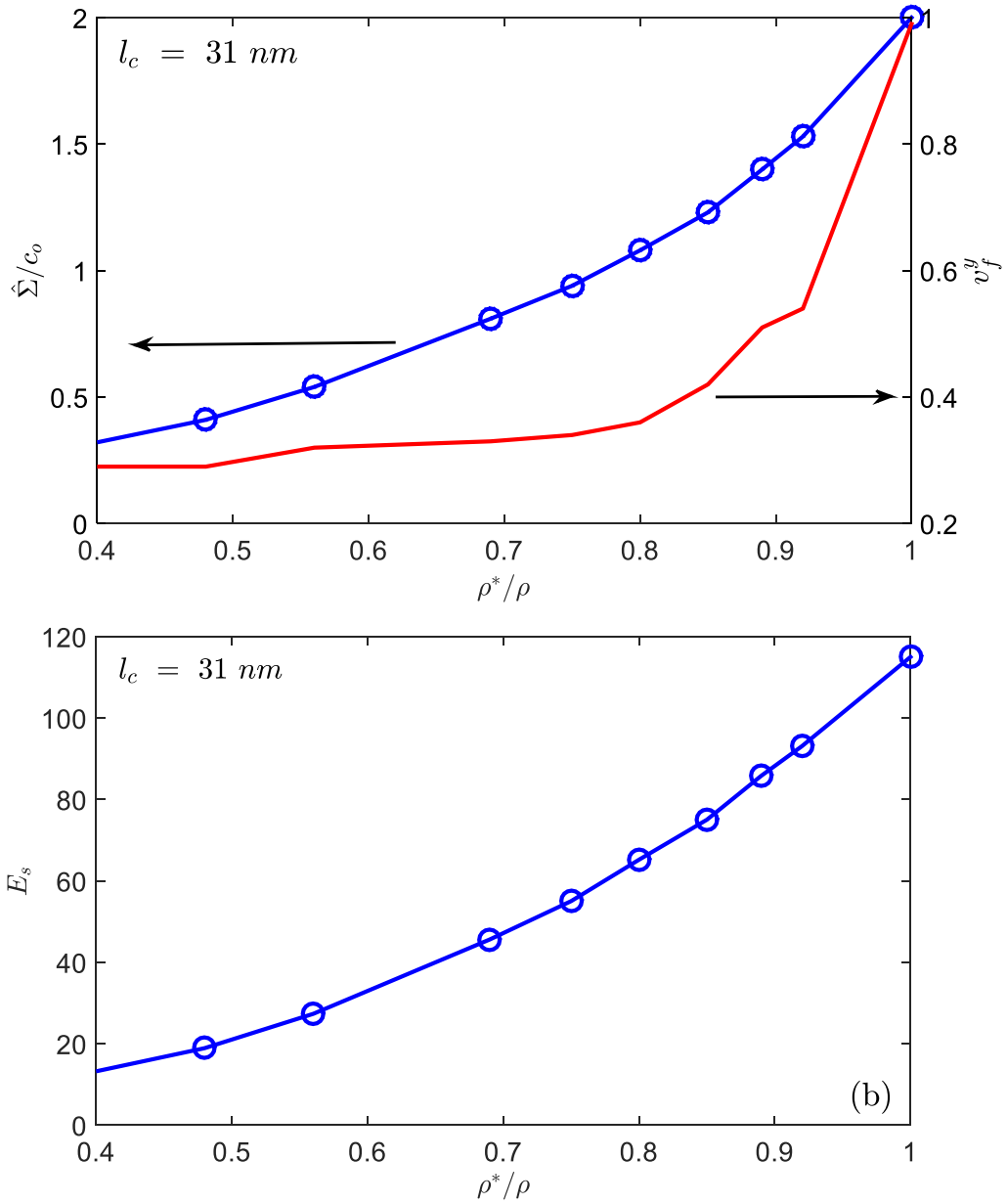

Figure 6.3 (a) The variation of normalized peak stress, $\hat{\Sigma}/c_0$ (refer left ordinate) with respect to relative density, ρ^*/ρ of cellular MG for $l_c = 31\ nm$. Also, displayed in this figures is the volume fraction of material yielded, V_f^y near peak stress stage (right ordinate) versus ρ^*/ρ curve. (b) The variation of the slope of stress-strain curves, E_s recorded for all the samples versus their relative density, ρ^*/ρ. Here symbol 'o' corresponds to values obtained from finite element simulations, while solid line curve represents best fitting of these values.

6.4.2 Evolution of plastic strain

In order to understand the effect of t on the evolution of plastic strain in MG cellular structures, contour plots of maximum principal logarithmic plastic strain, $log\lambda_1^p$ corresponding to successive stages are displayed for different specimens in Figs. 6.4-6.6. Figs. 6.4(a)-(c) show the contour plots of $log\lambda_1^p$ at three stages of $E_2 = 0.015, 0.02$ and 0.03, respectively, for sample H_4 with $l_c = 31\ nm$. It can be seen from Fig. 6.4(a) that yielding begins at corners of the vertical edges of the cells due to high stress concentration resulting in plastic strain to evolve well before the onset of macroscopic yielding in this sample (refer curve corresponding to H_4 in Fig. 6.2). As loading progresses, two lobes of putative shear bands begin to emanate from these yielded corners and appear to interact with neighboring cells lying in rows below and above the current row (refer Fig. 6.4(b)). When plastic yielding spreads over significant volume of the material, nominal stress begins to drop as noticed in Fig. 6.2. Subsequent loading intensifies plastic strain inside the bands connecting neighboring cells, and makes such bands to get aligned along a direction near to the direction of maximum shear stress. Eventually, a dominant shear band forms connecting one free surface to another free surface of the specimen at around $E_2 = 0.03$ (see Fig 6.4(c)).

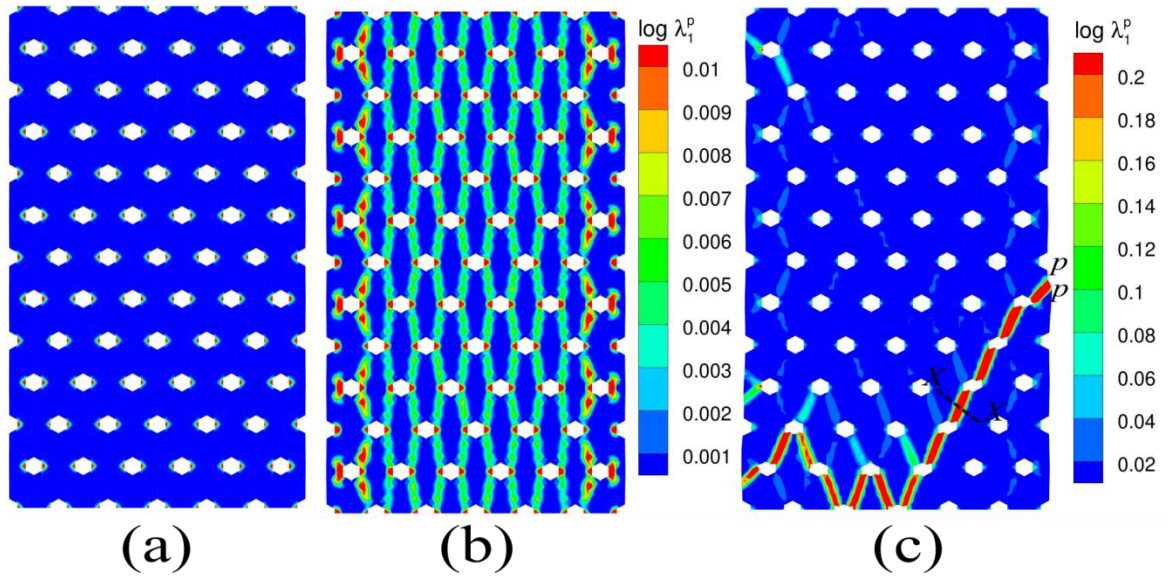

Figure 6.4 Contour plots of maximum principal logarithmic plastic strain, $log\lambda_1^p$ for sample H_4 with $l_c = 31\ nm$ at (a) $E_2 = 0.015$, (b) $E_2 = 0.02$, and (c) $E_2 = 0.03$.

In contrast, the distribution of plastic strain in the specimen H_2 (with moderate cell-wall thickness) remains almost uniform up to E_2 of 0.035 (See Figs. 6.5(a) and (b)). Though

cell-edges experiencing strain localization are getting aligned along a direction closer to the direction of maximum shear stress at significantly large E_2, specimen continues to exhibit multiple shear bands up to $E_2 = 0.045$ (see Fig. 6.5(c)). Interestingly, sample H_1 which has very small t is able to exhibit homogeneous deformation for significantly large E_2 (see Figs. 6.6(a) and (b)). At around, E_2 of 0.08, significant bending of inclined edges of some of the cells can be perceived, but the strain levels inside these edges are less than 10% (refer Fig. 6.6(c)).

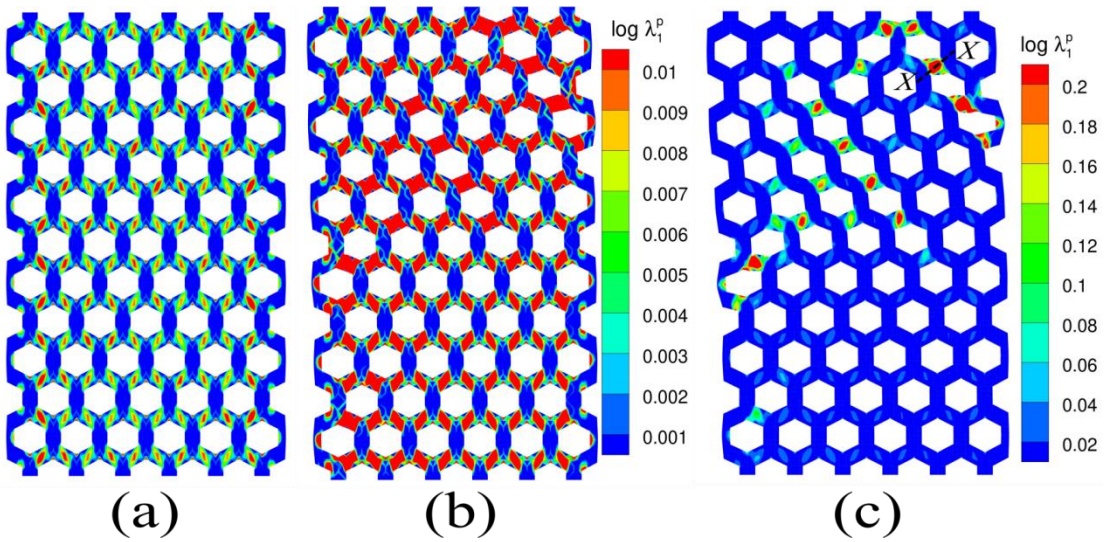

Figure 6.5 Contour plots of maximum principal logarithmic plastic strain, $log\lambda_1^p$ for sample H_2 with $l_c = 31\ nm$ at (a) $E_2 = 0.025$, (b) $E_2 = 0.035$, and (c) $E_2 = 0.045$.

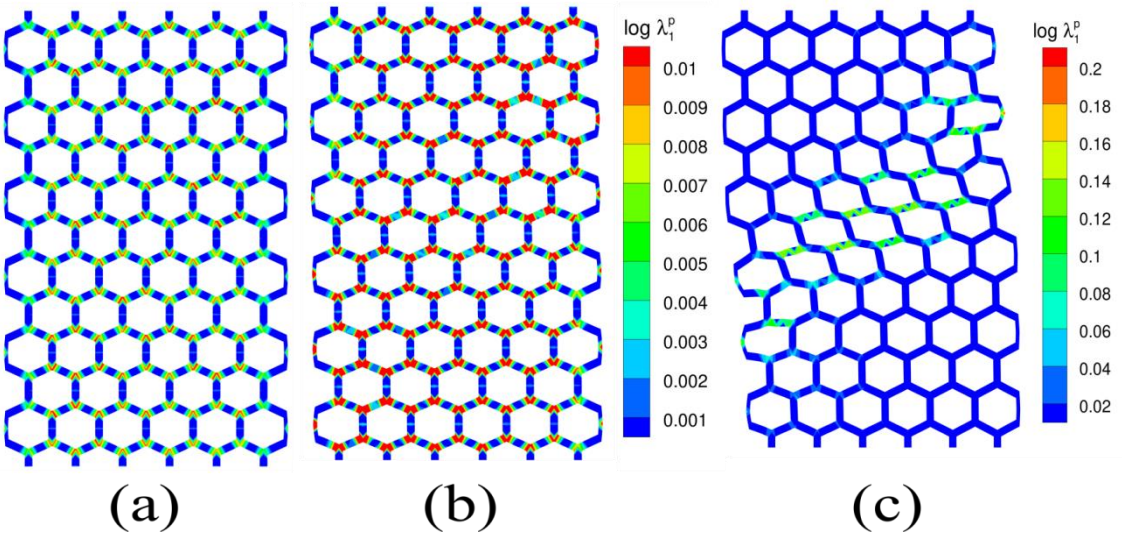

Figure 6.6 Contour plots of maximum principal logarithmic plastic strain, $log\lambda_1^p$ for sample H_1 with $l_c = 31\ nm$ at (a) $E_2 = 0.04$, (b) $E_2 = 0.05$, and (c) $E_2 = 0.08$.

A close observation of Figs. 6.4-6.6 suggests that plastic deformation in a hexagonal cellular structure depends on cell-wall thickness. In the case of sample with large wall thickness (sample H_4), a shear band with large plastic strain spreads from one surface to another surface of the specimen. It must be noted that the failure would take place by crack propagation within a shear band, when the free volume (Shao et al., 2014; Maaß et al., 2015) or shear offset (Schuh et al., 2007) or plastic strain (Anand and Su, 2005; Tandaiya et al., 2009, 2013; Singh and Narasimhan, 2016; Singh et al, 2016) exceeds a critical level. Following the work of Tandaiya et al. (2009), the critical value of $\log \lambda_1^p$ can be taken as 0.2, and thus, it can be deduced from Fig. 6.4(c) that the specimen H_4 would break in two to three pieces at E_2 = 0.03. Since this failure is a macroscopic failure, it is referred to as global failure. In specimen H_2, the values of $\log \lambda_1^p$ have not exceeded beyond 0.2 at every point inside a band connecting two free surfaces of the specimen, however, it has increased above this level in inclined edges of some of the cells (refer Fig. 6.5(c)). Therefore, failure is expected to begin but remain confined to these cells in the sample H_2 at around E_2 of 0.045, which may be considered as local failure. The stages of global and local failures predicted by adopting the critical strain criterion of Tandaiya et al. (2009) are marked by '×' and '*' symbols, respectively, in Fig. 6.2. By contrast, in specimen H_1 with very small cell-wall thickness, plastic deformation is more homogeneous and the magnitude of $\log \lambda_1^p$ < 10% in the inclined edges of the cells. Therefore, in this specimen, bending of the cell edges is preceded by strain localization in a shear band. Thus, the Figs. 6.4-6.6 exhibit two transitions in deformation with reduction in t: the first transition takes place from global failure to local failure of specimen when t is reduced from 12 to 6 nm, while another transition from local failure to prolonged homogeneous deformation (along with the considerable bending of the inclined edges prior to the onset of localization) occurs when t is reduced to 3 nm. These observations corroborate well with the recent MD simulations performed by Zhang et al. (2016) and experimental observations on cellular structure of Zr-based MGs (Sarac and Schroers, 2013b).

In order to get more insights on the evolution of plastic strain in MG cellular samples, line plots of $\log \lambda_1^p$ across a shear band (refer dash line x-x in Figs. 6.4 and 6.5) corresponding to different stages of global strains E_2 are shown against normalized distance, s/l_c for H_2, H_3 and H_4 in Figs. 6.7(a) - (c), respectively. These figures correspond to $l_c = 31\ nm$. The values of $log\lambda_1^p$ inside the cell wall at $E_2 = 0.02$ is very small for all

samples, but rises with increase in E_2 more rapidly in samples H_3 and H_4 than sample H_2. For example, the maximum value of $log\lambda_1^p$ inside the band in samples H_3 and H_4 increases to 0.3 and 0.4, respectively, as E_2 is increased to 0.03, while it remains below 0.05 in sample H_2. The value of $log\lambda_1^p$ inside cell wall of sample H_2 also increases beyond 0.3 at E_2 of 0.035.

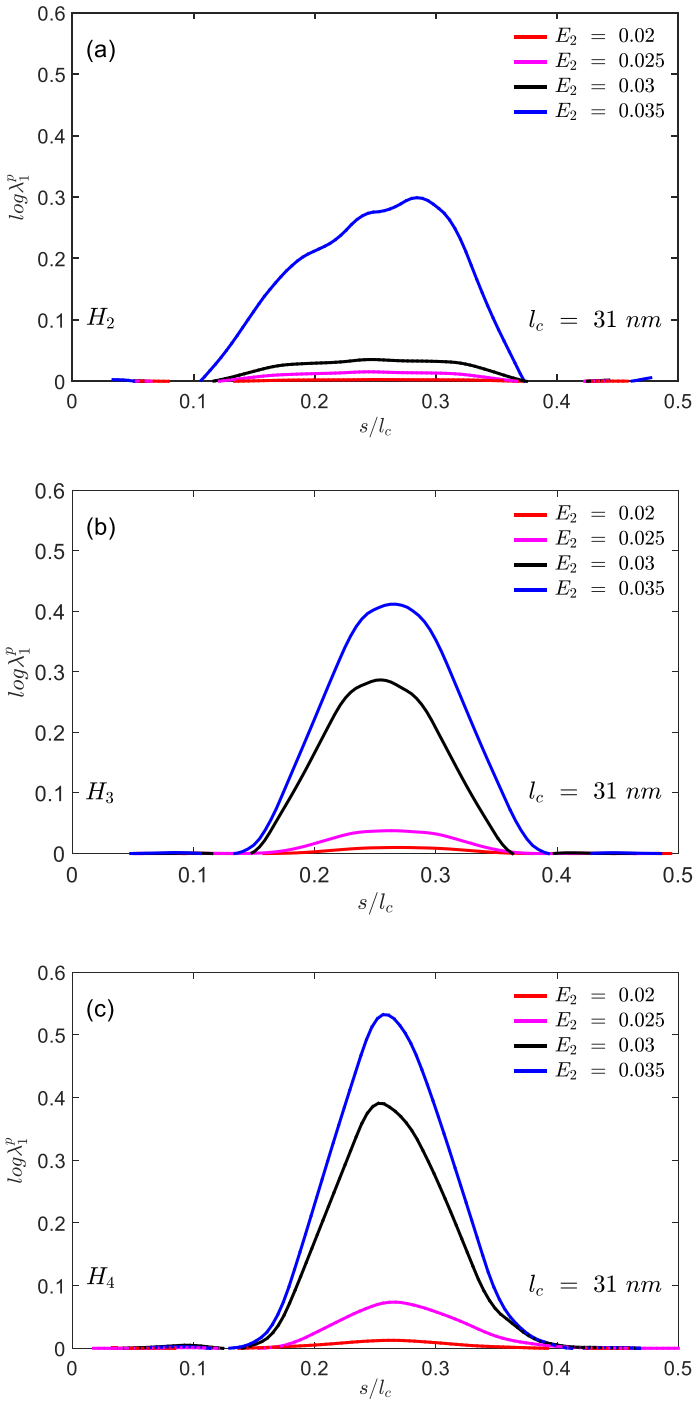

Figure 6.7 Variation of $log\lambda_1^p$ with normalized distance, s/l_c across the shear band for (a) H_2, (b) H_3, (c) H_4 at different level of global strain, E_2 corresponding to $l_c = 31\ nm$.

Thus, these figures suggest that the plastic strain evolves more rapidly in a sample with thicker cell wall. It can also be noticed from these figures that shear band width increases with increase in E_2 and eventually saturates at around $0.25 - 0.28\, l_c$. It must be mentioned that though the shear band width is found to increase with enhancement in l_c, but the scaling of shear band width with l_c could not be verified for higher l_c because the plastic strain spreads over entire wall thickness of the cells which restricts further widening of shear band. On the other hand, shear band width in a monolithic MG is found to scale with l_c and it is around $0.15 - 0.3 l_c$. Thus, shear band width in both MG and their cellular structure is almost identical (around $7 - 9\ nm$) for $l_c = 31\ nm$.

It is important to note from Table-6.1 that for the sample H_4, $t > 9\ nm$, while $t < 7\ nm$ for sample H_1. However, for samples H_2 and H_3, t is almost similar to the shear band width. Since, t in sample H_4 is larger than shear band width corresponding to $l_c = 31\ nm$, strain localizes in cell-walls aligned along approximately the direction of the maximum shear stress leading to the formation of a dominant shear band (refer Fig. 6.4). On the other hand, enough material is not available for localization to take place in the cell-walls of sample H_1 corresponding to $l_c = 31\ nm$, hence sample does not exhibit localized deformation, rather its inclined cell-walls bend in Fig. 6.6. However, t in sample H_2 in Fig. 6.5 is close to the shear band width, therefore some of the cell walls experience large plastic deformation but they don't get aligned as easily as in sample H_4. These observations suggest that the wall thickness of cells in MG honeycomb structures with respect to shear band width in monolithic MG (used to produce them) governs the transitions in the deformation behavior. Since shear band width scales with l_c in MGs, above noted transition in deformation behavior could also be realized by changing the l_c, which is investigated in the following section.

6.4.3 Influence of l_c on the deformation behavior

Fig. 6.8 shows the variation of Σ_2/c_o with respect to E_2 for specimen H_2 corresponding to different values of l_c. It must be mentioned that finite element simulations with higher $l_c = 186\ nm$ showed numerical difficulties beyond the stage of E_2 = 0.045, therefore the curves pertaining to other values of l_c are also plotted up to only E_2 of 0.045. Note from Fig. 6.8, the slope of the stress-strain curves in elastic regime as well as the yield-stress are identical for all the values of l_c. However, the stress beyond the peak-stress stage drops more gradually for higher l_c than that for lower l_c. A similar trend has been observed for other

specimens too suggesting that the increase in l_c retards the strain localization in the cellular MG structures.

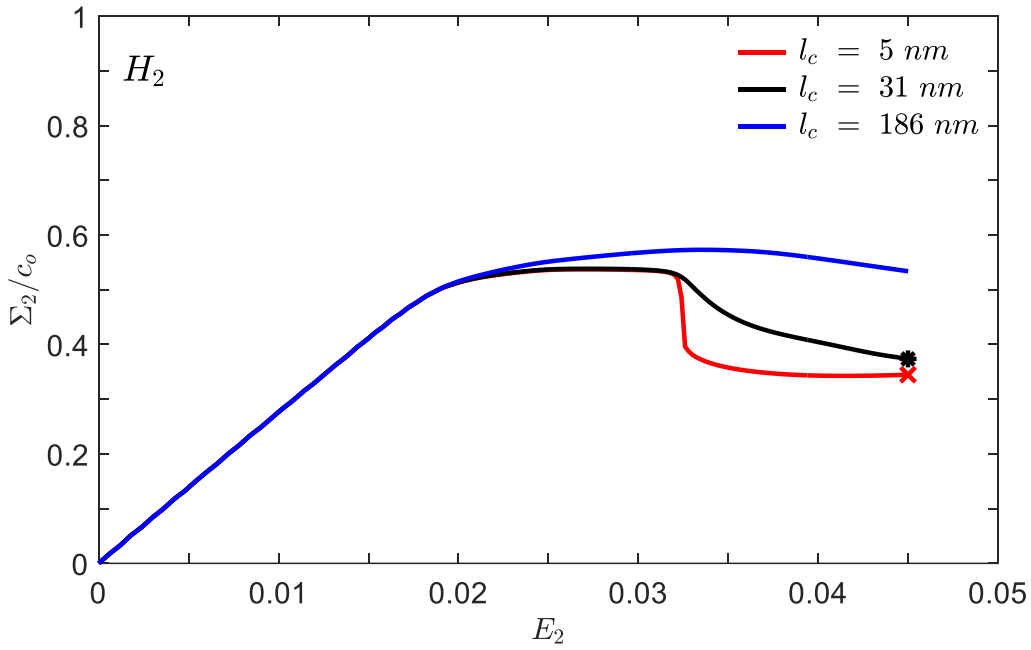

Figure 6.8 Normalized nominal stress versus nominal strain curves pertaining to various values of l_c for sample H_2. The stages of global and local failures are marked by '×' and '*' symbol, respectively.

The above observation can be further confirmed by comparing the spatial distribution of $\log \lambda_1^p$ shown in Figs. 6.9(a) and (b) for $l_c = 186$ and $5\ nm$, respectively. Note that the strain distribution is almost homogeneous for higher l_c in Fig. 6.9(a), while it has localized in a dominant shear band for same cellular structure but with very low l_c, in Fig. 6.9(b). Since $\log \lambda_1^p$ has exceeded beyond 0.2 at every point inside the band in Fig. 6.9(b), sample with l_c of $5\ nm$ is expected to fail globally due to crack propagation in a dominant shear band (Tandaiya et al., 2009). The stages corresponding to global and local failures are marked by '×' and '*' symbols, respectively, in Fig. 6.8. Further, recall from Fig. 6.5(c) that the specimen with similar cellular structure, but with intermediate level of $l_c = 31\ nm$, exhibits local failure with damage confined to few cells. Thus, Figs. 6.9 and 6.5 *confirms that a transition in deformation behavior from global failure to local failure takes place when* l_c *is enhanced from a very low value to a moderate level. However, localization is delayed up to a large macroscopic strain for sufficiently higher* l_c. As pointed out in the previous section that the strain localization can also be delayed by reducing the cell wall thickness while keeping l_c fixed. Thus, it can be deduced from the present analysis that strain localization in a MG

cellular structure can be retarded either by reducing the cell wall thickness or by increasing the material length scale l_c. *In other words, transition in the deformation behavior from global failure to local failure and then to prolonged homogenous deformation is governed by cell-wall thickness with respect to the intrinsic material length (i.e., the ratio t/ l_c).*

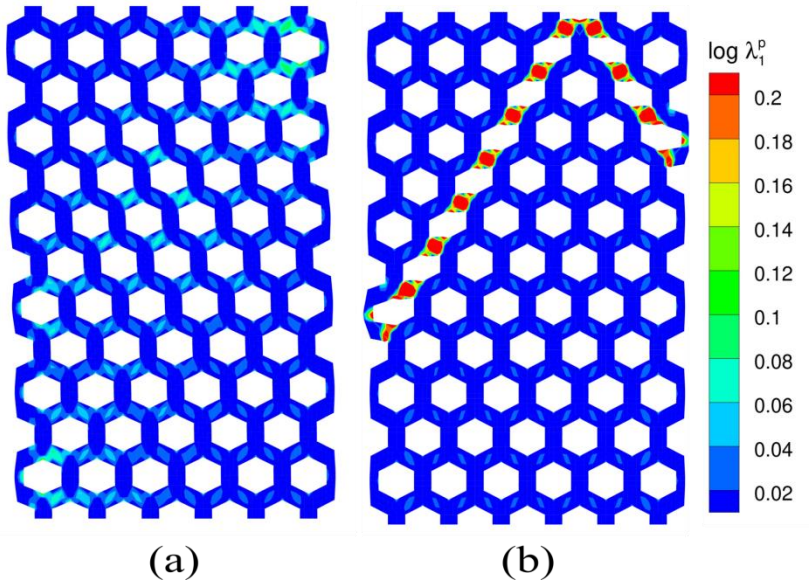

Figure 6.9 Contour plots of $log\lambda_1^p$ for sample H_2 at nominal strain, E_2 of 0.045 for (a) $l_c = 186\ nm$ and (b) $l_c = 5\ nm$.

The mechanistic reasons for above noted influence of l_c and t on the deformation behavior of MG cellular structures can be understood by analyzing the spatial distribution of interaction stress τ_{int}. Therefore, contours plots of τ_{int}/c_0 at E_2 of 0.02 for specimen H_2 pertaining to two different values of $l_c = 31$ and $186\ nm$ are displayed in Figs. 6.10 (a) and (b), respectively. Due to large stress concentration, plastic yielding commences causing free volume to evolve near the corners of cells at early stages than other positions. As a result, a large free volume (or STZs concentration) gradient develops in the cell walls, leading to the evolution of interaction stress between flow defects (STZs) (refer Eq. (5.2)). Note from Fig. 6.10(a) that τ_{int} is positive at corners and inside a narrow band connecting corners of cells in two neighboring rows, while it is negative at other locations. When l_c is increased, τ_{int} inside these bands becomes more positive, while it becomes more negative outside the bands, as can be seen by comparing Figs. 6.10(a) and (b). Since, the positive valued τ_{int} retards further development of plastic strain, while $\tau_{int} < 0$ promotes the evolution of plastic strain (refer Eq. (5.2)). Therefore, it can be understood from Figs. 6.10 (a) and (b) that the increase in l_c retards the evolution of plastic strain near the corners and inside the band connecting these

corners, while it promotes the spread of plasticity outside these regions in a MG cellular structure. In other words, enhancement in l_c retards the shear localization and makes the distribution of plastic strain more uniform. Consequently, strain localization is delayed causing homogeneous deformation to prevail up to a larger value of E_2 in a sample with larger l_c. The contour plots of τ_{int} for sample H_1 shown in Fig. 6.10(c) reveals that the volume fraction of material experiencing negative τ_{int} is more than that in sample H_2 (refer Fig. 6.10(a)). In addition, the probability of triggering enough STZs to align for shear localization is less in sample H_1 with thinner cell wall. As a result, negative τ_{int} is able to make plastic strain distribution uniform in sample H_1 leading to delayed localization in this sample even for low l_c.

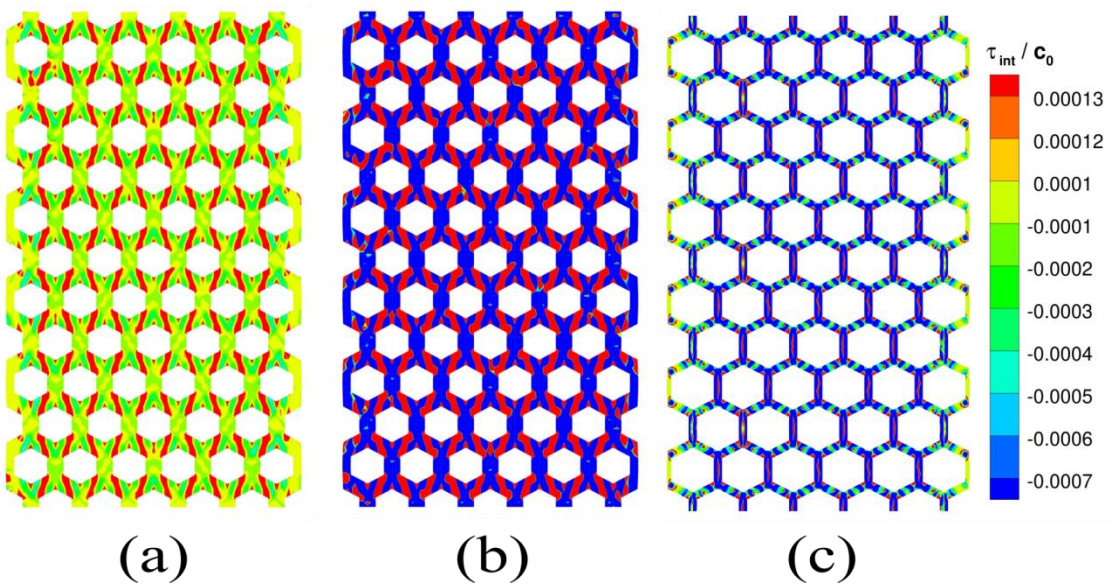

Figure 6.10 Contour plots of normalized interaction stress, τ_{int}/c_0 at $E_2 = 0.02$ for sample H_2 with (a) $l_c = 186\ nm$, (b) $l_c = 31\ nm$, and (c) corresponding plots at $E_2 = 0.03$ for sample H_1 with $l_c = 31\ nm$.

At this juncture, it must be mentioned that Zhang et al. (2009) have shown from their MD simulations that the shear band width in CuZr metallic glass depends on their compositions. Further, another atomistic simulation performed by Zhong et al. (2016) reported critical thickness of sample corresponding to transition from localized to homogeneous deformation depends on the glass composition. Moreover, the continuum simulations of Dutta et al. (2018) have confirmed that change in l_c in model of Thamburaja (2011) produces qualitatively similar effects in the deformation behavior as to obtain by changing the composition of glass in the atomistic simulations. Thus, it can be considered

that l_c value in the non-local plasticity model of Thamburaja (2011) pertains to specific composition of glass, and the influence of the composition on the mechanical response of the glass can be captured by changing l_c in the finite element simulations. *In the view of above discussion, it can be deduced from present continuum analysis that the threshold value of cell-wall thickness will be lower in the cellular structure of a glass which exhibits thinner shear band, while it will be higher for composition showing wider shear band.* In other words, design of the cellular structure with glass composition exhibiting wider shear band is more suitable.

6.4.4 Influence of specimen size on the deformation behavior

In order to study the influence of specimen size on the deformation behavior of the MG cellular structure, simulations are performed on a smaller specimen ($54 \times 93.5\ nm$) with the arrangement of cells and the cell-wall thickness identical to that in sample H_2. The sample sizes 54×93.5 and $108 \times 187\ nm$ (used in previous section) are referred to as Specimen A and Specimen B, respectively, in the following discussion. Fig. 6.11 shows normalized macroscopic stress Σ_2/c_0 versus global strain E_2 for both the specimens corresponding to $l_c = 186\ nm$. It can be seen that the stress-strain curves differ marginally suggesting marginal influence of specimen size on the mechanical response of MG cellular structures. Further, the contour plots of $\log \lambda_1^p$ in both the samples are displayed in Fig.6.12 at two levels of $E_2 = 0.02$ and 0.045. This figure shows almost similar trend in the evolution of plastic strain in both the samples A and B. As mentioned in previous section that the simulations with very large $l_c = 186\ nm$ could not be continued further beyond $E_2 = 0.045$ due to numerical difficulties. Therefore, it is concluded from Figs. 6.11 and 6.12 that *the deformation behavior of hexagonal cellular MGs up to moderate levels of applied global strain is moderately affected by specimen size.*

In summary, the deformation behavior of nanoscale MG hexagonal cellular structures subjected to plane strain compressive loading has been investigated through finite element simulations using thermodynamically consistent non-local plasticity model for MGs. The results not only collaborate well with the experiments (Sarac and Schroers, 2013b) and atomistic simulations (Zhang et al., 2016), but also address the important issues related to the underlying deformation mechanism.

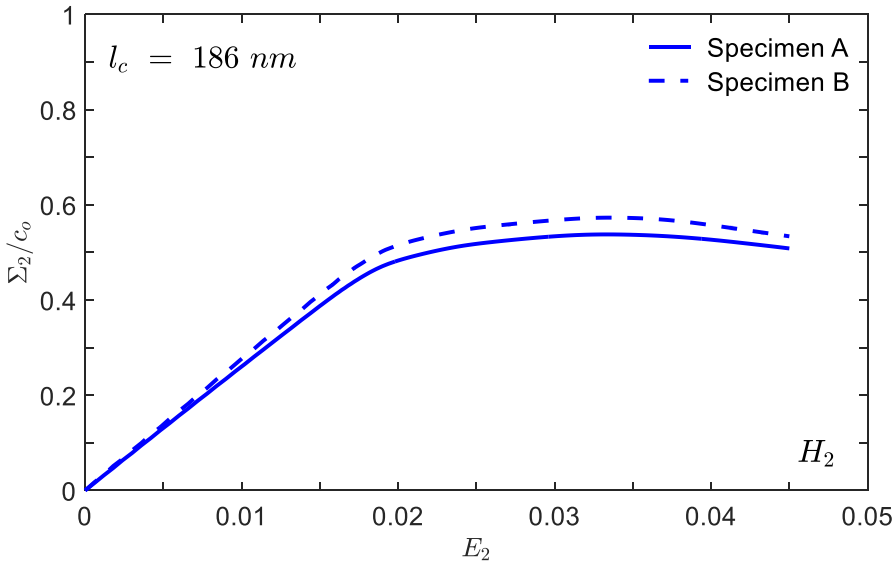

Figure 6.11 Normalized macroscopic stress versus global strain curves for sample H_2 with $l_c = 186\ nm$ corresponding to specimen A and specimen B.

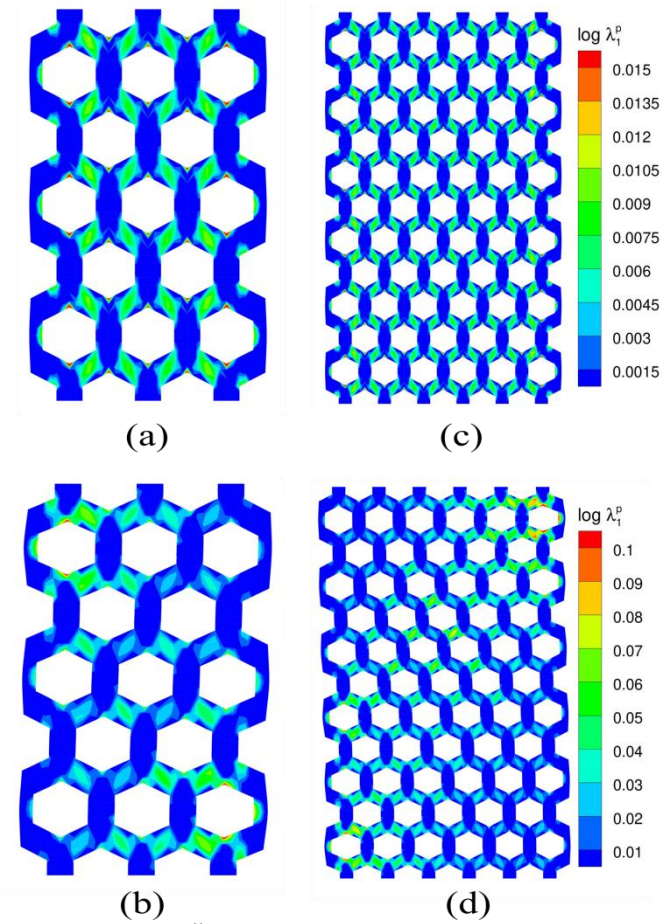

Figure 6.12 Contour plots of $log\lambda_1^p$ for specimen A having arrangements of cells similar to H_2 with $l_c = 186\ nm$ at (a) $E_2 = 0.02$ and (b) $E_2 = 0.045$. Corresponding plots for specimen B are shown in (c) and (d).

CHAPTER 7

Conclusion

The important conclusions from the work reported in Chapter 2-6 are summarized in this chapter.

7.1 Investigation of pressure sensitive plastic flow in nanoglasses from finite element simulations.

In chapter 2, finite element simulations of indentation on $Sc_{75}Fe_{25}$ NGs and MGs have been analyzed using extended Drucker Prager and Von-Mises plasticity model. The important conclusions of this work are as follows.

- Simulation indentation $P-h$ curve obtained by using Von- mises plasticity model deviate significantly from experimental data. While, $P-h$ curve obtained through extended Drucker Prager plasticity model shows good agreement with experimental data suggesting that yield phenomena in $Sc_{75}Fe_{25}$ NGs and MGs is characterized more accurately by pressure sensitive extended Drucker Prager plasticity model.
- The value of pressure sensitive index, α for NGs and MGs is determined by fitting the recent experimental data. In fact, α for NGs is found to be around three time higher than that of MGs of identical composition suggesting indentation response of the former is more pressure sensitive than the latter. In other words, NGs is harder than MGs of identical composition. In addition, α for glassy interface is much higher than the glassy grain of NG.
- The present study reveals that plastic zone size and constraint factor, C for NGs is larger than for MGs of identical composition because of higher α in NGs.

7.2 Investigation of softening induced indentation size effect in nanoglass and metallic glass

In chapter 3, microindentation as well as nanoindentation experiments are performed on $Cu_{60}Zr_{40}$ NGs and MGs. In addition, the complementary finite element simulations of indentations are performed by employing the finite strain viscoplastic constitutive theory for amorphous metals. The simulations results are in good agreement with experiments. The important conclusions as follows:

- SEM images of micrographs obtained from the bonded interface experiments show that shear bands in MG are smooth and almost semi-circular in shape, while wavy shear bands form in NG. Further, the primary shear band densities in the MG are higher than that in NG. However, the plastic zone size below the indenter is larger in NG than that in MG.
- The AFM imaging of impressions generated through nanoindentation reveals almost homogeneous plastic deformation around the indent in NGs, while it shows discrete shear bands for MG.
- NG exhibit almost smooth indentation load, P vs. depth, h curves, while MG shows serrated curves. The hardness, H of NGs is higher than MGs for all the applied loads, and it decreases more rapidly with increase in P in the latter than the former. Thus, the indentation size effect (ISE) in MG is more profound than that in NG.
- The less pronounced ISE in NG than MG is because of slower free volume generation leading to slower softening during indentation in the former than the latter. The finite element simulations show that the value of friction coefficient, μ for NG is higher than MG due to higher μ for interfaces in the former. Also, the higher μ retards the free volume generation and hence softening resulting in less pronounced ISE in NG.

7.3 Mixed mode (I and II) fracture behavior in nanoglass and metallic glass.

In chapter 4, the stationary crack tip plasticity in NG and MG under the mixed mode (I and II), plane strain, SSY condition has been investigated through finite element simulations using a constitutive model for MGs proposed by Anand and Su (2005). The results collaborate well with the observations made from experiments and continuum simulations of fracture on bulk MGs. The salient conclusions are summarized below:

- The plastic strains ahead of the crack tip are more diffused in NGs than that of MGs. Also, the plastic zone in both NGs and MGs appears to rotate in anticlockwise direction with increase in mode I contribution.
- The spread of the plastic strain ahead of the notch tip reduces with increase in mode mixity, M^e. However, it is always longer in NG than that in MG, irrespective of the values of M^e. Further, the plastic zone size in NG is significantly larger than that in MG for identical loading conditions.

- The notch tip of both the alloys, under to mixed mode loading, deforms in a shape with a blunted lower part and sharpened upper part. Further, the stretching and bulging forward of the lower part of the notch is more pronounced in the case of NG than MG, while the upper part of the notch profile is sharper in the case of latter.
- The notch opening displacement, δ_I and notch shear displacement, δ_{II} increase linearly with normalized energy release rate $\frac{J}{c_{og} b_0}$ for both alloys. Further, the magnitude of δ_I and δ_{II} in NG is always slightly higher than that in MG irrespective of mode-mixity.
- The strain-based fracture criterion predicts that NGs may not show significant higher fracture toughness in comparison to MG with identical composition, though they exhibit significant larger tensile ductility.

7.4 Finite element analysis of tensile deformation of nanoglass-metallic glass laminate composites

In chapter 5, the deformation behavior of NG-MG laminate composites subjected to plane strain tensile loading has been investigated through finite element simulations using non-local plasticity model. The results are in good qualitative agreement with recent atomistic simulations, and also provide insights about the underlying deformation mechanism. The important conclusions of this work are as follows.

- The peak stress, $\hat{\Sigma}$ attained in NG-MG nanolaminate composite are lower than monolithic composites and decreases further with increase in NG layer thickness, t_{NG}.
- The peak stress $\hat{\Sigma}$ decreases rapidly as volume fraction $V_{f,MG}$ of MG layer in laminate composite with single NG layer is reduced from 1 to 0.7, while it changes marginally for further decrease in $V_{f,MG}$. Thus $\hat{\Sigma}$ don't follow rule of mixture which is found to be true, irrespective of intrinsic material length, l_c or composition of glass.
- The volume fraction of the material in MG layer undergoing plastic deformation $V_{f,MG}^{y}$ near the peak stress stage reduces drastically as volume fraction $V_{f,MG}$ of MG layer in NG-MG nanolaminate composites is decreased from 1 to 0.7, while it remains almost unaltered for further reduction in $V_{f,MG}$. Thus, both $\hat{\Sigma}$ and $V_{f,MG}^{y}$ decreases with $V_{f,MG}$ almost in a similar manner signifying that peak stress is mainly governed by

$V_{f,MG}^{y}$ and weakly by $V_{f,MG}$, therefore peak stress in laminate composite with single NG layer don't follow of mixture.

- Shear band width scales with the intrinsic material length, l_c, associated with the interaction stress, τ_{int} between flow defects such as STZs, and it is around $0.08-0.12$ l_c irrespective of t_{NG}.
- Spatial distribution of τ_{int} plays a central role in the deformation behavior of laminate composites. Positive valued τ_{int} prevailing inside glassy interfaces retards strain localization, while negative τ_{int} in glassy grains and MG layer promote homogeneous deformation. When l_c is increased, τ_{int} becomes more positive inside interfaces (in NG layer as well as between NG and MG layer), whereas it becomes more negative inside grains and MG layer. Thus, enhancement in l_c delays localization of plastic strain.
- The deformation behavior of laminate composites transitions from localized to super plastic flow when MG layer thickness, t_{MG} is decreased below a threshold level which depends on the material length l_c or composition of the glass. In other words, t_{MG} with respect to intrinsic material length l_c governs the transition.

7.5 Finite element analysis of deformation and failure mechanisms in nanoscale hexagonal cellular structures of metallic glasses

In chapter 6, the deformation behavior of nanoscale MG hexagonal cellular structures subjected to plane strain compressive loading has been investigated through finite element simulations using thermodynamically consistent non-local plasticity model for MGs. The results collaborate well with the experiments and atomistic simulations. The important conclusions are as follows:

- The peak stress, $\hat{\Sigma}$ and the slope E_s of the stress-strain curves for MG cellular structures are lower than monolithic MG, and they decrease further with reduction in relative density, ρ^*/ρ (or cell wall thickness t).
- The rise in the volume fraction of material experiencing plastic deformation V_f^y near peak stress stage and $\hat{\Sigma}$ with increase in ρ^*/ρ follow a similar trend which suggests that $\hat{\Sigma}$ in cellular MG structure is mainly governed by V_f^y and weakly by ρ^*/ρ. Therefore, the variation of $\hat{\Sigma}$ with ρ^*/ρ is nonlinear.

- The cellular MG structures exhibit two transitions in the deformation behavior with decrease in t. The first transition takes place from global failure due to crack propagation in a dominant shear band to local failure with damage confined to few cells of specimen when t is reduced from a large value to become similar to shear band width in monolithic MG with identical composition. However, another transition from local failure to prolonged homogeneous deformation with considerable bending of the inclined edges prior to localization occurs when t is reduced much below the shear band width.
- Spatial distribution of τ_{int} plays an important role in the evolution of plastic strain in MG cellular structures. Positive valued τ_{int} prevailing at corners and in a narrow band connecting corners of the neighbouring cells in parallel rows retards the shear localization while negative valued τ_{int} prevailing in the remaining areas assists the spread of plasticity in these regions. When l_c is increased, the positive τ_{int} become more positive near corners and bands connecting these corners, while negative τ_{int} becomes more negative in remaining areas. Consequently, enhancement in l_c retards the shear localization and promotes homogeneous deformation.
- The transition in the deformation behavior from global failure to local failure and then to prolonged homogenous deformation is governed by the ratio t/l_c.
- The moderate change in specimen size of the MG cellular structures has a marginal effect on their deformation behavior up to moderate levels of E_2.

7.6 Scope for future study

The present work is focused on understanding the deformation behavior of NG and MG structures. The insights gained from the present study can provide the necessary background to carry out further research in this area. Some of the specific studies are suggested below.

- The experiments have shown that the plastic flow in MGs is sensitive to normal stress/pressure at temperature below glass transition temperature, T_g (Prasad et al, 2007). In Chapter 2 and 3, the pressure sensitive plastic flow in NGs is investigated at room temperature. In future, this study can be extended to investigate the effect of temperature on the pressure sensitivity index, α in NGs.

- NGs and MGs have been shown to exhibit an intrinsic material length scale, l_c associated with the stresses arising due to the interaction between flow defects (STZs) (Thamburaja, 2011; Singh et al. 2014). The influence of l_c on the size dependent indentation response in NGs and MGs have not been investigated till now. Such studies would help understanding the physics of ISE in these alloys better. Therefore, continuum simulations of indentation response in NGs and MGs can be performed by employing a non-local plasticity model such as model of Thamburaja (2011).
- Recently, Guo et al. (2019) investigated nanoindentation creep behavior in Ni- based NG and MG at room temperature. They reported significant creep deformation in NG than MG of identical composition. It would be interesting to perform such studies on Cu-based NGs and MGs also to see if similar trend can be observed in this composition as well.
- In chapter 4, the effect of fracture toughness, J_c on mode mixity, M^e was predicted through continuum simulations. In future, mixed mode fracture experiments can be conducted to confirm the trend reported in this chapter.
- The notch size is kept constant in the analysis performed in Chapter 4. This study can be extended further to analyze the effect of notch size on the dependence of J_c on M^e.

APPENDIX A

A. 1 Expanding cavity model

Narasimhan (2004) modified expanding cavity model of Johnson (1970) to study the indentation mechanics of pressure sensitive solids. Key equations of the model are given below:

The hydrostatic pressure p inside core is related with plastic zone size r_p as:

$$p = D\sigma_y^c \left(\frac{r_p}{a}\right)^{2q} - \frac{B}{q}\sigma_y^c, \tag{A.1}$$

where, parameters B, q and D are given by:

$$B = \frac{1-\tan\frac{\alpha}{3}}{1+\tan\frac{\alpha}{3}}; q = \frac{\tan\alpha}{1+2\tan\frac{\alpha}{3}} \; and \; D = \frac{B}{q} + \frac{2}{3}\left(1-\tan\frac{\alpha}{3}\right). \tag{A.2}$$

The plastic zone size, r_p evolves with contact radius, a as:

$$\frac{\sigma_y^c}{E}\left[2qM\left(\frac{r_p}{a}\right)^{2q-1} - \frac{3L}{2}\left(\frac{r_p}{a}\right)^{s-1}\right]\frac{dr_p}{da} = \frac{\tan\beta}{2} \tag{A.3}$$

Note that for initial stages of loading, only spherical tip of 'Berkovich equivalent' conical indenter makes contact with the sample (refer schematic shown in Fig. A(a)), while surface of conical part of the indenter also in makes contact with the specimen for larger indentation depth (Fig. A1(b)). Thus, following Johnson (1985), Eq. (A. 3) can be written as:

$$\frac{\sigma_y^c}{E}\left[2qM\left(\frac{r_p}{a}\right)^{2q-1} - \frac{3L}{2}\left(\frac{r_p}{a}\right)^{s-1}\right]\frac{dr_p}{da} = \begin{cases} \frac{a}{R} & for\ a < a_{cr} \\ \frac{\tan\beta}{2} & for\ a > a_{cr} \end{cases} \tag{A.4}$$

Eq. (A. 4) is integrated from a contact radius a_y pertaining to initial yielding by employing Runge-Kutta integration algorithm, and r_p is determined as a function of a. Stress components in spherical coordinates are given by:

$$\sigma_{zz} = -(p + \bar{\sigma}), \tag{A.5}$$

$$\sigma_{rr} = \sigma_{\theta\theta} \simeq -\left(p - \frac{\bar{\sigma}}{2}\right). \tag{A.6}$$

Here, $\bar{\sigma}$ is defined as:

$$\bar{\sigma} = \frac{2\sigma_y^c}{3}\left[1 + \tan\alpha\left(\frac{p}{\sigma_y^c} - \frac{1}{3}\right)\right] \tag{A.7}$$

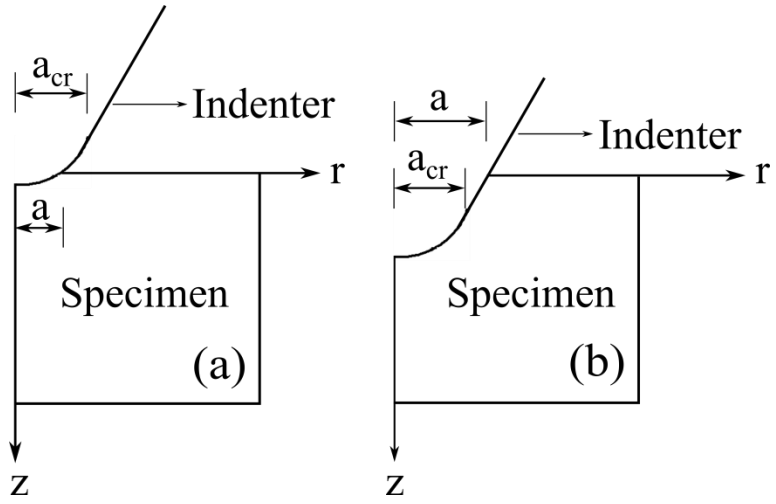

Figure A1 Schematic showing (a) spherical tip of the 'Berkovich equivalent' conical indenter in contact with the specimen. (b) Conical surface of the 'Berkovich equivalent' conical indenter also in contact with the specimen.

A. 2 Calculation of Young's modulus for iso-strain and iso-stress conditions

If E_g denote Young's modulus of glassy grains, V_f^g volume fraction of glassy grains, E_i Young's modulus of glassy interfaces and V_f^i volume fraction of glassy interfaces, Young's modulus, E_{NG} for nanoglass can be written employing iso-strain conditions as:

$$E_{NG} = V_f^g E_g + V_f^i E_i. \tag{A.8}$$

For NG1, $E_{NG} = 69.35\ Gpa$ (Liu et al., 2018), $E_g = 74Gpa$ (Franke et al., 2014),$V_g^f = 0.73$ and $V_f^i = 0.27$. Thus, $E_i = 56.77Gpa \approx 57Gpa$.

For iso-stress condition, E_{NG} can be expressed as:

$$E_{NG} = \frac{E_g E_i}{V_f^g E_g + V_f^i E_i}, \tag{A.9}$$

which results to $E_i = 59.5\ Gpa$.

REFERENCES

Abaqus 2017, Theory manuals, Version 6.5. Hibbit, Karlsson and Soresen Inc., RI, USA.

Adibi S., Sha Z. D., Branicio P. S., Joshi S. P., Liu Z. S., Zhang Y. W. (2013), A transition from localized shear banding to homogeneous superplastic flow in nanoglass, *Applied Physics Letters*, 103, 211905 (doi.org/10.1063/1.4833018).

Adibi S., Branicio P. S., Zhang Y.W., Joshi S.P. (2014), Composition and grain size effects on the structural and mechanical properties of CuZr nanoglasses, *Journal of Applied Physics*, 116, 043522 (doi.org/10.1063/1.4891450).

Adibi S. Branicio P. S., Ballarini R. (2016), Compromising high strength and ductility nanoglass-metallic glass nanolaminates, *RSC Advances*, 6, 13548-13553(doi.org/10.1039/C5RA24715B).

Adjaoud O., Albe K. (2019), Influence of microstructural features on the plastic deformation behavior of metallic nanoglasses, *Acta Materialia*, 168, 393-400 (doi.org/10.1016/j.actamat.2019.02.033).

Aliaga L. C. R., Beringues J. F., Surinach S., Baro M.D., Kiminami C. S., Bolfarini C., Botta W. J., Vinas J. S. (2013), Comparative study of nanoindentation on melt-spun ribbon and bulk metallic glass with Ni60Nb37B3 composition, *Journal Materials Research*, 28, 2740-2746 (doi.org/10.1557/jmr.2013.260).

Anand L. and Su C. (2005), A theory for amorphous viscoplastic materials undergoing finite deformations, with application to metallic glasses, *Journal of the Mechanics and Physics of Solids*, 53(6), 1362-1396 (doi.org/10.1016/j.jmps.2004.12.006).

Anand L., Su C. (2007), A constitutive theory for metallic glasses at high homologous temperatures, *Acta Materialia*, 55, 3735-3747 (doi.org/10.1016/j.actamat.2007.02.020).

Aoki S., Kishimoto K., Yoshida T., Sakata M., Richard H. A. (1990), Elastic-Plastic fracture behavior of an aluminum alloy under mixed mode loading, *Journal of Mechanics and Physics of Solids*, 38, 195-213 (doi.org/10.1016/0022-5096(90)90034-2).

Argon A. S. (1979), Plastic deformation in metallic glasses, *Acta Metallurgica*, 27, 47-58 (doi.org/10.1016/0001-6160(79)90055-5).

Bardia P., Narasimhan R. (2006), Characterisation of pressure-sensitive yielding in polymers, *Strain*, 42, 187-196 (doi.org/10.1111/j.1475-1305.2006.00272.x).

Bei H., Xie S., George E. P. (2006), Softening cause by profuse shear banding in a bulk metallic glass, *Physical Review Letters*, 96, 105503 (doi.org/10.1103/PhysRevLett.96.105503).

Bhattacharyya A., Singh G., Prasad K. E., Narasimhan R., Ramamurty U. (2015), On the strain rate sensitivity of plastic flow in metallic glasses, *Materials Science and Engineering A*, 625, 245-251 (doi.org/10.1016/j.msea.2014.12.004).

Bhowmick R., Raghavan R., Chattopadhyay K., Ramamurty U. (2006), Plastic flow softening in a bulk metallic glass, *Acta Materialia*, 54, 4221-4228 (doi.org/10.1016/j.actamat.2006.05.011).

Borg U. (2007), Strain gradient crystal plastisity effects on flow localization, *International Journal of Plasticity*, 23, 1400-1416 (doi.org/10.1016/j.ijplas.2007.01.003).

Bruck H. A., Rosakis A. J., Johnson W. L. (1996), The dynamic of compressive behavior of berylliumbearing bulk metallic glasses, *Journal of Materials Research*, 11, 503-511 (doi.org/10.1557/JMR.1996.0060).

Chen J., Ghosh S. (2013b), Computational modelling of plastic deformation and shear banding in metallic glasses, *Computational Materials Science*, 69, 494-504 (doi.org/10.1016/j.commatsci.2012.12.014).

Chen N., Frank R., Asao N., Louzguine-Luzgin D. V., Sharma P., Wang J. Q., Wang G. Q., Ishikawa Y., Hatakeyama N., Lin Y. C., Esashi M., Yamamoto Y., Inoue A. (2011), Formation and properties of Au-based nanograined metallic glasses, *Acta Materialia*, 59, 6433-6440 (doi.org/10.1016/j.actamat.2011.07.007).

Chen N., Louzguine-Luzgin D. V., Xie G. Q., Sharma P., Perepezko J. H., Esashi M., Yavari A. R., Inoue A. (2013), Structural investigation and mechanical properties of a representative of a new class of materials: Nanograined metallic glasses, *Nanotechnology*, 24, 045610 (doi.org/10.1088/0957-4484/24/4/045610).

Chen S. H., Tang H. H., Zheng H. M., Chang W. J., Zhang J. C., Yang H. D., Zhang Z. F., Yu D. B., Chan K. C., Liu R. P. (2019), Achieving stable plastic flow in a Zr-based bulk

metallic glass undet tailored mixed-mode (I/II) loading conditions, *Materials Science and Engineering A*, 772, 138695(doi.org/10.1016/j.msea.2019.138695).

Chen W., Liu Z., Robinson H. M., Schroers J. (2014), Flaw tolerance vs. performance: a tradeoff in metallic glass cellular structures, *Acta Materialia*, 73, 259-274 (doi. org/10.1016/j.actamat.2014.04.026).

Conner R. D., Rosakis A. J., Johnson W. L., Owen D. M. (1997), Fracture toughness deternination for Be- bearing bulk metallic glass, *Scripta Materialia*, 37, 1373-1378 (doi.org/10.1016/S1359-6462(97)00250-9).

Concustell A., Sort J., Alcala G., Mato S., Gebert A., Eckert J., Baro M. D., (2005), Plastic deformation and mechanocal softening of $Pd_{40}Cu_{30}Ni_{10}P_{20}$ bulk metallic glass during nanoindentation, *Journal of Materials Research*, 20, 2719-2725 (doi.org/10.1557/JMR.2005.0331).

Dutta T., Chauniyal A., Singh I., Narasimhan R., Thamburaja P., Ramamurty U. (2018), Plastic deformation and failure mechanisms in nano-scale notched metallic glass specimens under tensile loading, *Journal of the Mechanics and Physics of Solids*, 111, 393-413 (doi.org/10.1016/j.jmps.2017.11.011).

Dutta T., Chauniyal A., Singh I., Narasimhan R. (2020), Numerical investigation of tensile response of notched bulk metallic glass composite specimens, *Modelling and Simulation in Materials Science and Engineering*, 28(8), 085002 (doi.org/10.1088/1361-651X/abb98f).

Fang J. X., Vainio U., Puff W., Wurschum R., Wang X. L., Wang D., Ghafari M., Jiang F., Sun J., Hahn H., Gleiter H. (2012), Atomic structure and structural stability of $Sc_{75}Fe_{25}$ nanoglasses, *Nano Letters*, 12, 458-463 (doi.org/10.1021/nl2038216).

Flores K. M., Dauskartdt R. H. (2006), Mode II fracture behavior of Zr- based bulk metallic glass, *Journal of the Mechanics and Physics of Solids*, 54, 2418-2435 (doi.org/10.1016/j.jmps.2006.05.003).

Fornell J., Concustell A., Surinach S., Li W. H., Cuadrado N., Gebert A., Baro M. D., Sort J. (2009), Yielding and intrinsic plasticity of Ti-Zr-Ni-Cu-Be bulk metallic glass, *International Journal of Plasticity*, 25,1540-1559 (doi.org/10.1016/j.ijplas.2008.11.002).

Franke O., Leisen D., Gleiter H., Hahn H. (2014), Thermal and plastic behavior of nanoglasses, *Journal of Materials research*, 29, 1210-1216 (doi.org/10.1557/jmr.2014.101).

Gao X. L., Jing N., Subhash G. (2006), Two new expanding cavity models for indentation deformations of elastic strain-hardening materials, *International Journal of Solids and Structures*, 43, 2193-2208 (doi.org/10.1016/j.ijsolstr.2005.03.062).

Gao Y. F. (2006), An implicit finite element method for simulating inhomogeneous deformation and shear bands of amorphous alloy based on the free volume model, *Modelling and Simulation in Materials Science and Engineering*, 14, 1329-1345 (doi.org/10.1088/0965-0393/14/8/004).

Gerberich W. W., Tymiak N. I., Grunlan J. C., Horstemeyer M. F., Baskes M. I. (2002), Interpretations of indentation size effects, *Journal of Applied Mechanics*, 69, 433-442 (doi.org/10.1115/1.1469004).

Ghosal A. K., Narasimhan R. (1994), A finite element analysis of mixed mode fracture initiation by ductile failure mechanisms, *Journal of the mechanics and Physics of Solids*, 42, 953-978 (doi.org/10.1016/0022-5096(94)90080-9).

Gleiter H. (2013), Nanoglasses: a new kind of noncrystalline materials, *Beilstein Journal of Nanotechnology*, 4, 517-533 (doi.org/10.3762/bjnano.4.61).

Gurtin M. E., Fried E., Anand L. (2010), The mechanics and thermodynamics of continua, Cambridge University Press, New York.

Guo C., Fang Y., Wu B., Lan S., Peng G., Wang X. L., Hahn H., Gleiter H., Feng T. (2017), Ni-P nanoglass prepared by multi-phase pulsed electrodeposition, *Materials Research Letters*, 5, 293-299 (doi.org/10.1080/21663831.2016.1264495).

Guo C., Fang Y., Chen F., Feng T. (2019), Nanoindentation creep behavior of electrodeposited Ni-P nanoglass flims, *Intermetallics*, 110, 106480 (doi.org/10.1016/j.intermet.2019.106480).

Hinton E., Campbell J. S. (1974), Local and global smoothing of discontinuous finite element functions using a least squares method, *International Journal for Numerical Methods in Engineering*, 8,461-480 (doi.org/10.1002/nme.1620080303).

Hofmann D. C., Suh J.Y., Wiest A., Duan G., Lind M. L., Demetriou M. D., Johnson W. L. (2008), Designing metallic glass matric composites with high toughness and tensile ductility, *Nature*, 451, 1085-1089 (doi.org/10.1038/nature06598).

Huang R., Suo Z., Prevost J., Nix W. D. (2002), Inhomogeneous deformation in metallic glasses, *Journal of the Mechanics and Physics of Solids*, 50, 1011-1027 (doi.org/10.1016/S0022-5096(01)00115-6).

Huang Y., Shen J., Sun Y., Sun J. (2010), Indentation size effect of hardness of metallic glasses, *Materials & Design*, 31, 1563-1566 (doi.org/10.1016/j.matdes.2009.09.046).

Ivanisenko Y., Kubel C., Nandam S. H., Wang C., Mu X., Adjaoud O., Albe K., Hahn H. (2018), Structure and properties of nanoglasses, *Advanced Engineering Materials*, 20,1800404 (doi.org/10.1002/adem.201800404).

Jang J. I., Yoo B. G., Kim Y. J., Oh J. H., Choi I. C., Bei H. (2011), Indentation size effect in bulk metallic glass, *Scripta Materialia*, 64, 753-756 (doi.org/10.1016/j.scriptamat.2010.12.036).

Jing J., Kramer A., Birringer R., Gleiter H., Gonser U. (1989), Modified atomic structure in Pd-Fe-Si nanoglass: a Mossbauer study, *Journal of Non Crystalline Solids*, 113, 167-170 (doi.org/10.1016/0022-3093(89)90007-0).

Jiang M. Q., Dai L. H. (2009), On the origin of shear banding instability in metallic glasses, *Journal of the Mechanics and Physics of Solids*, 57, 1267-1292 (doi.org/10.1016/j.jmps.2009.04.008).

Johnson K. L. (1970), The correlation of indentation experiments, *Journal of the Mechanics and Physics of Solids*, 18,115-126 (doi.org/10.1016/0022-5096(70)90029-3).

Johnson K. L. (1985), Contact mechanics, Cambridge: Cambridge University Press.

Keryvin V. (2007), Indentation of bulk metallic glasses: Relationships between shear bands observed around the prints and hardness, *Acta Materialia*, 55, 2565-2578 (doi.org/10.1016/j.actamat.2006.12.005).

Keryvin V. (2008), Indentation as a probe for pressure sensitivity of metallic glasses, *Journal of Physics: Condensed Matter*, 20, 114119 (doi.org/10.1088/0953-8984/20/11/114119).

Keryvin V., Prasad K. E., Gueguen Y., Sangleboeuf J. C., Ramamurty U. (2008), Temperature dependence of mechanical properties and pressure sensitivity in metallic glasses below glass transition, *Philosophical Magazine*, 88, 1773-1790 (doi.org/10.1080/14786430802286971).

Kim J.Y., Jang D., Greer J.R. (2011), Nanolaminates utilizing size-dependent homogeneous plasticity of metallic glasses, *Advanced Functional Materials*, 21, 4550-4554 (doi.org/10.1002/adfm.201101164).

Lam D. C. C., Chong A. C. M. (2001), Model and experiments on strain gradient hardening in metallic glass, *Materials Science and Engineering A*, 318, 313-319 (doi.org/10.1016/S0921-5093(01)01329-6).

Lee J. C., Park K. W., Kim K. H., Fleury E., Lee B. J., Wakeda M., Shibutani Y. (2007), Origin of the plasticity in bulk amorphous alloys, *Journal of Materials Research*, 22, 3087-3097 (doi.org/10.1557/jmr.2007.0382).

Lichinchi M., Lenardi C., Haupt J., Vitali R. (1998), Simulation of berkovinch nanoindentation experiments on thin films using finite element method, *Thin Solid Films*, 312, 240-248 (doi.org/10.1016/S0040-6090(97)00739-6).

Li F. C., Wang T. Y., He Q. F., Sun B. A., Guo C. Y., Feng T., Yang Y. (2018), Micromechanical mechanism of yielding in dual nano-phase metallic glass, *Scripta Materialia*, 154, 186-191 (doi.org/10.1016/j.scriptamat.2018.05.050).

Li H., Ghosh A., Han Y. H., Bradt R. C. (1993), The frictional component of the indentation size effect in low load microhardness testing, *Journal of Materials Research*, 8, 1028-1032 (doi.org/10.1557/JMR.1993.1028).

Li M. C., Jiang M. Q., Jiang F., He L., Sun J. (2017), Testing effects on hardness of a Zr-based metallic glass under nanoindentation, *Scripta Materialia*, 138, 120-123 (doi.org/10.1016/j.scriptamat.2017.05.046).

Li N., Chan K. C., Liu L. (2008), The indentation size effect in $Pd_{40}Cu_{30}Ni_{10}P_{20}$ bulk metallic glass, *Journal of Physics D: Applied Physics*, 41, 155415 (doi.org/10.1088/0022-3727/41/15/155415).

Li N., Liu L., Chan K. C. (2009), Deformation behavior and indentation size effect in amorphous and crystallized $Pd_{40}Cu_{30}Ni_{10}P_{20}$ alloy, *Journal of Materials Research*, 24,1693-1699 (doi.org/10.1557/jmr.2009.0222).

Liu L., Hasan M., Kumar G. (2014), Metallic glass nanostructure: fabrication, properties, and applications, *Nanoscale*, 6, 2027 (doi.org/10.1039/C3NR05645G).

Liu W. H., Sun B. A., Gleiter H., Lan S., Tong Y., Wang W. L., Hahn H. (2018), Nanoscale structural evolution and anomalous mechanical response of nanoglasses by cryogenic thermal cyling, *Nano Letters*, 18, 4188-4194 (doi.org/10.1021/acs.nanolett.8b01007).

Liu Z., Chen W., Carstensen J., Ketkaew J., Mota R. M. O., Guest J. K., Schroers J. (2016), 3D metallic glass cellular structures, *Acta Materialia*, 105, 35-43 (doi.org/ 10.1016/j.actamat.2015.11.057).

Lu J., Ravichandran G. (2003), Pressure-dependent flow behavior of $Zr_{41.2}Ti_{13.8}Cu_{12.5}Ni_{10}Be_{22.5}$ bulk metallic glass, *Journal of Materials Research*, 18, 2039-2049 (doi.org/10.1557/JMR.2003.0287).

Maaß R., Birckigt P., Borchers C., Samwer K., Volkert C.A. (2015), Long range stress fields and cavitation along a shear band in a metallic glass: the local origin of fracture, *Acta Materialia*, 98, 94-102 (doi.org/10.1016/j.actamat.2015.06.062).

Manika I., Maniks J. (2006), Size effects in micro- and nanoscale indentation, *Acta Materialia*, 54, 2049-2056 (doi.org/10.1016/j.actamat.2005.12.031).

Miracle D.B., Greer A.L., Kelton K.F. (2008), Icosahedral and dense random cluster packing in metallic glass structures, *Journal of Non Crystalline Solids*, 354, 4049-4055 (doi.org/10.1016/j.jnoncrysol.2008.05.006).

Nandam S. H., Ivanisenko Y., Schewaiger R., Snoadecki Z., Mu X., Wang D., Chellali R., Boll T., Kilmametov A., Bergfeldt T., Gleiter H., Hahn H. (2017), Cu-Zr nanoglasses: Atomic structure, thermal stability and indentation properties, *Acta Materialia*, 136, 181-189 (doi.org/10.1016/j.actamat.2017.07.001).

Nandam S. H., Adjaoud O., Schwaiger R., Ivanisenko Y., Chellali M. R., Wang D., Albe K., Hahn H. (2020), Influence of topological structure and chemical segregation on the thermal

and mechanical properties of Pd-Si nanoglasses, *Acta Materialia*, 193, 252-260 (doi.org/10.1016/j.actamat.2020.03.021)

Narasimhan R. (2004), Analysis of indentation of pressure sensitive plastic solids using the expanding cavity model, *Mechanics of Materials*. 36, 633-645 (doi.org/10.1016/S0167-6636(03)00075-9).

Narayan R. L., Tandaiya P., Garrett G. R., Demetriou M. D., Ramamurty U. (2015), On the variability in fracture toughness of 'ductile' bulk metallic glasses, *Scripta Materialia*, 102, 75-78 (doi.org/10.1016/j.scriptamat.2015.02.017).

Nix W. D., Gao H. (1998), Indentation size effect in crystalline materials: A law for strain gradient plasticity, *Journal of the Mechanics and Physics of Solids*, 46, 411-425 (doi.org/10.1016/S0022-5096(97)00086-0).

Oliver W. C., Pharr G. M. (2004), Measurement of hardness and elastic modulus by instrucmented indentation: Adavances in understanding and refinements to methodology, *Journal of Materials Research*, 19, 3-20 (doi.org/10.1557/jmr.2004.19.1.3).

Pang J. J., Tan M. J., Liew K. M., Shearwood C. (2012), Nanoindentation study of size effect and loading rate effect on mechanical properties of a thin film metallic glass $Cu_{49.3}Zr_{50.7}$, *Physics B: Condensed Matter*, 407, 340-346 (doi.org/10.1016/j.physb.2011.10.050).

Patnaik M. N. M., Narasimhan R., Ramamurty U. (2004), Spherical indentation response of metallic glasses, *Acta Materialia*, 52, 3335-3345 (doi.org/10.1016/j.actamat.2004.03.028).

Prasad K. E., Raghavan R., Ramamurty U. (2007), Temperature dependence of pressure sensitivity in metallic glass, *Scripta Materialia*, 57, 121-124 (doi.org/10.1016/j.scriptamat.2007.03.033).

Prasad K. E., Keryvin V., Ramamurty U. (2009), Pressure sensitive flow and constraint factor in amorphous materials below glass transition, *Journal of Materials Research*, 24, 890-897 (doi.org/10.1557/jmr.2009.0113).

Prasad K. E, Chollacoop N., Ramamurty U. (2011), Role of indenter angle on the plastic deformation underneath a sharp indenter and on representative strains: An experimental and numerical study, *Acta Materialia*, 59, 4343–4355 (doi.org/10.1016/j.actamat.2011.03.058).

Qiao J., Jia H., Liaw P.K. (2016), Metallic glass matrix composites, *Materials Science and Engineering R: Reports*, 100, 1-69 (doi.org/10.1016/j.mser.2015.12.001).

Ramamurty U., Jana S., Kawamura Y., Chattopadhyay K. (2005), Hardness and plastic deformation in a bulk metallic glass, *Acta Materialia*, 53, 705-717 (doi.org/10.1016/j.actamat.2004.10.023).

Rauf A., Guo C. Y., Fang Y. N., Yu Z., Sun B. A., Feng T. (2018), Binary Cu-Zr thin film metallic glasses with tunable nanoscale structures and properties, *Journal of Non Crystalline Solids*, 498, 95-102 (doi.org/10.1016/j.jnoncrysol.2018.06.015).

Rice J. R. (1968), Mathematical analysis in the Mechanics of fracture, In: Liebowitz H. (Ed.) Fracture Vol. II. Academic Press, New York.

Ritter Y., Sopu D., Gleiter H., Albe K. (2011), Structure, stability and mechanical properties of internal interface in $Cu_{64}Zr_{36}$ nanoglasses studied by MD simulations, *Acta Materialia*, 59, 6588-6593 (doi.org/10.1016/j.actamat.2011.07.013).

Rodriguez M., Molina-Aldareguia J. M., Gonzalez C., Llorca J. (2012), Determination of the mechanical properties of amorphous materials through instrumented nanoindentation, *Acta Materialia*, 60, 3953-3964 (doi.org/10.1016/j.actamat.2012.03.027).

Roy Y. A., Narasimhan R., Arora P.R. (1999), An experimental investigation of constraint effects on mixed mode fracture initiation in a ductile aluminium alloy, *Acta Materialia*, 47, 1587-1596 (doi.org/10.1016/S1359-6454(99)00015-4).

Sarac B., Ketkaew J., Popnoe D. O., Schroers J. (2012), Honeycomb structures of bulk metallic glasses, *Advanced Functional Materials*, 22, 3161-3169 (doi.org/10.1002/ adfm.201200539).

Sarac B., Schroers J. (2013b), From brittle to ductile: density optimization for Zr- BMG cellular structures, *Scripta Materialia*, 68, 921-924 (doi.org/10.1016/j. scriptamat.2013.02.030).

Schuh C. A., Lund A. C., Neih T. G. (2004), New regime of homogeneous flow in the deformation map of metallic glasses: Elevated temperature nanoindenation experiments and mechanistic modeling, *Acta Materialia*, 52, 5879-5891 (doi.org/10.1016/j.actamat.2004.09.005).

Schuh C. A., Nieh T. G.(2004), A survey of instrumented indentation studies on metallic glasses, *Journal of Materials Research*, 19, 46-57 (doi.org/10.1557/jmr.2004.19.1.46).

Schuh C.A., Hufnagel T.C., Ramamurty U. (2007), Mechanical behavior of amorphous alloy, *Acta Materialia*, 55, 4067-4109 (doi.org/10.1016/j.actamat.2007.01.052).

Sha Z. D., He L. C., Pei Q. X., Pan H., Liu Z. S., Zhang Y. W., Wang T. J. (2014), On the notch sensitivity of CuZr nanoglass, *Journal of Applied Physics*, 115, 163507 (doi.org/10.1063/1.4873238).

Sha Z. D., Branicil P. S., Pei Q. X., Liu Z. S., Lee H. P., Tay T. E., Wang T. J. (2015), Strong and surperplastic nanoglass, *Nanoscale*, 7, 17404-17409 (doi.org/10.1039/C5NR04740D).

Sha Z. D., Branicio P. S., Lee H. P., Tay T. E. (2017), Strong and ductile nanolaminate composites combining metallic glasses and nanoglasses, *International Journal of Plasticity*, 90, 231-241 (doi.org/10.1016/j.ijplas.2017.01.010).

Sharma A., Nandam S. H., Hahn H., Prasad K. E. (2021a), On the difference in shear band characteristics between a binary Pd-Si metallic and nanoglass, *Scripta Materialia*, 191, 17-22 (doi.org/10.1016/j.scriptamat.2020.09.009).

Sharma A., Nandam S. H., Hahn H., Prasad K. E. (2021b), Effect of structural relaxation on the indentation size effect and deformation behavior of Cu-Zr- Based Nanoglasses, *Frontiers in Materials*, 8, 1-10 (doi.org/10.3389/fmats.2021.676764).

Shete M. K., Singh I., Narasimhan R., Ramamurty U. (2016), Effect of strain hardening and volume fraction of crystalline phase on strength and ductility of bulk metallic glass composites, *Scripta Materialia*, 124, 51-55 (doi.org/10.1016/j.scriptamat.2016.06.020)

Shete M. K., Dutta T., Singh I., Narasimhan R., Ramamurty U. (2017), Tensile stress-strain response of metallic glass matrix composites reinforced with crystalline dendrites: Role of dendrite morphology, *Intermetallics*, 83,70-82 (doi.org/10.1016/j.intermet.2016.12.006).

Shao Y., Yang G. N., Yao K. F., Liu X. (2014), Direct experimental evidence of nano-voids formation and coalescence within shear bands, *Applied Physics Letters*, 105, 181909 (doi.org/10.1063/1.4901281).

Singh I., Narasimhan R., Zhang Y. W. (2014), Ductility enhancement in nanoglass: role of interaction stress between flow defects, *Philosophical Magazine Letters*, 94, 678-687 (doi.org/10.1080/09500839.2014.961584).

Singh I., Narasimhan R. (2016), Notch sensitivity in nanoscale metallic glass specimens: insights from continuum simulations, *Journal of the Mechanics and Physics of Solids*, 86,53-69 (doi.org/10.1016/j.jmps.2015.10.001).

Singh I., Narasimhan R., Ramamurty U. (2016), Cavitation-induced fracture causes nanocorrugations in brittle metallic glasses, *Physical Review Letters*, 117, 044302 (doi.org/10.1103/PhysRevLett.117.044302).

Singh I. (2016), Continuum analysis of cavitation induced failure and tensile deformation response of metallic glasses & nanoglasses, PhD Dissertation, *Indian Institute of Science.*

Sopu D., Albe K. Ritter Y., Gleiter H. (2009), From nanoglasses to bulk massive glasses, *Applied Physics Letters*, 94, 191911 (doi.org/10.1063/1.3130209).

Sopu D., Ritter Y., Gleiter H., Albe K. (2011), Deformation behavior of bulk and nanostructured metallic glasses studied via molecular dynamics simulations, *Physical Review B*, 83, 100202 (doi.org/10.1103/PhysRevB.83.100202).

Spaepen F. (1977), A microscopic mechanism for steady state inhomogeneous flow in metallic glasses, *Acta Metallurgica*, 25,407-415 (doi.org/10.1016/0001-6160(77)90232-2).

Steenberge N. V., Sort J., Concustell A., Das J., Scudino S., Surinach S., Eckert J., Baro M. D. (2007), Dynamic softening and indentation size effect in a Zr- based bulk glass-forming alloy, *Scripta Materialia*, 56, 605-608 (doi.org/10.1016/j.scriptamat.2006.12.014).

Su C., Anand L. (2006), Plane strain indentation of a Zr- based metallic glass: Experiments and numerical simulation, *Acta Materialia*, 54, 179-189 (doi.org/10.1016/j.actamat.2005.08.040).

Subhash G., Dowding R. J., Kecskes L. J. (2002), Charcterization of uniaxial compressive response of bulk amorphous Zr-Ti-Cu-Ni-Be alloy, *Materials Science and Engineering A*, 334, 33-40 (doi.org/10.1016/S0921-5093(01)01768-3).

Subramanya H. Y., Viswanath S., Narasimhan R. (2009), Constraint effects on multiple voids interaction in pressure sensitive plastic solids, *Engineering Fracture Mechanics*, 76, 1049-1073 (doi.org/10.1016/j.engfracmech.2009.01.007).

Symington M., Shih C. F., Ortiz M. (1998), Tables of plane strain HRR fields, Tech. Rep. MRG/DMR-8714665/1, Brown University, Providence, RI, USA.

Tandaiya P., Narasimhan R., Ramamurty U. (2007), Mode I crack tip fields in amorphous materials with application to metallic glasses, *Acta Materialia*, 55,6541-6552 (doi.org/10.1016/j.actamat.2007.08.017).

Tandaiya P., Ramamurty U., Ravichandran G., Narasimhan R. (2008), Effect of poisson's ratio on crack tip fields and fracture behavior of metallic glasses, *Acta Materialia*, 56,6077-6086 (doi.org/10.1016/j.actamat.2008.08.018).

Tandaiya P., Ramamurty U., Narasimhan R. (2009), Mixed mode (I and II) crack tip fields in bulk metallic glasses, *Journal of the Mechanics and Physics of Solids*, 57, 1880-1897 (doi.org/10.1016/j.jmps.2009.07.006).

Tandaiya P., Ramamurty U., Narasimhan R. (2011), On numerical implementation of an isotropic elastic-viscoplastic constitutive moel for bulk metallic glasses, *Modelling and Simulation in Materials Science and Engineering*, 19, 015002 (doi.org/10.1088/0965-0393/19/1/015002).

Tandaiya P., Narasimhan R., Ramamurty U. (2013), On the mechanism and the length scales involved in the ductile fracture of a bulk metallic glass, *Acta Materialia*, 61, 1558-1570 (doi.org/10.1016/j.actamat.2012.11.033).

Telford M. (2004), The case for bulk metallic glass, *Materials Today*, 7, 36-43 (doi.org/10.1016/S1369-7021(04)00124-5).

Thamburaja P., Ekambaram R. (2007), Coupled thermo-mechanical modelling of bulk-metallic glasses: Theory, finite-element simulations and experimental verification, *Journal of the Mechanics and Physics of Solids*, 55, 1236-1273 (doi.org/10.1016/j.jmps.2006.11.008).

Thamburaja P. (2011), Length scale effect on the shear localization process in metallic glasses: A theoretical and computational study, *Journal of the Mechanics and Physics of Solids*, 59, 1552-1575 (doi.org/10.1016/j.jmps.2011.04.018).

Thamburaja P., Liu J. (2014), Effect of microscopic boundary conditions on the deformation behavior of small-volume metallic glasses, *International Journal of Solids and Structures*, 51, 4580-4595 (doi.org/10.1016/j.ijsolstr.2014.09.011).

Vaidyanathan R., Dao M., Ravichandran G., Suresh S. (2001), Study of mechanical deformation in bulk metallic glass through instrumented indentation, *Acta Materialia*, 39, 898-1015 (doi.org/10.1016/S1359-6454(01)00263-4).

Wang X., Zhang W., Zhao Y., Bei H., Gao Y. (2020), Micromechanocal investigation of the role of percolation on ductility enhancement in metallic glass composites, *Materials Science and Engineering A*, 769, 138531-138541 (doi.org/10.1016/j.msea.2019.138531).

Wang X. L., Jiang F., Hahn H., Li J., Gleiter H., Sun J., Fang J. X. (2015), Plasticity of a scandium-based nanoglass, *Scripta Materialia*, 98, 40-43 (doi.org/10.1016/j.scriptamat.2014.11.010).

Wang X.L., Jiang F., Hahn H., Li J., Gleiter H., Sun J., Fang J. X. (2016), Sample size effects on strength and deformation mechanism of Sc75Fe25 nanoglass and metallic glass, *Scripta materialia*, 116, 95–99 (doi.org/10.1016/j.scriptamat.2016.01.036).

Wright W. J., Saha R., Nix W.D. (2001), Deformation mechanisms of the $Zr_{40}Ti_{14}Ni_{10}Cu_{12}Be_{24}$, *Materials Transactions Japan Institute of metals*, 42, 642-649 (doi.org/10.2320/matertrans.42.642).

Xu F., Ding Y. H., Deng X. H., Zhang P., Long Z. L. (2014), Indentation size effect in the nano- and micro-hardness of Fe-based bulk metallic glass, *Physica B: Condensed Matter*, 450, 84-89 (doi.org/10.1016/j.physb.2014.05.057).

Xue F., Wang F., Huang P., Lu T. J., Xu K. W. (2016), Structural inhomogeneity and strain rate dependent indentation size effect in Zr- based metallic glass, *Materials Science and Engineering A*, 655, 373-378 (doi.org/10.1016/j.msea.2015.12.083).

Yang F., Geng K., Liaw P. K., Fan G., Choo H. (2007), Deformation in a Zr_{57} $Ti_5Cu_{20}Ni_8Al_{10}$ bulk metallic glass during nanoindentation, *Acta Materialia*, 55, 321-327 (doi.org/10.1016/j.actamat.2006.06.063).

Yang Q., Mota A., Ortiz M. (2006), A finite-deformation constitutive model of bulk metallic glass plasticity, *Computational Mechanics*, 37, 194-204 (doi.org/10.1007/s00466-005-0690-5)

Yoo B. G., Kim Y. J., Oh J. H., Ramamurty U. (2009), On the hardness of shear bands in amorphous alloys, *Scripta Materialia*, 61, 951-954 (doi.org/10.1016/j.scriptamat.2009.07.037).

Zhang J. C., Chen C., Pei Q. X., Wan Q., Zhang W. X., Sha Z. D. (2016), Deformation and failure mechanisms of nanoscale cellular structures of metallic glasses, *RSC Adavances*, 6, 100899-100907 (doi.org/10.1039/c6ra22483k).

Zhang L., Cheng Y. Q., Cao A. J., Xu J., Ma E. (2009), Bulk metallic glasses with large plasticity: composition design from the structural perspective, *Acta Materialia*, 57, 1154-1164 (doi.org/10.1016/j.actamat.2008.11.002).

Zhong C., Zhang H., Cao Q. P., Wang X. D., Zhang D. X., Ramamurty U., Jiang J. Z. (2016), On the critical thickness for non localized to localized plastic flow transition in metallic glasses: a molecular dynamics study, *Scripta Materialia*, 114, 93-97 (doi.org/10.1016/j.scriptamat.2015.12.012).

Zhou Q., Du Y., Han W., Ren Y., Zhai H., Wang H. (2019), Identifying the origin of strain rate sensitivity in a high entropy bulk metallic glass, *Scripta Materialia*, 164, 121-125 (doi.org/10.1016/j.scriptamat.2019.02.002).